



UNIVERSITY OF NAIROBI

**STRUCTURAL, ELECTRONIC
AND MAGNETIC PROPERTIES OF
 X_2YZ HEUSLER COMPOUNDS Mn_2VZ ($Z = Al, In$), Co_2YIn ($Y = V, Nb, Ti$)
AND XYZ HALF HEUSLER COMPOUNDS $CoYIn$ ($Y = V, Nb, Ti$)
FOR SPINTRONIC APPLICATION**

**BY
MUTHUI ZIPPORAH WANJIKU**

I80/96929/2014

**A Thesis Submitted in Fulfilment of the Requirements for Award of the
Degree of Doctor of Philosophy in Physics of the University of Nairobi**

December, 2017

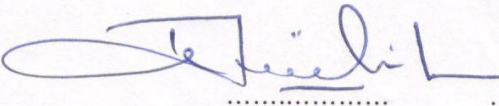
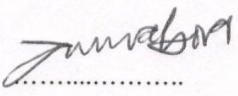
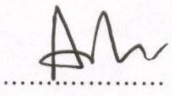
DECLARATION

I declare that this thesis is my original work and has not been submitted elsewhere for examination, the award of a degree or publication. Where other people's work or my own work has been used, this has properly been acknowledged and referenced in accordance with the University of Nairobi's requirements.

Signature Muthui Date 11/12/2017

Muthui Zipporah Wanjiku
I80/96929/2014
Department of Physics
School of Physical Sciences
University of Nairobi

This thesis is submitted for examination with our approval as research supervisors:

	Signature	Date
Dr Robinson Musembi Department of Physics University of Nairobi P.O Box 30197-00100 Nairobi Kenya musembirj@uonbi.ac.ke		<u>11/12/2017</u>
Prof. Julius Mwabora Department of Physics University of Nairobi P.O Box 30197-00100 Nairobi Kenya mwabora@uonbi.ac.ke		<u>11.12.2017</u>
Prof. Arti Kashyap School of Basic Sciences Indian Institute of Technology Mandi Mandi – 175001, HP, India. arti@iitmandi.ac.in		<u>11/12/2017</u>

DEDICATION

To God be the glory, great things He has done

ACKNOWLEDGEMENTS

First and foremost, I acknowledge that Almighty God has been the master planner of my studies, placing several special people and opportunities in my path that have been the pillars in the pursuit and completion of my studies.

My host supervisor at the Indian Institute of Technology, Mandi, Prof. Arti Kashyap, the words ‘you can make it’ coming from you, carried immense power that fuelled and multiplied my efforts. Prof. Arti not only introduced me into computational physics, but with great skill, understanding and encouragement, guided me through. In the same breath, I deeply appreciate my home supervisors at the University of Nairobi, Prof. Julius Mwabora and Dr Robinson Musembi. Words cannot express my gratitude to you for your support. I can only say thank you very much to you and the University of Nairobi for granting me your invaluable support.

Special thanks and deep gratitude to Prof. Arti’s research group members, from whom I learnt a lot and enjoyed great hospitality. Thanks to Dr Murkherjee of IIT, Mandi for allowing me to prepare my samples in his laboratory, and for personally assisting me to do so together with Mr Mohit. I also take this opportunity to thank IIT, Mandi, for hosting me during my research visits. It is rare that one would accept to offer assistance in the characterisation of samples to a total stranger, with no reference at all, this is exactly what Prof. Mao and Dr Li of Tulane University, New Orleans, USA did for me. I will always be deeply grateful to you.

I will always cherish the invaluable support I have continued to receive from Chuka University, my employer, who granted me study leave and extended great support to me in allowing me time off to concentrate on my studies, gratefully acknowledged is Dr Ombaka, my Head of Department.

I owe special gratitude to OWSD for funding my studies and stay at IIT, Mandi during the sandwich programme and DAAD for funding my studies at University of Nairobi and research visit at University of Duisburg-Essen, Germany.

Many people contributed directly and indirectly to this work and I would wish to thank you all, for this could not have been possible without you.

Finally, my deep gratitude goes to my loving and very supportive family; Steve, John and Job, who allowed me to be away, making great sacrifices to cope in my absence. I will forever be deeply indebted and grateful to you.

ABSTRACT

Heusler compounds have been predicted to be half-metallic possessing integer magnetic moments due to complete spin polarisation at the Fermi level, a property highly desirable in spintronics. However, there are yet to be any reports of 100% spin polarisation experimentally. In order to realise this predicted property and to avail these materials as a viable spin source, their structural properties need to be optimised. In this study, the structural, electronic and magnetic properties of selected Manganese (Mn) and Cobalt (Co) Heusler compounds have been investigated using Density Functional Theory (DFT) as implemented in the Vienna ab Initio Simulation package (VASP). In addition, polycrystalline samples were prepared by arc melting and their structural and magnetic properties were studied using magnetometry and electron microscopy techniques. The optimised lattice constants for Mn_2VAl is 5.800\AA while those of Mn_2VIn , Co_2VIn and Co_2NbIn are 6.250\AA , 6.000\AA and 6.200\AA , respectively, with band structures having small band gap energies in one of the spin channels of approximately 0.2 eV and integer magnetic moments of $2\ \mu_B$ as predicted by the Slater-Pauling rule. While full-Heuslers Mn_2VAl , Co_2VIn and Co_2NbIn and half Heusler $CoVIn$ are predicted to be half-metallic at the optimised lattice constants, Mn_2VIn is half-metallic at a reduced lattice constant of 6.000\AA and displays additional properties such as tetragonal distortion and perpendicular magnetic anisotropy energy of 96.800 meV when doped with Co as well as $2.090\text{meV} - 6.790\text{ meV}$ for angstrom and nanometer range thickness Mn_2VIn films. While Co_2TiIn has a pseudo gap in the minority spin channel, the half-Heuslers $CoTiIn$ and $CoNbIn$ are found to be metallic. Single phase $L2_1$ structure for Mn_2VAl and multiple cubic and tetragonal phases in Co_2VIn and Mn_2VIn were detected in the arc melted samples by XRD using Cu-K α radiation and quantitative analysis and phase separation done by Rietveld refinement using the FullProf software. The lattice parameters for Mn_2VAl , Co_2VIn and Mn_2VIn are 5.900\AA , 5.890\AA and 5.830\AA respectively, which are comparable to the optimised values especially for Mn_2VAl and Co_2VIn . Composition and homogeneity were determined using Energy dispersive X-ray (EDX) spectroscopy and the scanning electron microscope (SEM), in which non-stoichiometric compounds $Mn_{1.79}VAl_{1.14}$, $Co_{1.8}VIn_{0.1}$ and $Mn_{2.29}V_{0.6}In$ were found due to In melting separately and V segregation in the In based compounds. $Mn_{1.79}VAl_{1.14}$ was found to have a coercivity of $5.370 \times 10^{-3}\text{ T}$ and a saturation magnetisation of $1.740\ \mu_B/f.u.$, while the coercivity of $Co_{1.8}VIn_{0.1}$ is $3.400 \times 10^{-2}\text{ T}$ and magnetisation of $5.767 \times 10^{-4}\ \mu_B/f.u.$ Mn-V-In displayed martensitic and superparamagnetic characteristics with a blocking temperature of 40 K , a remanent magnetisation of $0.500\ \mu_B/f.u.$ at 2 K and a coercive field of $4.678 \times 10^{-1}\text{ T}$. The versatility of Heusler compounds has been displayed in this work with the compounds showing from ab initio investigations, highly relevant properties to technology such as half-metallic near antiferromagnetism from Co doping, superparamagnetism, martensitic transformation and volume derived magnetic anisotropy in Mn_2VIn , while in Co_2YIn ($Y = V, Nb, Ti$), half-metallicity has been displayed.

PUBLICATIONS

1. Structural, Electronic and Magnetic Properties of the Heusler Alloy Mn_2VIn : A Combined DFT and Experimental Study. Zipporah W. Muthui, Robinson Musembi, Julius Mwabora, Ralph Skomski and Arti Kashyap. *IEEE Transactions on Magnetics*. (2017). DOI: 10.1109/TMAG.2017.2756618.
2. Perpendicular magnetic anisotropy in Mn_2VIn (001): *ab initio* study. Zipporah W. Muthui, Robinson Musembi, Julius Mwabora and Arti Kashyap. *AIP Advances*, Volume 8 Issue 5, 2017.
3. Perpendicular Magnetic anisotropy in nearly fully compensated Ferrimagnetic Heusler alloy $Co_{1.75}Mn_{0.25}VIn$: An *ab initio* study. Zipporah W. Muthui, Robinson Musembi, Julius Mwabora and Arti Kashyap. *Journal of Magnetism and Magnetic Materials* Volume 442, 2017.
4. First-Principle investigation of the structural, electronic and magnetic properties of Co_2VIn and $CoVIn$ Heusler compounds. Zipporah W. Muthui, Rohit Pathak, Robinson Musembi, Julius Mwabora, Ralph Skomski and Arti Kashyap. *AIP Advances*, Volume 7 , Issue 5, 2017.

TABLE OF CONTENTS

DECLARATION	ii
ABSTRACT	v
PUBLICATIONS	vi
LIST OF TABLES	xi
LIST OF FIGURES	xii
LIST OF ABBREVIATIONS AND SYMBOLS	xvii
CHAPTER 1: INTRODUCTION	1
1.1: Background of the Study	1
1.2: Statement of the Problem	7
1.3: Objectives	7
1.3.1: <i>General Objective</i>	7
1.3.2: <i>Specific Objectives</i>	8
1.4: Justification and Significance	8
CHAPTER 2: LITERATURE REVIEW	10
2.1: Theoretical and Experimental Studies on Heusler Compounds	10
2.2: Heusler Structure	17
2.3: Electronic Structure of Compounds	19
2.4: Magnetic Properties of Compounds	19
2.5: Magnetic Anisotropy	21
CHAPTER 3: THEORETICAL FRAMEWORK	23
3.1: The Schrödinger Equation	23
3.1.1: <i>Born – Oppenheimer Approximation</i>	23
3.1.2: <i>Hartree Fock (H-F) Method</i>	25
3.2: Density Functional Theory (DFT)	26
3.3: Approximation of the Unknown Exchange Correlation Functional	29
3.4: Band Calculations in Perfect Crystals	31
3.5: Pseudopotential (PP) method	31
3.6: Augmented Plane Wave Method	32
3.7: Projector Augmented Wave (PAW) Method	33

3.8: Computational Techniques	33
3.9: Experimental Techniques	37
3.9.1: <i>Arc Melting</i>	38
3.9.2: <i>X-ray diffraction (XRD) Analysis</i>	39
3.9.3: <i>Energy Dispersive X-ray (EDX) Spectrometry</i>	40
3.9.4: <i>Scanning Electron Microscope (SEM)</i>	42
3.9.5: <i>Superconducting quantum interference device (SQUID)</i>	43
CHAPTER 4: METHOD AND MATERIALS.....	45
4.1: Computational Method – Vienna ab initio simulation package (VASP).....	45
4.1.2: <i>Convergence tests</i>	50
4.1.2.1: <i>Convergence of k Points</i>	51
4.1.2.2: <i>Convergence with respect to the cut off energy</i>	51
4.1.3: <i>Relaxation of unit cells and super cells</i>	52
4.1.4: <i>Structure Optimisation</i>	53
4.1.5: <i>Electronic Structure and Magnetic Properties</i>	53
4.1.6: <i>Magnetic Anisotropy Energy (MAE) calculations</i>	54
4.1.7: <i>Supercell calculations</i>	54
4.2: Materials	54
4.3: Experimental Method	57
4.3.1: <i>Preparation of samples by arc melting</i>	57
4.3.2: <i>XRD Analysis</i>	59
4.3.3: <i>EDX Spectroscopy on the SEM Analysis</i>	60
4.3.4: <i>SQUID Magnetometry</i>	60
5.0. RESULTS AND DISCUSSION	62
5.1: Structural, Electronic and Magnetic Properties of Mn ₂ VAl and Mn ₂ VIn	62
5.1.1: <i>Structural Properties</i>	62
5.1.2: <i>Electronic properties</i>	67
5.1.3: <i>Magnetic properties</i>	74
5.2: Half-metallicity in Mn ₂ VIn by Co Doping in Mn sites.	76
5.2.1 <i>Electronic and Structural Properties</i>	76
5.2.2 <i>Magnetic Properties</i>	81

5.3: Half-Metallic Co_2VIn and CoVIn Heuslers.....	84
5.3.1: <i>Structural properties</i>	84
5.3.2: <i>Electronic Properties</i>	87
5.3.3: <i>Magnetic Properties</i>	91
5.4: Structural Characterisation of Mn-V-Al and X-V-In (X=Co,Mn)	96
5.5: Magnetic Properties of $\text{Mn}_{1.79}\text{VAl}_{1.14}$, $\text{Co}_{1.8}\text{VIn}_{0.1}$ and Mn-V-In.....	103
5.6: Electronic and Magnetic Properties of Co_2YIn (Y=Nb, Ti) and CoYIn (Y = Nb, Ti)	
.....	111
5.6.1: <i>Structural properties</i>	111
5.6.2: <i>Electronic Properties</i>	111
5.6.3: <i>Magnetic Properties</i>	117
5.7: Structural, Electronic and Magnetic properties of X_2VIn (X=Co, Mn) (001) thin films	118
5.7.1: <i>Structural Properties</i>	118
5.7.2: <i>Electronic Properties</i>	124
5.7.3: <i>Magnetic Properties</i>	131
6.0: CONCLUSIONS AND RECOMMENDATIONS	134
7.0 REFERENCES	138
APPENDIX.....	150
Appendix 1 - POSCAR FILE	150
Appendix 2 - KPOINTS File	151
Appendix 3 - k points convergence for the X_2YZ and XYZ Heusler systems	152
Appendix 4 - Cut off energy convergence for the X_2YZ and XYZ Heusler systems.....	153
Appendix 5 - Space group information.....	154

LIST OF TABLES

Table 5.1: The calculated results for spin polarisation and atom resolved magnetic moments at the lattice constants of the relaxed structures of $Mn_{2-x}Co_xVIn$ compounds.....	82
Table 5.2: The calculated results for spin Polarisation and Band Gaps for Co_2VIn and $CoVIn$ obtained using L(S)DA, L(S)DA+U, GGA, GGA+U, PBE-GGA and PBE-GGA+U.....	90
Table 5.3 (a): The calculated results for magnetic moments for Co_2VIn and $CoVIn$ obtained using L(S)DA, L(S)DA+U, GGA, GGA+U, PBE-GGA and PBE-GGA+U approximations.....	94
Table 5.3 (b): The calculated results for magnetic moments for Co_2VIn and $CoVIn$ obtained using L(S)DA, L(S)DA+U, GGA, GGA+U, PBE-GGA and PBE-GGA+U approximations.....	94
Table 5.4: Composition of Mn-V-Al sample	99
Table 5.5: Composition of first phase in Mn-V-In.....	99
Table 5.6: Composition of the second phase in Mn-V-In.....	100
Table 5.7: Composition of the third phase in Mn-V-In.....	101
Table 5.8: Composition of Co-V-In sample.....	101
Table 5.9: Spin polarisation, Band gap energies, Total and atomic magnetic moments of the Heusler compounds.....	117
Table 5.10: Co_2VIn Supercell dimensions after relaxation.....	121
Table 5.11: Mn_2VAl Supercell dimensions after relaxation.....	122
Table 5.12: Mn_2VIn Supercell dimensions after relaxation.....	122
Table 5.13: Magnetic moments for Co_2VIn , Mn_2VIn and Mn_2VAl films of different thickness as well as for each atom in the system.....	131
Table 5.14: Orbital magnetic moments for Co, Mn, V and In as well as magnetic anisotropy energy for the thin films.....	132

LIST OF FIGURES

Figure 2.1: B2 Structure: Prototype CsCl structure. Source (Pauling <i>et al.</i> , 1993).....	17
Figure 2.2: L2 ₁ Structure: Prototype Cu ₂ MnAl – Heusler: Source (Pauling <i>et al.</i> , 1993).....	18
Figure 3.1: Pseudopotential used to represent core electrons. Source: (Segall M. 1997) http://www.tcm.phy.cam.ac.uk/~mds21/thesis/thesis.html	32
Figure 3.2: The Brillouin zone of an fcc structure showing the origin at $\Gamma = 0$	36
Figure 3.3: Photograph of the Arc melting furnace at IIT, Mandi Laboratory	38
Figure 3.4: The main parts of a Scanning Electron Microscope.Source (Ford <i>et al.</i> , 2010)	41
Figure 3.5: Josephson junction.Source: http://hyperphysics.phy-astr.gsu.edu/hbase/Solids/Squid.html#c3	44
Figure 4.1: Flow of programs in the self consistent solution of the Kohn – Sham equations (Kresse <i>et al.</i> , 2016).....	46
Figure 4.2: Flow diagram showing the major calculations carried out and their output	55
Figure 4.3: Digital LMUC series Spectrachrom Instruments ultrasonic cleaner.....	58
Figure 4.4: Samples in the arc melting furnace before melting	58
Figure 4.5: (a) Arc melting in progress (b) close up view of melting metals and (c) the resulting ingot	58
Figure 4.6: sealing of ingots in quartz tubes for annealing.....	59
Figure 4.7 (a) Photograph of the XRD machine RIGAKU D-2000 available at IIT, Mandi, a view of the inside showing (b) the source of Xrays, (c) the sample stage and (d) the detector and low temperature facility	59
Figure 5.1 (a): Mn ₂ VZ in the Cu ₂ MnAl structure with Wyckoff positions (0.25, 0.25, 0.25), (0.5, 0.5, 0.5) and (0,0,0) for Mn , V and In respectively and (b) the Hg ₂ TiCu structure for Mn ₂ VZ (Z = Al, In) with Wyckoff positions (0.25, 0.25, 0.25) and (0.5, 0.5, 0.5) for Mn and (0,0,0) and (0.75, 0.75, 0.75) for Z and V respectively.....	63
Figure 5.2 (a): Tetrahedral Zinc blende structure and (b) the rock salt structure Source: Graf <i>et al.</i> , 2011	64
Figure 5.3: The energy for the Hg ₂ TiCu and Cu ₂ MnAl crystal structures for (a) Mn ₂ VAl and (b) Mn ₂ VIn.....	65
Figure 5.4: Volume optimization for (a) Mn ₂ VAl and (b) Mn ₂ VIn	66

Figure 5.5: Total density of states (TDOS) and partial density of states (PDOS) for Mn ₂ VAl. Inset shows a blow up of the <i>d</i> , <i>p</i> and <i>s</i> states of Al near the Fermi level	67
Figure 5.6: Total density of states (TDOS) and partial density of states (PDOS) for Mn ₂ VIn	69
Figure 5.7: Total density of states (TDOS) for Mn ₂ VIn at lattice constant $a = 6 \text{ \AA}$	69
Figure 5.8: Total density of states (TDOS) for Mn ₂ VIn at lattice constant $a = 5.95 \text{ \AA}$	70
Figure 5.9: Total density of states (TDOS) and partial density of states (PDOS) for Mn ₂ VIn at $a = 5.83 \text{ \AA}$	71
Figure 5.10: Total energy as a function of <i>c/a</i> ratio for (a) Mn ₂ VAl and (b) Mn ₂ VIn. Inset is the line graph without smoothening, emphasizing the two minima	72
Figure 5.11: Total density of states (TDOS) for tetragonally distorted Mn ₂ VIn at $c/a=0.93$	73
Figure 5.12: Total density of states plots (TDOS) for (a) Mn _{1.75} Co _{0.25} VIn and (b) Mn _{1.5} Co _{0.5} VIn. Inset in each figure is the corresponding structure showing the impurity Co atom in Mn sites...	77
Figure 5.13: Total density of states plots (TDOS) for (a) Mn _{1.25} Co _{0.75} VIn and (b) Mn _{0.75} Co _{1.25} VIn. Inset in each figure is the corresponding structure showing the impurity Co atom in Mn sites	78
Figure 5.14: Total density of states plots (TDOS) for (a) Mn _{0.5} Co _{1.5} VIn and (b) Mn _{0.25} Co _{1.75} VIn. Inset in each figure is the corresponding structure showing the impurity Co atom in Mn sites...	79
Figure 5.15: Total density of states plot (TDOS) for Mn _{0.25} Co _{1.75} VIn	80
Figure 5.16: Total density of states (TDOS) and partial density of states (PDOS) for Mn _{0.25} Co _{1.75} VIn	81
Figure 5.17(a): Relaxed Structure of Co ₂ VIn - L2 ₁ structure with Wyckoff position 8c ($\frac{1}{4}, \frac{1}{4}, \frac{1}{4}$) for the two Co atoms, 4a (0,0,0) and 4b ($\frac{1}{2}, \frac{1}{2}, \frac{1}{2}$) for In and V atoms respectively, space group Fm-3m, space group no. 225 and (b) Relaxed Structure of CoVIn. One of the ($\frac{1}{4}, \frac{1}{4}, \frac{1}{4}$) site for one of the Co atoms is vacant resulting in a Cl _b structure space group F-43m, space group no. 216	85
Figure 5.18 (a): Ferromagnetic and paramagnetic volume optimization for Co ₂ VIn and (b) Ferromagnetic and paramagnetic volume optimization for CoVIn	86
Figure 5.19 (a): Total density of states (TDOS) for Co ₂ VIn using the LDA approximation, (b) Total density of states (TDOS) for Co ₂ VIn using the GGA approximation, (c) Total density of states (TDOS) for Co ₂ VIn using PBE-GGA and (d) Total density of states (TDOS) for Co ₂ VIn using DFT+U method.	87

Figure 5.20 (a): Spin down electronic band structure of Co_2VIn at the equilibrium lattice parameter using GGA+U and (b) Spin up electronic band structure of Co_2VIn at the equilibrium lattice parameter using GGA+U approximation	89
approximation	89
Figure 5.21: TDOS and Partial DOS for Co_2VIn for Co, V and In using PBE-GGA approximation	90
Figure 5.22 (a): Total density of states (TDOS) for CoVIn using PBE-GGA approximation and (b) Total density of states (TDOS) for CoVIn using GGA +U approximation	91
Figure 5.23 (a): Spin up electronic band structure of CoVIn at the equilibrium lattice parameter using GGA+U and (b) Spin down electronic band structure of CoVIn at the equilibrium lattice parameter using GGA+U approximation.....	92
Figure 5.24: TDOS and Partial DOS for CoVIn for Co, V and In using PBE-GGA approximation	93
Figure 5.25: XRD pattern and difference plot for Mn-V-Al obtained after Rietveld refinement. The black line is the calculated pattern, the red line the experimental data and the blue line the difference between the two	96
Figure 5.26: XRD pattern and difference plot for Co-V-In obtained after Rietveld refinement. The black line is the calculated pattern, the red line the experimental data and the blue line the difference between the two	96
Figure 5.27: XRD pattern and difference plot for Mn-V-In obtained after Rietveld refinement. The black line is the calculated pattern, the red line the experimental data and the blue line the difference between the two	97
Figure 5.28: SEM and EDX results for Mn-V-Al ingot.	98
Figure 5.29: SEM and EDX results for the first phase in Mn-V-In ingot.	99
Figure 5.30: SEM and EDX results for the second phase in Mn-V-In ingot.....	100
Figure 5.31: SEM and EDX results for the third phase in Mn-V-In ingot.	100
Figure 5.32: SEM and EDX results for Co-V-In ingot.....	101
Figure 5.33: Variation of magnetic moment with applied magnetic field at 10K for $\text{Mn}_{1.79}\text{VAl}_{1.14}$	103
Figure 5.34: Variation of magnetic moment with applied magnetic field at 250 K for $\text{Mn}_{1.79}\text{VAl}_{1.14}$	103

Figure 5.35: ZFC and FC curves for $Mn_{1.8}VAl_{1.14}$	104
Figure 5.36: Variation of magnetic moment with applied magnetic field at 2K for (a) $Co_{1.8}VIn_{0.1}$ and (b) Mn-V-In.....	105
Figure 5.37: Variation of magnetic moment with applied magnetic field at 400K for (a) $Co_{1.8}VIn_{0.1}$ and (b) Mn-V-In	107
Figure 5.38: ZFC and FC curves for (a) $Co_{1.8}VIn_{0.1}$ and (b) Mn-V-In.....	108
Figure 5.39 (a): Total density of states (TDOS) for Co_2NbIn using PBE-GGA approximation and (b) band structure of minority states of Co_2NbIn	112
Figure 5.40: Total density of states (TDOS) and PDOS for Co_2NbIn using PBE-GGA approximation	113
Figure 5.41: Total density of states (TDOS) for Co_2TiIn using PBE-GGA approximation.....	113
Figure 5.42: Total density of states (TDOS) and PDOS for Co_2TiIn using PBE-GGA approximation	114
Figure 5.43(a): Minority states band structure and (b) Majority states band structure for $CoTiIn$	115
Figure 5.44: Total density of states (TDOS) for (a) Co_2TiIn and (b) $CoTiIn$ using PBE-GGA approximation	116
Figure 5.45: Total density of states (TDOS) and PDOS for $CoTiIn$ using PBE-GGA approximation.	116
Figure 5.46: Co_2VIn supercell of thickness 6 Å corresponding to one unit cell thickness grown in the z direction. A vacuum of 12Å is applied in the z direction	118
Figure 5.47: Supercells for (001) films having (a) 5 monolayers (ML's), (b) 9 ML's and (c) 13 ML's.....	119
Figure 5.48: Relaxed Co_2VIn supercells. All of them are tetragonally distorted from the bulk dimensions following a reduction in the a and b parameter, while the c parameter increases in each case.	120
Figure 5.49: Relaxed Mn_2VAl supercells. All of them are tetragonal following a slight reduction in the a and b parameter, while the c parameter increases in each case.	121
Figure 5.50: Relaxed 5, 9 and 13 ML Mn_2VIn supercells. The a and b parameters decrease, while the c parameter increases in each case	123

Figure 5.51: Total density of states (TDOS) for (a) 5 ML thick Co_2VIn and (b) 9 ML thick Co_2VIn film.....	125
Figure 5.52: Total density of states (TDOS) for 13 ML thick Co_2VIn film.....	126
Figure 5.53: Total density of states (TDOS) for 5 ML thick Mn_2VAl film.....	126
Figure 5.54: Total density of states (TDOS) for (a) 9 ML Mn_2VAl and (b) 13 ML thick Mn_2VAl films	128
Figure 5.55: Total density of states (TDOS) for (a) 5 ML thick Mn_2VIn and (b) and 9 ML thick Mn_2VIn films	129
Figure 5.56: Total density of states (TDOS) for (a) 13 ML thick Mn_2VIn and (b) and tetragonally distorted Mn_2VIn bulk system	130

LIST OF ABBREVIATIONS AND SYMBOLS

APW	Augmented plane wave method
B3LYP	Beke, 3 – parameter, Lee Yang-Parr
C_{st}	Concentration of element in calibration standard
DFT	Density functional theory
DFT + U	Density functional theory with Coulomb interaction
DIPS	Digital Image Processing System
DMFT	Dynamical mean field theory
EDX	Energy Dispersive X-ray
E_{max}	Energy of accelerated electron beam
FC	Field Cooled
FPLO	Full Potential non-orthogonal local orbital
FP – LAPW	Full-potential linearized augmented plane wave
GGA	Generalized gradient approximation
GMR	Giant magneto resistance
GW	Green's function and dynamically screened coulomb interaction
H-F	Hatree Fock
HSE	Heyd – Scuseria – Ernzerhof
I_{sp}	X-ray Intensities of elements in sample
I_{st}	X-ray Intensities of elements in calibration standard
INCAR	VASP input file with computational parameters
KPOINTS	VASP input file with k points in reciprocal space
LCAO	Linear combination of atomic orbitals
LDA	Local density approximation
LDA+U	Local density approximation with Coulomb interaction
LMTO	Linear Muffin Tin Orbital
LSDA	Local spin density approximation

MEMS	Microelectomechanical systems
MP	Monkhorst-Pack
MR	Magneto resistance
MRAM	Magneto resistive random access memory
MTJ	Magnetic Tunnelling Junction
NMR	Nuclear Magnetic Resonance
OPW	Orthogonal plane wave
OSZICAR	VASP summary output file
OUTCAR	VASP detailed output file
PBE	Perdew Burke Ernzerhof
PDOS	Partial Density of States
PMA	Perpendicular Magnetic Anisotropy
POSCAR	VASP input file with system geometry details
POTCAR	VASP input file with system potentials
R.A.M	Relative Atomic Mass
SDFT	Spin Density Function Theory
SEM	Scanning Electron Microscope
SIC	Self interaction correlation
SQUID	Superconducting Quantum Interference Device
TDOS	The Total Density of States
T_B	Blocking Temperature
TMR	Tunnel magneto resistance
UHV	Ultra High Vacuum
UNIX	UNiplexed Information Computing System
VASP	Vienna ab initio simulation package
XMCD	X-ray magnetic circular dichroism
XRD	X-ray diffraction
ZFC	Zero Field Cooled
σ_F	Fermi Temperature

CHAPTER 1: INTRODUCTION

1.1: Background of the Study

Spintronics technology utilises both the fundamental electronic charge of the electron and the intrinsic spin together with the associated magnetic moment in solid state devices. Electron transport phenomena that take into account the electron spin in solid state devices have led to discoveries which include the injection of spin polarised electrons to a normal metal from a ferromagnet and Magneto Resistance (MR), in particular, Giant Magneto Resistance (GMR) and Tunnel Magneto Resistance (TMR). MR is sensitive to spin polarisation and is applied in making Magnetic Tunnelling Junctions (MTJ's) whose performance depends on the spin polarisation of the current emitted and collected by the ferromagnetic electrodes (Klaer *et al.*, 2012).

Metal based spintronic devices include TMR and GMR read heads of modern hard drives with higher head sensitivity, able to read weak magnetic signals, spin transfer torque devices and the next generation non-volatile Magneto Resistive Random Access Memory (MRAM), which utilise spin filters and spin injectors in addition to its low power usage as well as good shock robustness (Lacaze and Lacroix, 2014). Others are spin wave logic devices which transmit information using the phase as well as spin wave scattering and interference to perform logic operations, magnetic field sensors, biosensors, microelectromechanical systems (MEMS), spin filters and compasses in devices such as mobile phones and tablet computers amongst others (Parker, 2003). The creation of spin helices of synchronized electrons was mapped by IBM scientists in 2012, which are able to persist for more than a nanosecond. This has opened new possibilities for using electron spin for information processing (Kushwaha *et al.*, 2013).

Ferromagnetism is the foundation for electrical and electromechanical devices, for instance, generators, electric motors, transformers, electromagnets and magnetic storage such as hard disks and tape recorders used in modern technology and industry (Takami, 2014). To generate a spin polarised current in a metal, a current can be passed through a ferromagnetic material, into the metal (Rougemaille *et al.*, 2002). However, the ferromagnetic 3d metals have a spin polarisation of between 40% - 50% (Luo *et al.*, 2008a).

Half-metallic ferromagnets give rise to a 100% spin polarised current and can replace the ferromagnetic $3d$ metals which apart from their lower spin polarisations, have a large difference between the resistances of metal and the semiconductor substrates resulting in problems in spin dependent devices (Luo *et al.*, 2008a). Half-metals have a metallic band structure for one spin channel and an insulating band gap at the Fermi level for the opposite spin. This provides a complete polarisation of conducting electrons. The first materials to be predicted to be half-metallic ferromagnets were the half Heusler compounds of general formula XYZ, where, X is a $3d$ transition metal element, Y is either a transition metal or a rare earth metal element and Z is a main group sp element. The space group for these alloys according to the Hermann-Maguin convention is the face-centred F-43m space group, space group number 216, which is referred to as the $C1_b$ structure according to the *Strukturbericht* notation and whose prototype is Magnesium Silver Arsenic (MgAgAs) as shown in more details in Appendix 5. These were Nickel Manganese Antimony (NiMnSb) and Platinum Manganese Antimony (PtMnSb), whose half-metallic character was discovered by de Groot *et al.*, (1983) using first principles calculations based on Density functional theory (DFT) (Luo *et al.*, 2008b; Leitner, 2017). MTJ's made using half-metallic materials with the spin polarisation of one, would have infinite MR values, hence the importance of half-metallic thin films (Parker, 2003).

Apart from NiMnSb and PtMnSb, several other Heusler compounds, including full Heusler compounds of general formula X_2YZ , having one more X element compared to the half-Heuslers have been found to be half-metallic (Luo *et al.*, 2008a). The space group for the regular full-Heuslers according to the Hermann-Maguin convention is the face-centred Fm-3m space group, with space group number 225, which is referred to as the $L2_1$ structure, according to the *Strukturbericht* notation and whose prototype is Copper Manganese Aluminum (Cu_2MnAl) as shown in more detail in Appendix 5 (Leitner, 2017). From experiment, most Heusler compounds exhibit ferromagnetic coupling in stoichiometric composition and saturate in weak applied fields. They have a major advantage because their structures are similar to binary semiconductors used industrially and have high Curie temperatures as compared to other half-metallic materials (Galanakis *et al.*, 2008). Most half-metallic Heusler Compounds that exhibit half-metallicity are Cobalt (Co)-based and are being utilised in MTJ's because they exhibit half-metallic ferromagnetism as well as high Curie temperatures. Manganese (Mn)-based

Heusler Compounds are relatively new compared to Co, Fe and Ni based ones and are of great interest, with Mn_3Ga being the most famous member, finding application in spin torque MRAM (Graf *et al.*, 2011).

Heusler compounds have found application in MTJ's with very high MR values (Tanaka *et al.*, 2012), such as $\text{Co}_2\text{MnSi}/\text{MgO}/\text{Co}_2\text{MnSi}$ with TMR ratios of 1900% at low temperatures (Wollmann *et al.*, 2014). They also find application in the next generation spin-dependent semiconductor devices such as current-perpendicular-to-plane giant magnetoresistance (CPP-GMR) read heads, spin torque oscillators (STO), spin transistors (Wen *et al.*, 2015), magnetic sensors (Wei *et al.*, 2011) and others such as the non-volatile MRAM (Ren *et al.*, 2016; Holmes and Pepper, 2003). The predicted spin gapless band structure of Mn_2CoAl was realised by Ouardi *et al.*, (2013) and is promising for room temperature spintronics (Graf *et al.*, 2011; Ouardi *et al.*, 2013).

Amongst the desirable properties of Heusler compounds are half-metallic ferromagnetism with compounds such as Co_2FeSi having high predicted spin polarisations, high Curie temperatures (T_c) with Co_2FeSi having the highest reported T_c (Graf *et al.*, 2011; Wurmehl, 2006), well above room temperature (Hazra *et al.*, 2016; Galanakis *et al.*, 2008; Feng *et al.*, 2014; Umamaheswari *et al.*, 2014) as compared to other half-metallic materials. They are also structurally similar to binary semiconductors used industrially (Galanakis *et al.*, 2008; Feng *et al.*, 2014; Umamaheswari *et al.*, 2014) and are able to exhibit varying localised magnetic moments on transition metal atoms such as Co (Carbonari *et al.*, 1996). Other properties include, larger spin stiffness in interfaces such as $\text{Co}_2\text{MnSi}/\text{MgO}$ as compared to $3d$ metals, important for MTJ's (Trudel *et al.*, 2010), perpendicular magnetic anisotropy (PMA) energy density in Heusler alloy multilayers such as $\text{Co}_2\text{FeAl}/\text{MgO}$ comparable to Co/Pd,Pt multilayers (Wang *et al.*, 2010) and tunable physical properties by alloying with a fourth element as in CoCrFeAl and CoFeAlSi (Trudel *et al.*, 2010).

Ferrimagnetism is common in X_2YZ ($\text{X} = \text{Mn}$) Heusler compounds such as Mn_2VAl and Mn_2CoGa . Doping can introduce ferrimagnetism in a system which is quite significant for practical applications because materials can be prepared for spintronics devices with either

strong or weak ferromagnetic or non-magnetic properties coupled with high spin polarisation by altering the compositions of the atoms. Doping with Co in Heusler compounds Mn_2VAl and Mn_2VSi has resulted in the design of fully compensated ferrimagnets (Galanakis *et al.*, 2007). In Co_2MnZ ($Z = Al, Ga, Si, Ge, Sn$) Heusler compounds, half-metallic ferrimagnetism has also been induced by introducing Mn atoms in Co sites. The Fermi level can also be shifted within the half-metallic gap by changing the total number of valence electrons. This has been experimentally observed in $Co_2FeAl_{0.5}Si_{0.5}$ and $Co_2Fe_{1-x}Cr_xSi$ in which a high TMR (175%) and an increase in spin polarisation respectively was attributed to the central positioning of the Fermi level (Graf *et al.*, 2011; Özdogan *et al.*, 2007). In Co_2TiGa and Co_2CrGa , doping with Mn and Fe respectively for the Y element increased the stability of the L_{21} structure as well as the half-metallic gap (Umetsu *et al.*, 2005; Okubo *et al.*, 2010). This technique has also been used to decrease the phase transition temperature in Heusler compounds having Al as the Z element, which often exhibit a B2 (CsCl) type of disorder as evidenced by XRD measurements. $Co_2FeAl_{0.5}Si_{0.5}$ and $CoFeAlSi$ exhibit higher spin polarisation as compared to the stoichiometric compound Co_2FeSi , with $CoFeAlSi$ being used today in MTJ's. A TMR of 16% at room temperature and 26.5% at 5K was found in $Co_2Cr_{0.6}Fe_{0.4}Al$ films while $Co_2FeAl_{1-x}Si_x$ and $Co_2MnAl_{1-x}Si_x$ are stable ordered half-metallic ferromagnets resulting from doping with Si in Co_2YAl ($Y = Fe, Mn$) (Inomata *et al.*, 2003; Graf *et al.*, 2011).

Materials whose magnetic order varies unconventionally with respect to temperature and field are of particular interest in research. Effects such as superparamagnetism and spin glass effect, mainly brought about by crystal anisotropy and reduced dimensionality displaying phenomena such as non-exponential relaxation, ageing and memory effects in systems like polymers, high- T_c superconductors, spin glasses, and granular materials are of great interest in condensed matter physics. Slow dynamics has been studied in various systems like transition-metal oxides, magnetic nanoparticle systems, supercooled liquids, and geometrically frustrated magnets (Sasaki *et al.*, 2005).

Spin glasses (SG), Cluster glass (CG) and superparamagnetic (SP) materials display similar features on their field cooled (FC) – zero field cooled (ZFC) curves whereby the curves separate below the blocking temperature (T_B), resulting in irreversibility. These systems exhibit slow

dynamics or memory effects. Depending on the relaxation times, the spin clusters may be classified as Néel–Arrhenius or Vogel–Fulcher type in which case they would be classified as SP or SG if they are non-interacting or interacting respectively (Sharma, 2017; Venkateswarlu *et al.*, 2014). The curves, therefore, have shapes that are dependent on whether the magnetic behaviour is driven by magnetocrystalline anisotropy or mutual particle interactions, with a peak in the FC curve being observed in the latter case (Suh *et al.*, 2006). In SP materials, the FC magnetisation always increases with a decrease in temperature due to the blocking or freezing of the spins in the direction of the field. In spin glass systems, the FC magnetisation does not increase but even decreases with a reduction of the temperature (Sasaki *et al.*, 2005).

Superparamagnetism (SPM) though rare in the family of Heusler compounds, has been found in a few Heusler compounds such as Fe₂VAl, Fe₂VGa, Fe₂TiSn and Ni₂FeAl (Zhang *et al.*, 2007). Heusler nanoparticles can find application as a nanogranular giant magnetoresistive sensor. This is if the assumption that the nanoparticles form a well arranged monolayer and are electrically connected by being fixed in a conducting matrix at a concentration where there is no interaction between the dipole stray fields is made (Felser and Hirohata, 2015).

Magnetic anisotropies, which are key in determining the mechanism of structural dependent magnetisation reversal, have also been studied in Heusler compounds. They have an effect on properties such as the coercive field and remanence of a material, with the easy magnetisation axis having a higher coercive field. Due to their cubic structure, the orbital moments in Heusler compounds are quenched, hence magneto crystalline anisotropy is not common in these systems. It has, however, been found in some Co-based systems (Trudel *et al.*, 2010). Perpendicular magnetic anisotropy (PMA) is, in particular, crucial in the design of high thermal stability MRAM electrodes as well as production of an enhanced output signal in spin torque switching. PMA electrodes should have a large tunnelling spin polarisation. The surface and interface states which promote PMA may, however, lead to the loss of spin polarisation. For Co₂MnSi, the half-metallic property is preserved in Mn-Mn termination, but lost for both Co and MnSi terminated surfaces (Trudel *et al.*, 2010). In Co₂FeAl/MgO interfaces, the Co terminated one's show PMA, while the FeAl one's exhibit in plane magnetocrystalline anisotropy. PMA has also been found in Co₂FeAl/MgO (Al₂O₃, GaAs, Pt buffered MgO) (Wang *et al.*, 2010) as well as in

CoFeB/MgO and Mn_{2.5}Ga (Vadapoo *et al.*, 2016) and MTJ's have in the last decade been made using Co₂YZ electrodes (Trudel *et al.*, 2010).

The lattice parameter has a significant effect on the spin polarisation in Heusler compounds. Hybridisation between *d* orbitals of transition metal atoms is favoured by the contraction of the lattice. The lattice parameter adopted affects half-metallicity, thus an appropriate substrate should be used in experiments in order to attain the highest possible spin polarisation (Galanakis *et al.*, 2002).

The intriguing properties predicted by band structure calculations are often not realised in real systems such as the high spin polarisations of Heusler compounds predicted by electronic structure calculations. This has been attributed to several factors such as, the lack of stoichiometry in thin films, temperature driven excitations and defects as well as assumed phases by band calculations not being present in the thermodynamic equilibrium condition. In addition, a number of full Heusler compounds have exhibited a half-metallic electronic structure in the bulk form, while, the corresponding surfaces and interfaces are found not to have the half-metallic character of the bulk compounds. This has hindered development of MTJ's with high TMR values (Galanakis *et al.*, 2008). In Mn₂VAl, low MR (<0.1% at 1T and 77K), measured on Mn₂VAl samples made it difficult to classify the Heusler compound as half-metallic (Jiang *et al.*, 2001). The low MR effect could be because of electronic structure or could have a micro magnetic origin. In the determination of magnetic properties, parameters such as crystal structure, composition, heat treatment, cleavage and electronic band structure are important (Mizutani, 2001). Studies in which predicted properties are compared to those obtained from the experiment are required so as to bridge the gap between the two approaches, leading to a better understanding of the systems studied.

In view of this, structure optimisation of full Heusler compound Mn₂VAl, which has received experimental and theoretical attention, and the least studied Mn₂VIn as well as Heusler Co₂YIn (Y = V, Nb, Ti) and half Heusler compounds CoYIn (Y= V, Nb, Ti) has been performed using DFT, which makes it possible for the properties of a large periodic system to be determined by reducing a 3N coordinate problem to 3 coordinates, while accounting for exchange and

correlation between the electrons, as implemented in the Vienna ab initio simulation package (VASP) code which uses pseudopotentials or the projector-augmented wave method and a plane wave basis set. The exchange and correlation in the systems has been treated in spin polarised calculations with the Perdew Burke Ernzerhof version of the generalised gradient approximation (PBE-GGA). These results have been compared with experimental results obtained for a Co and a Mn based Heusler system.

1.2: Statement of the Problem

In search of MTJ's with high Tunnel Magneto Resistance (TMR) values, MTJ's fabrication has been based on theoretical predictions of the spin polarisation of the materials used to fabricate the electrodes. The 100% spin polarisation as predicted for many Heusler compounds by band gap calculations have not been achieved in actual materials synthesised by the various fabrication technologies. This has hindered the development of MTJ's with high TMR values. More studies involving structure optimisation, as well as the determination of the spin polarised electronic and band structures of the materials used to fabricate the MTJ electrodes, such as Heusler compounds, will aid in revealing the optimum crystal structure required to produce the desired high spin polarisations and magnetic properties. This will aid in the fabrication of highly spin polarised memory electrodes, which will enable the fabrication of MTJ's with high TMR values, contributing to advancement in spintronics technology.

1.3: Objectives

1.3.1: General Objective

The main objective of this study is to perform structural optimisation and spin polarised electronic band structure calculations of Heusler compounds Mn_2VZ ($Z = Al, In$), Co_2YIn ($Y = V, Nb, Ti$) and half-Heusler compounds $CoYIn$ ($Y = V, Nb, Ti$) using the DFT method and to perform experimental verification of the structural and magnetic properties of Mn_2VAl and X_2VIn ($X=Co, Mn$).

1.3.2: Specific Objectives

The specific objectives are

- i. To determine the lowest energy crystal structure and the electronic structure of Mn_2VAl and Mn_2VIn using DFT employing the PBE-GGA exchange and correlation approximation.
- ii. To induce half-metallicity in Mn_2VIn through systematic substitution of Mn with Co using DFT employing the PBE-GGA exchange and correlation approximation.
- iii. To determine the lowest energy crystal structure, electronic and magnetic properties of Co_2VIn and $CoVIn$ using DFT+U and compare the results with those from the local spin density approximation (LSDA), GGA and PBE-GGA approximations.
- iv. To prepare Mn_2VAl and X_2VIn ($X = Co, Mn$) samples by arc melting method and to determine the structure and lattice constant of the samples using X-ray Diffraction (XRD).
- v. To compare the magnetic properties of Mn_2VAl and X_2VIn ($X = Co, Mn$) determined using DFT employing PBE-GGA exchange correlation with those obtained from a Super conducting Quantum Interference Device (SQUID) of the samples prepared by arc melting method.
- vi. To determine the effect of the Y element on the magnetic and electronic structure of Co_2YIn ($Y = Nb, Ti$) using DFT employing PBE-GGA exchange and correlation.
- vii. To determine the electronic structure and magnetic properties of X_2VIn ($X = Co, Mn$) and Mn_2VAl thin Heusler films using DFT based on PBE-GGA exchange and correlation.

1.4: Justification and Significance

Several full Heusler compounds have been shown to be half-metallic in bulk form. However, low MR has been observed possibly because of electronic structure or due to effects that could have a micro-magnetic origin. More studies need to be carried out to bridge the gap between theoretical expectations and properties exhibited by actual materials. In this study, the properties of Mn_2VZ ($Z = Al, In$), Co_2YIn ($Y = V, Nb, Ti$) and half-Heusler compounds $CoYIn$ ($Y = V, Nb, Ti$) have been determined using spin polarised DFT calculations as implemented in the VASP code. Employing the PBE-GGA exchange and correlation approximation, DFT has been used to

perform structure optimisation and to determine the magnetic properties and the electronic structure of the compounds. These properties have been compared with those measured on Mn_2VAl and X_2VIn ($X = Mn, Co$) samples. The study of the structural, electronic and magnetic properties of Mn_2VZ ($Z = Al, In$), Co_2YIn ($Y = V, Nb, Ti$) and half-Heusler compounds $CoYIn$ ($Y = V, Nb, Ti$) will contribute to the understanding of the electronic and magnetic properties of Heusler compounds and to advancement of technology options for more optimal performance of devices with a wider range of applications, in particular in spintronics.

CHAPTER 2: LITERATURE REVIEW

Heusler compounds were discovered in 1903 by Friedrich Heusler. It was found that elements whose valence electrons occupied *sp* orbitals, such as, Aluminum (Al), Indium (In), Tin (Sn), Strontium (Sb) and Bismuth (Bi), turned Copper – Manganese (Cu – Mn) alloy into a ferromagnetic material, even though the alloy does not contain any of the ferromagnetic elements (Hillebrands and Felser, 2006). In this section, a detailed treatise of prior studies on Heusler compounds will be discussed.

2.1: Theoretical and Experimental Studies on Heusler Compounds

Theoretical studies using electronic band structure calculations and experimental investigations have been carried out by several researchers on the structure, electronic and magnetic properties of Heusler compounds. Mn_2VAl is one of the Heusler systems that has received considerable attention, both theoretically and experimentally. A study done by Kawakami *et al.* (1981), on the magnetic properties of Mn_2VAl using Nuclear Magnetic Resonance (NMR) concluded that it is a simple ferromagnet based on the magnetic field dependence of the NMR frequencies and the observed high field susceptibility. DFT calculations conducted on Mn_2VAl employing the Generalised Gradient Approximation (GGA), led to a prediction of half-metallic ferrimagnetism, with only the spin down electrons available for conduction. Atomic moments of $1.5\mu_B$ and $-0.9\mu_B$, for Mn and V atoms respectively were reported (Weht and Pickett, 1999). However, magnetisation and resistivity measurements for Mn_2VAl prepared by arc melting, found that the dipole moment was $1.94 \mu_B/f.u$ at 5K and the residual resistivity was $1.3 \times 10^{-8} \Omega m$ for temperature dependence below 60 K. In this study, low magneto resistance of $< 0.1 \%$ at 1T at 77K, measured on the samples or pressed powder made it difficult for the samples to be classified as half-metallic as had been predicted by electronic band structure calculations (Jiang *et al.*, 2001).

In search for half-metallic ferrimagnetism in Vanadium based Heusler alloys Mn_2VZ ($Z=Al, Ga, In, Si, Ge, Sn$), using full potential non-orthogonal local orbital method (FPLO) in combination with LSDA, the total spin constants were found not to be integers, and thus the systems were reported not to be half-metallic at equilibrium lattice constants. Nevertheless, the ferrimagnetic state was found to be most stable in Mn_2VZ , ($Z=Al, In$) and the stability of the ferrimagnetic

state increased as the *sp* element became heavier. Previous work on Mn₂VAl was recorded in this study, including a neutron diffraction experiment, in which ferrimagnetic ordering was detected and an electronic structure determination of a close to half-metallic ground state for Mn₂VAl was made (Özdoğan *et al.*, 2006). A study conducted on [Mn_{1-x}X_x]₂VAl and [Mn_{1-x}X_x]₂VSi, where, X is Co or Fe, using FPLO and the local density approximation (LDA), proposed a half-metallic band structure for Mn₂VAl, with a gap in the spin-up band (Galanakis *et al.*, 2007; Meinert, 2013). In yet another study, NMR studies on polycrystalline bulk samples of Mn₂VAl detected an antiparallel coupling between Mn and V magnetic moments as did a study on epitaxially grown L₂₁ Mn₂VAl film, demonstrated by soft X-ray magnetic circular dichroism (XMCD). L₂₁ good order was attained when deposited directly on a MgO (001) single crystalline substrate. The saturation magnetisation, however, was small (M_s = 150 emu/cc) compared to expectation from ideal Slater - Pauling behaviour which might have been due to suppressed degrees of L₂₁ or B2 ordering (Kubota *et al.*, 2009). The spin moments for Mn and V in Mn₂VAl were found to be antiparallel, while the V spin and orbital moments were antiparallel since V *d* valence shell is less than half-filled (Galanakis, 2005). In a further study, Mn₂VAl was found to be a half-metallic ferrimagnet, with a net magnetic moment of 1.98μ_B by LSDA and to have a T_C of 663K. It was found to crystallise in the Cu₂MnAl type structure, with Mn not being nearest neighbours and the magnetic transition temperature determined by the Mn-V exchange interaction (Kübler, 2006). Neutron diffraction gave a ferrimagnetic structure for Mn₂VAl with 1.2 and -0.7 μ_B for Mn and V respectively (Nakamichi and Stager, 1983). Annealed at 1023K for 48 hrs, Mn₂VAl powder neutron diffraction showed an L₂₁ structure for Mn_{1.88} V_{1.12}Al_{1.00} (Itoh *et al.*, 1983).

Despite the numerous studies on Mn₂VAl and other Heusler systems, there are still unanswered questions mainly revolving around whether their electronic band structures are 100% spin polarised, for which many more theoretical and experimental investigations are necessary. Numerous studies have been conducted on other Mn based Heusler compounds. A study on the microscopic mechanism responsible for formation of magnetic moments in Heusler compounds having Mn as the Y element found that magnetisation is confined to Mn atoms and that the magnetic properties are determined by conduction *sp* electron concentration as well as the position of the unoccupied Mn 3*d*-states with respect to the Fermi level (Sandratskii and Bruno,

2008). The Slater – Pauling behaviour and electronic structure of Heusler compounds Mn_2CuZ ($Z = Ge$ and Sb) was studied using first principles. While Mn_2CuSb was predicted to be half-metallic at the equilibrium lattice constant, Mn_2CuGe was half-metallic with a slight expansion of the lattice (Luo *et al.*, 2011).

Another Mn based Heusler system, Mn_2CoZ ($Z=Al, Ga, In, Si, Ge, Sn, Sb$), was studied using the Full-Potential Linearized Augmented Plane Wave (FP-LAPW) potential, in which a mean magnetisation that obeys the generalised Slater-Pauling rule was revealed. In this study, the alloys were fabricated using the arc melting method and the experimentally determined lattice constants were used to determine the electronic structure using the self consistent FP-LAPW method based on LDA within DFT. The structure of the alloys was found to be Hg_2CuTi type, similar to half-Heusler alloys rather than $L2_1$ structure expected of full Heusler alloys (Liu *et al.*, 2008). FP-LAPW calculations performed on Mn_2CrZ ($Z=Al, Ga, Si, Ge, Sb$) alloys predicted Mn_2CrAl and Mn_2CrSb to be half-metallic ferromagnets. The calculations indicated a large and localised magnetic moment of Cr, which increased with increasing atomic number of Z and was antiparallel to that of Mn (Luo *et al.*, 2008a) .

Co based Heusler systems have received even more attention than the Mn based ones and even more considerations such as the partial localisation of d -states have been taken into account in various studies. In general, Heusler compounds exhibit localised magnetic moments with the magnetic moments of the Heusler half-metallic systems following the localised part of the Slater-Pauling curve. In metals, the d -electrons are delocalised while in transition metal based compounds, the onsite Coulomb interaction between d -electrons may be preserved to some extent. In order to account for partial localisation of the d -electrons while determining the magnetic moment of Co_2FeSi , the inclusion of electron-electron correlation was necessary. This was accomplished by using the Local density approximation Local density approximation with Coulomb interaction (LDA+U) method. Different values of the effective Coulomb-exchange interaction (U_{eff}), determined as $U_{eff} = U - J$ were used in order to reproduce the experimental value of the magnetic moment. U_{eff} from 2.5eV to 5.0eV for Co and simultaneously 2.4eV to 4.8eV for Fe resulted in a magnetic moment of $6\mu B$. These U_{eff} values were calculated from the corresponding Slater integrals using Cowan's program and correspond to about 7 - 20% of the

free atom values. This indicated that U to a great extent corrects the orbital dependence which is missing in the potential in L(S)DA.

On site correlation was attributed to be one of the reasons as to why incomplete spin polarisation was found in Co_2FeSi . The inclusion of effective Coulomb exchange correlation energies of about 2.5eV to 4.5eV to LDA+U calculations gave results that were in good agreement with the measured total and site specific magnetic moments and the compound was predicted to be a half-metallic ferromagnet. In the case of Co_2MnSi , correlation energy of 2.5eV closed the half-metallic gap (Kandpal *et al.*, 2006). In another study on Co_2MnSi and Co_2FeSi , the experimental magnetic state was well described, using the LDA+U method with semi empirical Coulomb interaction values U of $U_{\text{Co}} = 1.9$ eV, $U_{\text{Fe}} = 1.795$ eV and $U_{\text{Mn}} = 1.768$ eV. These values correspond to those for the Coulomb interaction U_{dd} between *d*-electrons in elemental 3*d* transition metals, determined prior to the introduction of the LDA+U method (Graf *et al.*, 2016). It may, therefore, be necessary to include electron-electron correlation beyond L(S)DA and GGA in the theoretical study of potential half-metallic materials and, in particular, for Heusler compounds. Nevertheless, Heusler compounds X_2YZ ($\text{X} = \text{Co}$, $\text{Y} = \text{Mn}$, $\text{Z} = \text{Ge}$, Sn), showed half-metallic ferromagnetic character, determined using the density of states and band structures from first principles' calculations using GGA exchange correlation and FP – LAPW (Rai and Thapa, 2012). Additionally, in a study of the structural, electronic and magnetic properties of half-Heusler CoFeIn and full Heusler Co_2FeIn compounds investigated using DFT, they were found to be metallic and half-metallic ferromagnets respectively (ElAmineMonir, *et al.*, 2015).

Superparamagnetism (SP) has been found in a few Heusler compounds such as Fe_2VAl , Fe_2VGa and Fe_2TiSn as well as in melt spun Ni_2FeAl , due to the presence of structural disorder resulting from the fast quenching. However, comparison with the typical superparamagnetic behaviour showed that intergranular interactions were not negligible (Zhang *et al.*, 2007). Superparamagnetic behaviour was also observed in Ni_2MnIn Heusler film synthesised by the co-evaporation process (Kurfiß and Anton, 2003). $\text{Fe}_{2+x}\text{V}_{1-x}\text{Al}$ and $\text{Fe}_{2+x}\text{V}_{1-x}\text{Ga}$ Heusler alloys display unusual magnetic and transport behaviour. The bulk magnetic behaviour of arc melted Fe_2VAl and Fe_2VGa is mainly determined by large clusters which are superparamagnetic, as well as magnetic defects caused by Fe antisite disorder, responsible for the reported GMR behaviour

(Suh *et al.*, 2006). Among magnetically dilute or granular 3d transition metal alloys, Fe₂VGa has the highest GMR effect of approximately 50% (Lue *et al.*, 2001a). Similarly, the magnetisation of Cu₂Mn_{0.75}Fe_{0.25}Al alloy above 60 K exhibits very small hysteresis ($H_C = 30$ Oe at 60 K; negligible above 200 K), a characteristic of a superparamagnetic phase. This kind of a small hysteresis loop has also been observed in systems like Fe₂VAl (Venkateswarlu *et al.*, 2014).

Off-stoichiometric versions of the Heusler alloys, having compositions of the form Ni₅₀Mn_{25+y}X_{25-y}, have additionally been found to have competing ferromagnetic and antiferromagnetic interactions between Mn atoms in the bulk samples, and have exhibited intrinsic exchange bias (EB) effects. Nanoscale magnetic phase separation, with a liquid like spatial distribution of superparamagnetic clusters in a non ferromagnetic matrix, pointing to SP and EB effects was displayed by small angle neutron scattering (SANS) experiments on polycrystalline Ni_{50-x}Co_xMn₄₀Sn₁₀ with $x = 6$ and 8 (Yuan *et al.*, 2016). In the ternary intermetallic compound Ho₂Ni₂Pb, two distinct magnetic transitions were observed as well as unconventional metamagnetic transitions and hysteresis at low temperatures (Muñoz-Sandoval *et al.*, 2001).

Electronic structure calculations allow the flexibility of conveniently studying the effect on the properties of a system for varying aspects such as the concentration of constituent elements. The electronic structure and optical properties of GaAs_{1-x}Bi_x alloy were studied using first principles, using DFT employing the GGA for exchange and correlation. Calculations were performed to different Bi concentrations and the lattice constant increased with increased Bi concentration but the alloy remained in the Zinc Blende structure. The band gap shrunk with Bi concentration (You and Zhou, 2014).

Several experimental techniques have been used to prepare and characterise Heusler compounds. Amongst these are arc melting, ultra high vacuum co-sputtering, RF induction and epitaxial growth. In an experimental study of Heusler compound Mn₂NiSb, preparation of the ingots was done by arc melting of stoichiometric amounts of the constituent elements in a high purity argon atmosphere. The raw materials had a purity of 99.9% or higher (Hongzhi *et al.*, 2009b).

A similar method was used to prepare $Mn_{3-x}Co_xGa$, Mn_2CoZ alloys with different Z elements and Co_2TiSn ingots in separate studies (Klaer *et al.*, 2012; Liu *et al.*, 2008; Kandpal *et al.*, 2007b). In a study of ferrimagnetism and disorder in $Mn_{2-x}Co_xVAl$, the deposition of samples was carried out using an ultra high vacuum co-sputtering system (Meinert *et al.*, 2011).

In the preparation of Fe_2CrAl , chromium and aluminum chunks were wrapped in iron foil to reduce any loss of aluminum by evaporation and melted by striking arc for a period of one minute. To ensure homogeneity, the ingot obtained from the first melting was melted repeatedly six times. The weight loss was 0.5% which is well within the acceptable level for samples prepared by arc melting. The ingots prepared by arc melting were annealed at 800°C for one week. After annealing, the samples were cooled slowly to room temperature in the furnace (Venugopalan, 2007).

Heat treatment determines to a great extent the order of the elements in the resulting structures. Arc melted Mn_2VAl ingots were annealed at 800 °C for 30 days resulting in the $L2_1$ structure Fm-3m space group. Mn_2CoGa ingots prepared by the same method were annealed at 850 °C for 14 days resulting in $MnCoMnGa$ structure, F-43m space group. Mn_2CoSn ingots were annealed at 800°C for 7 days, resulting in Mn, Co disorder. On annealing at 800 °C for 72 hrs MnCo and MnSn phases, F-43m space group were formed and at 800 °C for 14 days resulted in $(MnCo)_2MnSn$, Fm-3m space group (Kreiner *et al.*, 2014). Cobalt-based Co_2YZ (Y = V, Nb, Ta, Cr; Z = Al, Ga) Heusler ingots were homogenised at 900 °C for 24 hrs and cooled slowly. They were then annealed at 800 °C for 24-72 hrs and quenched with water, resulting in $L2_1$ structures (Carbonari *et al.*, 1996). Mn_2VGa ingots were prepared by arc melting with 2.5% excess Mn due to its volatility. Single phase micro structure resulted after annealing at 1075K for one week at 10^{-6} mbar in vacuum (Ramesh Kumar *et al.*, 2008). Almost single phase Co_2VSn resulted after annealing at 800°C for 100hrs in vacuum (Fujita *et al.*, 1972). $CoMnVAl$ ingots were annealed at 1300K for 15 days yielding a non-magnetic state without disorder (Wang *et al.*, 2015). Mn_2NiZ (Z=In, Sn, Sb) ingots were annealed at 1073 K for 72 hrs under an argon atmosphere. The body-centred cubic (bcc) structure which was a single phase was obtained in Mn_2NiSn and Mn_2NiSb (Hongzhi *et al.*, 2009a). Mn_2CoZ (Z=Al, Ga, In, Si, Ge, Sn, Sb) ingots were annealed at 1073K

for 72hrs forming bcc structure with a small amount of face-centred cubic (fcc) structure (Liu *et al.*, 2008).

Half-Heusler CoVSn was prepared using an RF induction furnace, following attempts to prepare it by arc melting, which resulted in segregation problems, indicating either metastability or the formation of a nearby phase of CoVSn during the process of cooling of the arc-melted ingots annealed at 600 °C for one week. CoSn₂, CoSn and V₂Sn₃ phases were identified (Lue *et al.*, 2001b). Co₂MnSn_xSb_{1-x}, was formed after 3-4 melts and annealing in vacuum at 10⁻⁴ Torr and 850 °C for 24 hrs in a quartz tube (Paudel, 2008) . Co₂Cr_{0.6}Fe_{0.4}Al was formed by arc melting followed by annealing in evacuated quartz tubes for two weeks at 1073K (Balke *et al.*, 2013). X₂YSn (X=Fe, Co or Ni, Y=Ti or V) ingots prepared by arc melting were annealed at 800 °C for 100 hrs in vacuum. All resulted in almost single phase fcc except Fe₂VSn (Fujita *et al.*, 1972). Ni_{2-x}Mn_{1-x}Ga and NiMn_{25+x}Z_{25-x} (Z = Sb, Sn) were prepared by arc melting. Samples were wrapped in Tantalum foil to avoid contamination and then sealed in a quartz tube with one open end attached to a diffusion pump. The Ga-based alloy was annealed at 800 °C for 144 hrs while the Sb and Sn alloys were annealed at 850°C for 24 hrs and then slowly cooled down to room temperature (Khan, 2007). Single phase Pd₂MnSb(Sn) was prepared by arc melting and annealing at 800 °C for 24 hrs (Maier and Vianden, 2008).

Heusler compounds Co₂VAl and Co₂VGa have been studied and found to be half-metallic (Kandpal *et al.*, 2007a). The properties of Co₂VIn which is isoelectronic and possibly isostructural to these Heusler compounds, containing the larger Indium atom and, therefore, larger lattice parameter, have, however, not been reported. Similarly, the properties of Mn₂VIn, which is isoelectronic to Mn₂VAl and Mn₂VGa, have not been reported.

In view of this, a study on the properties of Indium-based compounds will provide the knowledge needed for the fabrication and design of devices with realistic expectations of properties from these materials, based on the predictions made theoretically and results from experimental investigations. In addition, it will contribute to the understanding of the behaviour of Heusler compounds that will greatly aid in the continued search for materials possessing their

desirable properties and have the potential to lead to the design of devices with novel applications.

2.2: Heusler Structure

Heusler structure is formed from the ordered combination of two binary B2 alloys XY and XZ crystallising in the Cesium Chloride (CsCl) type crystal structure (Buschow, 2003) shown in Figure 2.1 (Pauling *et al.*, 1993). The X element is normally a $3d$ transition metal element such as Cr, Mn, Fe, Co, Ni, while $3d$, $4d$ or $5d$ elements enter as the Y element. sp elements enter the Z position.

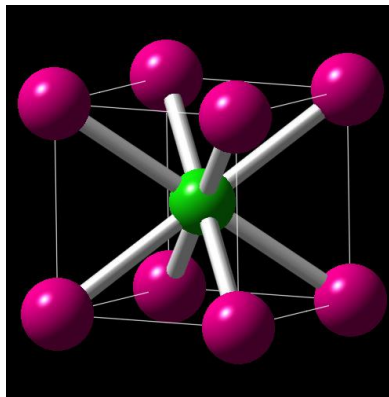


Figure 2.1: B2 Structure: Prototype CsCl structure. Source (Pauling *et al.*, 1993)

The CsCl structure is an interpenetrating primitive cubic structure. Each of the constituent atoms forms their own primitive cubic lattice. The separate primitive lattices interpenetrate such that an atom of one type occupies the centre of the cube of the other type. It is similar to the bcc structure, the difference being that the atoms at the different lattice sites alternate. It can also be viewed as a simple cubic with a different atom at the centre of the cube. At the stoichiometric composition, full Heusler alloys (X_2YZ) crystallise in the $L2_1$ structure in the cubic space group $Fm-3m$ (similar to NaCl), space group no. 225, prototype Cu_2MnAl (Graf *et al.*, 2011), which is shown in Figure 2.2 (Pauling *et al.*, 1993). The $L2_1$ structure has a unit cell that consists of four interpenetrating fcc sublattices with the Wyckoff positions $8c$ ($\frac{1}{4}, \frac{1}{4}, \frac{1}{4}$) for X atoms, $4b$ ($\frac{1}{2}, \frac{1}{2}, \frac{1}{2}$) for Y and $4a$ (0 0 0) for the Z atom. It, therefore, consists of 4 interpenetrating fcc sublattices, two of which are equally occupied by X atoms.

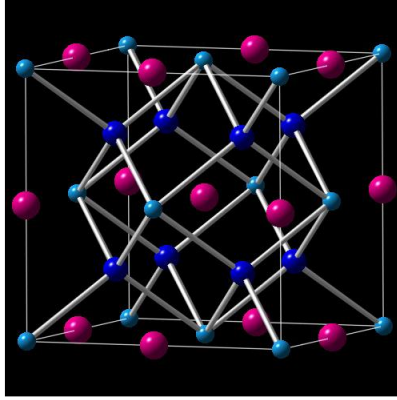


Figure 2.2: L₂₁ Structure: Prototype Cu₂MnAl – Heusler: Source (Pauling *et al.*, 1993)

A rock salt type (NaCl) lattice is formed by the Y and Z elements, which are the most and least electropositive elements respectively, due to their ionic character and are octahedrally coordinated. The X atoms fill all the tetrahedral holes. The structure can be viewed as a zinc blende type sub lattice, made up of one X and Z. The remaining tetrahedral holes are occupied by the second X, whereas Y fills the octahedral holes. At stoichiometric compositions, the atoms may partially interchange their positions, resulting in disorder. When the Y and Z atoms partially occupy each other's sub lattice an L₂₁ – B2 type disorder results. When half of Y and Z atoms interchange, a B2 type structure can be obtained, which results in an antiferromagnetic ordering due to smaller inter-atomic distances in B2 type structure. The ratio of L₂₁/B2 depends on the heat treatments. Y, Z disorder does not affect properties of half-metals significantly (Graf *et al.*, 2011).

The Z atom provides the *sp* states and, therefore, the energy of the *p* electrons is dependent on the Z atoms. It hybridises with *d*-electrons and determines the degree of occupation of the *p-d* orbitals. They, therefore, have a role in determining the total number of occupied and empty states which leads to the positioning of the Fermi level within the band gap (Trudel *et al.*, 2010). The magnetic order and the formation of the magnetic moment are dependent on the *sp* electron concentration (Liu *et al.*, 2008). In particular, it plays a major role in the formation of the magnetic moments at the X site by changing the lattice parameter (Kulkova *et al.*, 2006)

The half-Heusler compounds have a $C1_b$ structure. The $C1_b$ structure can be obtained from the $L2_1$ by leaving half of the tetrahedral sites vacant or by systematically replacing half of the X sites with a different atom.

The half-metallic gap in full Heusler compounds occurs as a result of the strong $d-d$ hybridisation between d -states of the transition metal atoms, as well as a $p-d$ hybridisation involving the main group element, such that a gap for only one spin direction is formed, with the Fermi level positioned in it. The energy gap width decreases with expanded lattice and with increasing atomic number (Luo *et al.*, 2008b).

Mn element enters as the Y element in most of the Heusler alloys. Mn in X is rare for example in Mn_2VAI and Mn_2VGa , in which together with $CoMnSb$, ferrimagnetism has been detected. Heusler compounds, having Cobalt as the X element have exceptional electronic structure and outstanding properties that have made them the subject of a great amount of research activity in spintronics. Magnetism is more common in $3d$ and $4f$ materials than in $4d$ and $5d$ compounds but when it occurs, it's very interesting. Strong-magneto crystalline and magneto-optical effects may be observed due to more spin – orbit effects (Solovyev *et al.*, 2003).

2.3: Electronic Structure of Compounds

When an impurity atom is introduced, a screening potential is formed in a metal. This disturbs the periodic potential and the conduction electrons are scattered. Only electrons close to the Fermi level contribute to resistivity and resistivity increases upon impurity scattering (Mizutani, 2001). Alloys might exhibit physical and chemical properties that are very different from the ones of the individual constituents (Hirschl, 2002).

2.4: Magnetic Properties of Compounds

Magnetic order in magnetic materials can mainly be classified as being diamagnetic, paramagnetic, ferromagnetic, ferrimagnetic or antiferromagnetic. The dominant magnetic excitations in systems with a collective magnetic ordering comprising of ferromagnetism, ferrimagnetism or antiferromagnetism are collective spin wave excitations and single particle stoner excitations. While the magnetic moments are aligned parallel to each other in a

ferromagnetic material, they form two equivalent magnetic sub-lattices in an antiferromagnet, which are oppositely oriented to each other. When the oppositely oriented magnetic sub-lattices are not equivalent, it results in ferrimagnetic order. Very small ferromagnetic particles have a total randomly fluctuating magnetic moment, above a specific temperature referred to as a blocking temperature T_B and below which a ferromagnetic behaviour is displayed, a behaviour referred to as superparamagnetism. A distinction is also made between materials with localised and itinerant magnetic moments. While the former is caused by partially filled inner electron shells, the latter is carried by conduction electrons (Coey, 2010; Neugebauer and Hickel, 2013).

Most solid state materials are non-magnetic because the valence electrons are delocalised in the solid. Magnetism occurs only if the electrons have a sufficient degree of localisation. The tendency towards magnetism is increased in systems with lower dimensions such as metallic surfaces and interfaces, multi layers, ultra thin films, wires and magnetic clusters deposited on surfaces (Zeller, 2006).

Materials with partially filled inner electron shells have localised magnetic moments. Metals exhibiting local moments are usually alloys. The interaction between the states of the individual atoms gives rise to bonding and anti-bonding hybrids. The spectral weight is evenly distributed in both hybrids when the interacting states are degenerate. In magnetic systems such as magnetic alloys, which consist of atoms with different moments, a spectral weight shift of the densities of states occurs which has an effect on the magnetism. If one of the atoms has a larger moment, the interacting states are displaced relative to each other causing the spectral weight to be shifted within each hybrid. This leads to a charge transfer which gives rise to covalent magnetism. The hybridisation between the orbitals may occur such that the Fermi level falls between d -states. Generally, full Heusler compounds have 12 occupied minority bands while half-Heuslers have 9 and the total spin magnetic moment for the half-metallic systems obey the Slater-Pauling rule to a great extent (Felser and Hirohata, 2015).

The magnetic moment in $3d$ magnetic materials is mainly due to electron spin. This is because the interactions between the $3d$ -electrons hinder them from drawing a definite orbit, leading to a

very small orbital contribution to the magnetic moment (Inomata, 2014). The orbital moments in Heusler compounds containing the 3d Co and Mn atoms, are therefore not significant and can be disregarded when discussing the resulting magnetic properties.

Heusler alloys are ordered systems in which, well defined, local moments reside on atoms that are separated by non magnetic atoms. Stoner excitations may be important for the Heusler alloys in which both the X and Y atoms are magnetic as the atoms are close enough for hybridisation between the *d* wave functions to occur resulting in itinerant behaviour. Metals exhibit conduction electrons which are delocalised. These itinerant electrons can move nearly freely inside the metal. Metals can therefore either be paramagnetic or magnetic (Vadalá, 2008).

2.5: Magnetic Anisotropy

When the internal energy of a magnetic material depends on the direction of its spontaneous magnetisation with respect to the crystallographic axes, it is said to possess magnetic anisotropy. Magnetic anisotropy in real systems is described by anisotropy constant *K*. For a material with tetragonal symmetry, the anisotropic magnetic energy E_{mae} is given by a series expansion such that the first three terms are;

$$E_{mae}(\theta, \varphi) = K_1 \sin^2\theta + K_2 \sin^4\theta + K_3 \sin^4\theta \cos 4\varphi \quad (2.1)$$

where, K_1 , K_2 and K_3 are the anisotropy constants, θ is the angle between the direction of spontaneous magnetisation and the single uniaxial *c* axis and φ is the angle between the direction of spontaneous magnetisation and the *a* axis. K_1 and K_2 terms are usually sufficient to describe the anisotropy in a system. The preferred direction of magnetisation depends on whether K_1 is dominant or not. If it is and is greater than zero, magnetisation will be along the *c* axis, resulting in PMA and the magnetisation will be perpendicular to the *c* axis if K_1 is less than zero. If K_1 is not dominant, the magnetisation may point in other directions (Buschow and Boer, 2007).

Magnetic anisotropy may result due to factors such as shape anisotropy in which the geometry causes the magnetisation to lie in a particular direction, stress effects arising from epitaxial mismatch that may result in strain tetragonal distortions, surface roughness, interface states and

magneto crystalline effects due to spin orbit coupling. The directional character of orbital angular momentum, L causes dependence on orientation through anisotropic bonding in a crystal lattice. The study of magnetic anisotropy of materials is carried out through the investigation of the dependence of spin waves excitation on the relative orientation between the magnetisation and crystallographic axes orientations (Trudel *et al.*, 2010).

PMA mainly occurs due to orbital motion and interfacial hybridisation, an effect that is not long range and hence, becomes significant with decreasing thickness (Wang *et al.*, 2010). In thin films, the effect of interface anisotropy over magnetocrystalline anisotropy is enhanced by a great reduction in thickness. In addition, the presence of interface precipitates that form from intermixing due to reactions or diffusion at the interface may result in the formation of clusters that have their own PMA, enhancing PMA in the films (Dau *et al.*, 2015).

Heavy non-magnetic elements with strong spin-orbit coupling have been made use of in applications requiring PMA. However, in order to trigger PMA, which has an interfacial origin resulting from orbital hybridisation which is sometimes accompanied by intermixing at the interface, very thin films are required whose fabrication is complicated. Transition metal/insulator interfaces provide an alternative to these fully metallic systems. Full Heusler/MgO interfaces have also demonstrated high interfacial PMA and weak spin-orbit coupling and have the potential to find application in spintronics (Vadapoo *et al.*, 2016).

For full Heusler compound films, the intrinsic magnetic anisotropy lies along the plane while interface induced PMA has been exhibited in Co-based Heusler compounds (Dau *et al.*, 2015).

CHAPTER 3: THEORETICAL FRAMEWORK

The ultimate goal in theoretical condensed matter physics is to solve the multi particle Schrödinger equation including all nucleus and electrons in the system under consideration, as well as their interactions.

3.1: The Schrödinger Equation

This equation is given as (Fiolhais *et al.*, 2003):-

$$H\psi(A, B, \dots, 1, 2, \dots) = i\hbar \frac{\partial}{\partial t} \psi(A, B, \dots, 1, 2, \dots) \quad (3.1)$$

where, $\psi(A, B, \dots, 1, 2, \dots)$ is the eigen function, with the letters and numbers denoting the dynamical variables of nucleus and electrons respectively and H is the Hamiltonian, given by:

$$H = -\frac{\hbar^2}{2m} \sum_i \left(\frac{\partial^2}{\partial x_i^2} + \frac{\partial^2}{\partial y_i^2} + \frac{\partial^2}{\partial z_i^2} \right) - \frac{\hbar^2}{2M} \sum_n \left(\frac{\partial^2}{\partial x_n^2} + \frac{\partial^2}{\partial y_n^2} + \frac{\partial^2}{\partial z_n^2} \right) + V_{ee} + V_{en} + V_{nn} \quad (3.2)$$

where, n and i refer to the nuclei and the electrons respectively, while m and M to the mass of the electron and the masses of the different nuclei respectively. The first and the second terms of equation (3.2) represent the kinetic energy of the electrons and the nuclei respectively, while the last three terms are the Coulomb repulsion between the electrons, the Coulomb attraction between the electrons and the nuclei and the Coulomb repulsion between the nuclei respectively. If the number of electrons and nuclei is not extremely small, typically smaller than four, it is impossible to solve the stationary Schrödinger equation for this Hamiltonian directly on even the largest and fastest computers available. Since the number of particles in a system is of the order of 10^{23} , approximations whose application should be justified and whose errors estimated, have to be made (Sholl and Steckel, 2011; Thijssen, 2007).

3.1.1: Born – Oppenheimer Approximation

The considerations made in this approximation are that the mass of the electron is almost 2000 times smaller than the mass of constituents of the nuclei. The characteristic frequencies of the

electrons and nuclei, therefore, differ largely and the corresponding two parts of the many-particle wave functions can be decoupled. This approach leads to a Hamiltonian for the electron in the field generated by a static configuration of nuclei and a separate Schrödinger equation for the nuclei in which the electronic energy $E_{(R)}$ enters as a potential (Thijssen, 2007).

The Hamiltonian H^{elec} for a system of N electrons in the presence of nuclei at fixed positions is;

$$H^{elec} = -\frac{\hbar^2}{2m} \sum_{i=1}^N \left(\frac{\partial^2}{\partial x_i^2} + \frac{\partial^2}{\partial y_i^2} + \frac{\partial^2}{\partial z_i^2} \right) + V_{ee} + V_{en} \quad (3.3)$$

where, the first, second and third terms of equation (3.3) represent the kinetic energy of the electrons, the Coulomb repulsion between electrons and the Coulomb attraction between the electrons and the nuclei respectively. The solution of the electronic Schrödinger equation, based on equation (3.3) yields a set of wave functions and energies $E_{(R)}$, known as the structural Energy, that depend on the nuclear configuration (Claeys and Simoen, 2011). This electronic energy forms a part of the potential energy in the nuclear Hamiltonian as follows:-

$$H^{nuc} = -\frac{\hbar^2}{2M} \sum_{n=1}^N \left(\frac{\partial^2}{\partial x_n^2} + \frac{\partial^2}{\partial y_n^2} + \frac{\partial^2}{\partial z_n^2} \right) + V_{nn} + E_{(R)} \quad (3.4)$$

The potential energy, $V_{nn} + E_{(R)}$ determines the geometry of the molecule by minimisation while the solution of the nuclear Schrödinger equation yields the nuclear probability distribution. The total energy is sum of the energy of the electrons and the energy resulting from the Schrödinger equation satisfied by the nuclei (Thijssen, 2007).

In a further approximation, the motion of the nuclei is neglected and only the electrostatic energy of the nuclei is summed up together with the energy of the electrons within the Born–Oppenheimer approximation with static nuclei, to arrive at the total ground state energy. The nuclei are treated as classical particles with a potential energy, $V_{nn} + E_{(R)}$ and they move as classical point particles via Newton’s second law, which would take the form:-

$$M \frac{d^2 R}{dt^2} = -\frac{d}{dR} [V_{nn}(R) + E_R] \quad (3.5)$$

Even with the positions of the nuclei kept fixed, the problem of solving for the electronic wave function remains intractable since too many degrees of freedom are involved especially because of the term involving the interactions between electrons, V_{ee} , in equation (3.3) (Sholl and Steckel, 2011). Further approximations, therefore, need to be made for the electron interactions.

3.1.2: Hartree Fock (H-F) Method

The electronic Schrödinger equation, using equation (3.3) is, therefore, a many body problem. Its solution yields a set of wave functions Ψ , which is a function of each of the co-ordinates of all N electrons. i.e a function of $3N$ coordinates. Ψ , therefore, needs to be approximated. One of the approximations of Ψ is the Hartree product given as:-

$$\Psi(r_1, r_2, r_3, \dots, r_N) = \psi_1(r_1)\psi_2(r_2)\psi_3(r_3) \dots \psi_N(r_N) \quad (3.6)$$

where, Ψ is the electronic wave function and $\psi_i(r_i)$ are the individual electron wave functions (Sholl and Steckel, 2011; Mizutani, 2001).

The total energy is minimised when the wave function $\psi_i(r_i)$ satisfies the following Schrödinger equation:-

$$-\frac{\hbar^2}{2m} \left(\frac{\partial^2 \psi_{i(\vec{r})}}{\partial x_i^2} + \frac{\partial^2 \psi_{i(\vec{r})}}{\partial y_i^2} + \frac{\partial^2 \psi_{i(\vec{r})}}{\partial z_i^2} \right) + V_{H(r)} \psi_{i(\vec{r})} + V_r \psi_{i(\vec{r})} = \epsilon_i \psi_{i(\vec{r})} \quad (3.7)$$

where, $V_{H(r)} = e^2 \int \frac{n(r')}{|r-r'|} d^3r'$ is the Hartree potential, which is the Coulomb repulsion between the electron and total electron density. Here, each electron is considered to move in an average field created by all remaining electrons. The first and the third terms represent the kinetic energy of the electrons and the Coulomb attraction between the electrons and the nuclei respectively (Sholl and Steckel, 2011; Mizutani, 2001).

The product in equation (3.6) does not satisfy the principle of indistinguishability and fails to satisfy antisymmetry. This is taken care of in the H-F approximation, which is a one electron

approximation. Here, the antisymmetric wave function is approximated as a single Slater determinant of a matrix of single electron wave functions $\psi_i(r_i)$ i.e.,

$$\Psi(r_1, r_2, r_3, \dots, r_N) = \frac{1}{\sqrt{N!}} \begin{vmatrix} \psi_1(r_1) & \psi_1(r_2) & \dots & \psi_1(r_N) \\ \psi_2(r_1) & \psi_2(r_2) & \dots & \psi_2(r_N) \\ \vdots & \vdots & \ddots & \vdots \\ \psi_N(r_1) & \psi_N(r_2) & \dots & \psi_N(r_N) \end{vmatrix} \quad (3.8)$$

The wave function in equation (3.8) satisfies the principle of indistinguishability and antisymmetry (Mizutani, 2001). Pauli's exclusion principle is employed due to the repulsive interaction between electrons with parallel spins resulting in exchange energy. In the H-F approximation therefore, electron distribution depends on the direction of spin. The exchange energy alters the expectation value of the distance where the overlap of the wave functions of two or more indistinguishable particles occurs. It is responsible for ferromagnetism. The exact wave function, however, cannot be expressed as a single determinant as it ignores the Coulomb correlation. The difference between the Coulomb interaction and exchange energy is known as the correlation energy. In real metals, the Coulomb correlation is independent of the spin direction. Also, the equation is valid only for a homogenous electron gas. In real metals, the presence of ionic potentials makes the distribution of electrons not to be homogenous (Mizutani, 2001).

A new potential arises from the Slater determinant wave function obtained from self-consistent calculations of the Schrödinger equation. The inclusion of this new potential in the Schrödinger equation is known as the H-F method. The Coulomb correlation, however, needs to be incorporated (Mizutani, 2001).

3.2: Density Functional Theory (DFT)

Density functional theory allows the proper treatment of the Coulomb correlation as it introduces an exchange correlation term within the one-electron approximation. It takes into account the exchange correlation in interacting systems and only kinetic energy in non – interacting systems. It relies on the approximation of the unknown exchange correlation functional of the charge density. It is applicable in systems where the electron distribution is no longer homogenous. DFT has roots in Thomas–Fermi model. It was developed by Hohenberg and Khon (H – K) theorems.

In the first H – K theorem, the basic variable that determines the ground state properties is not the many particle wave functions depending on N^3 spatial variables, but the electron density, a function of three variables. The ground state energy of a many body system is given as a unique functional of the particle density given as (Hafner, 2012);

$$E_o = E[(n\vec{r})] \quad (3.9)$$

where, E_o is the ground state energy.

In the second H – K theorem, the energy functional is defined, which proves that this energy functional minimises the correct ground state electron density. It uses the total energy and variation principle such that the total energy of a system under a given external field $V(\mathbf{r})$ minimises when a true electron density is found. $E[(n\vec{r})]$, therefore, has its minimum relative to variations $\delta n(\vec{r})$ of the particle density at the equilibrium density $n_o(\vec{r})$ (Kohn *et al.* 1996;Hafner, 2012). i.e.,

$$E = E[n_o(\vec{r})] = \min\{E[(n\vec{r})]\} \quad (3.10)$$

and,

$$\frac{\delta E[n(\vec{r})]}{\delta n(\vec{r})} |_{n(\vec{r}) = n_o(\vec{r})} \geq 0 \quad (3.11)$$

The Hamiltonian for the many electron system with kinetic energy T and electron interaction V_{ee} in an external potential $V(\vec{r})$, is given as (Hafner, 2012) :-

$$H = T + V_{ee} + V(\vec{r}) \quad (3.12)$$

This leads to ground state energy (Mizutani, 2001),

$$E_o = \langle \psi_o | H | \psi_o \rangle \quad (3.13)$$

and probability density,

$$n_o(\bar{r}) = |\psi_o|^2 \quad (3.14)$$

The DFT functional is given as;

$$E(n) = T + \int V(\bar{r})n(\bar{r})d^3r + \frac{e^2}{2} \iint \frac{n(r)n(r')}{|r - r'|} d^3r d^3r' + E^{ion} + E^{xc} \quad (3.15)$$

where, the first term is the electron kinetic energy, the second is the Coulomb interaction between the electrons and the nuclei, the third is the Coulomb interactions between pairs of electrons, the fourth is the Coulomb interaction between pairs of nuclei and the last term is the exchange correlation energies (Sholl and Steckel, 2011).

If E^{xc} is known, single electron equations can be used to yield the electron density i.e.

$$\left[-\frac{\hbar^2}{2m} \left(\frac{\partial^2}{\partial x_i^2} + \frac{\partial^2}{\partial y_i^2} + \frac{\partial^2}{\partial z_i^2} \right) + V_{H(r)} + V_{xc(r)} + V_r \right] \psi_i(r_i) = \epsilon_i \psi_i(r_i) \quad (3.16)$$

where, $V_{H(r)}$ is the Hartree potential, $V_{xc(r)}$ is the correction to self interaction in $V_{H(r)}$ as well as exchange and correlation contributions to the single electron equations. V_r is the interaction between an electron and the collection of atomic nuclei. Equation (3.16) is known as a Kohn-Sham equation. ψ_i , the solution to this equation is, however, not a quantity of physical interest. Of physical interest is $\psi_i^*(r_1, \dots, r_N) \psi_i(r_1, \dots, r_N)$, as well as the density of electrons.

$$n(r) = 2 \sum_i \psi_i^*(r) \psi_i(r)$$

$n(r)$ is a function of 3 coordinates and contains physically observable information. The total energy calculated includes the sum of one electron energies and double counting corrections (Sholl and Steckel, 2011).

To solve the Kohn-Sham equation, $V_{H(r)}$ needs to be defined. To define $V_{H(r)}$, $n(r)$ needs to be known. To know $n(r)$, $\psi_i(r)$ needs to be known. To know $\psi_i(r)$, the Kohn-Sham equation

needs to be solved. The problem is therefore treated in an iterative way to break the cycle, as outlined in the following algorithm;

- i. Define an initial trial $n(r)$
- ii. Solve the Kohn-Sham equation to find $\Psi_i(r)$
- iii. Calculate $n_{KS}(r)$ defined by Kohn-Sham single particle wave functions from step (ii)

$$n_{KS}(r) = 2 \sum_i |\psi_i(r)|^2$$

- iv. Compare $n_{KS}(r)$ with $n(r)$. If the same, then this is the ground state electron density and it can be used to compute the total energy. If not equal, update $n(r)$ and continue from step (ii). This process should lead to a solution of the Kohn-Sham equation that is self consistent. However, the exchange correlation energy needs to be known (Sholl and Steckel, 2011).

3.3: Approximation of the Unknown Exchange Correlation Functional

Functionals most commonly employed are local e.g. LDA or semi local e.g. GGA (Neugebauer and Hickel, 2013). LDA approximates the functionals T and E^{xc} by the corresponding energies of a homogenous electron gas of same local density. LDA depends upon the value of the electronic density at each point in space and not derivatives of the density of the Kohn-Sham orbitals. It has been used to calculate the ground state energy in various systems, which agree with experimental data.

Local spin density functional theory works well for magnetically polarised substances. It has been used for the calculations of electronic structure of clusters. In magnetic systems like magnetic alloys, which are made up of atoms with different moments, the magnetism is explained by changes which depend on the spin in the covalent interaction between the electronic states of neighbouring atoms. In LSDA the exchange functional is adopted to spin polarised systems, in which the densities of opposite spins are treated according to the magnetic ordering (Zeller, 2006), i.e.

$$n(\bar{r}, \uparrow) \neq n(\bar{r}, \downarrow) \tag{3.17}$$

and,

$$n = n \uparrow + n \downarrow \quad (3.18)$$

The magnetism of itinerant electrons in solid state systems are, therefore, well described by powerful tools such as spin polarised calculations within the framework of DFT (SDFT). It allows the quantitative theoretical determination of spin magnetic moments which helps in the understanding of the interactions responsible for magnetism in solid state materials. SDFT is exact in principle and the exchange correlation potential, as well as the exchange correlation energy, are approximated using LSDA which depends locally on the spin densities and GGA which depends on the gradients of the spin densities, which have proved to be accurate for many applications (Zeller, 2006). The strong correlation in which each electron has a complex influence on the neighbouring ones is not well described by one electron theories, for instance, LDA of DFT or Hartree-Fock. Half-metal behaviour, a correlation effect, is described more effectively in terms of interacting entities (Towler, 2014). Electronic correlations must be included in theoretical models of the electronic structure (Mizutani, 2001).

The exchange correlation energy functional in DFT can also be approximated by the hybrid functionals. They incorporate a portion of exact exchange from Hartree-Fock with exchange correlation from other sources e.g. empirical sources. One of the most commonly used versions is Becke, 3 – parameter, Lee -Yang-Parr (B3LYP). Others are Heyd-Scuseria-Ern Zerhof (HSE) and M06 – L functional which is good for transition metals, inorganic and organometallics. Dynamical mean field theory (DMFT) method is used for strongly correlated materials. It is used in combination with LDA used in DFT. The Hubbard model is an approximate theory that can include detailed electron-electron interaction for materials such as Mott insulators within the DMFT. In DFT + U, Coulomb and exchange terms U and J are included to treat strong interactions between localised *d* and *f* electrons. GW self energy approximation, where G is the full interacting Green's function and W is the dynamically screened Coulomb interaction, provide band gaps of insulators and semiconductors in agreement with experiment, improving DFT, while the Self interaction correction (SIC) solves the problem of the electron's interaction with its own mean field in LDA leading to more accurate binding energies of negative ions (Perdew and Zunger, 1981).

The Vienna ab initio simulation package (VASP) implements DFT using a plane wave basis set for representing wave functions, electron densities and potentials. The exchange part of the exchange-correlation energy is exactly known through the Hartree-Fock theory. Different approximations of the exchange and correlation energies yield different results for ground state energies. GW and SIC results are largely equivalent to LDA + U. GW and SIC are, however, not implemented in VASP (Hafner, 2012).

3.4: Band Calculations in Perfect Crystals

The ranges of energy that an electron within a solid may have or may not have are describes in the band structure of the solid. An examination of the allowed quantum mechanical wave functions for an electron in a large periodic lattice of atoms or molecules is used to derive the bands and band gaps. Using the band theory, physical properties such as resistivity and optical absorption are explained and it forms the basis of the development of solid state devices such as transistors and solar cells.

In band calculations, the energy Eigen value of the Schrödinger equation at as many k states as possible in the irreducible wedge within the Brillouin zone are determined, following which the occupied and unoccupied density of states and the Fermi surface are determined. The following methods can be used:-

- Tight binding method – Linear combination of atomic orbitals (LCAO)
- Orthogonal plane wave method (OPW)
- Pseudopotential method (PP)
- Augmented plane wave method (APW)
- Projector augmented wave method (PAW)

The last three that are closely related to the calculations performed in this work will be discussed further.

3.5: Pseudopotential (PP) method

As the highly oscillating core electrons which have a negligible effect on bonding are localised, their wave functions have many nodes and very many plane waves would be required to expand them. This is not only computationally expensive but in addition the solutions obtained would be

of high kinetic energy, while the low energy ones representing valence electrons are more physically important. To overcome this, pseudopotentials as illustrated in Figure 3.1, that have the same effect on the valence electrons replace the core electrons, reducing the number of plane waves needed to represent them, leading to more efficient calculations (Sholl and Steckel, 2011).

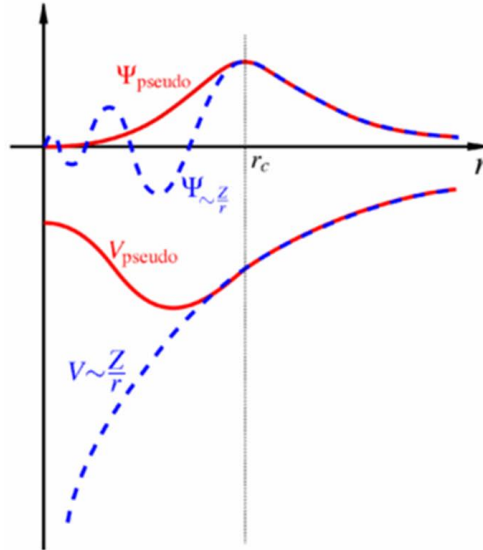


Figure 3.1: Pseudopotential used to represent core electrons. Source: (Segall M. 1997) <http://www.tcm.phy.cam.ac.uk/~mds21/thesis/thesis.html>

3.6: Augmented Plane Wave Method

In this method, there are two approaches, the first one being the one in which a trial wave function is formulated as a linear combinations of bases functions like plane waves. Here, all the matrix elements in the secular determinant are linear in energy, enabling a fast computation of the secular equation. In the second approach, the wave function is expanded into a set of energy-dependent partial waves. It then applies a matching condition for partial waves at the muffin tin sphere-like augmented plane wave. In this approach, the Schrödinger equation can be solved exactly in terms of the energy dependent partial wave expansions. The matrix has complicated non-linear energy dependence and hence, more computer time is needed. The Linear Muffin Tin Orbital method (LMTO) is a more efficient method as it combines the favorable features of the fixed basis and partial wave methods. It is fast and accurate (Mizutani, 2001).

FP – LAPW is an implementation of DFT which is used to compute the physical properties of solids and molecules. The use of augmented plane waves allows for tightly-bound core and semi-core electrons to be treated in a similar manner to valence electrons and provide an almost ideal basis set for the computation of the Hamiltonian matrix for a periodic solid. It is one of the codes that have the ability to perform exact exchange optimised effective potential calculations for non-collinear systems, while fully treating the core-valence interaction. It is one of the most accurate schemes for band structure calculations (Saleh, 2008).

3.7: Projector Augmented Wave (PAW) Method

It possesses the numerical advantages of PP calculations while retaining the physics of all electron calculations (Blöchl *et al.*, 2003). Apart from reconstructing the exact valence wave function with all nodes in the core region, it is capable of including upper core states together with the valence states in the self consistent iterations. In PAW, the region close to the atoms is treated separately with an atomic orbitals basis. Outside the atoms, another basis is used, such as plane waves. The pseudized wave function is transformed to the all electron wave function resulting in all electron precision (Holzwarth *et al.*, 1997; Kresse and Joubert, 1999). PAW creates PP that adjust to the instantaneous electronic structure and unifies all electron and PP methods (Blöchl, 1994).

The VASP performs quantum mechanical molecular dynamics simulations using pseudopotentials or PAW.

3.8: Computational Techniques

Simulation codes are used to perform electronic and band structure calculations to solve the Schrödinger Equation in order to determine the ground state properties of a system. The simulation code used in this work is VASP. It is an implementation of DFT and carries out first principle calculations which are governed by physical approximations such as the Born-Oppenheimer approximation and the exchange correlation functionals discussed in sections 3.1.1 and 3.3 respectively as well as numerical approximations of basis set size, the number of iterations and exit criteria (tolerances) as well as system size. Errors arising from numerical

approximations are minimised by carrying out convergence tests (Kanatzidis *et al.*, 2012; Kresse *et al.*, 2016).

The basis set used are plane waves in interstitial regions and atom-centred ones in non-overlapping spheres within the projector augmented wave (PAW) method. The plane waves are utilised as the basis set to expand the Kohn-Sham orbitals shown in equation (3.16). The use of plane waves is made possible by Bloch's theorem that provides that for a periodic system, an electronic wave function $\psi_{nk}(r)$ can be represented as a product of a plane wave and a function μ_{nk} with the same periodicity a as the lattice of the system i.e.,

$$\psi_{nk}(r) = \exp(ik \cdot r) \mu_{nk}(r) \quad (3.19)$$

where, r is the position vector, n the band index and k the wave vector, which has only certain allowed values determined by the size of the unit cell and,

$$\mu_{nk}(r) = \mu_{nk}(r + a) \quad (3.20)$$

The wave function can be described completely as an algebraic sum of plane waves if μ_{nk} is expanded in terms of plane waves determined by wave vectors of the reciprocal lattice vectors G , hence,

$$\psi_{nk}(r) = \sum_G c_{i,k+G} \exp(i(k + G) \cdot r) \quad (3.21)$$

where, $c_{i,k+G}$ are coefficients which when varied, determine the lowest energy solution. These coefficients must go to zero for high energy plane waves and hence, the plane wave basis set is truncated above a cut-off energy which is also element dependent. Equation (3.21) is a set of algebraic equations that can be solved using matrix algebra. The Brillouin zone (BZ) (k -space, reciprocal space) shown in Figure 3.2, describes the unique region of space closest to the gamma point ($r=0$) of an fcc structure at which the Kohn-Sham orbitals in equation (3.16) are periodic and onto which all other points are mapped by periodicity (Mizutani, 2001; Bach and Site, 2014). Fourier transform techniques are employed in expansions of both the electronic wave functions and the potential generated by the nuclei. After the Fourier transformation, solutions for only the

first (BZ) are required because by sampling the BZ, the whole of the bulk is sampled (Bach and Site, 2014).

Equation (3.22) shows the Integrals I over the BZ that are necessary for the determination of properties such as density of states and charge density.

$$I(E) = \frac{1}{\Omega_{BZ}} \int_{BZ} E_{nk} \Theta(E_{nk} - E_F) dk \quad (3.22)$$

where, $\Theta(E_{nk} - E_F)$ is the Dirac step function, Ω_{BZ} is the BZ volume, E_F the Fermi energy and E_{nk} is the energy of state with band index n and wave vector k. The total energy of the system is a function of the plane wave cut-off energy. To get a suitable cut-off energy, a convergence test in which the effect of the cut-off energy on the total energy is done so as to ensure convergence of properties in different systems. In a unit (super) cell, there is a finite number of electrons hence, a finite number of plane waves is used. There is, however, an infinite number of discrete k points over which the energy is calculated as an integral over all the points. However, an interpolation scheme with a finite number of k points can be used, due to the similarity of the wave functions at k points that are close together, converting the integrals used to determine the energy into a weighted sum over the k points. Errors associated with the finite number of k points are reduced by using a dense k point grid, which is a computational tool used to approximate the integrals of a particular property. A convergence test is also carried out to determine a suitable k point grid (Kohanoff, 2006).

Therefore, in order to evaluate the integrals computationally a discrete number of k points is required, hence, the weighted sum over special k points is taken, i.e.,

$$\frac{1}{\Omega_{BZ}} \int_{BZ} \rightarrow \sum_{nk} \omega_{k_i} \quad (3.23)$$

For metals, this sum that defines the band energies converges very slowly with the number of k points due to discontinuity in occupancies in a continuous density of states at the Fermi level as well as the energy of a number states being close to the Fermi energy level.

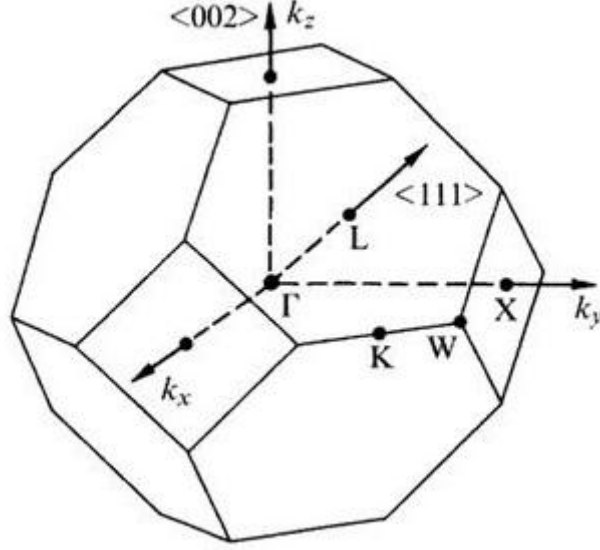


Figure 3.2: The Brillouin zone of an fcc structure showing the origin at $r = 0$

These states are therefore, sensitive to changes in energy that occur during a self-consistent cycle, which leads to instability due to changes in occupation numbers, making it difficult to converge the occupation step function that defines the occupancies of bands of a system at absolute zero temperature. Due to this, the step function is replaced by a smooth function such as a Gaussian or Fermi-Dirac function in the Gaussian method. This is known as smearing. For a discrete number of k points, if the step function is replaced by the Fermi-Dirac function,

$f\left(\frac{E_{nk}-E_F}{\sigma}\right) = \frac{1}{\exp\left(\frac{E_{nk}-E_F}{\sigma}\right) + 1}$, the right hand side of equation (3.22) becomes;

$$\sum_{nk} \omega_{k_i} E_{nk} \frac{1}{\exp\left(\frac{E_{nk}-E_F}{\sigma}\right) + 1} \quad (3.24)$$

The consequence of this is that the forces are derivatives of a generalised free energy F given by;

$$F = E - \sum_{nk} w_k \sigma S(f_{nk}) \quad (3.25)$$

where, S is the entropy. F may be interpreted as the free energy of the electrons at a finite temperature, the Fermi temperature for partial occupancies, $\sigma = k_B T$. An extrapolation for $\sigma \rightarrow 0$ from results at finite σ gives the ground state energy, i.e.

$$E(\sigma \rightarrow 0) = E_o \quad (3.26)$$

To improve the accuracy of forces, a complete orthonormal set of functions can be used in the Methfessel and Paxton smearing method to replace the step function, which are higher order approximations ($N=1,2,\dots$) with the Gaussian function being ($N = 0$). In this case, the entropy term which is an error difference between F and E ($\sigma \rightarrow 0$) is very small for a reasonable value of σ .

Another option is the linear tetrahedron method with Blöchl corrections, which divides the BZ into tetrahedra and then carries out a linear interpolation and an integration of the function within these tetrahedra. The Blöchl corrections correct the quadratic errors that cause an under or overestimation of the curve. In this method, E_{nk} is interpolated linearly between two k points with effective weights for each band and k point, the only drawback being that it is not variational with respect to partial occupancies and so cannot be used to determine forces accurately, but is excellent for total energy calculations.

3.9: Experimental Techniques

Various techniques can be employed to prepare Heusler compounds. Polycrystalline samples are widely prepared by arc melting and induction furnace while films are mainly prepared by magnetron sputtering, molecular beam epitaxy and high target utilisation sputtering.

Structural characterisation is primarily done by Transmission electron microscopy (TEM), selected area electron diffraction (SAED), and X-ray diffraction (XRD). Scanning Electron Microscope (SEM) and Energy Dispersive X-ray (EDX) spectrometry are commonly used to investigate composition and homogeneity.

Magnetic properties characterisation is commonly done using the vibrating sample magnetometry (VSM), superconducting quantum interference device (SQUID), X-ray magnetic circular dichroism (XMCD) and alternating gradient force magnetometry (AGFM).

Arc melting, XRD, EDX spectroscopy and the SEM used in this work will be discussed further

3.9.1: Arc Melting

By arc melting method, compounds are usually prepared by melting high purity constituent metallic elements in an argon atmosphere using an argon arc furnace like the one in Figure 3.3.



Figure 3.3: Photograph of the Arc melting furnace at IIT, Mandi Laboratory

Melting is repeated three to six times to ensure homogeneous mixing of the constituents. During melting, precaution is taken to compensate for the loss of material due to sublimation. The quantity of material to be added for compensation depends on the constituent elements and the duration of first melting.

To remove structural disorders and defects in compounds prepared by arc melting, annealing is carried out. The arc melted ingots are sealed in evacuated quartz tubes and put in a furnace maintained at a selected annealing temperature. The annealing temperatures are selected such that they are higher than the formation temperature of other phases of the elements. The duration of annealing can be decided from changes in the intensity and width of the X-ray diffraction lines of samples subjected to different time periods of annealing. After annealing, the samples are appropriately quenched by either slow cooling in the furnace if no intermediate phase formation is possible or fast quenching to room temperature to avoid formation of intermediate phases.

3.9.2: X-ray diffraction (XRD) Analysis

XRD is a non-destructive, versatile analytical technique for quantitative determination and identification of the crystalline compounds of different phases present in a sample. It is used to characterise unknown crystalline materials and is based on constructive interference of monochromatic X-rays to determine the inter-planar spacing of a crystalline sample. When the incident X-rays satisfy the Bragg's Equation, constructive interference occurs and a peak in intensity occurs (Bunaciu *et al.*, 2015).

The relationship between the wavelength λ , the lattice spacing d , and the diffraction angle θ is given by Bragg's law as:-

$$\lambda = 2d\sin\theta \quad (3.27)$$

Miller indices h, k, l and the lattice constant a can be used to express the lattice spacing in a cubic material, such that one can express Bragg's law as:

$$\sin\theta_{hkl} = \frac{\lambda}{2a} \sqrt{h^2 + k^2 + l^2} \quad (3.28)$$

The intensity of the peaks is related to the structure factor, $F(hkl)$ which is closely related to the crystal structure. It is derived as a Fourier transform of the charge density of the solid, giving

$$F(hkl) = \sum_j f_j(\theta_{hkl}) e^{2\pi i(hx_j + ky_j + lz_j)} \quad (3.29)$$

where, $f_j(\theta_{hkl})$ is the atomic form factor and x_j, y_j, z_j , are the coordinates of the site j in the unit cell (Aslanov *et al.*, 1998; Seeck and Murphy, 2015).

The resulting X-ray spectra from this technique are a structural fingerprint of the material. Polycrystalline phase can also be characterised and the relative heights of the Bragg's peaks can be used to obtain semi-quantitative estimates of the abundance of the various phases in the polycrystalline material (Bunaciu *et al.*, 2015).

The sample is placed on the sample holder and carefully mounted on the circular rotating chuck in such a way as to ensure that the reflection surface is exactly on the same plane as the

mounting surface. The rotating chuck ensures that X-ray detection is averaged over the sample to increase the accuracy of the measurement. The sample is rotated by the goniometer, which is comprised of the sample holder, detector arm and gears. In the $\theta - 2\theta$ goniometer, the sample moves by angle θ , the detector by 2θ and the X-ray tube is stationary. The time and the number of averaging points can be increased to capture the XRD scan with more definition. Identification of the sample is done by comparing the XRD pattern obtained from an unknown sample with an internationally recognised database such as the Joint Committee on Powder Diffraction Standards (JCPDS) containing the reference patterns for a large number of materials (Dutrow and Clark, 2007; Wong-Ng *et al.*, 2001).

3.9.3: Energy Dispersive X-ray (EDX) Spectrometry

EDXS provides a localised chemical analysis of a solid sample using the X-ray spectrum it emits on bombardment by a beam of electrons. It involves an electron probe analysis in which electrons are accelerated by a voltage twice higher than the highest excitation energy of any element present in the sample so as to get adequate X-ray intensity (Love and Scott, 2001).

The accelerated electrons interact with the sample in two main ways. They may decelerate and lose energy by their interaction with the atoms in the sample, which is given out in the form of photons called braking or Bremsstrahlung, whose intensity is given by:-

$$I(E)dE = k.i.Z.\left(\frac{E_{max}E}{E}\right) dE \tag{3.30}$$

where, i is the beam current, Z the specimens atomic number, E_{max} the energy of the accelerated electron beam which is equal to the accelerating voltage and k is a constant. This spectrum forms the main part of the background radiation.

The accelerated electrons are also decelerated by their interaction with the inner shell bound electrons, which per atom is related to the atomic number and therefore, proportional to the atomic weight of the element. This produces vacancies in the inner orbits of atoms into which electrons from outer orbits can fall into producing characteristic X-rays of which those in the energy range of 1 – 10 keV are used in the analysis of the sample (Severin, 2008).

Qualitative analysis in which the elements in an unknown specimen are identified is carried out using tables of energies or wavelengths to identify the lines in the X-ray spectrum. This is done by identifying the specific energy of the characteristic X-ray peaks for each element (Leng, 2009).

Quantitative analysis is carried out by determining the concentrations of the elements present in the sample and it is accomplished through measurement of the line intensities for each element in the sample I_{sp} and comparing with that of the same elements in a calibration standard of known composition, I_{st} . The measurement of the intensities is done by counting the pulses generated in the detector by the randomly emitted X-ray photons from the sample (Bell and Garratt-Reed, 2003). The concentration can then be determined from Castaing's approximation after further corrections dependent on the concentration of the matrix within which the element exists as well as other electron sample interactions, which relates the concentration of an element C to that of the element in the standard C_{st} , i.e.,

$$C = \frac{I_{sp}}{I_{st}} C_{st} \tag{3.31}$$

Other corrections may be made for absorption (A), atomic number effects (Z) and fluorescence (F), referred to as ZAF corrections (Donovan *et al.*, 1999).

'Maps' or element distribution images are produced by scanning the beam and displaying the intensity of a selected X-ray line. In addition, surface topography or mean atomic number difference is revealed by the images formed by electrons collected from the sample. If an X-ray spectrometer is added to the scanning electron microscope (SEM), which is primarily meant to produce electron images using an electron probe, element mapping and point analysis can be performed. Embedding the EDXS on SEM during the analysis of samples allows the exploitation of the overlap in the functions of these instruments (Donovan *et al.*, 1999).

3.9.4: Scanning Electron Microscope (SEM)

It is a non destructive characterisation technique useful in the determination of chemical compositions, crystal structures and orientations, elemental analysis, imaging samples, morphology and topography on samples and rapid phase discrimination by illustrating contrasts in the composition in multiphase samples. SEM uses a focused beam of high energy electrons to generate a variety of signals at the surface of solid specimens.

An electron gun generates and accelerates electrons to energies within the range of 0.1 – 30 KeV (Goldstein *et al.*, 2012). The kinetic energy of the accelerated electrons is dissipated as signals produced by their interaction with the sample as the incident electrons are decelerated (Reimer, 2013). To create a small focused electron probe of diameter in the range of 1 nm – 1 μ m on the specimen, electron lenses which are metal cylinders with a cylindrical hole and that operate in a vacuum in the range of 10^{-4} Pa is used (Goldstein *et al.*, 2012; Khursheed, 2011). These parts can be seen in Figure 3.4, including the detectors that collect the electrons after interaction with the sample (Ford *et al.*, 2010).

A magnetic field is generated inside the lens and it is varied to focus or defocus the electrons passing through the hole. The fine probe is scanned across the surface of the specimen by scanning coils emitting signals in the form of electromagnetic waves from each point that is struck by the accelerated electrons (Reimer, 2013).

Low energy secondary electrons and high energy back scattered electrons are collected by a detector and displayed on a monitor after amplification. Measurements are carried out such that a high current is produced from as small as possible probe area, such that data is collected over a selected area of the surface of the sample. An electronically synthesised 2-dimensional image, rather than one formed through optical transformations is generated, which displays spatial variations of various properties. The intensity of the generated signal and hence, the brightness of the image is proportional to the difference in the average atomic number hence, the ability to provide compositional contrast. The SEM is useful in the qualitative or semi quantitative determination of the chemical compositions of a sample using EDXS, as it can perform analyses of selected point locations on the sample as explained in section 3.9.3 (Goldstein *et al.*, 2012).

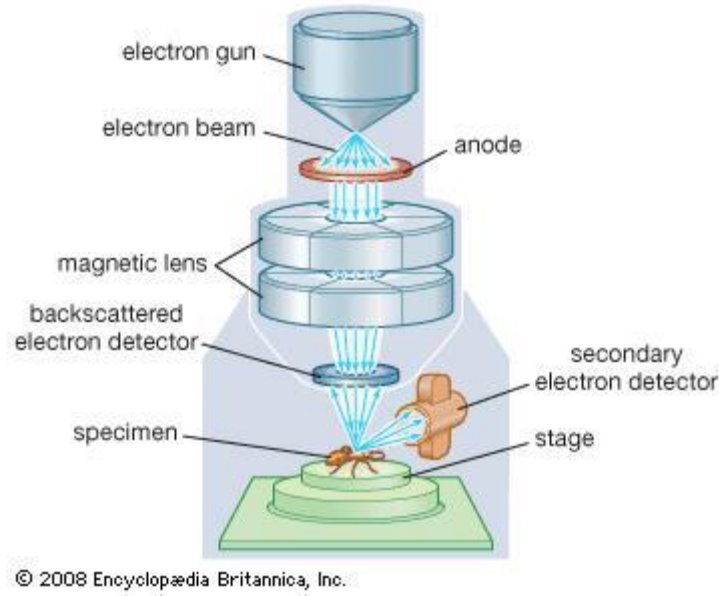


Figure 3.4: The main parts of a Scanning Electron Microscope. Source (Ford *et al.*, 2010)

3.9.5: Superconducting quantum interference device (SQUID)

SQUID's are the most sensitive detectors of magnetic fields and extremely small flux changes in the world. Flux quantisation in superconducting loops and Josephson effect constitute the basic phenomena in the operation of the SQUID (Ruggiero, 2013). In the SQUID there is a superconducting loop with two superconductors separated by thin insulating layers known as the Josephson junctions shown in Figure 3.5. Flux in a closed superconducting loop is quantised and a SQUID produces a voltage that is periodic with the flux and hence, it acts as a magnetic flux to voltage transducer. The period is one flux quantum, ϕ_o , i.e. (Tunstall and Barford, 1992),

$$\phi_o = \frac{h}{2e} \sim 2.07 \times 10^{-15} \text{ Wb} \quad (3.32)$$

The Josephson effect refers to the flow of a super current between two superconductors separated by a thin insulating layer, in the absence of a voltage due to Cooper pairs. The magnitude of the current depends on the phase difference between the superconductors (Gallop, 1991).

The Cooper pairs of electrons in a dc Josephson junction experience tunnelling in two parallel Josephson junctions. They can be represented on each side of the junction, by a wave function

similar to a free particle wave function, whose phase difference is proportional to a current flow in the junction in the absence of a voltage. For a constant biasing current in the SQUID device, the voltage measured oscillates with the phase changes at the two junctions, which is caused by the change in the magnetic flux. In the ac Josephson junction, a single junction exists in the superconducting loop and it oscillates with a characteristic frequency which is proportional to the voltage across the junction. A dc Josephson junction is more sensitive than the ac one and operates with a steady current bias while the ac one is operated with a radio frequency flux bias (Ruggiero, 2013).

On application of a magnetic flux perpendicular to the plane of the loop, a screening current that satisfies flux quantisation is produced. The SQUID can be used to measure any quantity that can be converted to a flux such as magnetic field, current and voltage. It may be configured as a magnetometer to detect very small magnetic fields with a threshold of 10^{-17} T (Vlad and Ciupa, 2014).

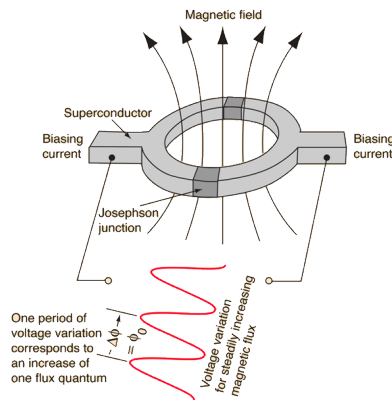


Figure 3.5: Josephson junction. Source: <http://hyperphysics.phy-astr.gsu.edu/hbase/Solids/Squid.html#c3>

CHAPTER 4: METHOD AND MATERIALS

In this section, theoretical and experimental methods employed in this work, as well as the materials used, will be discussed further.

4.1: Computational Method – Vienna ab initio simulation package (VASP)

VASP software installed in the high performance computing (HPC) cluster at Indian Institute of Technology – Mandi (IIT, Mandi), was used in performing calculations to optimise the crystal structures and to determine the electronic structure and magnetic properties of the compounds on a computer running the Microsoft Windows operating system. The commonly used UNiplexed Information Computing System (UNIX) interface popular in these type of calculations was provided by a virtualisation software known as puTTY which runs an interface similar to the Linux platform.

4.1.1: Computational details

The linear tetrahedron method with Blöchl corrections was used for total energy calculations as it gives a smooth electronic density of states. Care was taken not to break the symmetry by using a large number of k points as well as ensuring that the gamma point $\Gamma=0$, was always present. The Methfessel-Paxton scheme was used for larger supercells and in the calculation of forces. A small Fermi temperature of $\sigma_F = 0.02$ eV was set to smear the electronic density of states at the Fermi level to better represent the continuous density of states of the system. This resulted in smoothly varying functions at a small finite temperature and the total energy was extrapolated back to absolute zero.

To calculate the electronic ground state, VASP uses the self consistency cycle in combination with numerical methods such as the matrix diagonalisation schemes for evaluation of the self consistent solution to the Kohn-Sham functional in equation (3.16). A Pulay/Broyden charge density mixing is carried out where the calculated charge density is mixed with the input charge density as the new input. The Kohn-Sham equations are solved interactively to self consistency. Figure 4.1 illustrates the scheme of the self consistent solution of the Kohn-Sham equations. Charge densities are optimised in the outer loop while the wave functions are optimised in the inner loop.

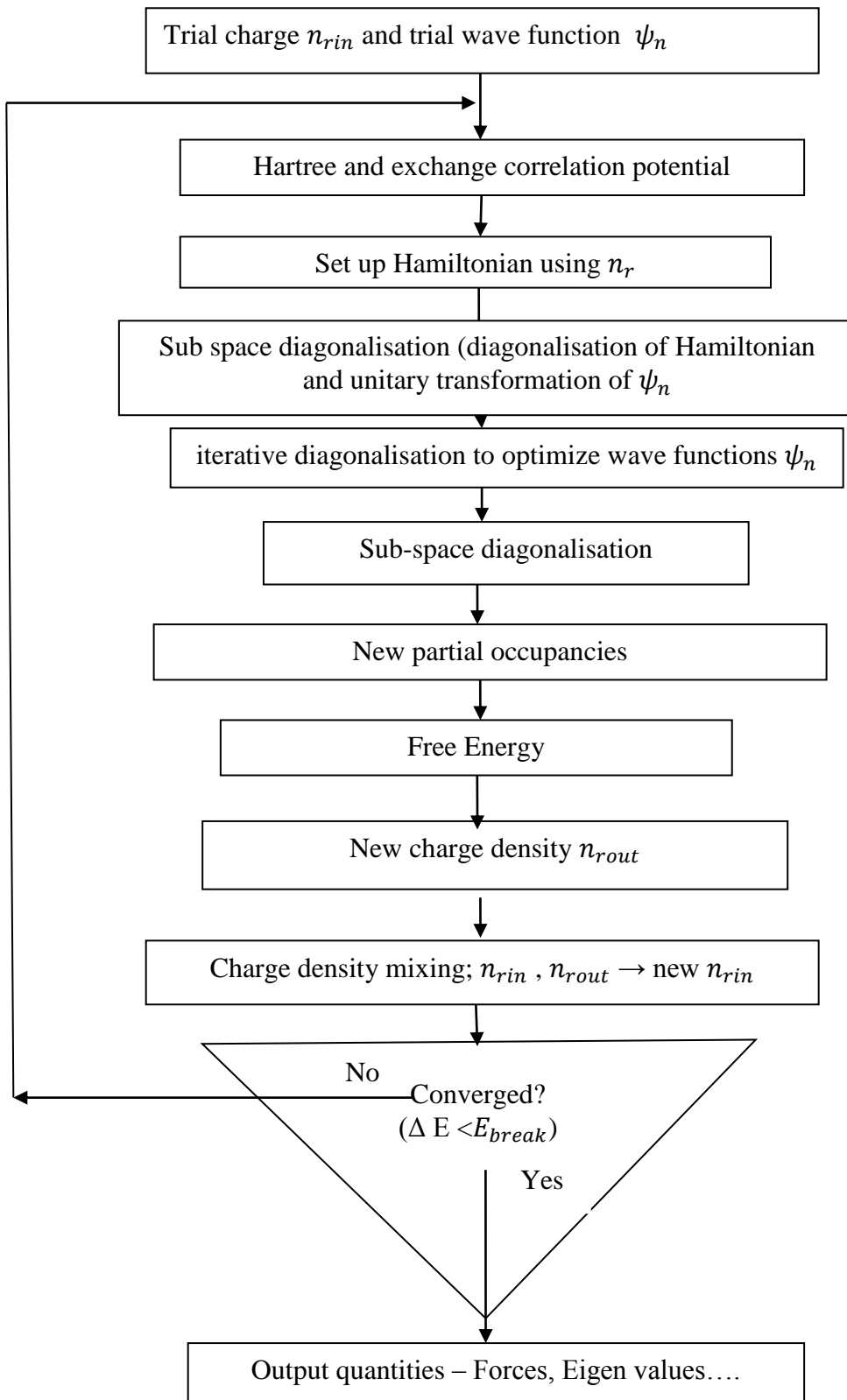


Figure 4.1: Flow of programs in the self consistent solution of the Kohn – Sham equations (Kresse *et al.*, 2016).

Most of the calculations in this work started with a superimposed electron density, n_r from all atoms in the unit cell, which was updated after each cycle. The external potential was computed as a sum of the Coulomb and exchange correlation potential using the total electron density as input. These were used to solve the Kohn-Sham equations for eigen values of orbital energies and eigen functions.

The eigen functions were used to determine the valence electron density and total energy calculations. The energy difference rather than total energy was used to ensure convergence. Net spin was determined as the difference between spin up and spin down densities. Upon convergence, the cycle was terminated at a specified tolerance for energy and forces. The appropriate choice of k vectors was critical. The density of states which is the number of electronic states in a particular energy range was determined from the sum over the supplied k points.

VASP uses four input files i.e POSCAR, POTCAR, KPOINTS and INCAR, which must be labelled as such. Several output files are produced after the completion of a calculation such as the OSZICAR, which provides a short overview while the OUTCAR contains all the output information. A brief description of each of the input files as used in this work is as follows:-

POSCAR

The POSCAR file contains details of the geometry of the system with the following information:-

- i. Title containing the atomic symbols of each ion in the structure
- ii. a scaling constant, which is the lattice constant in Ångströms
- iii. The unit cell lattice vectors with respect to the Cartesian lattice which are row vectors.
- iv. Identities of each atom.
- v. The number of each type of ion.
- vi. Indication of using a direct lattice i.e. fractional coordinates for ion positions in relation to the lattice vectors multiplied by the scaling constant.
- vii. The fractional coordinates of the ions.

An example is provided in Appendix 1.

POTCAR

This file contains the potentials including electron configuration and exchange correlation functional for each ion in the calculation. It contains the method in which case the PAW method described in section 3.17 was used. The PAW core potentials which are optimised for each atom and empirically based were provided together with the VASP package. The file contains an individual POTCAR piece for each ion in the same order as in the POSCAR and is created by concatenating atomic potential files. The main functions of the POTCAR file are:-

- i. To describe to VASP how to treat the potentials when describing the motion of the valence electrons.
- ii. To provide information to VASP on how to describe the motion of the valence electrons, that is, it defines the electron exchange and correlation functional.

The Perdew- Burke-Ernzerhof version of the generalised gradient approximation (PBE-GGA), which treats exchange and correlation as a function of the electron local density and its local gradient was used for the most part in this work.

KPOINTS

This file contains the k points which relate to the reciprocal lattice of the unit (super) cell. In this work, similar densities of k points along all reciprocal dimensions were used for the bulk calculations as the unit cells are cubic. After convergence tests for k points with total energy, a Monkhorst - Pack grid of 21 x 21 x 21 was used for all bulk calculations and for the supercells, fewer k points of 9 x 9 x 1 were used, as the supercells were grown in the z direction. For band structure calculations, explicit k points along high symmetry axes in the BZ were provided. For a periodic system, as described earlier in section 3.8, integrals over the finite first BZ replace integrals in real space over the infinitely extended system by application of Bloch's theorem. The function values of the integrand, for instance, the charge density are summed at a finite number of points called the k point mesh. A dense mesh is crucial for the convergence of the results. The

Chadi-Cohen and Monkhorst-Pack schemes can be used to generate k points. Expansions over the reciprocal lattice vectors G take care of long range interactions (Kresse *et al.*, 2016).

The scheme proposed by Monkhorst and Pack was used to choose the k points in this work. In this scheme, the k points are distributed homogeneously in the BZ. The rows or columns of k points run parallel to the reciprocal lattice vectors attached to the origin of the coordinate system in the BZ. In this way, one corner of the BZ rests in the origin $r = 0$ shown in Figure 3.2. The whole of the BZ is covered by small polyhedra of the same shape as the BZ. The k point pattern is then spread out over the whole BZ by translations of the polyhedra. The pattern consists only of a single point in the centre of the polyhedron, leading to the MP k point grid, formulated by the generation of periodic functions based on point group symmetries. The periodic functions are expanded in the reciprocal space by an accurate interpolation of the function between the points. In the grid, the symmetry operations reduce the number of k points which is specified as $n_1 \times n_2 \times n_3$ grids and the total number of k points is $n_1.n_2.n_3$. VASP has a symmetry code which determines the symmetry of systems automatically and is used to automatically set the MP grid of k points.

An example of the K POINT file for bulk, supercell and band structure calculations is provided in Appendix 2.

INCAR

It contains information about the computational parameters. These include:-

- i. The optimisation algorithms for both the electronic and geometric convergence. In this work, the Davidson block iteration scheme and conjugate gradient schemes were used respectively.
- ii. The kinetic energy cut off or highest plane waves to include for the valence electrons. A cut off of 430 eV was chosen after a convergence test.
- iii. The electron smearing method - the linear tetrahedron method with Blöchl corrections was chosen for the total energy calculations and the Methfessel-Packson for the ionic and full relaxations.
- iv. Smearing parameter which was set at 0.2 eV.

- v. The maximum number of electronic and geometric iterations to take, which were set at 60 and 100 respectively for most calculations.
- vi. Convergence criteria for the electronic and geometric relaxation in which a very tight criterion of 10^{-8} eV and 10^{-7} eV respectively was set, after which the iterations ended.

Three major types of calculations were carried out in this work and the INCAR for each type of calculation contained the information required for that particular type of calculation. These were self consistent calculations in which the total energy is minimised with respect to the occupation of Kohn-Sham orbitals, relaxation calculations in which forces in supercell calculations for surfaces as well as unit cells in which doping was carried out were determined and magnetic anisotropy energy calculations. Additionally, for the accurate density of states and band structure calculations, after a self consistent calculation, another one in which no charge update was allowed was carried out. For band structure calculations, the linear Methfessel-Paxton smearing was employed as the high symmetry k points for this type of calculation lie along a straight line rather than in a grid, in which case the tetrahedron integration scheme would break the symmetry.

Generally, all the calculations were spin polarised and total energy calculations began from scratch. A constant energy cut-off was used in the algorithms involving different volumes using the same energy cutoff for each calculation. For all the volume and cell shape relaxations, calculations were performed with a constant energy cut-off. As the energy changes are consistent with the calculated stress tensor, a large plane wave cut-off was used for relaxations so as not to underestimate the equilibrium volume. The energy cut-off value was arrived at after carrying out a convergence test.

4.1.2: Convergence tests

To ensure accuracy, various convergence tests were carried out. k point and cut-off energy convergence will be described further.

4.1.2.1: Convergence of k Points

To determine how many k points were needed, energy convergence test was carried out using an increasing number of k points. The convergence criteria of an energy difference of 10^{-5} eV between two consecutive sets of k point meshes was set. A balance is needed between convergence and tractability and so, an efficient yet manageable set of k points was determined so as to attain required accuracy as well as manage the computational time required. The symmetry of the unit cell was used to produce a primitive cell and consequently, the smallest number of k points possible was used.

Appendix 3 is an example of one of the k point convergence results obtained from this work for the bulk systems.

4.1.2.2: Convergence with respect to the cut off energy

A properly and carefully chosen cut-off energy ensures that the diagonal component of the stress tensor is correct. In the POTCAR, a maximum cut-off energy is provided which can be used as a guide, following which a convergence test is necessary. If the cut off energy is chosen such that the basis set is incomplete, an error referred to as ‘Pulay stress error’ results, which may decrease the volume compared to a fully converged calculation. Basis set is a fundamental approximation to the shape of the orbitals, and according to the variational principle, the ground state energy E_o is related to the orbitals ψ according to equation (4.9).

$$E_o \leq \frac{\langle \psi | H | \psi \rangle}{\langle \psi | \psi \rangle} \quad (4.9)$$

Therefore, a complete basis set represents the orbitals more accurately which lowers the computed ground state energy. In VASP the size and accuracy of the plane wave basis set is increased by adding more plane waves by increasing the cut off energy.

In this work, convergence was attained when the energy difference between two consecutive energy calculations was 1 meV/atom. A cut off of 430 eV was chosen from the convergence tests carried out.

Appendix 4 shows the cut off energy convergence result for the systems studied in this work

4.1.3: Relaxation of unit cells and super cells

Relaxation of the supercells and the unit cells was carried out to minimise the forces acting on the system. For the supercells, the surface atoms experience forces since the bulk symmetry is broken, while in the case of doping, the atomic radius of the atom that is introduced may be different from that of the atom it replaces, introducing some forces in the cell. A conjugate-gradient algorithm was used for all the relaxations to ensure relaxation of the ions to their ground state. Ions and cell shape were changed in the direction of the forces and stress tensor calculated i.e. along the direction of the steepest descent. In this method, a line minimisation is performed in the following steps:

- i) The initial configuration is read from the POSCAR file and is used to calculate the forces.
- ii) Then a trial step also known as a predictor step is done towards the search direction, controlling the length of the trial step by a scaling constant.
- iii) Then in the corrector step, the energy and the forces are recalculated and positions corresponding to the anticipated minimum are given.
- iv) Then the forces and energy are recalculated. If the forces contain a significant component parallel to the previous search direction, the line minimisation is improved by further corrector steps.

Close to the minimum, the size of the step close to a line minimisation along the search direction and the optimal step should be similar. While the former is calculated from a third order interpolation formula using forces and energy change from the start and trial step, the latter uses a second order or harmonic interpolation, which uses only information on the forces. A Hatree type preconditioning of the residual vector was used and sub-space diagonalisation was performed after iterative eigenvector optimisation. A modified Broyden charge density mixing scheme was used.

A criterion of forces less than $1 \text{ meV}/\text{\AA}$ was set to end the relaxation of the atomic geometries

4.1.4: Structure Optimisation

DFT calculations were performed based on the Kohn-Sham formalism of spin-polarised density functional theory as implemented by VASP. Calculations were performed using GGA and PBE-GGA exchange correlation functionals. Atomic cores were represented by the projector augmented wave method. A Monkhorst–Pack uniform k point grid with 21x21x21 k points for the bulk systems and 9 x 9 x 1 k points for the thin films was chosen for geometry optimisation and static total energy calculations. Geometries were optimised by relaxing both the unit cell and the positions of all the atoms within the unit cell using the conjugate-gradient algorithm until a stopping criterion of energy change less than 10^{-7} eV was attained. Uniform cut-off energy of 430eV was chosen for all calculations. To determine the lattice constants, the total energies were calculated as a function of the lattice constants. The minimum value of the total energy gave the optimised value of the lattice constant.

4.1.5: Electronic Structure and Magnetic Properties

Calculations were performed using PBE-GGA exchange and correlation functional. Atomic cores were represented by the projector augmented wave method. A Monkhorst–Pack uniform k point grid with 21 x 21 x 21 k points was chosen for static total energy calculations for the bulk systems while 9 x 9 x 1 was used for the thin films. Uniform cut-off energy of 430eV was chosen for all calculations. The integration over the irreducible part of the Brillouin zone was done using the linear tetrahedron method with Blöchl corrections. For the Co_2VIn and CoVIn systems, L(S) DA and GGA approximations were also used as well as DFT+U method in which Coulomb interaction was treated with U values, using the method based on simplified rotationally invariant Dudarev approach implemented in VASP, whereby, an effective Coulomb interaction $U_{\text{eff}} = U - J$ is applied. The values used for Co and V were $U = 2$ eV and $J = 1$ eV with PBE-GGA and $U = 1.92$ eV and $U = 1.34$ eV for Co and V respectively and $J = 0.5$ eV with L(S)DA and GGA. The U values used were used previously to describe the experimentally observed properties of similar Heusler systems comprised of the same transition elements (Kandpal *et al.*, 2007a). Net spin was determined as the difference between spin up and spin down densities. Band energies were estimated by integrating the one electron energies weighted by the density of states over the states occupied by electrons. For the thin films, the method of Methfessel-Paxton was used to determine the partial occupancy.

4.1.6: Magnetic Anisotropy Energy (MAE) calculations

For anisotropy calculations, self consistent, non collinear calculations in which spin-orbit coupling was allowed were performed. The total energy for the configurations in which the magnetic moments were set parallel to the spin quantisation axis and when they were perpendicular to the it were compared and used to determine the magnetic anisotropy energy. Symmetry was not switched on and therefore, calculations were performed for all the total number of k Points provided, for both the bulk and thin film systems. 729 irreducible k Points were used in a mesh of 9 x 9 x 1 k points for the thin film calculations. Charge densities up to *d*-states were taken into account.

4.1.7: Supercell calculations

Thin (0 0 1) film slabs of varying thickness having 5, 9 and 13 mono layers were grown in the z-direction. Static energy, relaxation and magnetic energy anisotropy (MAE) calculations were carried out for the different Heusler systems.

The major calculations carried out are illustrated in Figure 4.2.

4.2: Materials

Manganese (Mn) is a 3*d* transition element whose electronic configuration is $1s^2 2s^2 2p^6 3s^2 3p^6 4s^2 3d^5$. It is a hard, brittle silvery metal in group 7 and period 4 of the periodic table with atomic number 25. It has a melting point and boiling point of 1246 °C and 2061°C, respectively. Its density is 7300 kg/m^3 and its relative atomic mass (R.A.M) is 54.938 a.m.u (Gagnon, 2014). It is one of the most important alloying elements. It gives steel a hard yet pliant quality. When alloyed with aluminum and antimony, the resulting alloys are highly ferromagnetic. It is the fifth most abundant metal in the earth's crust. The most common Mn minerals are pyrolusite and rhodochroite and Mn minerals are generally widely distributed. Mn nodules which contain about 24% Mn together with smaller amounts of many other elements have been found on the floor of oceans (Bentor, 2012). The purity of Mn used was 99% and Mn $4s^2 3d^5$ electrons were treated as valence electrons for the electronic structure calculations.

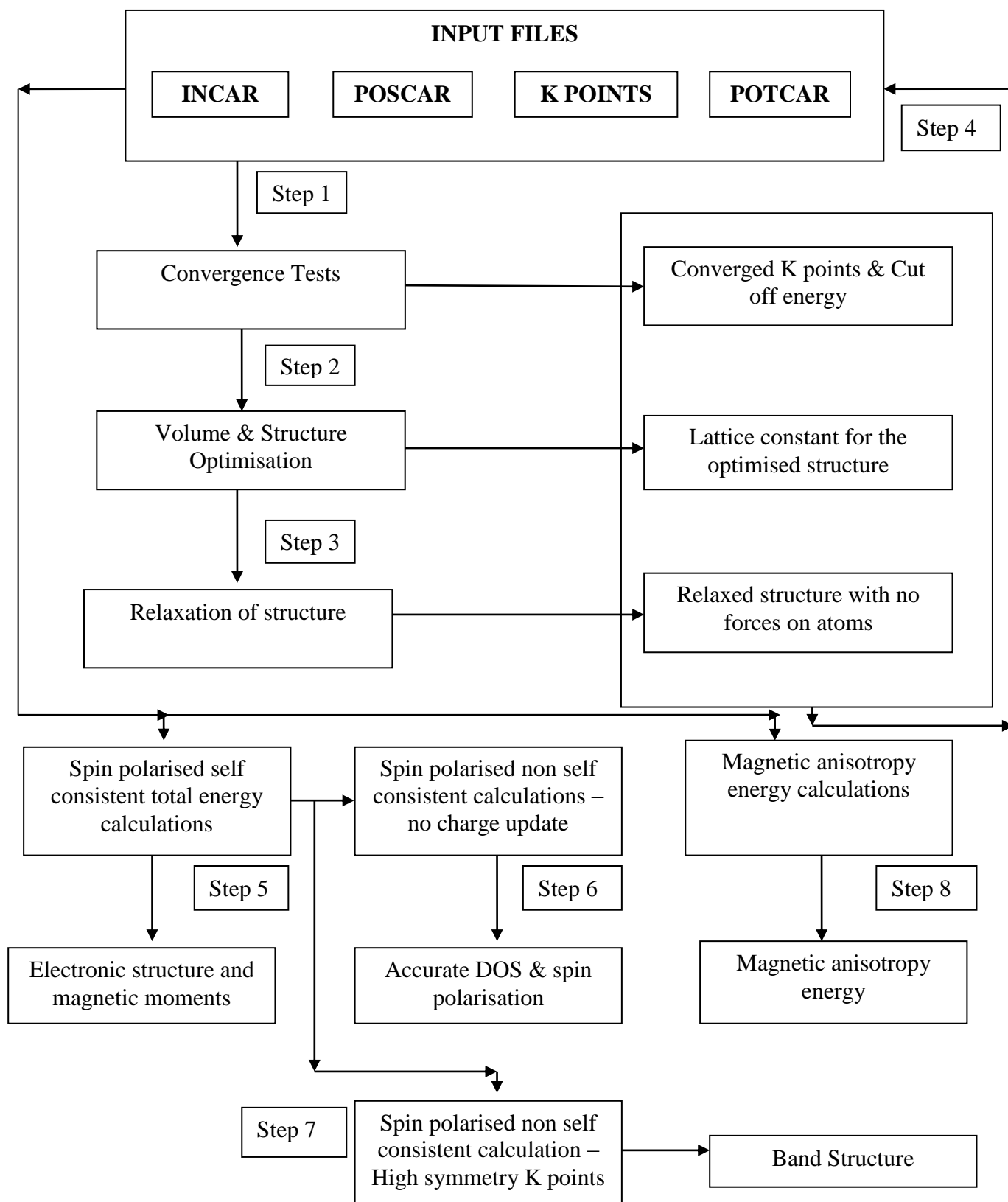


Figure 4.2: Flow diagram showing the major calculations carried out and their output

Cobalt (Co) is a silvery $3d$ transition metal that resists corrosion and has an electronic configuration of $1s^2 2s^2 2p^6 3s^2 3p^6 4s^2 3d^7$. It is in group 9 and period 4 of the periodic table with atomic number 27. It has a melting point and boiling point of 1495 °C and 2870 °C, respectively. Its density is 8900 kg/m^3 and its R.A.M is 58.933 a.m.u (Gagnon, 2014). It is used in alloys for aircraft engine parts, batteries, electroplating, and is corrosion resistant. It is found in mineral ores and is produced as a by product of nickel and copper mining. It can be found in DR Congo, Canada, Australia, Zambia and Brazil (Bentor, 2012). The purity of Co used was 99.7% and Co $4s^2 3d^7$ electrons were treated as valence electrons for the electronic structure calculations.

Vanadium (V) is also a $3d$ transition element whose electronic configuration is $1s^2 2s^2 2p^6 3s^2 3p^6 4s^2 3d^3$. It is a silvery metal that resists corrosion and is in group 5 and period 4 of the periodic table with atomic number 23. It has a melting point and boiling point of 1910 °C and 3407°C, respectively. Its density is 6000 kg/m^3 and its R.A.M is 50.942 a.m.u (Gagnon, 2014). It is used as a steel additive and it produces one of the toughest alloys for various applications such as armour plate, axles, piston rods and crankshafts. The purity of V used was 99.7% and V $3p^6 4s^2 3d^3$ electrons were treated as valence electrons for the electronic structure calculations.

Aluminum (Al) is a strong, light weight, silvery metal, whose electronic configuration is $1s^2 2s^2 2p^6 3s^2 3p^1$. It is in group 13 and period 3 of the periodic table and its atomic number is 13. Its melting point and boiling point are 660 °C and 2519 °C, respectively. Its density and R.A.M. are 270 kg/m^3 and 26.98 a.m.u., respectively (Gagnon, 2014). Discovered in 1825, Aluminum is used as parts of airplanes, rockets and in foils and kitchen utensils (Bentor, 2012). The purity of Al used was 99.99% and Al $s^2 p^1$ electrons were treated as valence electrons for the electronic structure calculations.

Indium (In) is a soft, ductile, malleable and lustrous silvery white metal, whose electronic configuration is $1s^2 2s^2 2p^6 3s^2 3p^6 4s^2 4p^6 3d^{10} 4d^{10} 5s^2 5p^1$. It is in group 13 and period 5 of the periodic table and its atomic number is 49. Its melting point and boiling point are 156 °C and 2072 °C, respectively. Its density and R.A.M. are 731 kg/m^3 and 114.82 a.m.u., respectively (Gagnon, 2014). Discovered in 1863, Indium is used as a low melting fusible alloy and a protective plate for bearings and other metal surfaces among other uses (Bentor, 2012). The

purity of In used was 99.99% and In $5s^2 5p^1$ electrons were treated as valence electrons for the electronic structure calculations.

4.3: Experimental Method

Experimental techniques were used to prepare and characterise the samples. Arc melting, X-ray Diffraction (XRD) analysis, Scanning Electron Microscope (SEM), Energy Dispersive X-ray (EDX) spectroscopy and Super Conducting Quantum Interference Device (SQUID) magnetometry were used.

4.3.1: Preparation of samples by arc melting

Approximately 2g of Mn_2VAl , Mn_2VIn and Co_2VIn ingots were prepared by arc melting of stoichiometric amounts of the constituent high purity elements using Edmund Buhler GmbH MAM 1 arc melting furnace. After cleaning the furnace with ethanol, melting was carried out in a high purity argon atmosphere to avoid oxygen contamination. Additionally, a Ti ball was used to bind the remaining oxygen. A weight loss of 4.6% was realised after the second melt of Mn, V and In. In addition, the sample was scattered with In melting separately. Due to the low melting point of In, V and Mn were first melted separately before combining with In. The weight loss was mainly attributed to vaporisation of Mn and the low melting point of In, which necessitated the addition of 10% of original amounts of both Mn and In. On subsequent melting, the weight loss was 1.7% after the fifth melt. The weight loss was less in Mn_2VAl at 1.5% after the fifth melt. In the case of Co, V and In, Co and V were first melted separately before combination with In. The weight loss was 1.57% after the second melt. Three additional meltings were carried out to yield a homogenous sample. For all the samples, the weight loss after the whole melting procedure was less than 2%.

The synthesis was carried out using the following procedure:-

- i. The furnace was cleaned using ethanol
- ii. In was cut from a rod using a hacksaw supported by a vice. V was in the form of small pieces, while Mn was in the form of chunks.



Figure 4.3: Digital LMUC series Spectrachrom Instruments ultrasonic cleaner available at IIT, Mandi Laboratory

- iii. Samples were weighed using a Mettler Toledo balance with a sensitivity of 0.1 mg.
- iv. The samples were then cleaned using acetone in a digital LMUC series Spectrachrom Instruments ultrasonic cleaner shown in Figure 4.3.
- v. The samples were weighed again and placed in the furnace as shown in Figures 4.4 and 4.5.

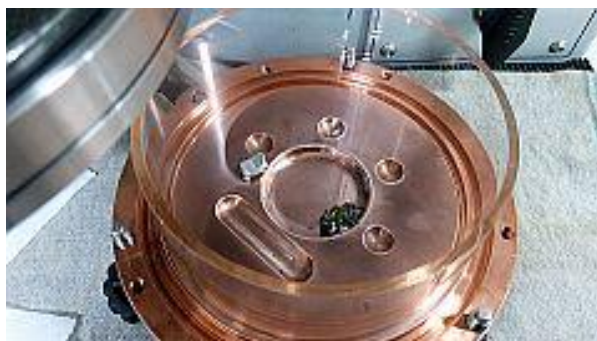


Figure 4.4: Samples in the arc melting furnace before melting

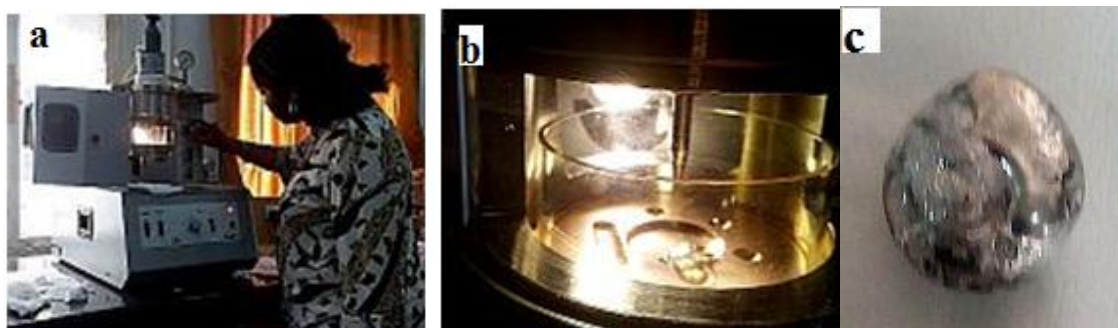


Figure 4.5: (a) Arc melting in progress (b) close up view of melting metals and (c) the resulting ingot



Figure 4.6: sealing of ingots in quartz tubes for annealing

The ingots shown in Figure 4.5 (c) were then sealed in quartz tubes shown in Figure 4.6. Mn-V-In and Co-V-In ingots were annealed at a temperature of 450 °C for 21 days, while Mn-V-Al was annealed at 800 °C for 7 days. The crystal structures of the products were investigated by means of powder XRD at room temperature.

4.3.2: XRD Analysis

The XRD machine RIGAKU D-2000 model, shown in Fig. 4.7 (a), available at IIT, Mandi was used in this work. Powder XRD was performed using excitation by monochromatic Cu-K α of wavelength $\lambda=1.5418 \text{ \AA}$ emitted from the source shown in Figure 4.7 (b), in the θ - 2θ scanning mode.

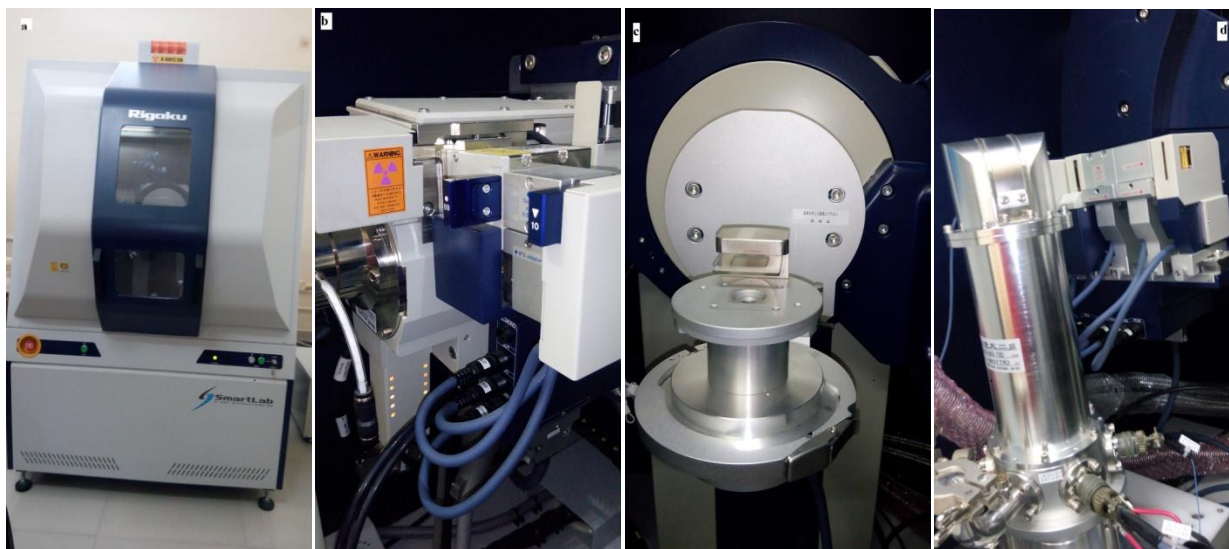


Figure 4.7 (a) Photograph of the XRD machine RIGAKU D-2000 available at IIT, Mandi, a view of the inside showing (b) the source of Xrays, (c) the sample stage and (d) the detector and low temperature facility

The samples were placed on the holders and carefully mounted on the circular rotating chuck shown in Figure 4.7 (c). A detector, Figure 4.7 (d), recorded and processed the X-ray signal and converted it to a count rate which was then sent as output to a computer monitor. Data was collected from 10° to 90° . As the sample and the detector rotated through their respective angles, the intensity of the diffracted X-rays was recorded continuously. A peak in intensity occurred when lattice plane d spacing appropriate to diffract X-rays at that particular value of θ were present in the sample. For determination of unit cell parameters, phase identification was carried out and each reflection was indexed to a specific hkl using Match 3! Program (Match!3 , 2016), which revealed the major phases in the samples. FullProf software was used to refine the identified structures by carrying out Reitveld refinement in which the α_1/α_2 splitting of the radiation was taken into account. 9 terms of a Legendre Polynomial was used to refine the background and the 2θ region chosen for analysis was $30^\circ - 90^\circ$. The peak form was assumed to have a Lorentz shape and the atomic and displacement factors were small.

4.3.3: EDX Spectroscopy on the SEM Analysis

The EDX spectroscopy detection system equipped with a SEM was used to determine the stoichiometry of the samples. The X-rays emitted by the sample measured at 3×10^{-5} mbar pressure using an acceleration voltage of 20 kV at an inspection angle of 30° , were detected and converted into electronic signals by the X-ray detector in the EDXS machine. The pulse processor measured the electronic signals and determined the energy of the X-rays from them. The X-ray data was then displayed and interpreted by the multiple channel analyser. The quantitative data was corrected using the ZAF method, which relies on atomic number (Z), absorption (A) and fluorescence (F) effects. The homogeneity of the samples was displayed by a scanning electron microscope (SEM) attached to the EDXS machine. The images were obtained through the Digital Image Processing System (DIPS).

4.3.4: SQUID Magnetometry

Magnetisation curves were measured by a Super Conducting Quantum Interference Device (SQUID) magnetometer with an applied field up to 0.1T, so as not to interfere with the intrinsic magnetism of the samples. The magnetic moments of the sample were measured against temperature and magnetic field. The type of magnetic ordering was confirmed from the curves

and phase transitions between different types of magnetic order were also investigated. The sample was cooled down to 2 K without an applied magnetic field, after which the sample was slowly warmed up to 400 K while measuring the magnetic moments in a magnetic field of 0.1 T. This was the Zero Field Cooled (ZFC) magnetisation measurements. For the Field Cooled (FC) magnetisation measurement, the samples were cooled down to 2 K without turning the magnetic field off, following which measurements of magnetic moments were taken while slowly warming up to 400K in a magnetic field of 0.1T. For the magnetisation measurements, the magnetic moments were measured at different applied magnetic fields at 2 K, 250 K and 400 K.

5.0. RESULTS AND DISCUSSION

5.1: Structural, Electronic and Magnetic Properties of Mn_2VAl and Mn_2VIn

The structural, electrical and magnetic properties of Mn_2VAl and Mn_2VIn have been studied, where comparison has been made on the effect of Indium atom which is larger as compared to the Aluminum atom at the Z positions of the Heusler compounds. The effect on these properties has clearly been demonstrated by the electronic structure results of the optimised structure of the compounds, which have a direct effect on the resulting magnetic properties

5.1.1: Structural Properties

The optimised structure for both Mn_2VAl and Mn_2VIn is found to be the $L2_1$ structure, prototype Cu_2MnAl , space group $Fm-3m$, space group no. 225 rather than the Hg_2TiCu prototype crystal structure preferred by some Heusler compounds (See Appendix 5). As Mn has a higher atomic number than V, it takes up the X position with the Wyckoff position 8c (0.25, 0.25, 0.25) as shown in Figure 5.1 (a). V and In (Al) take up the positions 4b (0.5, 0.5, 0.5) and 4a (0, 0, 0), respectively. In the Hg_2CuTi prototype, space group $F-43m$, space group no. 216, Mn occupies the 4c (0.25, 0.25, 0.25) and 4b (0.5, 0.5, 0.5) positions while the corresponding positions for V and In (Al) are 4d (0.75, 0.75, 0.75) and 4a (0, 0, 0) Wyckoff positions as shown in Figure 5.1 (b). Generally, for X_2YZ Heusler compounds the $L2_1$ structure has lower energy when the X element has a higher atomic number than the Y element, while the Hg_2CuTi crystal structure is more stable when the X atom is more electropositive and hence the optimisation results for Mn_2VZ ($Z=Al, In$), satisfy this expectation (Graf *et al.*, 2011).

The $L2_1$ structure can be viewed as a combination of the NaCl (rock salt) structure and the zinc blende (ZnS) structure. This causes compounds with the $L2_1$ structure to be compatible with semiconductors used industrially such as GaAs that have the ZnS structure. Figures 5.2(a) and (b) show the ZnS and NaCl structures, respectively. There are two sub-lattices in the $L2_1$ structure; a covalent ZnS like one between one of the X atoms and main group Z element, as in Figure 5.2 (a) and an ionic NaCl like one between the more electropositive Y element and the Z element which are coordinated octahedrally as shown in Figure 5.2 (b). The second X element occupies the rest of the tetrahedral voids resulting in the $L2_1$ structure shown in Figure 5.1 (a) (Graf *et al.*, 2011).

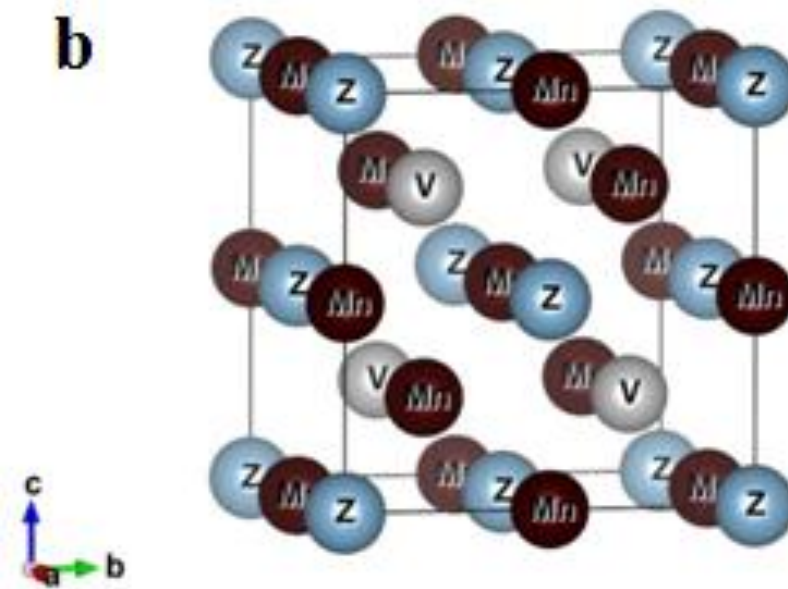
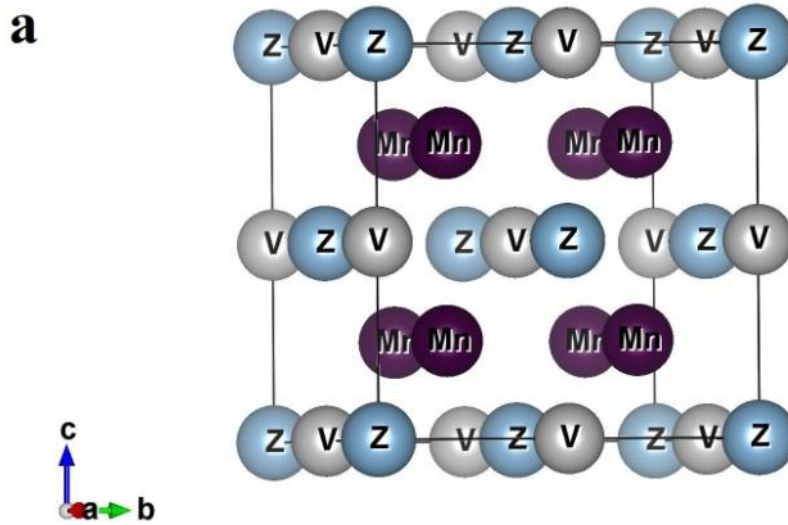


Figure 5.1 (a): Mn_2VZ in the Cu_2MnAl structure with Wyckoff positions $(0.25, 0.25, 0.25)$, $(0.5, 0.5, 0.5)$ and $(0,0,0)$ for Mn , V and In respectively and (b) the Hg_2TiCu structure for Mn_2VZ ($Z = Al, In$) with Wyckoff positions $(0.25, 0.25, 0.25)$ and $(0.5, 0.5, 0.5)$ for Mn and $(0.0,0)$ and $(0.75, 0.75, 0.75)$ for Z and V, respectively.

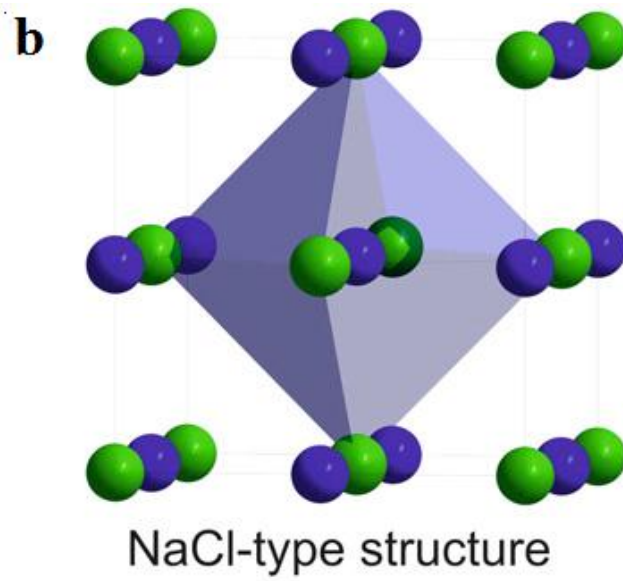
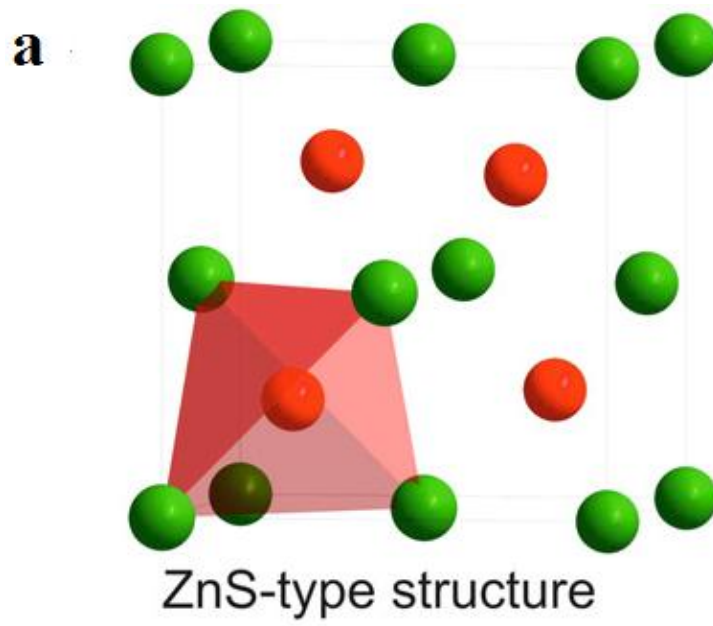


Figure 5.2 (a): Tetrahedral Zinc blende structure and (b) the rock salt structure Source: Graf *et al.*, 2011

The difference in energy at the optimised lattice constant between the Cu_2MnAl and Hg_2TiCu structures is higher in Mn_2VAl at 450 meV than in Mn_2VIn at 250 meV as shown in Figures 5.3 (a) and (b), hence the stability of the predicted $L2_1$ structure in Mn_2VAl is higher than in Mn_2VIn .

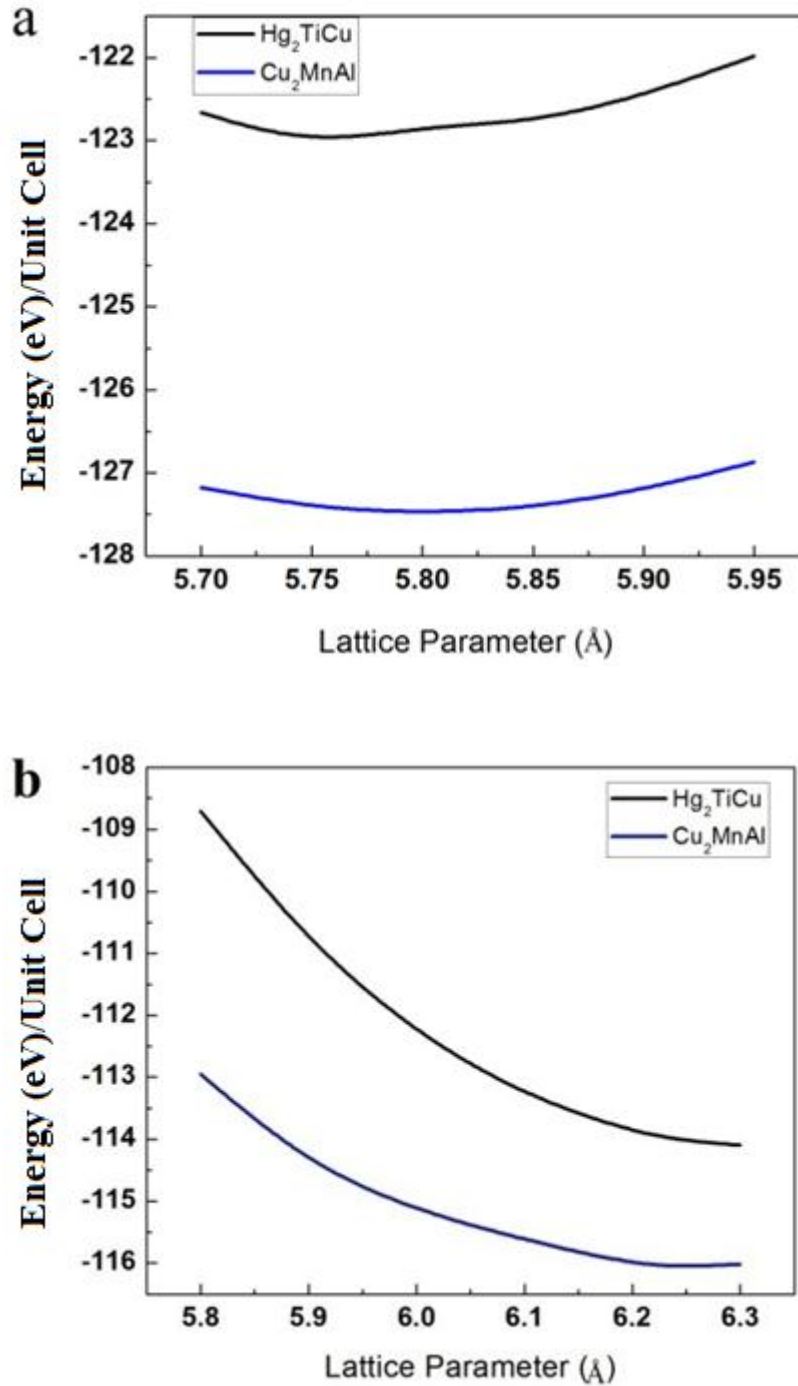


Figure 5.3: The energy for the Hg_2TiCu and Cu_2MnAl crystal structures for (a) Mn_2VAl and (b) Mn_2VIn

The optimised lattice parameters are 5.8 Å and 6.25 Å for Mn₂VAl and Mn₂VIn, respectively as shown in Figures 5.4 (a) and (b).

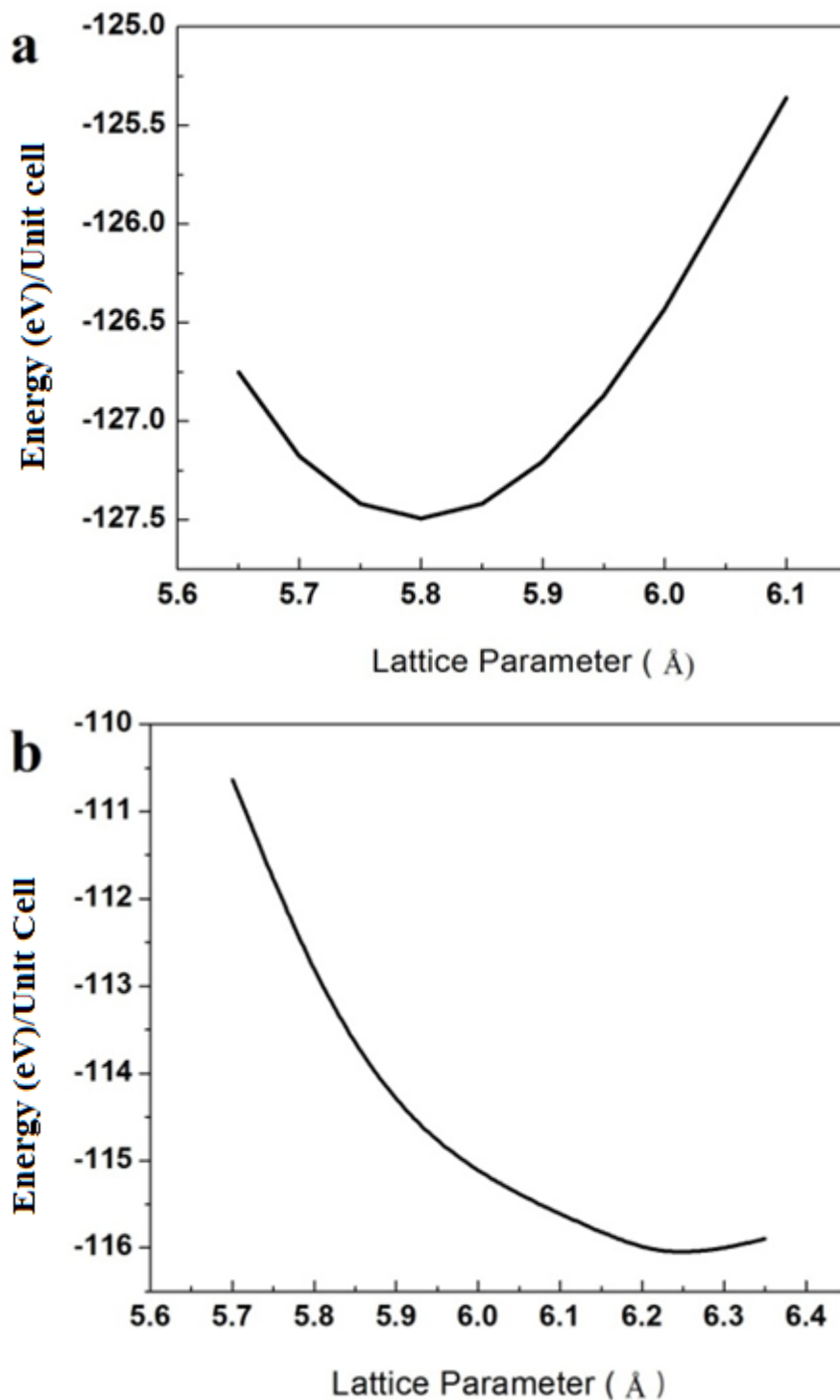


Figure 5.4: Volume optimization for (a) Mn₂VAl and (b) Mn₂VIn

The effect of the larger atomic radius of In as compared to Al is immediately realised in the large optimised lattice constant of optimised $L2_1$ structure of Mn_2VIn compared to Mn_2VAl . The increased lattice constant affects the hybridisation between the orbitals, which has a direct effect on the electronic structure and spin polarisation of the compound as described in section 5.1.2.

5.1.2: Electronic properties

While Mn_2VAl is found to be half-metallic at the optimised volume, the half-metallic gap is realised in Mn_2VIn at a lattice parameter lower than the optimal one. The total density of states (TDOS) and partial density of states (PDOS) for Mn_2VAl is shown in Figure 5.5.

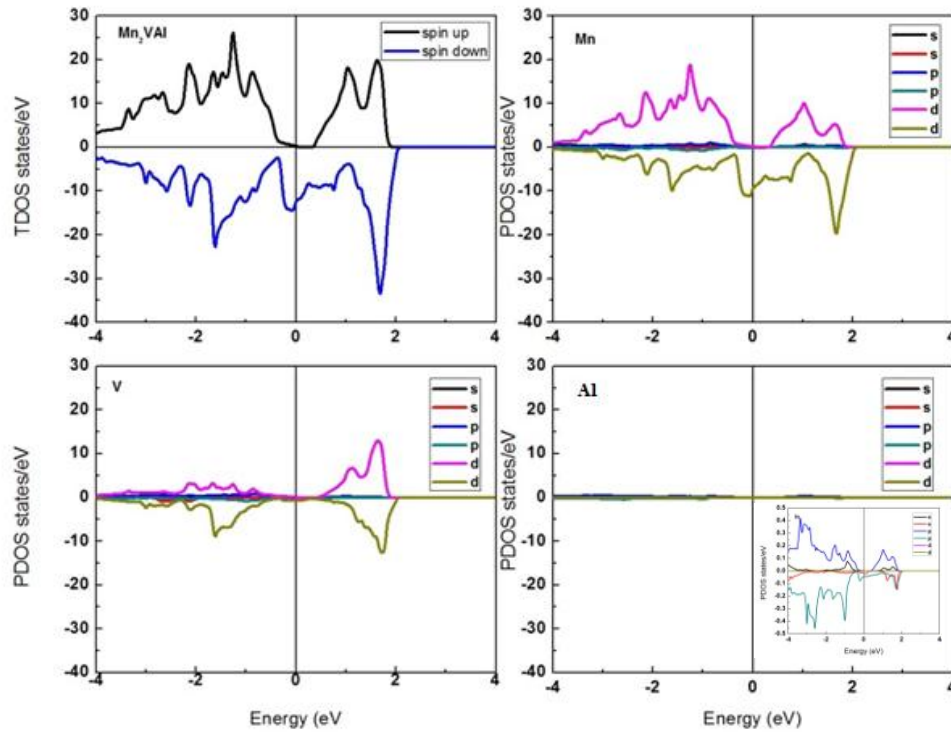


Figure 5.5: Total density of states (TDOS) and partial density of states (PDOS) for Mn_2VAl . Inset shows a blow up of the d , p and s states of Al near the Fermi level

The electron spin polarisation at the Fermi level is defined by the following expression

$$P = \frac{n^\uparrow(E_F) - n^\downarrow(E_F)}{n^\uparrow(E_F) + n^\downarrow(E_F)} \quad (5.1)$$

Where, $n \uparrow (E_F)$ and $n \downarrow (E_F)$ are the spin dependent densities of states at E_F for the majority and minority spin cases, respectively. As is evident from the density of states plot for Mn_2VAl , there is a gap in the spin up states at the Fermi level while the spin down states are conducting, resulting in almost complete spin polarisation at the Fermi level. The half-metallic gap develops as a result of the hybridisation of the bonding (t_{2g} , e_g) and anti-bonding (e_u , t_{1u}) states which are formed as a result of lifting of the degeneracy of the d -states due to crystal field splitting (Évarestov and Smirnov, 1997). The spin up states below the gap are dominated by Mn d -states, hence, the Mn moment is strongly t_{2g} in character. The less dominant V moments are also t_{2g} in character and the Al character at the Fermi level, which is mainly comprised of p -states, as shown in the inset of Figure 5.5, is so small giving a negligible contribution to the total magnetic moment. Below 0.5 eV in the spin down states, there are approximately equal amounts of V and Mn mixed d -states. Overall, the density of states is strongly Mn t_{2g} in character around E_F . Hence, the completely polarised charge carriers are almost entirely associated with Mn atoms.

In general therefore, the gap in the spin up channel in Mn_2 based alloys is the result of hybridisation of the X atoms on site 8c of the $L2_1$ structure with space group number 225, in the $Fm-3m$ space group, which are tetrahedrally coordinated with their neighbouring atoms. Strong exchange splitting is exhibited in Mn, hence the minority Mn d -states are unoccupied at the Fermi level. The final size of the gap is determined by the crystal field splitting of the e_g and t_{2g} states at the Γ point, which is determined by the symmetry and coordination of the Mn atoms (Wollmann *et al.*, 2014).

The Total Density of States (TDOS) and Partial Density of States (PDOS) for Mn_2VIn at the optimised lattice constant of 6.25 Å is shown in Figure 5.6. At the Fermi level, both the Mn and V d -states are present, hence the absence of a half-metallic gap in either spin channel. Hybridisation is inhibited by the larger lattice constant. The Mn t_{2g} states are much lower in energy below the Fermi level, inhibiting hybridisation with the V d -states, hence the presence of V states at the Fermi level in the Mn_2VIn TDOS as compared to the Mn_2VAl TDOS. The electronic structure is therefore not half-metallic at this lattice constant, having a very low spin polarisation of 15.38%. An investigation of the electronic properties of slightly compressed

structures with lower lattice constants was carried out, resulting in highly spin polarised electronic structures with the Fermi level in the middle of the gap.

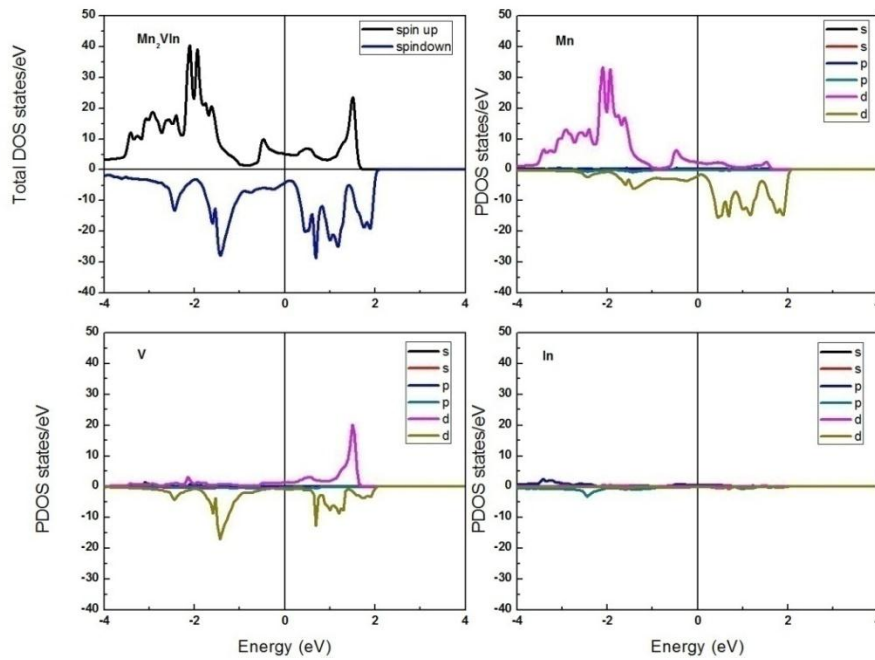


Figure 5.6: Total density of states (TDOS) and partial density of states (PDOS) for Mn_2VIn

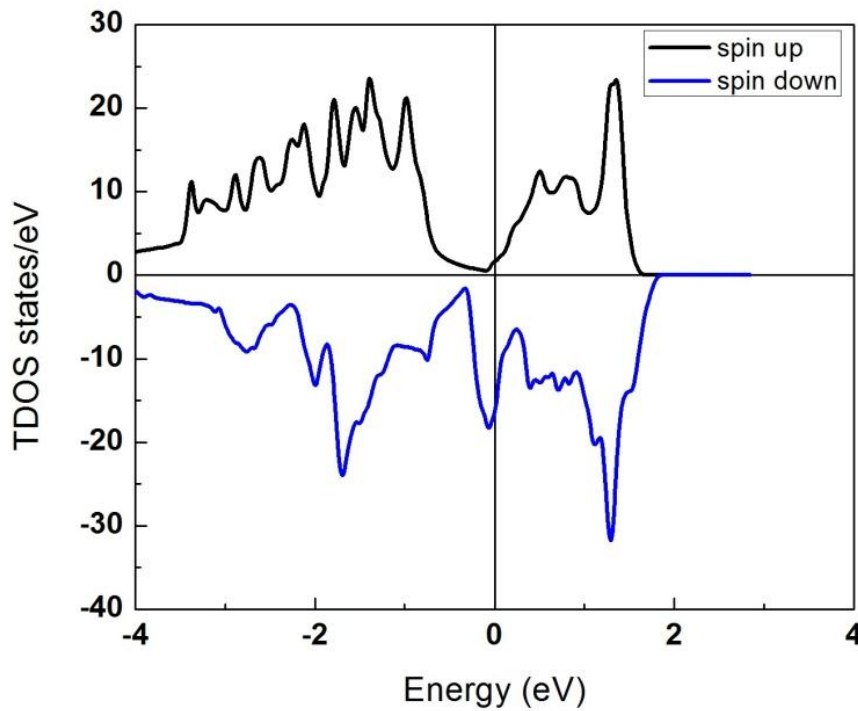


Figure 5.7: Total density of states (TDOS) for Mn_2VIn at lattice constant $a = 6 \text{ \AA}$

In Figure 5.7, the TDOS for Mn_2VIn at a lattice constant of 6\AA reveals a half-metallic gap with the Fermi level closer to the conduction band.

Compression to $a = 5.95\text{\AA}$ improves the stability of the half-metallic gap and the resulting TDOS plot is shown in Figure 5.8. At this lattice constant, the spin polarisation is 99.6%.

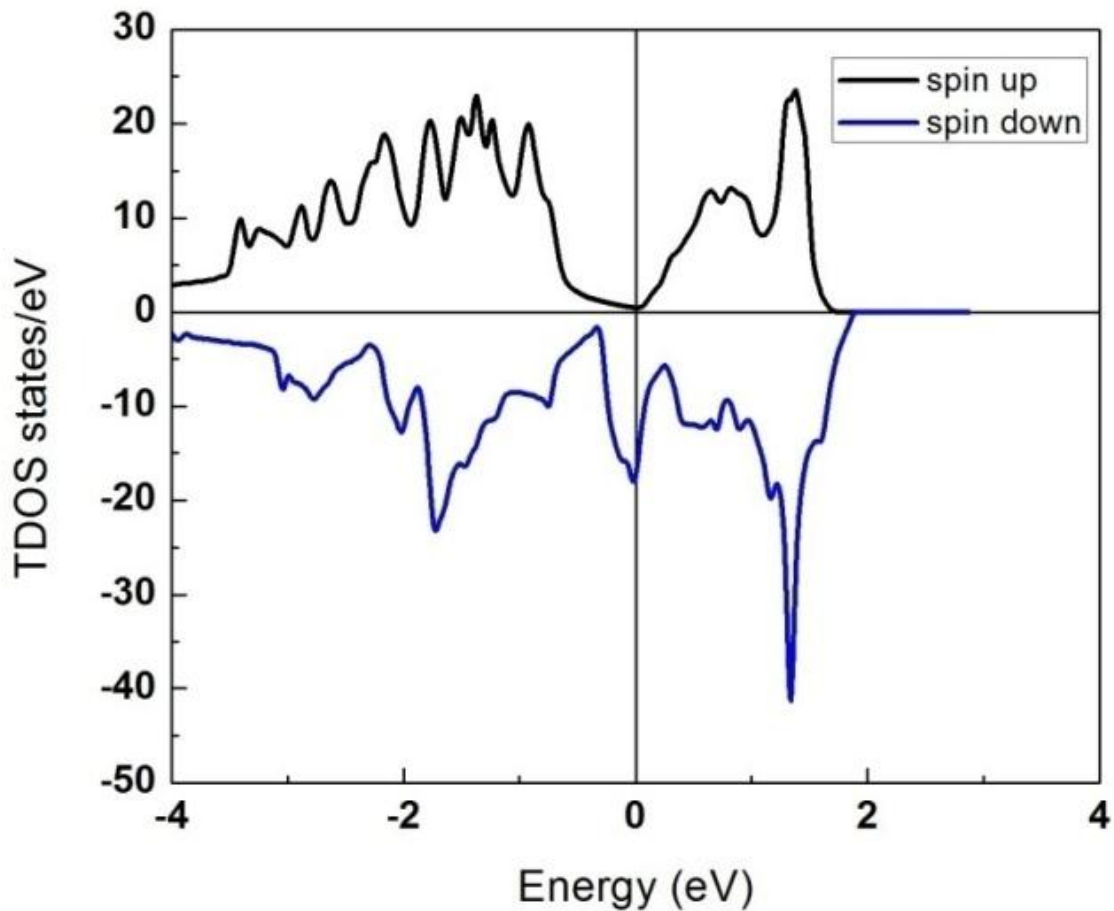


Figure 5.8: Total density of states (TDOS) for Mn_2VIn at lattice constant $a = 5.95\text{\AA}$.

A further compression to $a = 5.83\text{\AA}$ takes the Fermi level to the middle of the half-metallic gap making it even more robust. The TDOS and PDOS at this lattice constant is displayed in Figure 5.9. The density of states is highly spin polarised with a spin polarisation of 94.6%.

Structural energetics for Mn_2VIn was then investigated for possible structural instabilities that would possibly cause distortion in the structure of Mn_2VIn and the same was done for Mn_2VAl

for comparison. The calculated total energy for both compounds as a function of crystallographic axes ratios c/a is shown in Figures 5.10 (a) and (b).

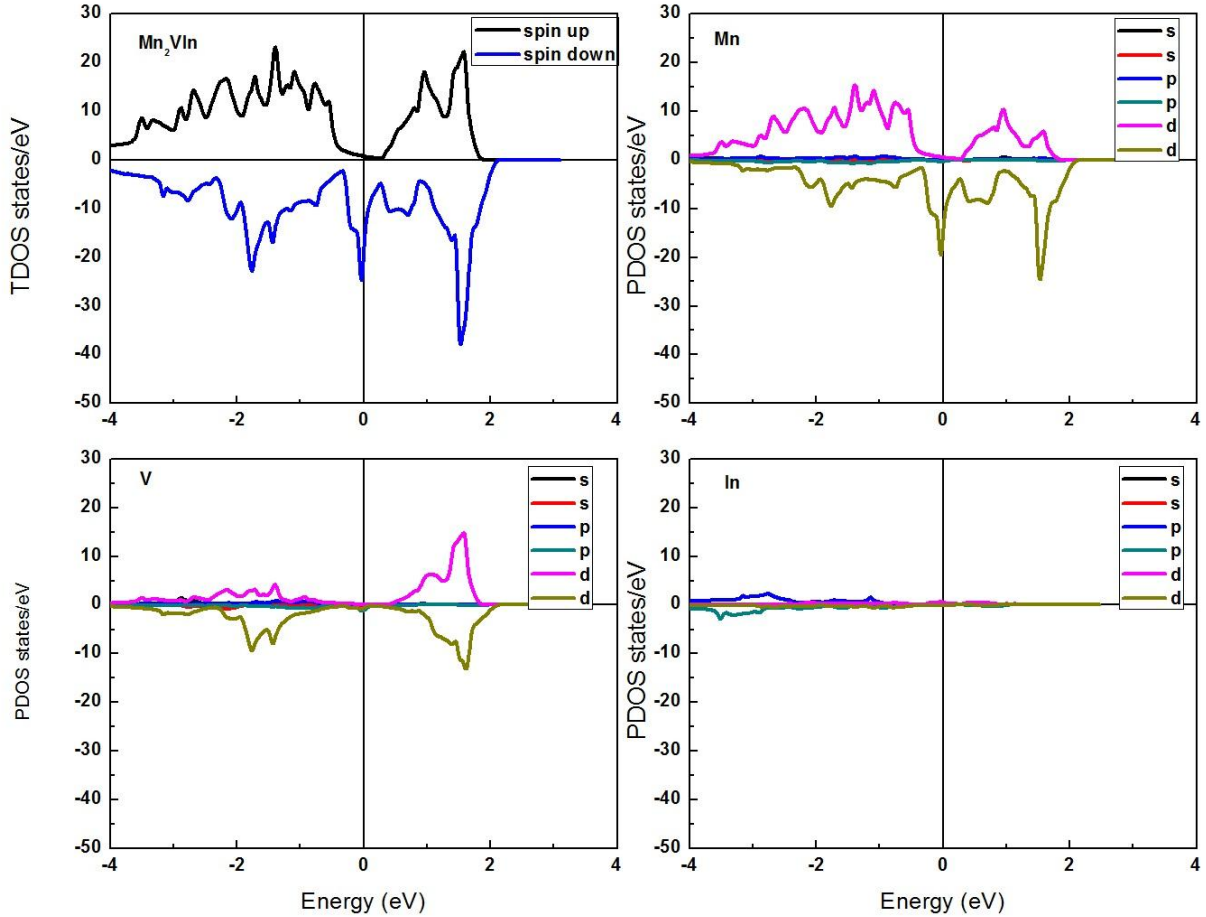


Figure 5.9: Total density of states (TDOS) and partial density of states (PDOS) for Mn_2VIn at $a = 5.83\text{\AA}$

The region of c/a from 0.9 to 1.1 was examined. A shallow low energy local minimum was observed at $c/a=0.93$ in Figure 5.10, which is 412 meV higher than the $L2_1$ structure. In Ni_2MnGa , a tetragonal distortion associated with a martensitic transition clearly demonstrated by c/a calculations for bulk crystals was found. The significance of these results is that they can be used to predict the effects of epitaxial stress in fabrication of thin films, which is a major factor in determining the structure and properties of the thin films (Godlevsky and Rabe, 2001). The electronic structure for the tetragonally distorted compound at lattice parameters corresponding to the ratio at the local minimum is shown in Figure 5.11.

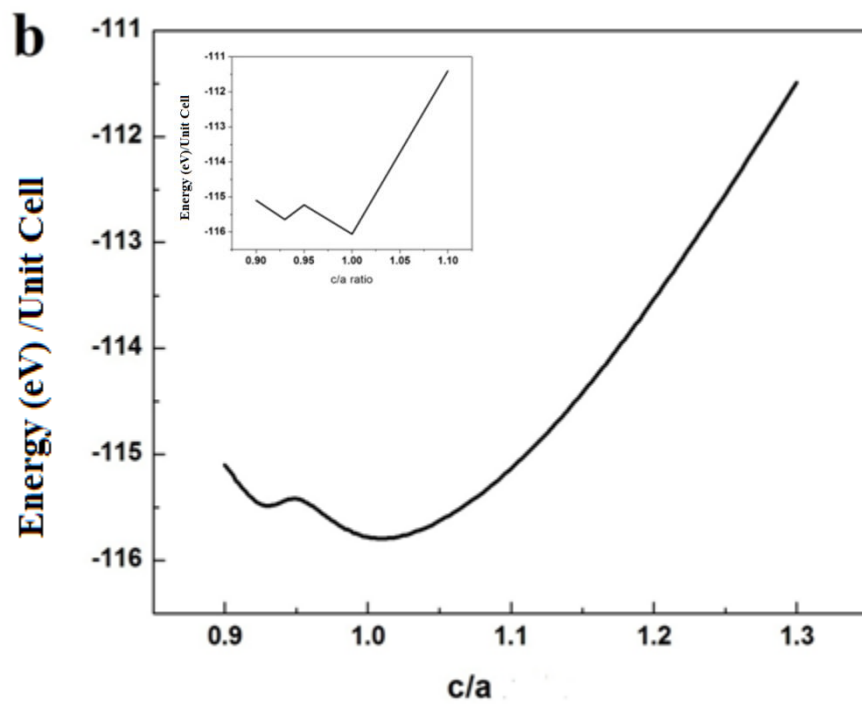
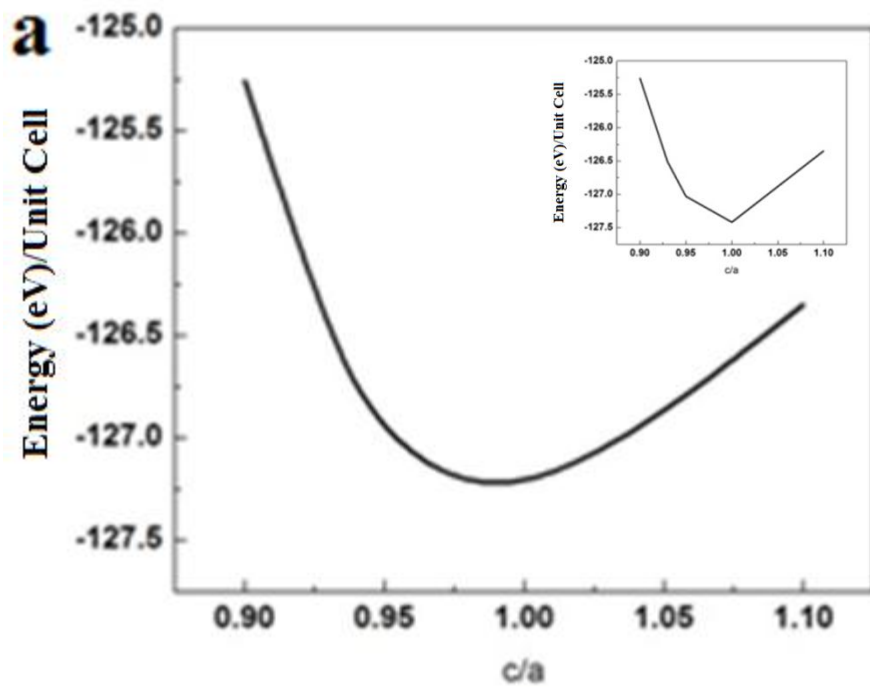


Figure 5.10: Total energy as a function of c/a ratio for (a) Mn_2VAl and (b) Mn_2VIn . Inset is the line graph without smoothening, emphasizing the two minima

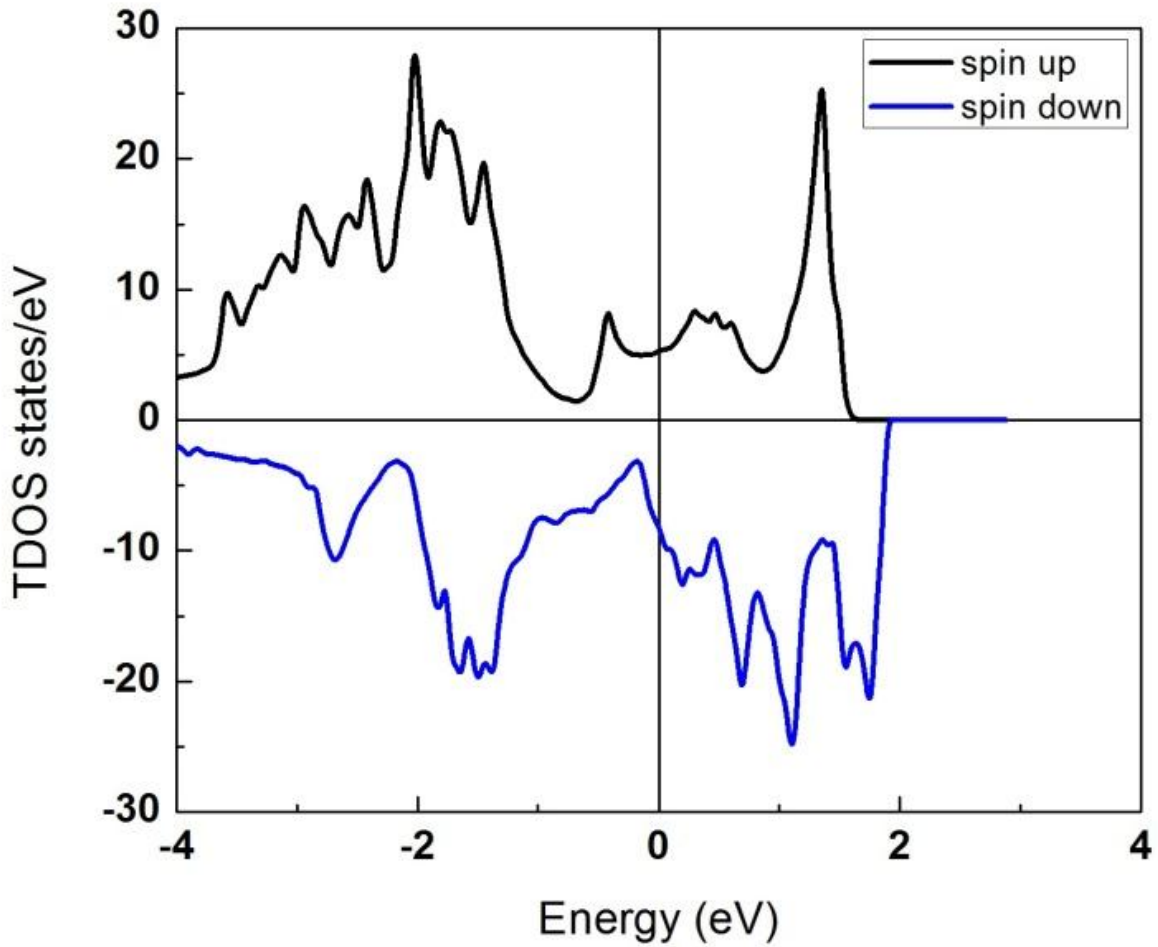


Figure 5.11: Total density of states (TDOS) for tetragonally distorted Mn_2VIn at $c/a=0.93$

The electronic structure is no longer half-metallic but has less minority states as compared to the majority states at the Fermi level resulting in spin polarisation. The half-metallic gap closes due to introduction of spin up states at the Fermi level. The occurrence of tetragonal distortion in Mn_2VIn clearly demonstrates the structure – property relation in Heusler compounds as evidenced by its effect on spin polarisation and inevitably the magnetic properties as well. These results can also be used to predict the properties of Mn_2VIn films and similar compounds containing a relatively large Z element. Additionally, tetragonal distortion points to the possibility of magnetic anisotropy in Mn_2VIn , an important property in spintronics, which was investigated and results given in section 5.1.3.

5.1.3: Magnetic properties

In both Mn_2VAl and Mn_2VIn , Mn and V have antiparallel spin moments. They would, therefore, create smaller external magnetic fields in devices, leading to smaller energy losses. In magneto electronic applications, half-metallic ferrimagnets are desirable over ferromagnets because a small magnetic moment does not give rise to strong stray fields in devices and are less affected by external magnetic fields (Kawakami *et al.*, 1981).

In Mn_2VAl , the total magnetic moment is $1.936 \mu_B$ per formula unit, with the Mn moment being $1.426 \mu_B$ while the V and Al moments are $-0.895 \mu_B$ and $-0.021 \mu_B$, respectively. A ferrimagnetic coupling is exhibited between the Mn and V moments, confirming the ferrimagnetic nature of the compound. A slight expansion of the lattice to 5.9 \AA results in a total magnetic moment of $1.995 \mu_B$, almost the integer value of $2 \mu_B$ as would be required by the Slater-Pauling rule for full Heusler compounds where the magnetic moment is given by the relation $M_T = Z_T - 24$. The magnetic moments are $1.665 \mu_B$, $-1.309 \mu_B$, $-0.026 \mu_B$, for Mn, V and Al, respectively. This confirms the half-metallic character of Mn_2VAl .

Similarly, in Mn_2VIn , Mn and V exhibit an antiparallel coupling and there is hardly any hybridisation in the structure with the optimised lattice constant, in which the Mn moment is $3.009 \mu_B$ and the V and In moments are $-1.979 \mu_B$ and $-0.059 \mu_B$ respectively. For the compressed lattices, in which hybridisation is possible, the same antiparallel coupling is observed and the total moment per formula unit is very close to the expected $2 \mu_B$ in accordance with the Slater-Pauling rule for half-metallic Heusler compounds with a total number of 22 valence electrons. For a lattice constant of 6 \AA , the Mn moment is reduced to $1.629 \mu_B$, while those of V and In are $-1.245 \mu_B$ and $-0.039 \mu_B$ giving a total moment of $1.974 \mu_B$ per formula unit. At a lattice constant of 5.95 \AA , the magnetic moment for Mn is $1.536 \mu_B$ while those of V and In are $-1.115 \mu_B$, $0.029 \mu_B$, giving a total of $1.927 \mu_B$. The calculated total magnetic moment for Mn_2VIn at lattice parameter 5.83 \AA is $1.87 \mu_B$, while Mn, V and In have magnetic moments of $1.38 \mu_B$, $-0.88 \mu_B$ and $0.01 \mu_B$, respectively, hence a ferrimagnetic coupling. A general trend is observed, in which the total magnetic moment per formula unit decreases on decrease in lattice parameter. A similar effect was observed for half-Heusler system NiMnSb , in which, compression of the lattice was found to push the majority p states to higher energies while the

resulting contraction increased hybridisation between the d orbitals of the different transition metal atoms, resulting in a decrease of the spin moment of Mn. To preserve the integer value, the spin of the other component increased or even changed sign, changing from ferrimagnetic to ferromagnetic coupling (Şaşıoğlu *et al.*, 2005). The tetragonally distorted structure of Mn_2VIn is found to exhibit inplane magnetic anisotropy energy of 1.25 meV. An investigation of magnetic anisotropy in thin films of Mn_2VIn was carried out and reported in section 5.7, because reduced dimensions enhance spin orbit effects as well as hybridisation, which favour PMA, a highly desirable property in thin films for spintronic devices such as MRAM (Wang *et al.*, 2010).

Compression of the Mn_2VIn lattice caused the Fermi level to move towards the valence band whereas it moved closer to the conduction band for an expanded lattice. In addition, spin polarisation increased for a slightly compressed lattice as compared to that of the optimised volume of Mn_2VIn .

The shifting of the Fermi level with size of lattice constant was also observed by Galanakis and Mavropoulos, 2007, from their study of the effect of size of lattice parameter on the electronic properties of Mn_2VAl , whereby they observed that upon compression the Fermi level moved in the direction of the conduction band while on expansion, it moved towards the valence band, conserving the half-metallic character in both cases (Galanakis and Mavropoulos, 2007). A substrate with a smaller lattice constant than the optimised lattice constant for Mn_2VIn would probably be favourable for improving the spin polarisation in the system.

5.2 Half-metallicity in Mn₂VIn by Co Doping in Mn sites.

Mn₂VIn studied in section 5.1 was shown to display unique characteristics such as tetragonal distortion and half-metallicity on compression. The atomic radius of the In atom being larger than that of Al is responsible for the structural and, consequently, electronic property differences between the two isoelectronic compounds which would otherwise be expected to display very similar if not identical electronic properties. Other than lattice compression/expansion, doping with a fourth element has been found to shift the position of the Fermi level in Heusler compounds. In this section, the structure of Mn₂VIn is further modified by doping with Co atoms with a view to enhancing spin polarisation, resulting in half-metallicity. Doping was carried out on Mn_{2-x}Co_xVIn, where x ranges from 0.25 to 1.25 in steps of 0.25.

5.2.1 Electronic and Structural Properties

As in the case of Mn₂VIn studied in section 5.1 which has a very low spin polarisation of 15.38% at the lattice constant of the system with the lowest energy, the spin polarisations of the doped compounds that are stable at a lattice constant > 6.1 Å, in particular those containing 1 and 2 Co antisites, are very low. The resulting concentrations with x = 0.25 and x = 0.5 resulted in total density of states plots (TDOS) in which both spin channels are heavily conducting hence, no half-metallic gap as shown in Figures 5.12 (a) and (b). However, the majority states are greatly enhanced for x = 0.5 due to the presence of Co *d*-states near the Fermi level. The resulting spin polarisations for x = 0.25 and x = 0.5 are 30.70% and 11.43%, respectively, which in the case of x = 0.25 is higher than that of Mn₂VIn and reduces for x = 0.5 due to the combined effect of lattice contraction and increased Co *d*-states population at the Fermi level with increased Co concentration. Both compounds maintained the cubic structure on full relaxation with lattice constants of 6.189 Å and 6.165 Å for Mn_{1.75}Co_{0.25}VIn and Mn_{1.5}Co_{0.25}VIn, respectively.

The electronic structure for MnCoVIn has a spin polarisation of 73.89% with the emergence of a half-metallic gap in the spin up states, with the Fermi level closer to the conduction band. This is as a result of the reduced lattice constant of the fully relaxed structure at a = b = 6.003, c = 6.068, which, however, displays a small degree of tetragonal distortion, but at which effective overlap of the orbitals takes place resulting in hybridisation. The spin polarisation is however, less than expected due to the tetragonal distortion which pulls the *d*-states towards the Fermi level.

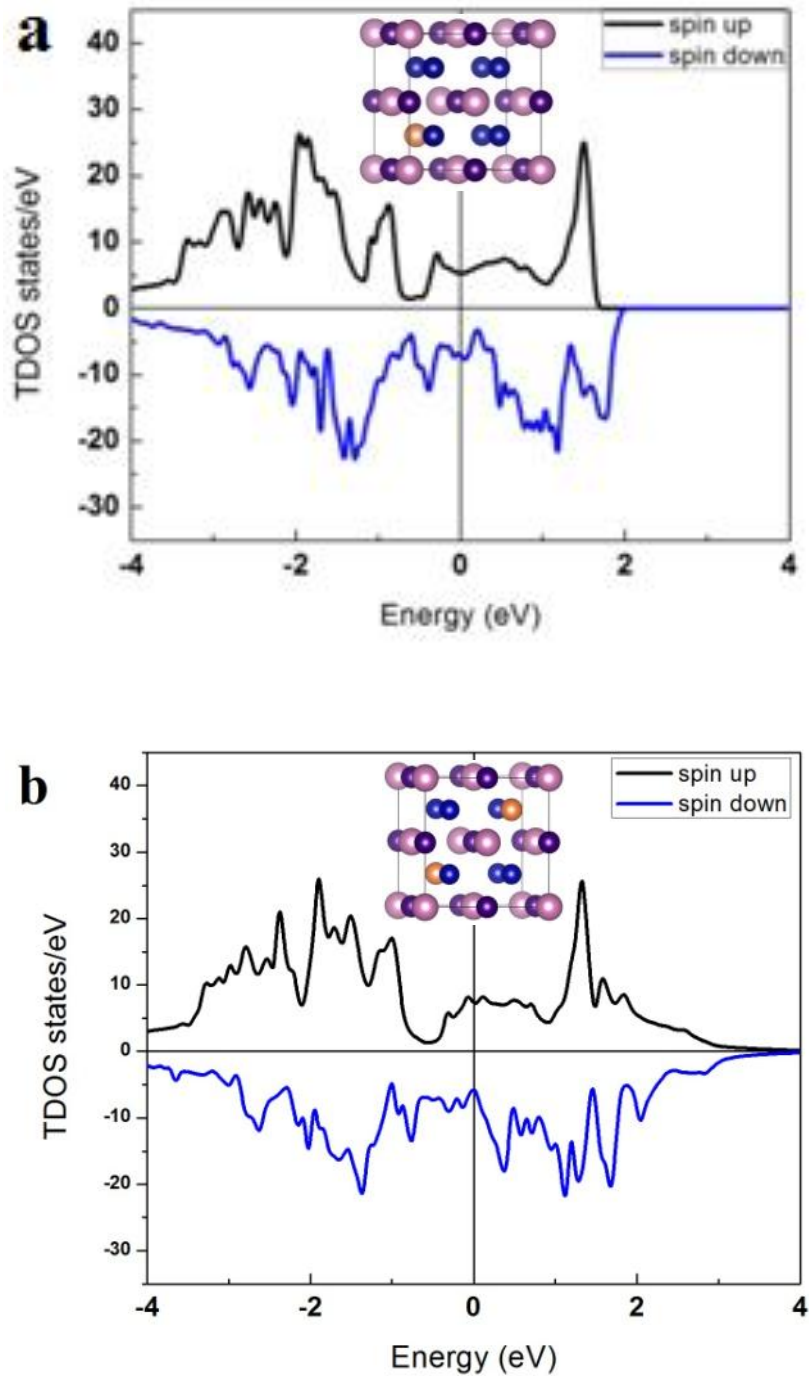


Figure 5.12: Total density of states plots (TDOS) for (a) $\text{Mn}_{1.75}\text{Co}_{0.25}\text{VIn}$ and (b) $\text{Mn}_{1.5}\text{Co}_{0.5}\text{VIn}$. Inset in each figure is the corresponding structure showing the impurity Co atom in Mn sites

The high spin polarisation is also found in $\text{Mn}_{1.25}\text{Co}_{0.75}\text{VIn}$ and $\text{Mn}_{0.75}\text{Co}_{1.25}\text{VIn}$, whose relaxed structures are also tetragonally distorted with lattice constants of $a = b = 6.028 \text{ \AA}$, $c = 6.042 \text{ \AA}$

and $a = b = 5.989 \text{ \AA}$, $c = 6.055 \text{ \AA}$, respectively. The resulting density of states is highly spin polarised at 86% and 80.6% respectively. This is depicted in Figures 5.13 (a) and (b). Interestingly, while the half-metallic gap is in the majority states for the Mn rich variant, it is switched to the minority states in the Co rich variant. This is a property that can be exploited in design of spintronic devices.

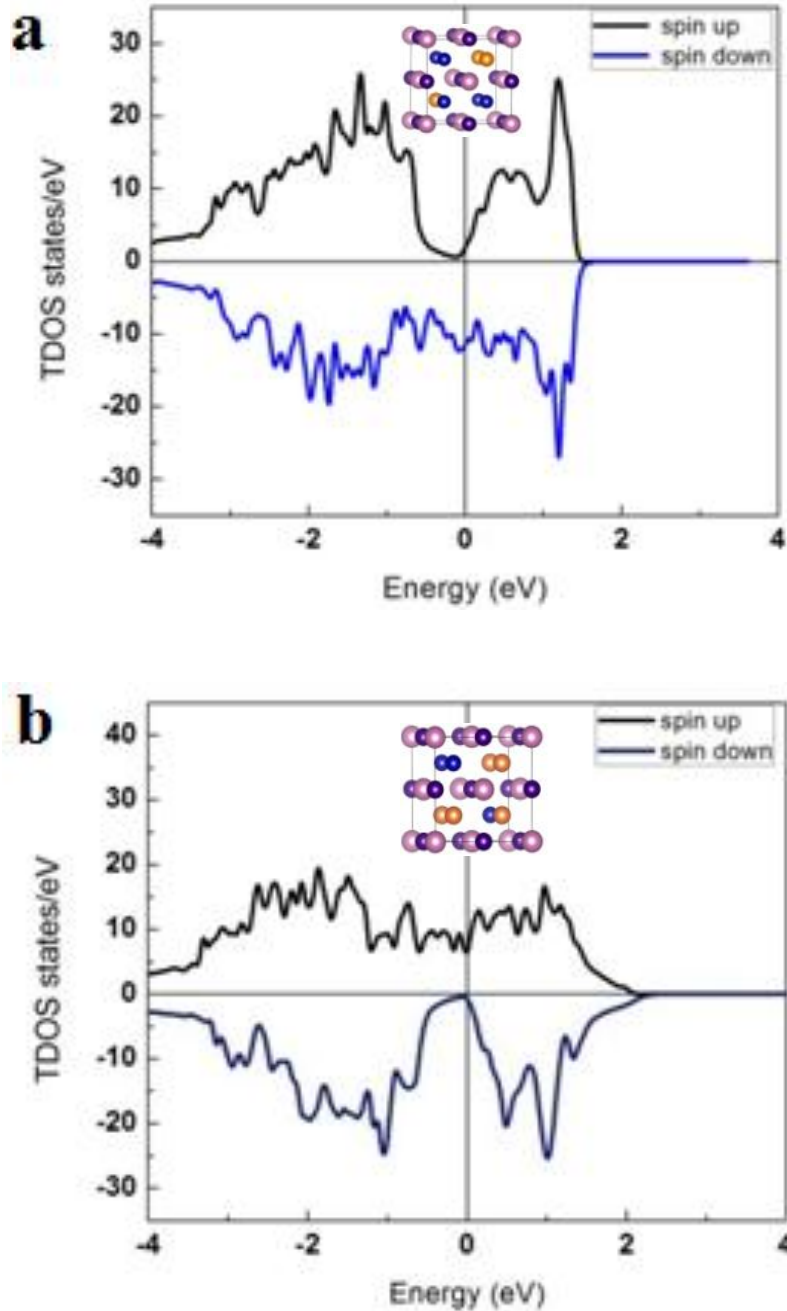


Figure 5.13: Total density of states plots (TDOS) for (a) $\text{Mn}_{1.25}\text{Co}_{0.75}\text{VIn}$ and (b) $\text{Mn}_{0.75}\text{Co}_{1.25}\text{VIn}$. Inset in each figure is the corresponding structure showing the impurity Co atom in Mn sites

The Fermi level falls in the half-metallic gap in the spin down states of $\text{Mn}_{0.5}\text{Co}_{1.5}\text{VIn}$ which maintains a cubic structure with $a = 6.011\text{\AA}$ and having a spin polarisation of 82% while in $\text{Mn}_{0.25}\text{Co}_{1.75}\text{VIn}$, having $a = 6.003\text{\AA}$, the Fermi level falls almost at the centre of the half-metallic gap in the spin down states, with a resulting spin polarisation of 93.6% as shown in Figures 5.14 (a) and (b).

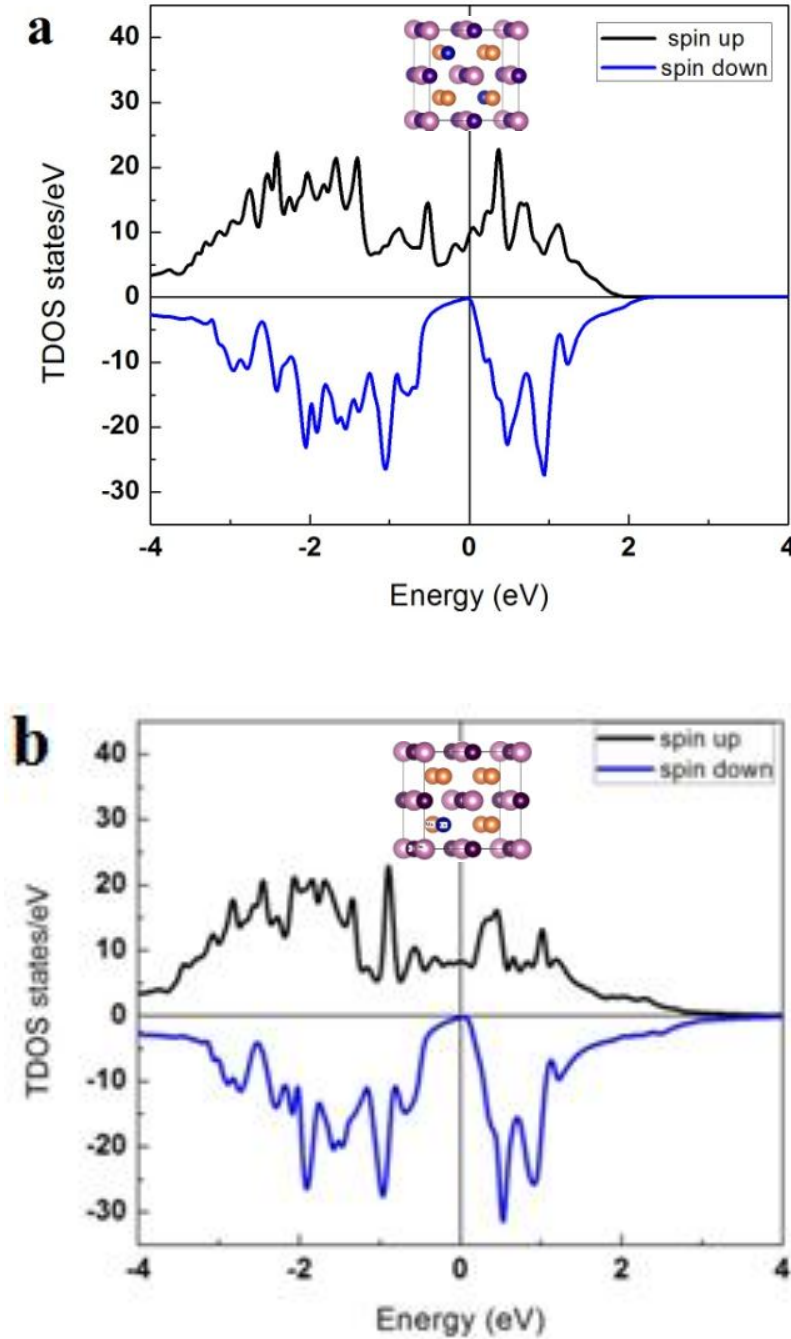


Figure 5.14: Total density of states plots (TDOS) for (a) $\text{Mn}_{0.5}\text{Co}_{1.5}\text{VIn}$ and (b) $\text{Mn}_{0.25}\text{Co}_{1.75}\text{VIn}$. Inset in each figure is the corresponding structure showing the impurity Co atom in Mn sites

The location of the Fermi level almost at the centre of the gap as well as a stable density of majority states, devoid of Van Hove singularity, points to the stability of the half-metallic gap in this composition. $\text{Mn}_{0.25}\text{Co}_{1.75}\text{VIn}$ has the highest spin polarisation at 93.6 % and its TDOS is plotted separately in Figure 5.15 in which a clear half-metallic gap is seen in the spin down states.

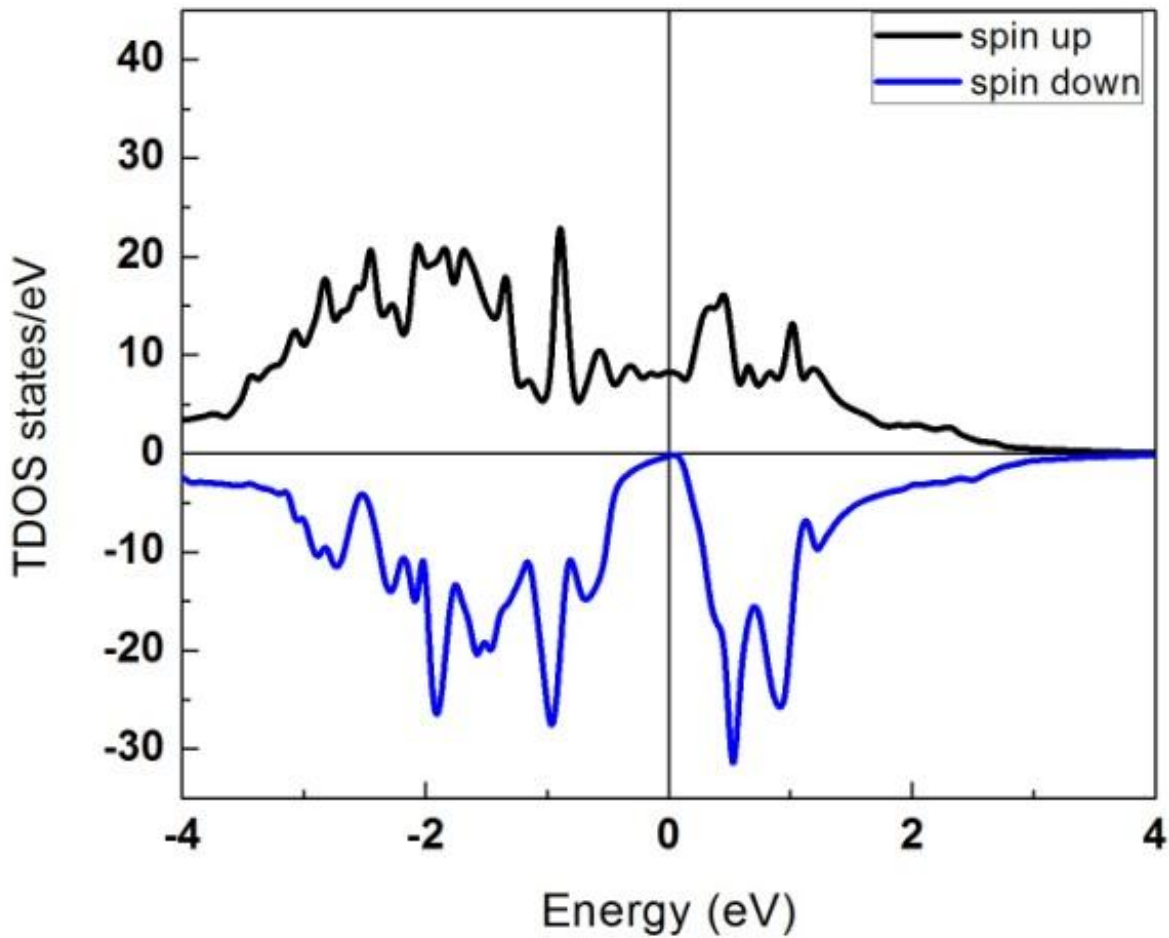


Figure 5.15: Total density of states plot (TDOS) for $\text{Mn}_{0.25}\text{Co}_{1.75}\text{VIn}$

The atom resolved partial density of states in Figure 5.16 highlights the contribution of the states of each atom to the electronic structure.

It is evident that the TDOS has an overwhelming Co character and the Mn and In contribution at the Fermi level is almost negligible. Notable is the contribution of the majority V *d*-states that hybridise with the majority Co *d*-states at the Fermi level contributing to the increased majority

states in the TDOS and the absence of minority states at the Fermi level resulting in a half-metallic gap. From the results of the electronic structure, it emerges that Co and V states hybridise in a manner favourable to the formation of a half-metallic electronic structure. This was investigated further and the results are given in section 5.3 for Co_2VIn . $\text{Mn}_{0.25}\text{Co}_{1.75}\text{VIn}$ is more stable in the Cu_2MnAl structure than the Hg_2CuTi .

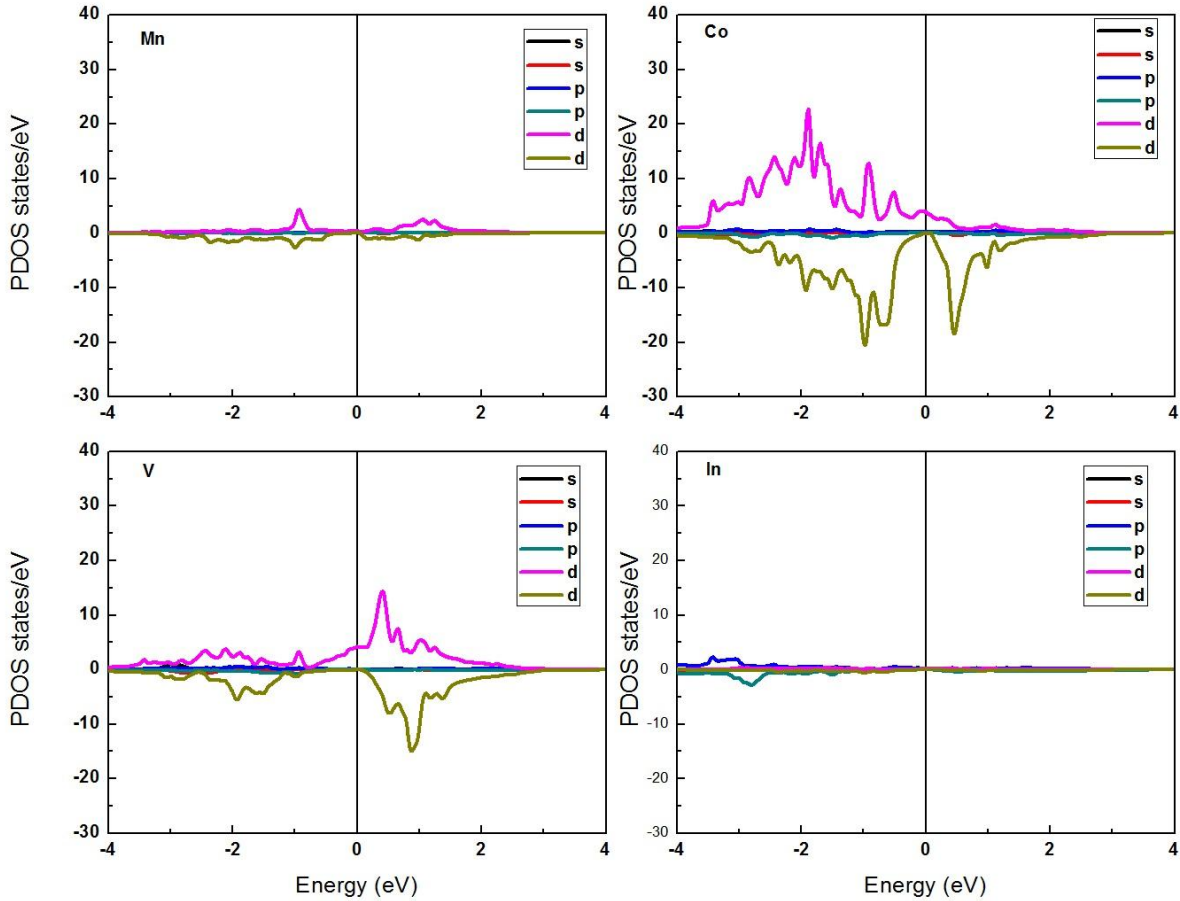


Figure 5.16: Total density of states (TDOS) and partial density of states (PDOS) for $\text{Mn}_{0.25}\text{Co}_{1.75}\text{VIn}$

5.2.2 Magnetic Properties

The magnetic moments of the elements in the doped variants were found to have a great dependence on whether hybridisation is possible at their equilibrium lattice constants as well as on the crystal structures of the unit cells. Table 5.1 highlights the magnetic moments for each

element in the unit cells as well as their corresponding lattice constants and the resulting spin polarisations.

Table 5.1: The calculated results for spin polarization and atom resolved magnetic moments at the lattice constants of the relaxed structures of $Mn_{2-x}Co_xVIn$ compounds

$Mn_{2-x}Co_xVIn$	Unit cell parameters (Å)	Mn (μ_B)	Co (μ_B)	V (μ_B)	In (μ_B)	Total μ_B /f.u.	Slater- Pauling μ_B /f.u.	Spin pol. %
Mn_2VIn	a = 6.250	3.009	-	-1.979	-0.059	3.980	2.0	15.380
$Mn_{1.75}Co_{0.25}VIn$	a = 6.189	2.767	-1.161	-1.820	-0.049	2.683	1.5	30.700
$Mn_{1.5}Co_{0.5}VIn$	a = 6.165	2.714	-0.454	-1.583	-0.048	2.213	1	11.430
$Mn_{1.25}Co_{0.75}VIn$	a = b = 6.028 c =6.042	1.651	-0.698	-1.035	-0.015	0.493	0.5	86.000
$MnCoVIn$	a = b = 6.003 c=6.068	1.518	-0.691	-0.839	-0.008	0.020	0	73.890
$Mn_{0.75}Co_{1.25}VIn$	a = b = 5.989 c =6.055	-1.355	0.751	0.628	-0.015	0.536	0.5	80.600
$Mn_{0.5}Co_{1.5}VIn$	a = 6.011	-1.465	0.849	0.504	-0.022	1.023	1	82.79
$Mn_{0.25}Co_{1.75}VIn$	a = 6.003	-1.231	0.897	0.327	-0.047	1.543	1.5	93.600

A general observation is made that there is a parallel alignment of Co and V spin moments in all the Co substituted compositions. Additionally, for all structures having a < 6.1 Å, the Slater-Pauling rule for predicting the total magnetic moments of half-metallic Heusler compounds is obeyed. This is true for $Mn_{1.25}Co_{0.75}VIn$, $MnCoVIn$, $Mn_{0.75}Co_{1.25}VIn$, $Mn_{0.5}Co_{1.5}VIn$ and $Mn_{0.25}Co_{1.75}VIn$. In all these compositions, the Mn magnetic moment is antiparallel to the Co and V moments. Tetragonal distortions resulted in three cases, right at the middle of the substituted variants for x = 0.75,1 and 1.25. In these three, there are vanishing total magnetic moments, and are therefore nearly antiferromagnetic. In fact, $MnCoVIn$ is as good as antiferromagnetic, with the small total magnetic moment value of 0.02 μ_B /f.u being as a result of the slight distortion of the structure.

The tetragonal distortions in $Mn_{0.75}Co_{1.25}VIn$ and $Mn_{1.25}Co_{0.75}VIn$ triggered an investigation of magnetic anisotropy energy which is of great significance to technological application. Unlike the in plane magnetic anisotropy found in tetragonally distorted Mn_2VIn , perpendicular magnetic anisotropy energy of 96.8 meV was established to be present in the $Mn_{0.75}Co_{1.25}VIn$ bulk system. The great significance of this finding is that this effect if present in the bulk is expected to be much higher in thin films used in industry, where spin orbit effects become significant at reduced

dimensions enhancing perpendicular magnetic anisotropy. On the other hand, $\text{Mn}_{1.25}\text{Co}_{0.75}\text{VIn}$ has an inplane magnetic anisotropy energy of 0.351 meV.

$\text{Mn}_{0.75}\text{Co}_{1.25}\text{VIn}$, MnCoVIn and $\text{Mn}_{1.25}\text{Co}_{0.75}\text{VIn}$ are nearly fully compensated ferrimagnets, with highly spin polarised electronic structures a very significant result for application in spintronic devices .

Mn_2VIn has demonstrated flexibility in which desirable properties result from energetically allowable structural distortions as well as the introduction of impurities. It is noteworthy that the spin polarisation increased in very low concentrations of impurity Co atoms. $\text{Mn}_{0.25}\text{Co}_{1.75}\text{VIn}$, having a composition closer to Co_2VIn than to Mn_2VIn , has the highest spin polarisation amongst all the compositions as well as ferromagnetic coupling between Co and V moments.

The doping and Fermi level tuning in $\text{Mn}_{2-x}\text{Co}_x\text{VIn}$ has demonstrated the usefulness of the technique in achieving materials with higher spin polarisation and the resulting system may be used as candidates for spin valves and magnetic tunnel junction applications.

5.3 Half-Metallic Co₂VIn and CoVIn Heuslers

In section 5.1 and 5.2, the versatility of Heusler compounds has been demonstrated, in which structural distortion and presence of impurities are exploited to predict the highly desirable spin polarisation as well as perpendicular magnetic anisotropy. Substitution for Mn with Co in Mn₂VIn has provided a route to decreasing the total magnetic moments, resulting in near antiferromagnetic coupling in the tetragonally distorted structures. In addition, ferromagnetic coupling between V and Co has resulted in the highest spin polarisations in the compounds. This was studied further and the results of the study of the structural, electronic and magnetic properties of full Heusler Co₂VIn and half Heusler CoVIn are reported in this section.

5.3.1: *Structural properties*

The two Co atoms occupy the 8c ($\frac{1}{4}, \frac{1}{4}, \frac{1}{4}$) position and V and In occupy the ($\frac{1}{2}, \frac{1}{2}, \frac{1}{2}$) and (0, 0, 0) positions respectively as shown in the optimised structure of Co₂VIn in Figure 5.17 (a) while Figure 5.17 (b) shows the optimised structure of CoVIn, in which the Co atom occupies the 4c ($\frac{1}{4}, \frac{1}{4}, \frac{1}{4}$) and ($\frac{3}{4}, \frac{3}{4}, \frac{3}{4}$) positions and V and In occupy the ($\frac{1}{2}, \frac{1}{2}, \frac{1}{2}$) and (0, 0, 0) positions respectively. The optimised lattice constant for Co₂VIn is 6.001 Å while that of CoVIn is 5.849 Å. On relaxation of the unit cell and ionic positions, the cubic structure is maintained.

The structural properties are calculated in both the paramagnetic and ferromagnetic states. Figure 5.18 (a) and (b) show that the total energies optimised in the ferromagnetic state are lower than the ones in the paramagnetic state, which confirms that the compounds are stable in the ferromagnetic phase. The energy difference between the magnetic and nonmagnetic states is 0.876 meV and 0.160 meV for Co₂VIn and CoVIn, respectively.

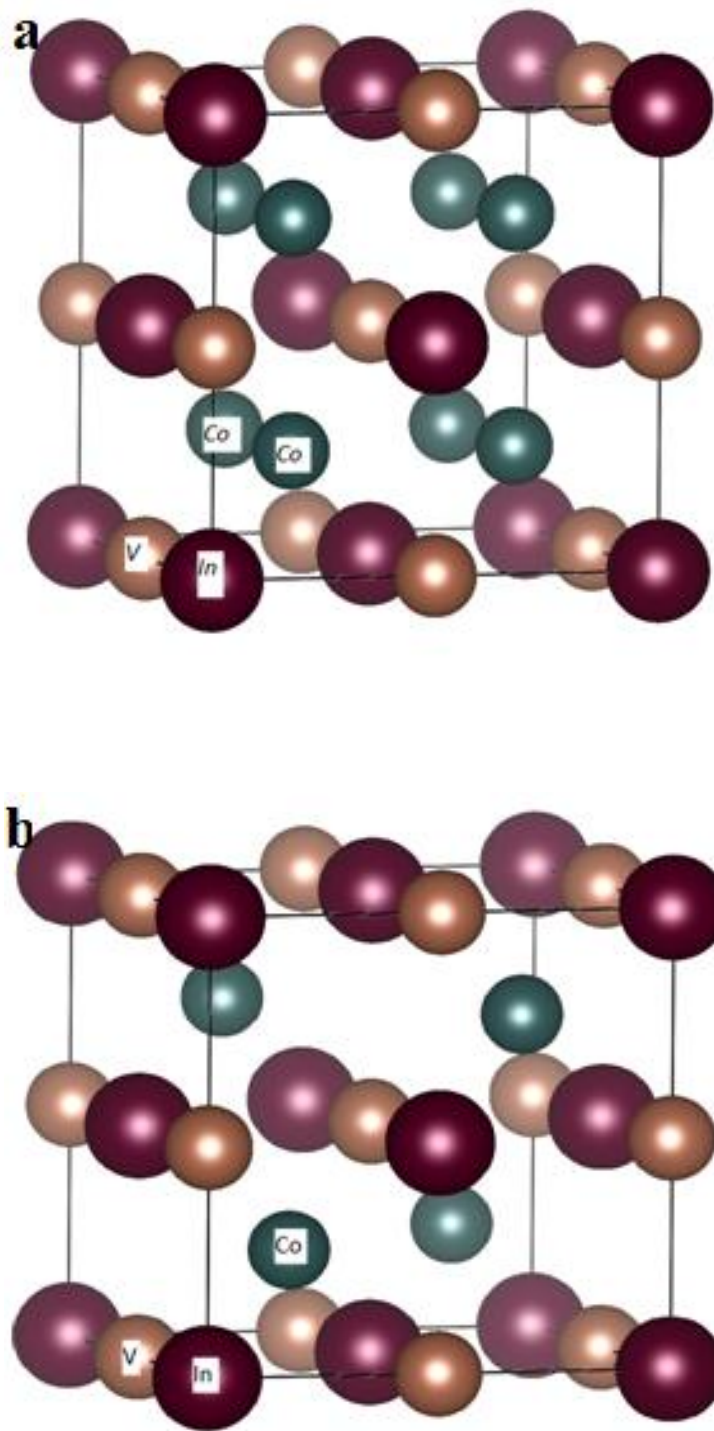


Figure 5.17(a): Relaxed Structure of Co_2VIn - L21 structure with Wyckoff position $8c$ ($\frac{1}{4}, \frac{1}{4}, \frac{1}{4}$) for the two Co atoms, $4a$ (0,0,0) and $4b$ ($\frac{1}{2}, \frac{1}{2}, \frac{1}{2}$) for In and V atoms respectively, space group Fm-3m , space group no. 225 and (b) Relaxed Structure of CoVIn . One of the ($\frac{1}{4}, \frac{1}{4}, \frac{1}{4}$) site for one of the Co atoms is vacant resulting in a Cl_b structure space group F-43m , space group no. 216.

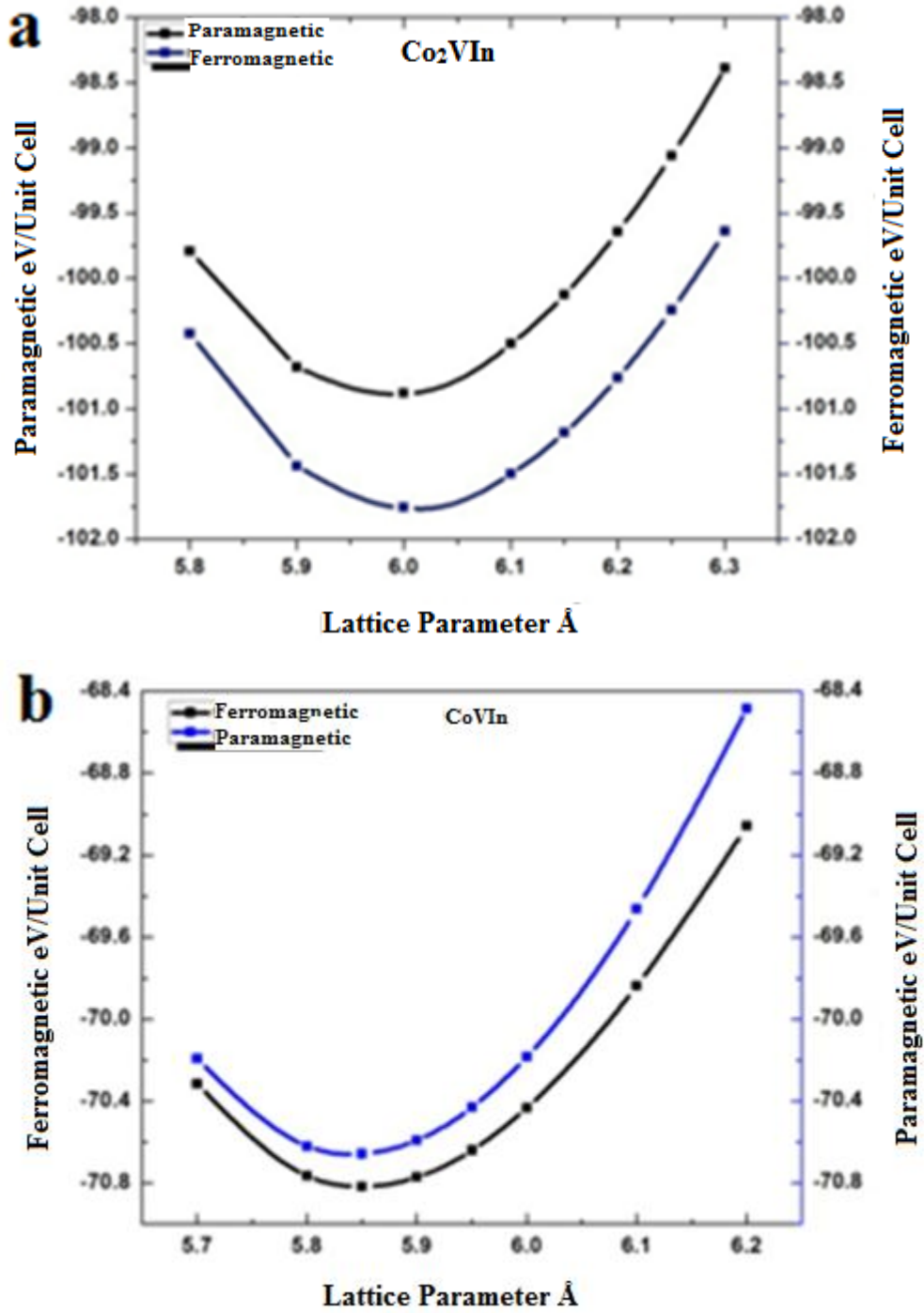


Figure 5.18 (a): Ferromagnetic and paramagnetic volume optimization for Co₂VIn and (b) Ferromagnetic and paramagnetic volume optimization for CoVIn

5.3.2: Electronic Properties

Spin polarised calculations of the CoVIn and Co₂VIn Heusler compounds were carried out at the equilibrium lattice parameters by employing the LSDA, GGA and PBE-GGA approximations. The electronic structure of Co₂VIn obtained from the LSDA calculation revealed a gap in the minority states, with the Fermi level closer to the conduction band. The gap in the minority states widened when the GGA approximation was employed and widened even further with the PBE-GGA approximation, with the Fermi level moving closer to the centre of the gap. This is depicted in the total density of states plots for Co₂VIn in Figures 5.19 (a) to (c).

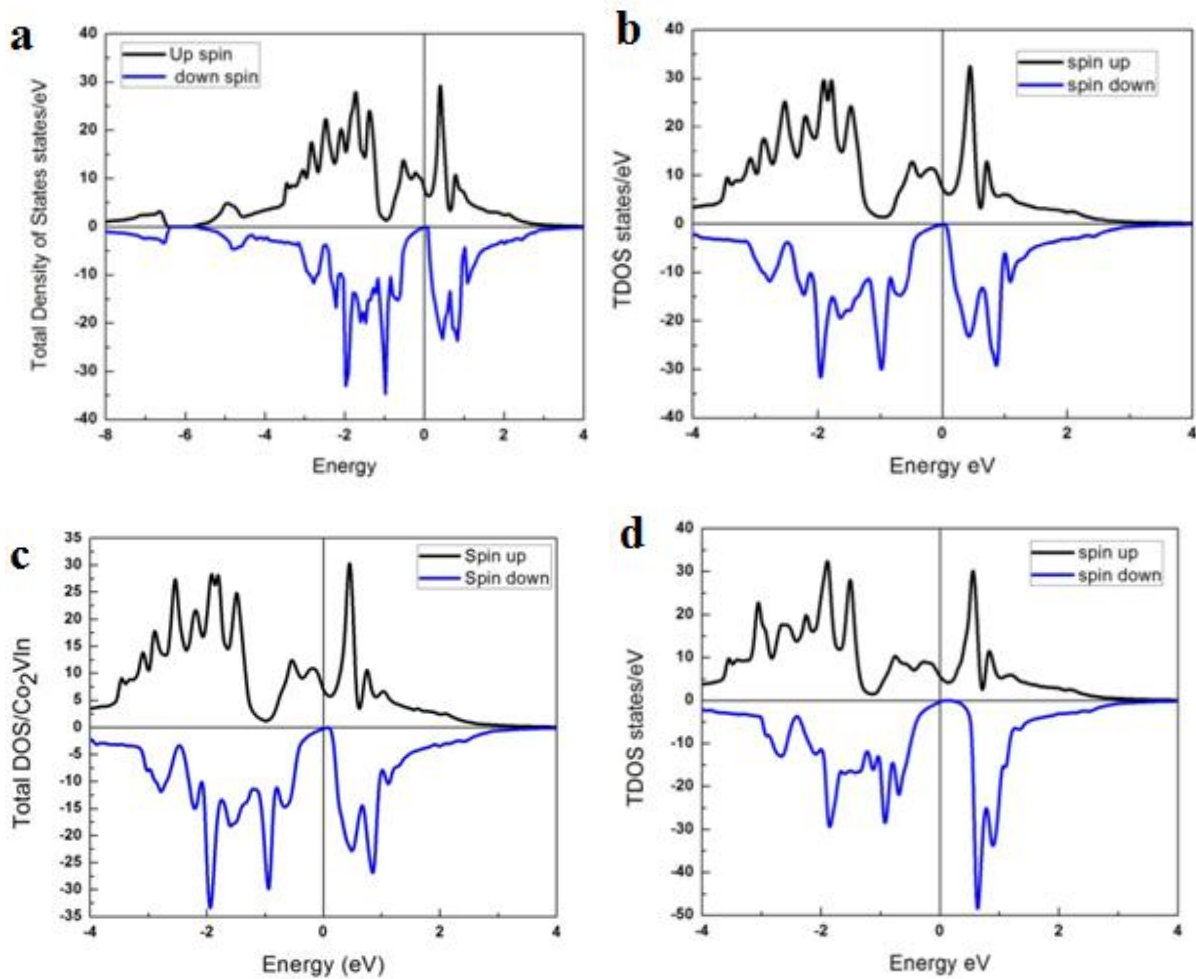


Figure 5.19 (a): Total density of states (TDOS) for Co₂VIn using the LDA approximation, (b) Total density of states (TDOS) for Co₂VIn using the GGA approximation, (c) Total density of states (TDOS) for Co₂VIn using PBE-GGA and (d) Total density of states (TDOS) for Co₂VIn using DFT+U method.

As can be clearly seen from the TDOS plots, highest spin polarisation is attained from the PBE-GGA calculation. The obtained spin polarisations for all approximations are summarised in Table 5.2.

To obtain a clearer picture of the electronic band structure, DFT+U calculations were carried out in order to treat the electron-electron correlations on localised d -states of Co and V with the L(S)DA, GGA and PBE-GGA approximation. The $U_{\text{eff}} = U - J$, was used to correct the double counted terms. The effect of this is shown in Figure 5.19 (d). The inclusion of U_{eff} in the calculation causes the band gap in the minority states of Co_2VIn to open up to 0.2 eV on average, with the lowest conduction band at the G point (origin) shifting to higher energies as recorded in Table 5.2. On inclusion of Coulomb correlation, 100% spin polarisation is realised with all approximations with the Fermi level almost at the centre of the gap. This confirms the half-metallic characteristic with the charge transport being dominated by the spin up electrons.

The corresponding spin resolved band structures along the high symmetry directions are consistent with the total density of states plots as shown in Figures 5.20 (a) and (b). The gap in the minority states is 0.21 eV, 0.2 eV and 0.19 eV for LSDA+U, GGA+U and PBE-GGA +U respectively. The band gap in Co_2VIn can be explained to be as a result of hybridisation between the two Co and V 3 d orbitals. The e_g and t_{2g} states of the Co and V sites dominate the part of the plots near E_F as shown in Figure 5.21 for both spin channels, resulting in a $d - d$ band gap.

The L(S)DA calculation for CoVIn yielded a total density of states with a gap in the majority states and the Fermi level located closer to the valence band as shown in Figures 5.22 (a) and 5.22 (b). As in the case of Co_2VIn , the spin polarisation was not 100% as some majority states were present at the Fermi level. The density of states plots are similar for the three approximations and are represented by Figure 5.22 (a) the only difference being the slight shift of the Fermi level towards the centre of the gap as the approximations were varied from L(S)DA to PBE-GGA. The DFT+U scheme, in particular GGA+U resulted in 100% spin polarisation of states with only the minority states at the Fermi level, which is located approximately at the center of the gap. This is well illustrated in Figure 5.22 (b). L(S)DA+U and PBE-GGA+U

schemes did not predict 100% spin polarisation for CoVIn. The spin polarisation results as well as band gaps are summarised in Table 5.2.

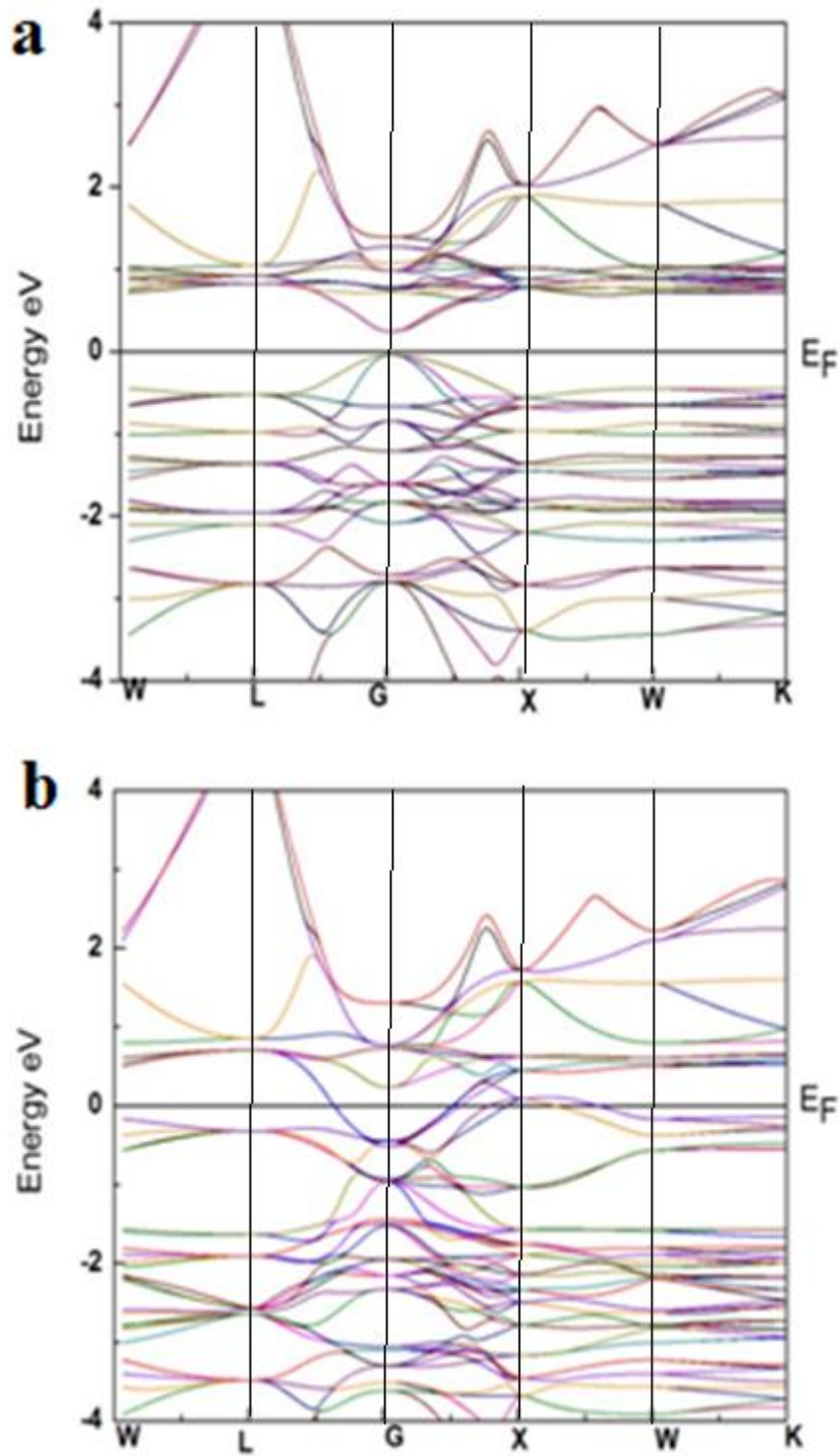


Figure 5.20 (a): Spin down electronic band structure of Co_2VIn at the equilibrium lattice parameter using GGA+U and (b) Spin up electronic band structure of Co_2VIn at the equilibrium lattice parameter using GGA+U approximation

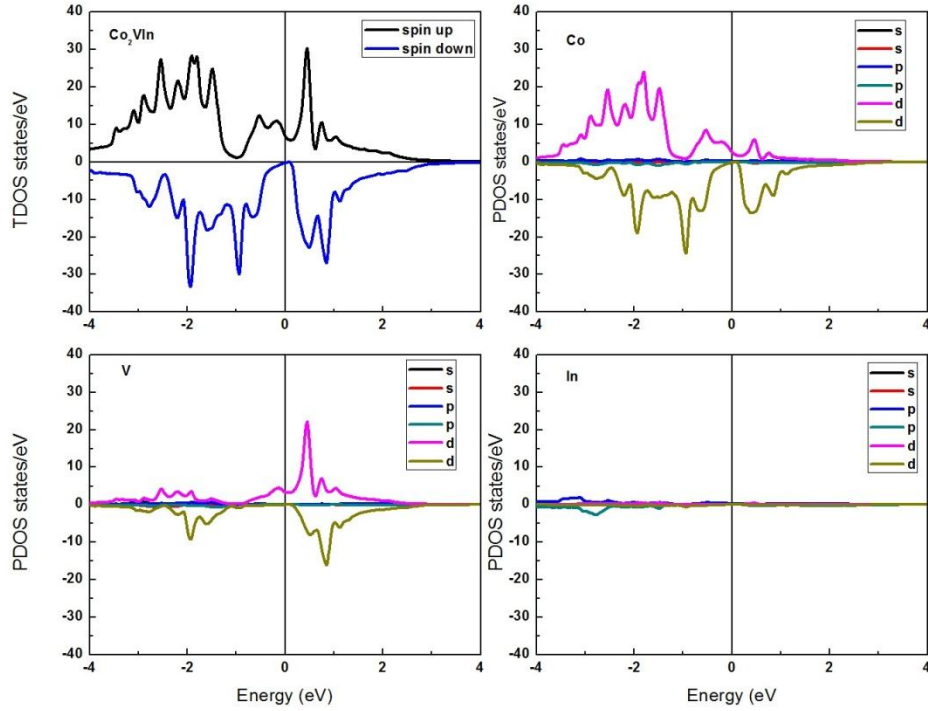


Figure 5.21: TDOS and Partial DOS for Co_2VIn for Co, V and In using PBE-GGA approximation

Table 5.2: The calculated results for spin Polarization and Band Gaps for Co_2VIn and CoVIn obtained using L(S)DA, L(S)DA+U, GGA, GGA+U, PBE-GGA and PBE-GGA+U approximations.

	Co_2VIn		CoVIn	
	Spin Polarization	Minority states Band Gap (eV)	Spin Polarization	Majority states Band Gap (eV)
L(S)DA	86.28%	0.00	87.32%	0.20
GGA	98.38%	0.07	88.65%	0.20
PBE-GGA	99.40%	0.09	94.07%	0.27
PBE-GGA+U	100.00%	0.19	100.00%	0.08
L(S)DA+U	100.00%	0.21	100.00 %	0.18
GGA+U	100.00%	0.20	100.00%	0.18

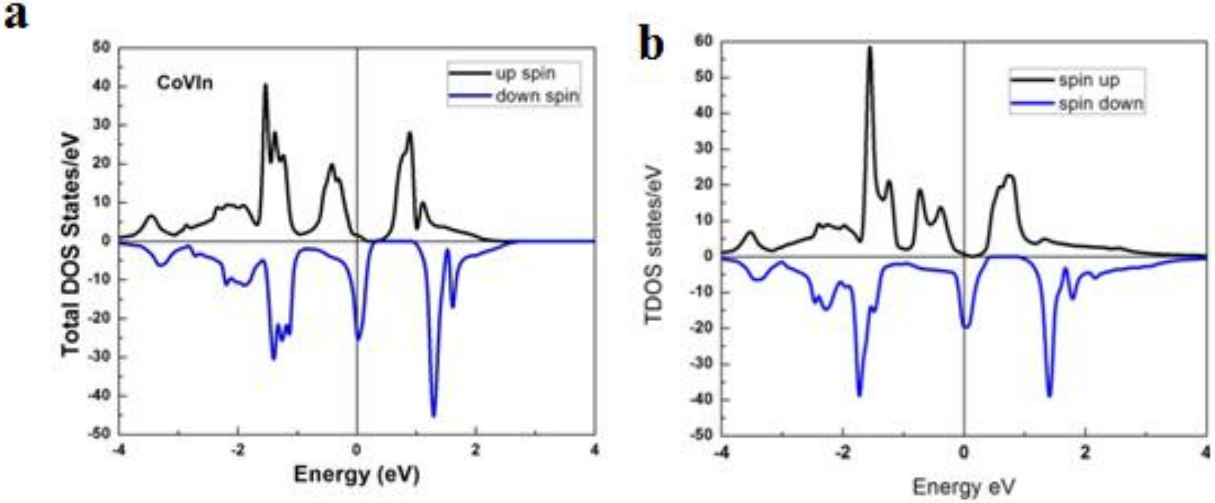


Figure 5.22 (a): Total density of states (TDOS) for CoVIn using PBE-GGA approximation and (b) Total density of states (TDOS) for CoVIn using GGA +U approximation

The spin resolved band structures obtained using GGA+U for CoVIn are illustrated in Figures 5.23 (a) and (b). It is clearly seen that the minority states are conducting while a band gap exists at the Fermi level of the majority states. As is evident from the partial density of states in Figure 5.24, the domination of the $3d$ V electrons around the Fermi level in the case of the minority spin channel explains the presence of states at the Fermi level in CoVIn.

For both Heusler compounds Co_2VIn and CoVIn , the majority and the minority spin channels of both Heusler alloys do not display similar distribution, implying spin polarisation. Both compounds should be magnetic as the spin down channel is located at higher energies relative to the spin up channel at the Fermi level.

5.3.3: Magnetic Properties

The Slater-Pauling rule predicts the total magnetic moment in Heusler alloys. For the full Heusler alloy it is $M_T = Z_T - 24$ and for the half-Heusler alloys it is $M_T = Z_T - 18$, where M_T is the total magnetic moment per unit cell and Z_T is the total number of valence electrons (Krishnaveni *et al.*, 2015). For Co_2VIn and CoVIn , the magnetic moments predicted by the Slater-Pauling rule are $2 \mu_B$ and $1 \mu_B$, respectively.

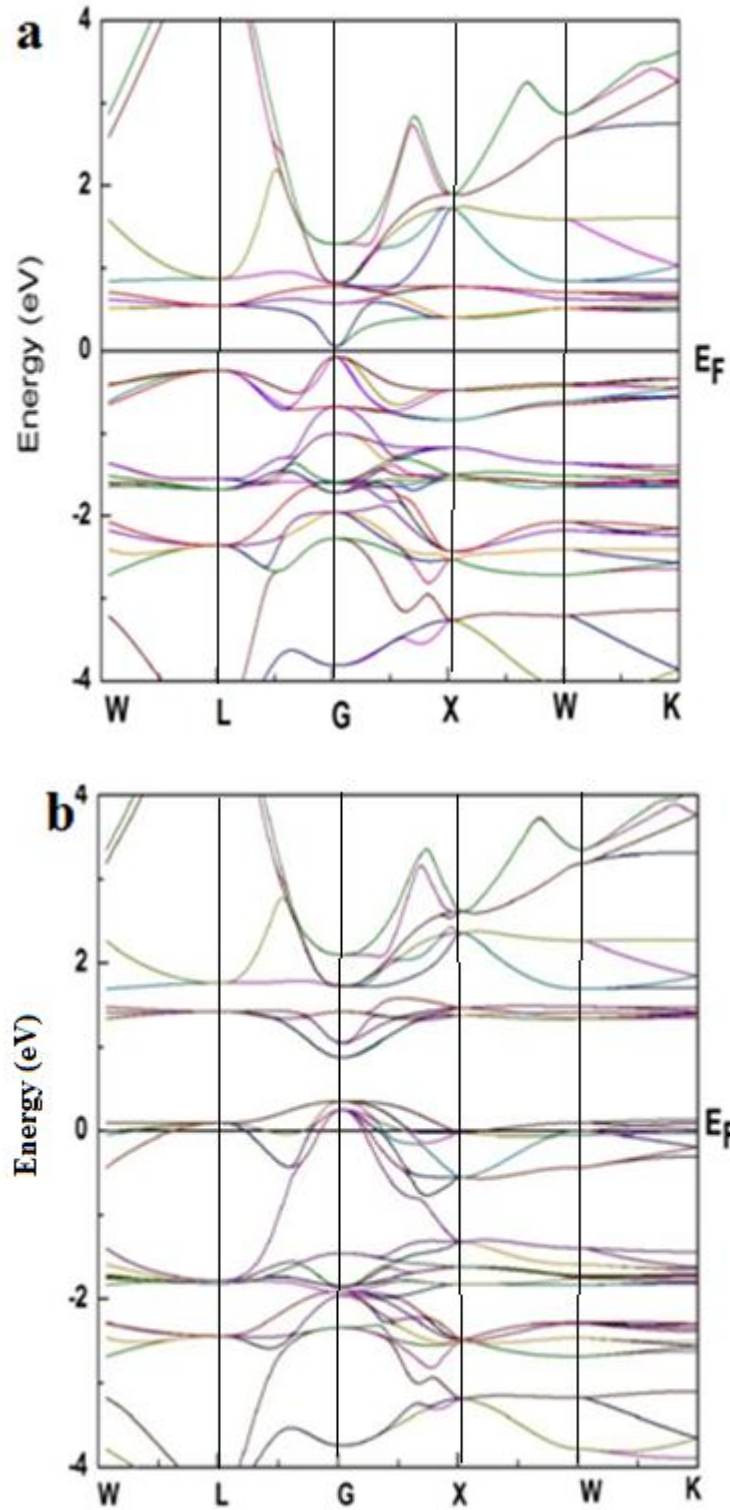


Figure 5.23 (a): Spin up electronic band structure of CoVIn at the equilibrium lattice parameter using GGA+U and (b) Spin down electronic band structure of CoVIn at the equilibrium lattice parameter using GGA+U approximation

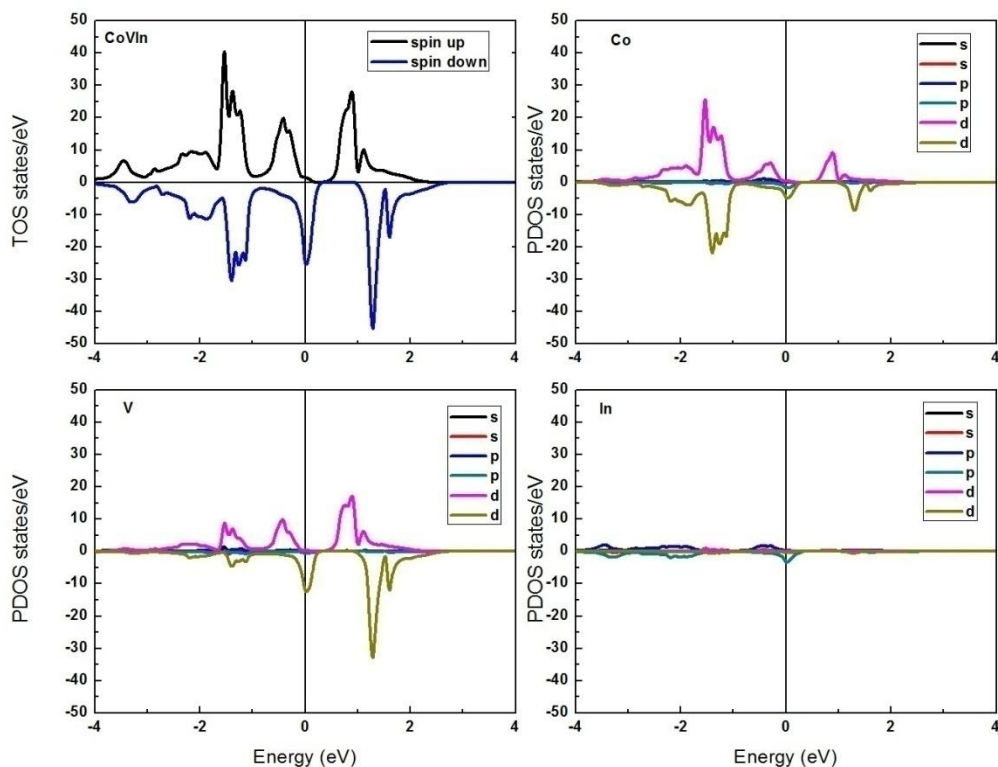


Figure 5.24: TDOS and Partial DOS for CoVIn for Co, V and In using PBE-GGA approximation

In this case, the calculated values are very close to these predicted integer values and are summarised in Table 5.3 (a) and (b) together with the moments for each site.

As is evident from Tables 5.3 (a) and (b) the more electron correlation is put into consideration, the higher the magnetic moments. The magnetic order, however, changes with different schemes. In the case of Co_2VIn , ferromagnetic coupling is predicted between Co and V except by the GGA+U and PBE-GGA+U schemes. In a study of magnetic properties of Co_2FeSi , L(S)DA+U was found to yield magnetic moment values in agreement with experiment but not GGA or LDA (Kandpal *et al.*, 2006). Ferromagnetic coupling was exhibited between Co and V, in Co_2VAl and Co_2VGa which are isoelectronic and isostructural to Co_2VIn , with magnetic moment values of 0.94 and 0.22 μ_B for Co and V respectively in Co_2VAl and 0.98 and 0.15 μ_B for Co and V respectively in Co_2VGa (Kulkova *et al.*, 2006). This trend is well replicated in the present results where a reduction in the V moment is resulting in an increase in the Co moment, with the total moment varying not by more than 1.5%, excluding L(S)DA results, leading to a change of order

in the case of GGA+U and PBE-GGA+U. The total magnetic moment is also slightly higher for the In containing compound as compared to the corresponding Heusler compounds containing Al and Ga.

Table 5.3 (a): The calculated results for magnetic moments for Co₂VIn and CoVIn obtained using L(S)DA, L(S)DA+U, GGA, GGA+U, PBE-GGA and PBE-GGA+U approximations.

Co ₂ VIn	Total Magnetic Moment	Co	V	In
L(S)DA	1.985	0.892	0.235	-0.034
L(S)DA+U	2.016	1.037	0.005	-0.063
GGA	2.001	0.928	0.192	-0.047
GGA+U	2.030	1.091	-0.074	-0.078
PBE-GGA	2.011	0.968	0.131	-0.056
PBE-GGA+U	2.031	1.069	-0.029	-0.078

The total magnetic moments and site magnetic moments for CoVIn are summarised in Table 5.3(b). All except GGA and L(S)DA schemes predict a ferrimagnetic coupling between Co and V in CoVIn .

Table 5.3(b): The calculated results for magnetic moments for Co₂VIn and CoVIn obtained using L(S)DA, L(S)DA+U, GGA, GGA+U, PBE-GGA and PBE-GGA+U approximations.

CoVIn	Total Magnetic Moment	Co	V	In
L(S)DA	0.828	0.159	0.596	0.073
L(S)DA+U	0.899	-0.240	1.065	0.074
GGA	0.853	0.095	0.684	0.074
GGA+U	0.905	-0.532	1.370	0.067
PBE-GGA	0.879	-0.020	0.829	0.070
PBE-GGA+U	0.919	-0.780	1.658	0.041

The ferrimagnetic order predicted for CoVIn by GGA+U is the most likely and additionally 100% spin polarisation is realised with this approximation as indicated in Table 5.2. Similarly, a

study of the electronic properties of closely related CoVSb, revealed an antiparallel coupling of the moments on Co and V atoms, which were found to be -0.20 and $1.12 \mu_B$ respectively, when calculated using the full potential linearized augmented plane wave method (FLAPW) employing the PBE-GGA exchange correlation functional (Kulkova *et al.*, 2006).

The total magnetic moment of Co_2VIn is mainly contributed by the Co and V sites. The In atoms have a negligible local moment with opposite sign in comparison with the Co and V elements. Its $5p$ -states have an antiparallel interaction with the $3d$ Co and V orbitals of the transition elements and p - d hybridisation occurs. In the case of CoVIn , $3d$ V states contribute most of the moment which is coupled ferrimagnetically to the Co moment.

Both Co_2VIn and CoVIn are predicted to possess similar properties with their isoelectronic and isostructural counterparts, with a slight increase in magnetic moments as sp element size increases. The ability of the DFT+U method to correctly treat the partial localisation of the d -states is demonstrated by the results in this section. Apart from increasing the lattice constant and affecting the electronic structure, the sp element has also been shown to cause the magnitude of the magnetic moment to increase which is a direct consequence of increase in lattice parameter within a range where hybridisation still occurs, but to a slightly reduced extent.

Experimental work was done for Co_2VIn and Mn_2VIn compounds to investigate if there exists any discrepancy between electronic properties predicted from first principles method and empirical results. In the subsequent section 5.4, structural experimental results of Co_2VIn whose properties have been predicted in this section as well as Mn_2VIn discussed in section 5.1 are discussed with a view of reconciling theory and experiment.

5.4 Structural Characterisation of Mn-V-Al and X-V-In (X= Co, Mn)

Experimental powder X-ray diffraction profiles and difference plots of Rietveld refinement of Mn-V-Al ingot synthesised by arc melting in Figure 5.25 shows the presence of a single phase compound Mn_2VAl of $L2_1$ structure, space group number 225. The characteristic 111, 200, 220 and 311 peaks are clearly identified at 26, 30, 43 and 51 degrees, respectively. The atomic parameters for the $L2_1$ phase are 0.25, 0.5 and 0.0 for Mn, V and Al, respectively. The lattice parameter is $a = 5.90 \text{ \AA}$. The vertical bars indicate the Bragg's positions of the diffraction peaks expected.

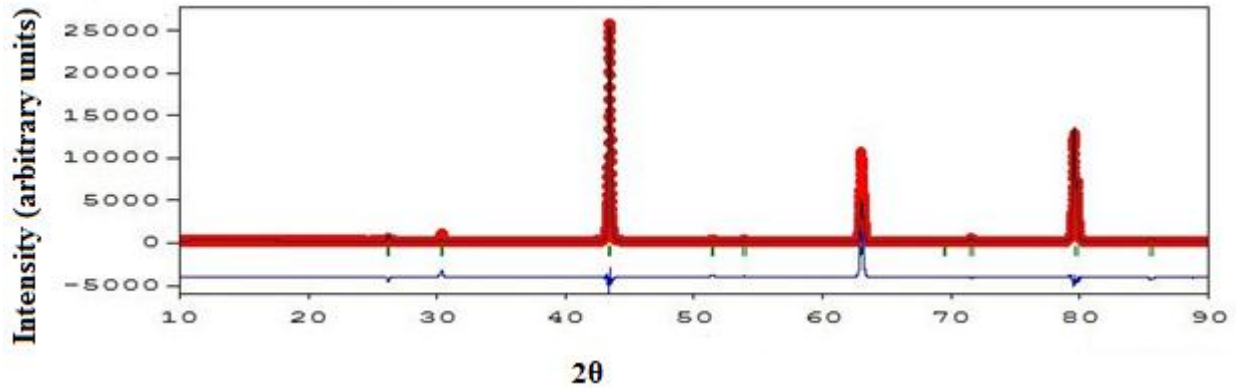


Figure 5.25: XRD pattern and difference plot for Mn-V-Al obtained after Rietveld refinement. The black line is the calculated pattern, the red line is the experimental data and the blue line is the difference between the two

The powder X-ray diffraction profiles and difference plots of Rietveld refinement of Co-V-In ingots in Figure 5.26 show the presence of two major phases in the sample.

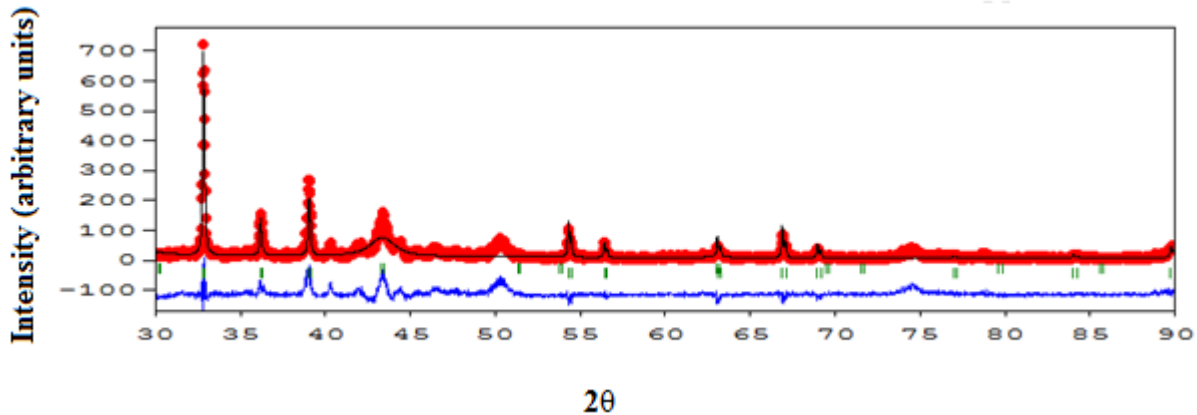


Figure 5.26: XRD pattern and difference plot for Co-V-In obtained after Rietveld refinement. The black line is the calculated pattern, the red line is the experimental data and the blue line is the difference between the two

These include 61.38% Co_2VIn of $L2_1$ structure, space group number 225, together with 38.62% tetragonal In, space group number 139 in the Co-V-In ingots prepared. The atomic parameters for the $L2_1$ phase are 0.25, 0.50 and 0.00 for Co, V and In, respectively. The lattice parameter is $a = 5.89 \text{ \AA}$. The atomic parameter for the tetragonal phase is 0.00, while the lattice parameters are $a = b = 3.25 \text{ \AA}$, $c = 4.94 \text{ \AA}$.

Figure 5.27 shows the presence of 56.88% of Mn_2V , space group number 227, 8.00 % Mn_2VIn of $L2_1$ structure, space group number 225, together with 35.12% In, tetragonal phase, space group number 139 present in the Mn_2VIn ingot prepared by arc melting.

The atomic parameters for the Cubic phase space group number 227 are 0.00 and 0.63 for V and Mn respectively. The lattice parameter is 7.94 \AA . The atomic parameter for the tetragonal phase is 0.00, with lattice parameters $a = b = 3.25 \text{ \AA}$, $c = 4.94 \text{ \AA}$. The atomic parameters for the $L2_1$ phase, space group number 225 are 0.25, 0.50 and 0.00 for Mn, V and In, respectively with a lattice parameter of $a = 5.83 \text{ \AA}$. Interestingly, at this lattice parameter, Mn_2VIn was predicted by DFT to undergo a tetragonal distortion in section 5.1.

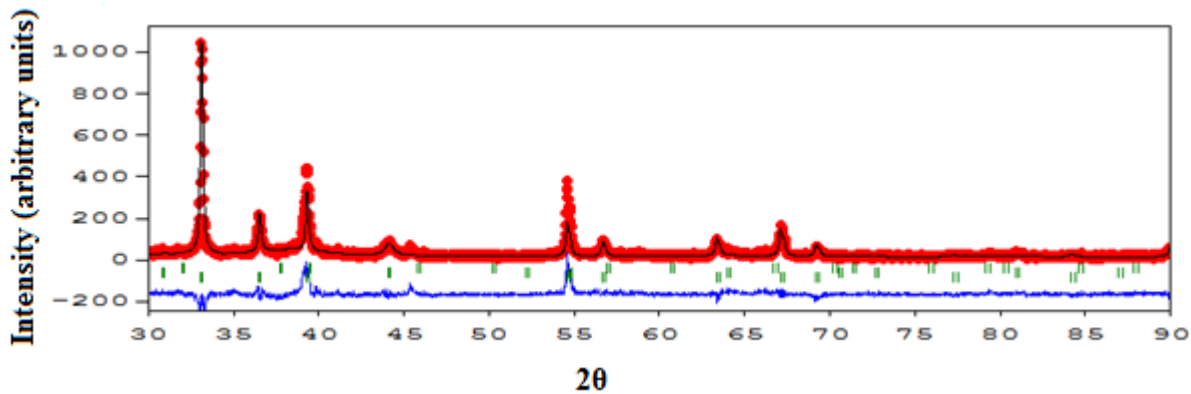


Figure 5.27: XRD pattern and difference plot for Mn-V-In obtained after Rietveld refinement. The black line is the calculated pattern, the red line is the experimental data and the blue line is the difference between the two

The observed phase with space group 227 is one of the ordering variants of Heusler compounds and falls under the class of known but rare disordered Heusler structures in which the X atoms of one sub-lattice intermix with the Y sites, while the other X atoms mix with the Z sites resulting

in the B32a structure whose prototype is NaTl. This phase was observed after annealing the Mn-V-In sample, in which space group 229 had been observed for the as cast sample. This space group corresponds to the W type crystal structure resulting from A2 type of disorder, in which all the positions are equivalent. This observation points to the possibility of the presence of a disordered Heusler structure.

The L2₁ phase consists of two formula units of the X₂YZ compound. In the case of Mn₂VAl, the characteristic peaks for the L2₁ phase which are the 111, 200, 220, 311, 400, 331, 420, 422, 511, 333 reflections were observed. For both Co₂VIn and Mn₂VIn, with two formula units X₈V₄In₄ (X = Co, Mn), the peaks indexed to the cubic phase include 220, 311, 400, 422, and 440 reflections. The absence of some reflections can be attributed to the fact that the samples are disordered, resulting in a diffraction pattern, where no superstructure reflections appear. Also, the constituent elements Mn and V are from the 4th row of the periodic table, which have similar scattering factors, a factor that leads to the absence of the (111) and (200) reflections, or to very low intensities of the same, if the standard laboratory sources with Cu-K α radiation are used.

The Mn-V-Al samples were homogeneous as shown in the SEM image in Figure 5.28, alongside which, the composition of the ingots as determined by EDX spectroscopy is shown.

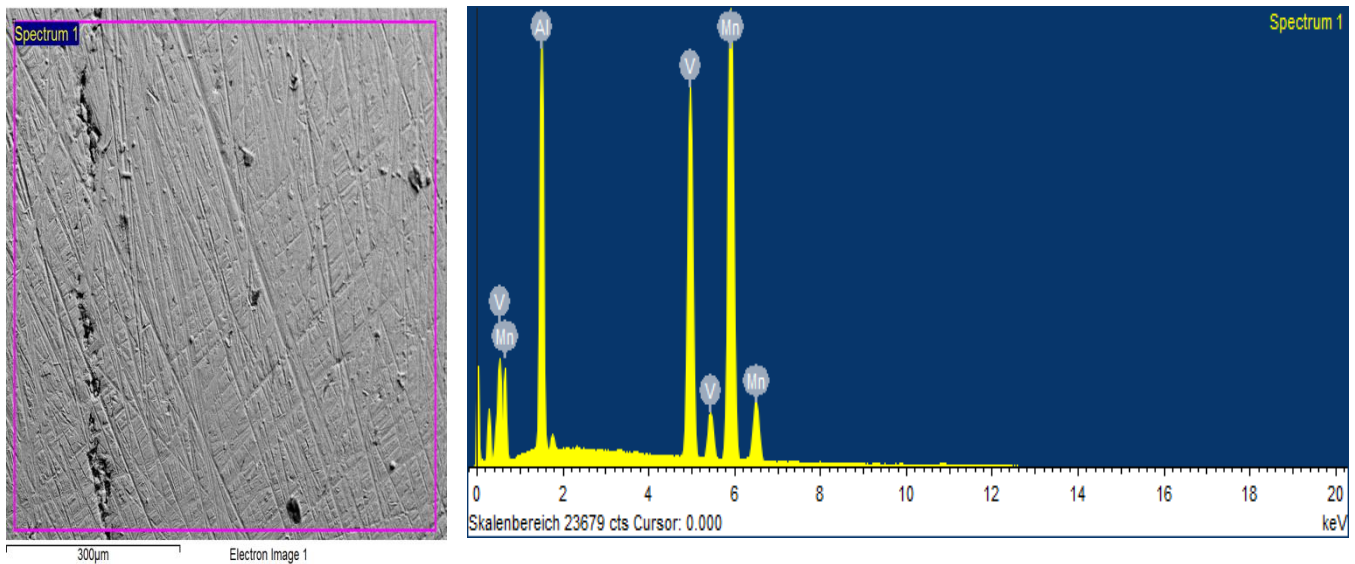


Figure 5.28: SEM and EDX results for Mn-V-Al

The composition is given in Table 5.4, the resulting composition being $Mn_{1.79}VAI_{1.14}$, very close to the expected Mn_2VAI composition, whose magnetic properties are discussed in section 5.5.

Table 5.4: Composition of Mn-V-Al sample

Element	Weight%	Atomic%
V K	28.31	25.45
Mn K	54.61	45.55
Al L	17.09	29.00
Totals	100.00	100.00

The different phases in Co-V-In and Mn-V-In were observed clearly in SEM images and their corresponding compositions were obtained from EDX spectroscopy measurements. For Mn-V-In, three phases were visible. The first was shiny, in which there was almost no V in the samples as shown in Figure 5.29. The composition is given in Table 5.5.

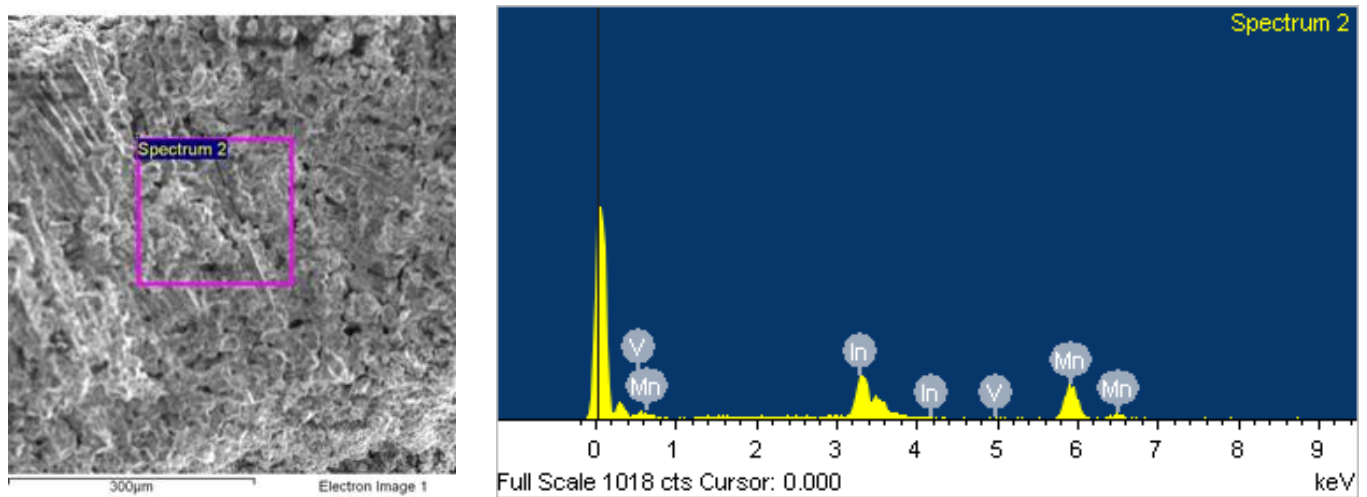


Figure 5.29: SEM and EDX results for the first phase in Mn-V-In ingot.

Table 5.5: Composition of first phase in Mn-V-In

Element	Weight%	Atomic%
V K	0.23	0.35
Mn K	41.79	59.89
In L	57.98	39.76
Totals	100.00	

The second phase contained more Vanadium, shown in Figure 5.30 and its composition is as given in Table 5.6

Table 5.6: Composition of the second phase in Mn-V-In

Element	Weight%	Atomic%
V K	6.42	9.86
Mn K	35.49	50.55
In L	58.10	39.60
Totals	100.00	100.00

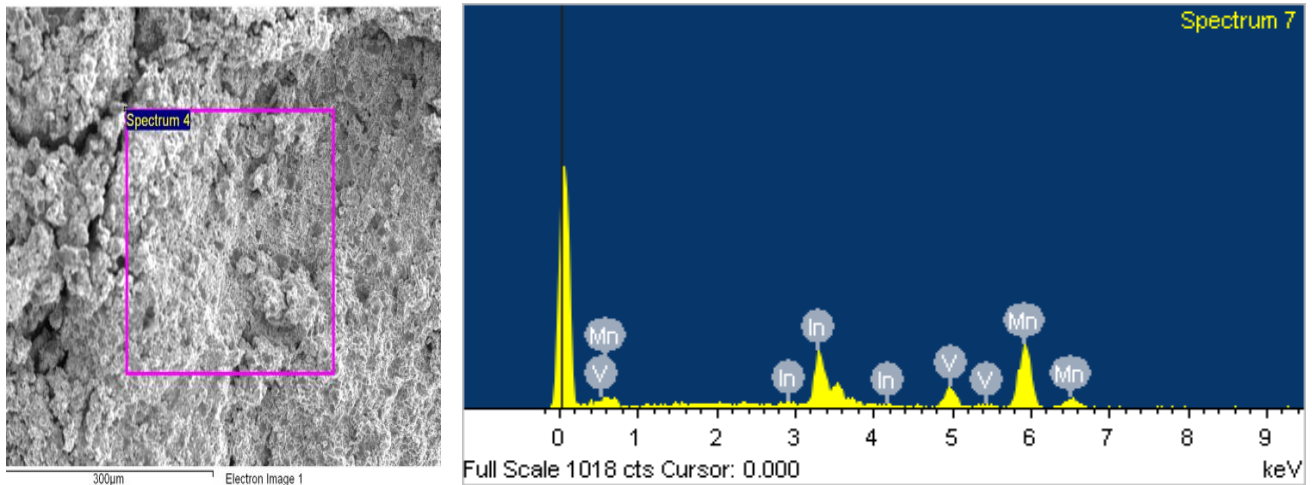


Figure 5.30: SEM and EDX results for the second phase in Mn-V-In ingot.

More Vanadium was in the last phase having a composition of $Mn_{2.29}V_{0.6}In$ as displayed in Table 5.7 and was dark gray as in the corresponding EDX Figure 5.31.

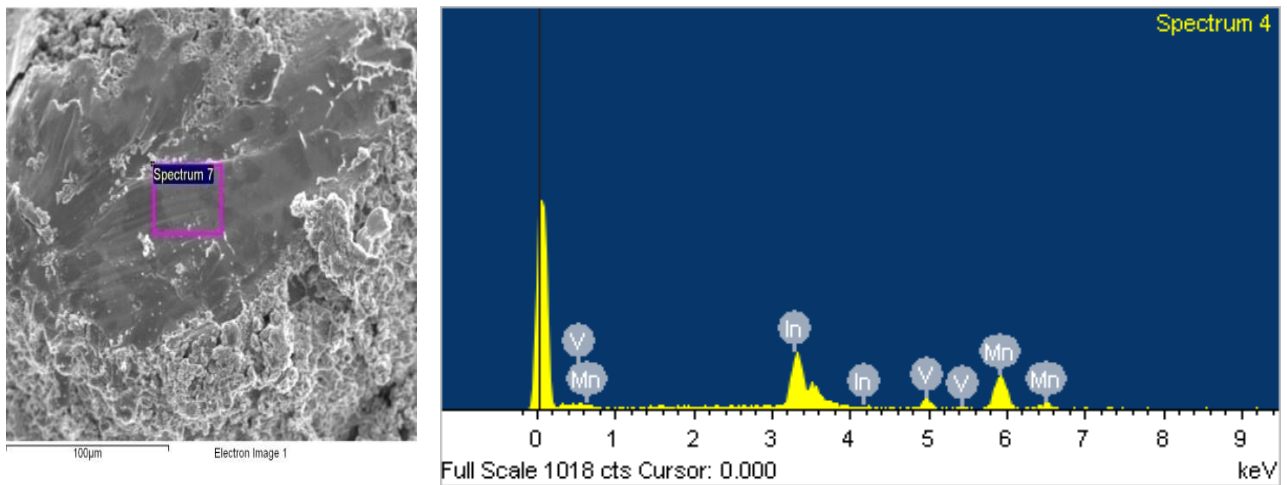


Figure 5.31: SEM and EDX results for the third phase in Mn-V-In ingot.

Table 5.7: Composition of the third phase in Mn-V-In

Element	Weight%	Atomic%
V K	11.40	15.59
Mn K	46.36	58.78
In L	42.24	25.63
Totals	100.00	100.00

There were also dark regions composed of Vanadium only, pointing to Vanadium segregation. The magnetic properties of the Mn-V-In ingot containing the $Mn_{2.29}V_{0.6}In$ phase are discussed in section 5.5.

Co-V-In was more uniform with a resulting composition of $Co_{1.8}VIn_{0.1}$ as shown in Table 5.8.

Table 5.8: Composition of Co-V-In sample

Element	Weight%	Atomic%
V K	29.95	34.39
Co K	61.95	61.49
In L	8.10	4.13
Totals	100.00	100.00

The electron image indicating composition is shown in Fig. 5.32.

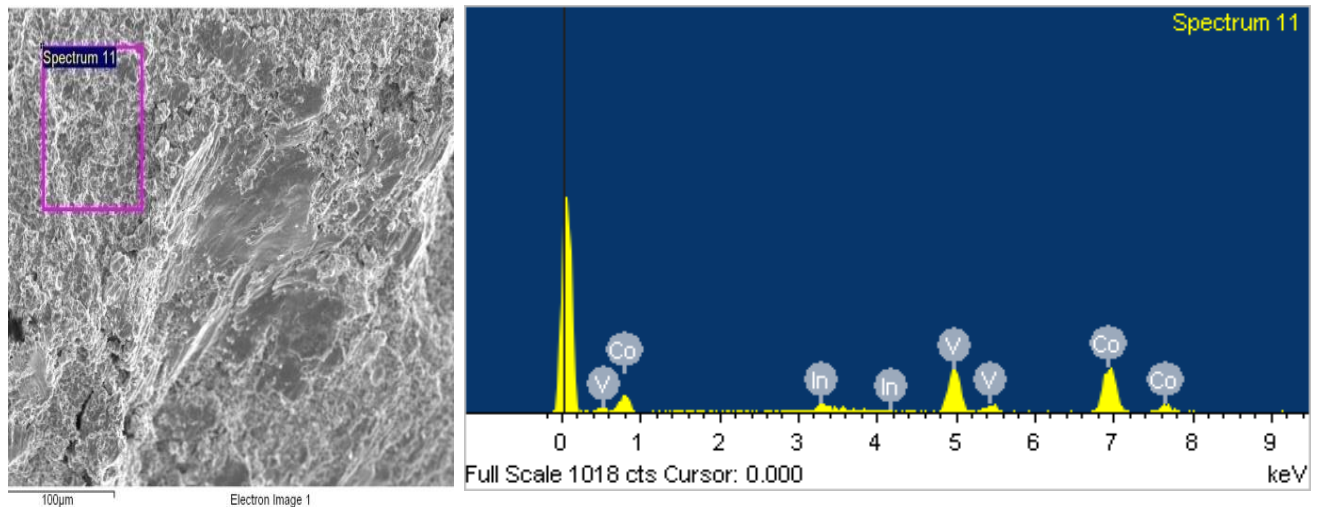


Figure 5.32: SEM and EDX results for Co-V-In ingot

The ratio of Co:V is 1.8:1, but the In is much less explaining the observed In segregation in the sample. The magnetic properties of the resulting off-stoichiometric sample of composition $\text{Co}_{1.8}\text{VIn}_{0.1}$ are discussed in section 5.5.

The samples prepared by arc melting reveal to a great extent the reason as to why the predicted electronic properties are difficult to observe in real materials. The high polarisations predicted assume an $L2_1$ crystal structure while in the real material such as the ones prepared by careful arc melting in this work, this structure co-exists with other phases and not in stoichiometric amounts as required in the $L2_1$ structure for the half-metallic property to be observed. Where the structure exists, there are also possibilities of tetragonal distortions as may be the case in Mn_2VIn whose lattice parameter for the $L2_1$ phase was found to be 5.83 Å and surprisingly at which tetragonal distortions were predicted in section 5.1.

From this section, it is clear that there is a high correlation between the DFT predictions and expected properties. Improved and more sophisticated methods of material preparation, as well as high purity grade materials prepared in clean rooms, may result in almost the predicted material structure and properties. Disorder of the type suggested for the Mn_2VIn structure in this section from the observed phases from XRD results is also expected to interfere with the hybridisation between the states of the atoms resulting in appearance of states within the half-metallic gap.

5.5 Magnetic Properties of $Mn_{1.79}VAl_{1.14}$, $Co_{1.8}VIn_{0.1}$ and Mn-V-In

The variation of the magnetic moments with magnetic field of $Mn_{1.79}VAl_{1.14}$ prepared by arc melting is displayed in Figure 5.33 at 10 K, in which the curve has a narrow hysteresis, with a shape characteristic of ferrimagnetic coupling, as clearly seen in the inset of Figure 5.33.

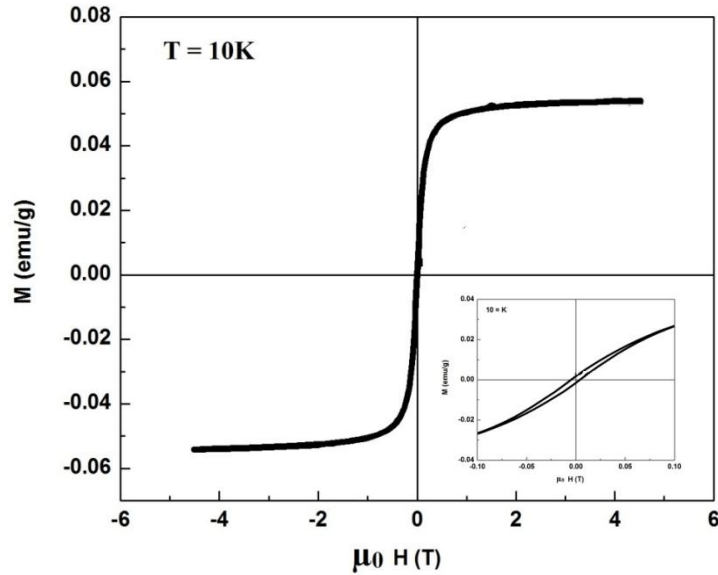


Figure 5.33: Variation of magnetic moment with applied magnetic field at 10K for $Mn_{1.79}VAl_{1.14}$

The ferrimagnetic order is exhibited even at 250K as shown in Figure 5.34. The coercivity is 5.375×10^{-3} T in each case.

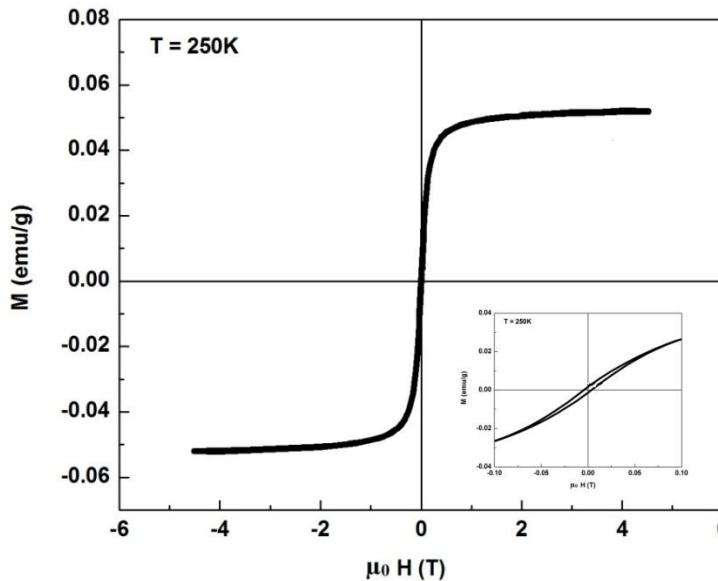


Figure 5.34: Variation of magnetic moment with applied magnetic field at 250K for $Mn_{1.79}VAl_{1.14}$

The ferrimagnetic coupling is further well displayed by the ZFC-FC curves in Figure 5.35, measured at 0.1T, where no bifurcation between the two curves takes place, but rather decrease in the same direction with increasing temperature. The $\text{Mn}_{1.79}\text{VAl}_{1.14}$ sample is found to have a saturation magnetisation of $1.74 \mu_{\text{B}}/\text{f.u}$ at 10K, in good agreement with the magnetic moment predicted by DFT of $2 \mu_{\text{B}}/\text{f.u}$ at 0K, for stoichiometric Mn_2VAl .

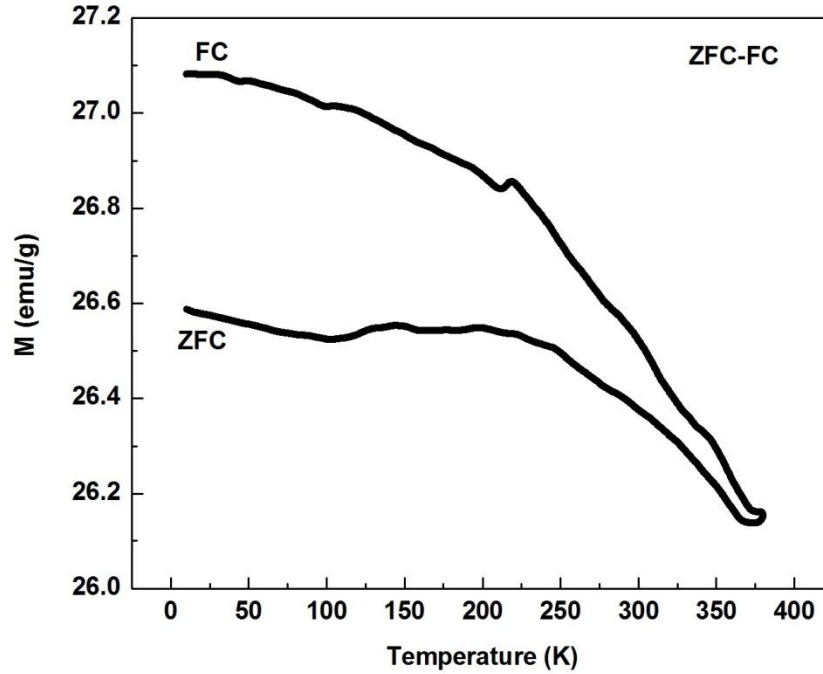


Figure 5.35: ZFC and FC curves for $\text{Mn}_{1.8}\text{VAl}_{1.14}$

The variation of the magnetic moments with magnetic field of the off-stoichiometric compositions $\text{Co}_{1.8}\text{VIn}_{0.1}$ and Mn-V-In, containing the $\text{Mn}_{2.29}\text{V}_{0.6}\text{In}$ phase, is displayed in Figures 5.36 (a) and (b) at 2K for $\text{Co}_{1.8}\text{VIn}_{0.1}$ and Mn-V-In samples, respectively. In $\text{Co}_{1.8}\text{VIn}_{0.1}$, a very slight hysteresis is displayed at 2K, in an otherwise paramagnetic curve, with a coercivity of 3.400×10^{-2} T, while Mn-V-In shows more hysteresis at 2 K with a coercive field of 4.678×10^{-1} T. Assuming that the magnetic moment is contributed only by the L_{21} phase determined by XRD in section 5.4, the remanent magnetisation is $0.500 \mu_{\text{B}}/\text{f.u}$ and $5.767 \times 10^{-4} \mu_{\text{B}}/\text{f.u}$ at 2 K for Mn-V-In and $\text{Co}_{1.8}\text{VIn}_{0.1}$, respectively, with no signs of saturation at this temperature, even at 6T. An observation similar to the Mn-V-In curve was made of CoO

particles and this behaviour was attributed to the presence of strong competing ferromagnetic and antiferromagnetic interactions in the system.

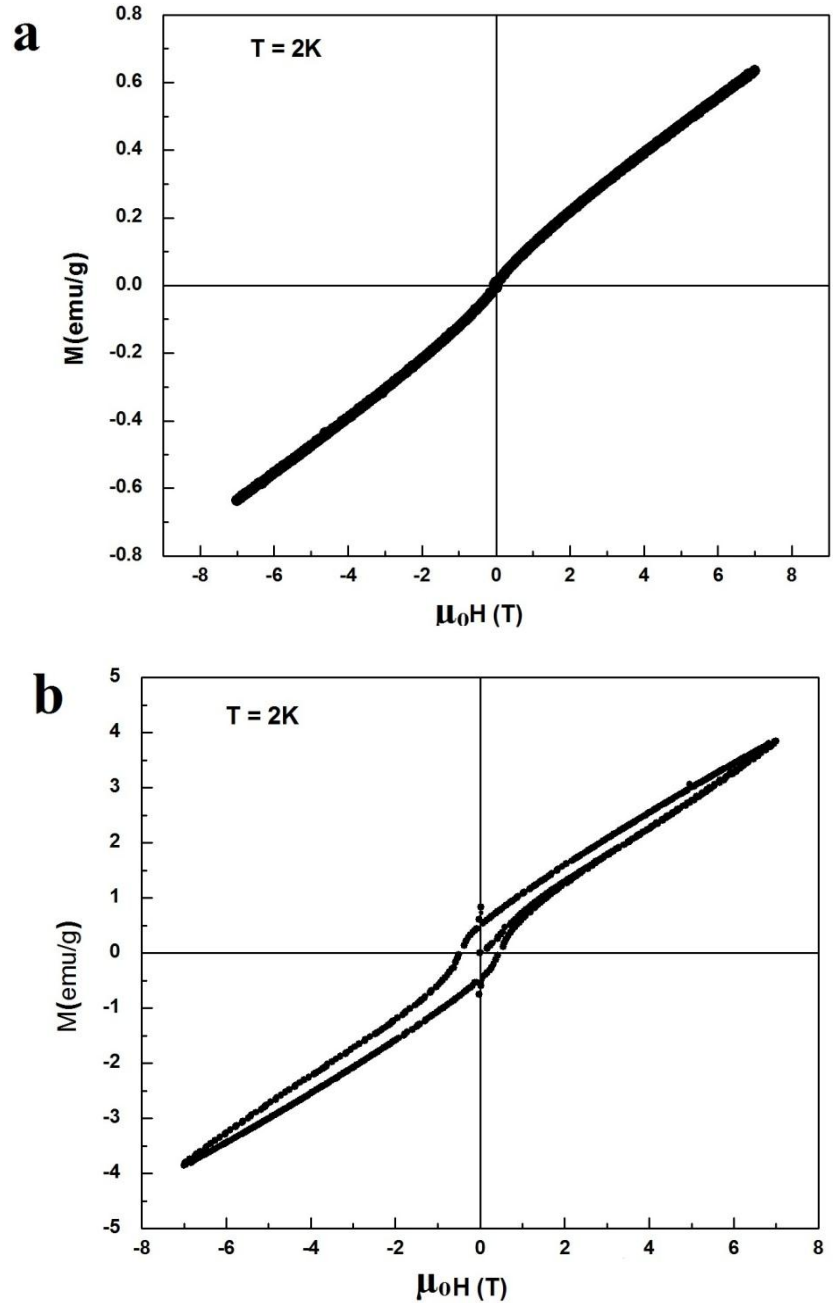


Figure 5.36: Variation of magnetic moment with applied magnetic field at 2K for (a) $\text{Co}_{1.8}\text{VIn}_{0.1}$ and (b) Mn-V-In

The linear part of the loop was mainly due to the antiferromagnetic volume phase while the curved part was attributed to the formation of the ferromagnetic phase (Shi and He, 2012). The

lack of saturation is also compatible with effects such as the presence of small superparamagnetic particles that are still fast relaxing at 2K (Peddis *et al.*, 2008). Additionally, the presence of a non-collinear spin structure as well as weak antiferromagnetic components can give a contribution to the observed lack of saturation, as reported in previous studies on nanoparticles (Sarkarainadar, 2011).

At 400K, a paramagnetic behaviour is displayed in Mn-V-In and $\text{Co}_{1.8}\text{VIn}_{0.1}$, although the latter still displays the slight hysteresis as shown in Fig. 5.37 (a) and (b). The behaviour of Mn-V-In reveals a transition from paramagnetism at high temperatures to ferromagnetism at low temperatures. This is indicative of superparamagnetism which is displayed by the bifurcation of the ZFC and FC curves shown in Figure 5.38 (b). Superparamagnets are characterised by a blocking temperature T_B which corresponds to the maximum moment of the ZFC curve above which the system is paramagnetic and below which its magnetisation curve has hysteresis and is similar to a magnetisation curve for a ferromagnet or a ferrimagnet. $\text{Co}_{1.8}\text{VIn}_{0.1}$ contains a ferromagnetic component with a Curie temperature higher than 400 K, hence the slight hysteresis observed in Figure 5.37 (a).

The ZFC and FC measurements were carried out during heating of the sample in an external magnetic field of 0.1T, resulting in curves which are different because of the different initial states of the samples and they give the net magnetisation value corresponding to the ferromagnetic contribution in the sample as shown in Figure 5.38 (a) and (b). In the ZFC case, the sample was prepared for measurement by being cooled from 400K in the absence of an external field. The FC sample was cooled in a 0.1T magnetic field.

The curves measured in ZFC and FC modes in the presence of an applied magnetic field of 0.1T for $\text{Co}_{1.8}\text{VIn}_{0.1}$ demonstrate that both the ZFC and FC curves coincide with each other without showing any bifurcation, typical of paramagnetic behaviour as shown in Figure 5.38 (a). This observation indicates the absence of any spin-flipping effect unlike what is displayed for Mn-V-In (Ahmmad *et al.*, 2016). There is however, a difference in the ZFC and FC curves which persists above room temperature which is supported by the very slight ferromagnetic curve recorded at 400 K. There are two maxima in the ZFC curve of Mn-V-In as shown in Figure 5.38

(b), a behaviour which shows the existence of two magnetic phases in the ground state, pointing to a transition from paramagnetism to ferromagnetism at low temperatures below 200 K (Svedberg *et al.*, 2011).

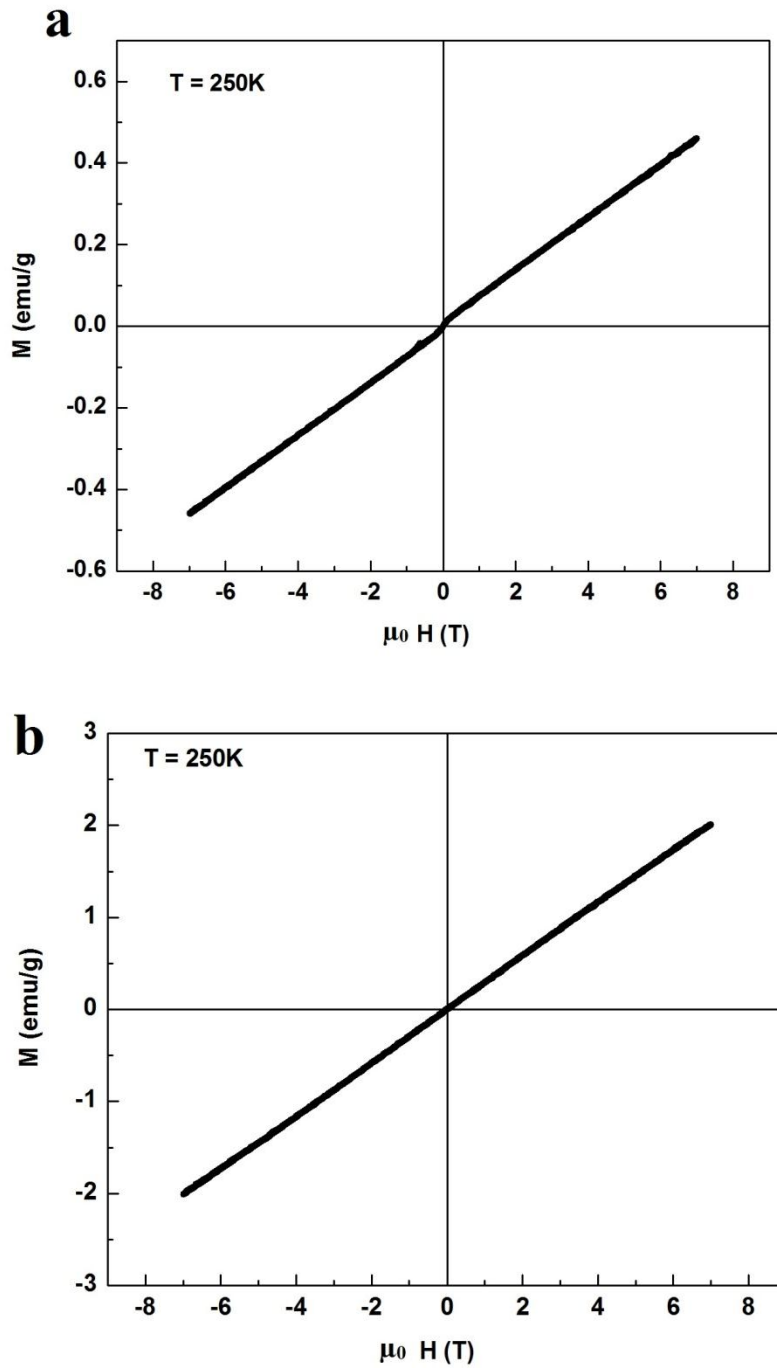


Figure 5.37: Variation of magnetic moment with applied magnetic field at 400K for (a) $\text{Co}_{1.8}\text{VIn}_{0.1}$ and (b) Mn-V-In

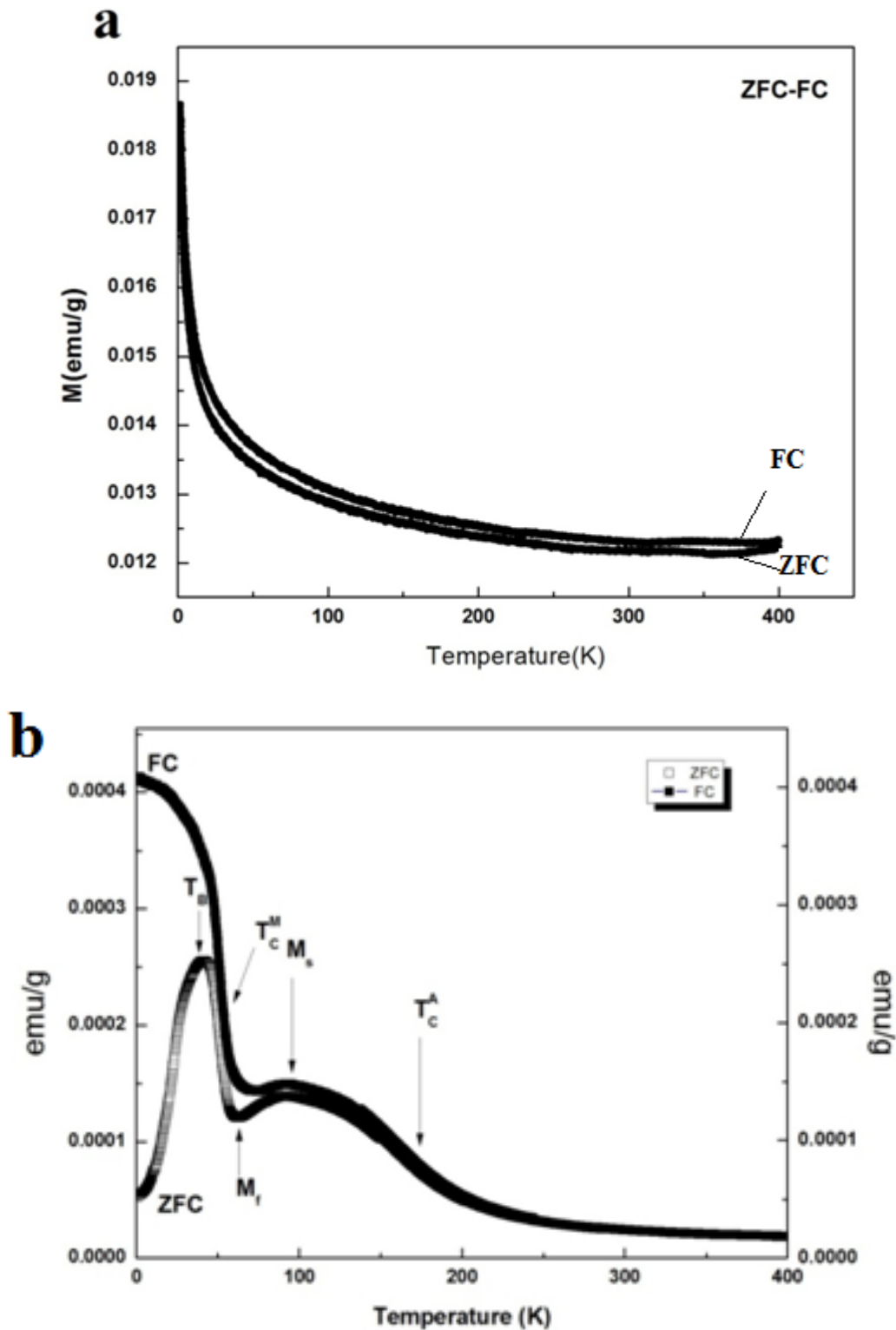


Figure 5.38: ZFC and FC curves for (a) $\text{Co}_{1.8}\text{VIn}_{0.1}$ and (b) Mn-V-In.

The graph displays the typical behaviour of alloys which undergo a martensitic transformation below the Curie temperature of the austenite.

The Curie temperature of the austenite phase was observed at $T_c^A = 174\text{K}$. Additionally, a martensitic transformation is observed at $M_s=102\text{ K}$. Upon further cooling, an up-turn is observed at $M_f = 63\text{ K}$, the temperature at which the martensitic transformation ends. The Curie temperature of the martensite phase occurs at $T_c^m = 55\text{ K}$. It is possible that the transition observed in Figure 5.38 (b) at 174 K could in fact be a ferrimagnetic transition as this is the coupling predicted for the Mn and V moments in Mn_2VIn by DFT results discussed earlier in section 5.1 at the lattice parameter obtained from XRD measurements in Section 5.4 at which a tetragonal distortion is also predicted. The samples show a bifurcation between the ZFC and FC curves below 50K and a ZFC magnetisation maximum at 40 K which is the blocking temperature, T_B . Such an irreversibility has been reported previously in samples which exhibited spontaneous magnetisation at low temperature (Zhang *et al.*, 2016). The observed maximum and irreversibility could be caused by the presence of an antiferromagnetic component trapped in a ferromagnetic matrix arising from disorder, as evidenced by the presence of the disordered phase detected by XRD reported in section 5.5. The antiferromagnetic component cannot align with the magnetic field direction at low fields, resulting in effects of frustration, leading to the non-saturation observed in Figure 5.34(b) (Nayak *et al.*, 2010). The ZFC maximum at high temperature is due to ordering phenomena as previously stated (Chen *et al.*, 2011).

The FC magnetisation continues to increase below T_B . This observation has been explained in other studies of magnetic systems to indicate that the antiferromagnetic moments can no longer pin the ferromagnetic domain and negligible interactions are implied (Wang and Liu, 2013). If the FC curve saturates below T_B and further cooling results in little change in magnetisation after the onset of irreversibility, strong interactions are implied and the system is classified as a spin glass. For semi-Heusler arc melted $\text{Cu}_{1-x}\text{Ni}_x\text{MnSb}$, a bifurcation in FC and ZFC curves and a constant value of magnetisation in FC curve pointed to the presence of competing antiferromagnetic and ferromagnetic interaction (Halder *et al.*, 2011).

If a material is made of very small single domain non interacting magnetic grains dispersed in a non-magnetic medium, it is said to be superparamagnetic. Superparamagnetism occurs below the Curie temperature because it results from the spontaneous magnetic moment of magnetic grains in the material. Their applications include ferrofluid used for liquid seals and hard disk drive

technology, to solve the problem of the ever decreasing size of magnetic grains (Peddis *et al.*, 2008).

While $\text{Mn}_{1.79}\text{VAl}_{1.14}$ displays the expected magnetic properties, some interesting and rare magnetic properties are observed in the Indium-based samples, in particular in Mn-V-In having the $\text{Mn}_{2.29}\text{V}_{0.6}\text{In}$ phase. The relationship between the magnetisation as a function of temperature for Mn-V-In, reveals some of the main features of a martensitic alloy as well as superparamagnetism, which is commonly exhibited by nanoparticles. T_B is an important parameter when characterising the magnetic behaviour of a magnetic nanoparticles system above which thermal fluctuations can flip the direction of the magnetic moment and no hysteresis is observed in the magnetisation measurement. Above T_B , superparamagnets can be described in the same way as ordinary paramagnets the only difference being that the magnetic moments of individual particles in superparamagnets are much higher (Coey, 2010).

The magnetic moments measured for our off-stoichiometric Mn-V-In sample containing the $\text{Mn}_{2.29}\text{V}_{0.6}\text{In}$ phase and $\text{Co}_{1.8}\text{VIn}_{0.1}$ sample are much less than the expected $2 \mu_B/\text{f.u.}$ for the fully stoichiometric Heusler compounds at $0.500 \mu_B/\text{f.u.}$ and $5.767 \times 10^{-4} \mu_B/\text{f.u.}$ and instead of half-metallicity, Mn-V-In displays martensitic and superparamagnetic properties. On the other hand, the magnetic moment for $\text{Mn}_{1.79}\text{VAl}_{1.14}$ is $1.74 \mu_B/\text{f.u.}$, very close to the expected $2 \mu_B/\text{f.u.}$ for the stoichiometric compound.

From section 5.4 and the present one, the structure property dependence is clearly brought out in which case factors such as disorder, non stoichiometry and structural distortions result in different magnetic properties, which can be explained using DFT calculations as discussed for the latter effect in the case of Mn_2VIn in section 5.1.2. While $\text{Co}_{1.8}\text{VIn}_{0.1}$ is largely paramagnetic with a weak ferromagnetic component, the observed magnetic behaviour of Mn-V-In containing $\text{Mn}_{2.29}\text{V}_{0.6}\text{In}$ is attributed to the structural transformations revealed by the DFT calculations, and exhibited in our XRD pattern in which the tetragonal and cubic phases which are very close in energy are observed. The components having different magnetic phases cause the frustration effects exhibited by the ZFC-FC curves.

5.6 Electronic and Magnetic Properties of Co_2YIn (Y=Nb, Ti) and CoYIn (Y = Nb, Ti)

The effect of lattice constant and number of valence electrons on spin polarisation achieved by replacing V in Co_2VIn , whose properties were discussed in section 5.3, with Ti and Nb, which belong to the same period and group respectively, is reported. The effect of Ti would be to decrease the number of valence electrons by one, while that of Nb would be to increase the lattice constant without an effect on the number of valence electrons. The properties of the corresponding half-Heuslers CoTiIn and CoNbIn are also reported.

5.6.1: *Structural properties*

Both Co_2NbIn and Co_2TiIn are more stable in the Cu_2MnAl structure, rather than the Hg_2CuTi structure. Their lattice constants are larger than for Co_2VIn at 6.2 Å and 6.05Å respectively as expected, due to the larger Nb and Ti atomic radii. CoNbIn and CoTiIn , both have an optimised lattice parameter of 6 Å, again higher than that of CoVIn studied in section 5.3 at 5.849 Å.

5.6.2: *Electronic Properties*

Full Heusler Co_2NbIn displays 100% spin polarisation, with a half-metallic gap in the minority states as shown in Figure 5.39 (b).

Its density of states has a gap of 0.1 eV at the Fermi level for the minority states as shown in Figure 5.39 (a) with the Fermi level closer to the conduction band.

The partial density of states plot in Figure 5.40 indicates the dominance of the Co states around the Fermi level, suggesting a gap in the crystal field split bands of Co, resulting in a $d - d$ band gap. As is the case with V in Co_2VIn , the Ti minority states in Co_2TiIn are far below the Fermi level, resulting in a gap with a Co like character while the In states are even less prominent at the Fermi level.

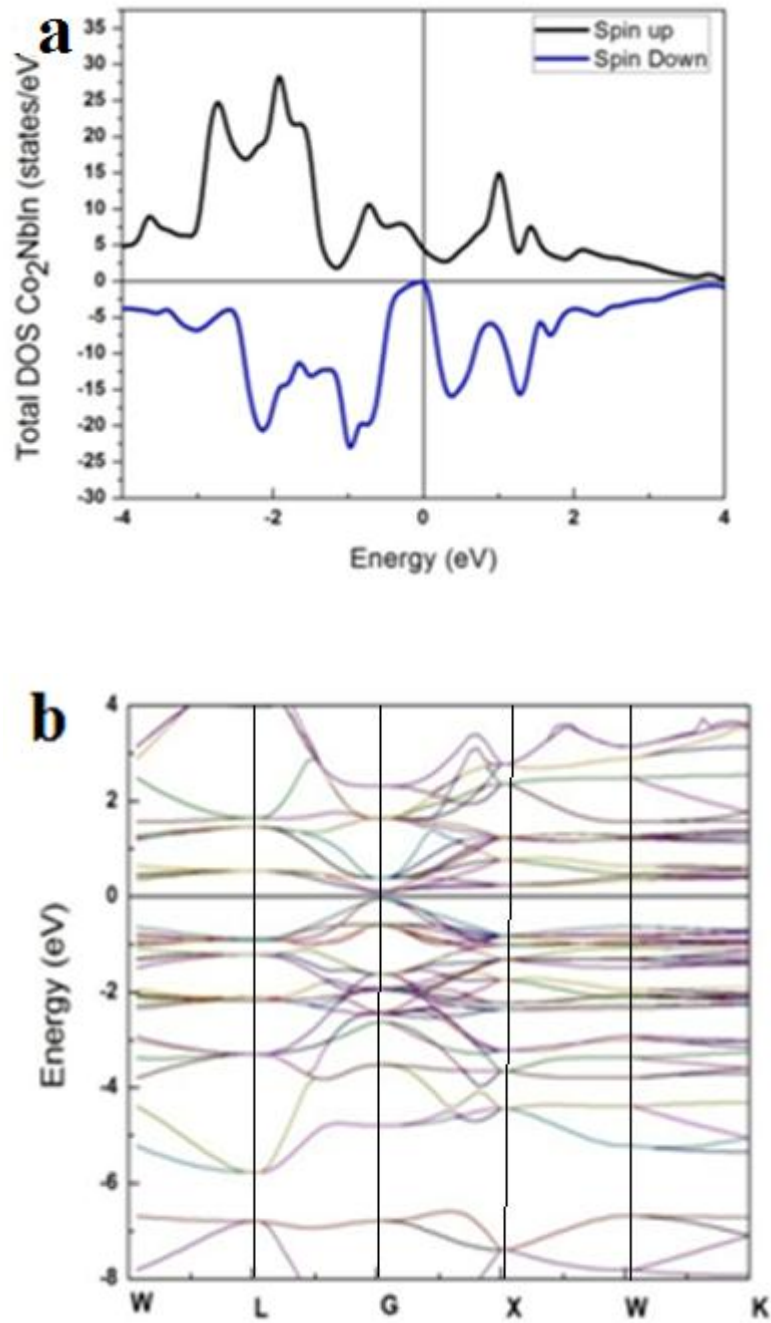


Figure 5.39 (a): Total density of states (TDOS) for Co_2NbIn using PBE-GGA approximation and (b) band structure of minority states of Co_2NbIn

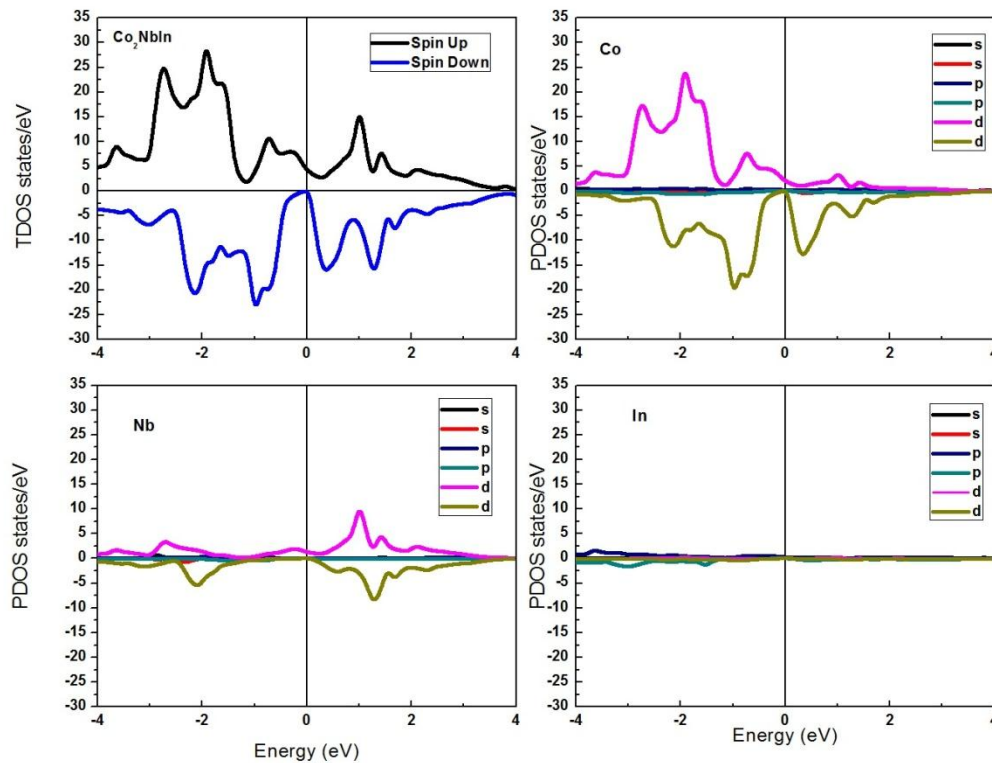


Figure 5.40: Total density of states (TDOS) and PDOS for Co_2NbIn using PBE-GGA approximation

Full Heusler Co_2TiIn displays a gap in the minority spin channel with a spin polarisation of 89.59%. This is shown in Figure 5.41.

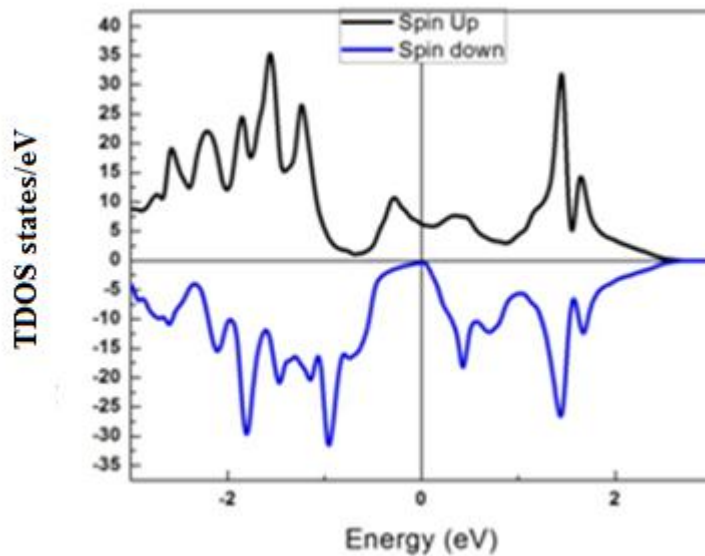


Figure 5.41: Total density of states (TDOS) for Co_2TiIn using PBE-GGA approximation

The partial density of states plot for Co_2TiIn in Figure 5.42 indicates the dominance of the Co-states just as in the case of Co_2VIn and Co_2NbIn around the Fermi level, as well as a gap in the minority states at the Fermi level. Ti contributes one less electron as compared to Nb and V per formula unit, causing a change in occupation of states at the Fermi level resulting in a reduction in the spin polarisation.

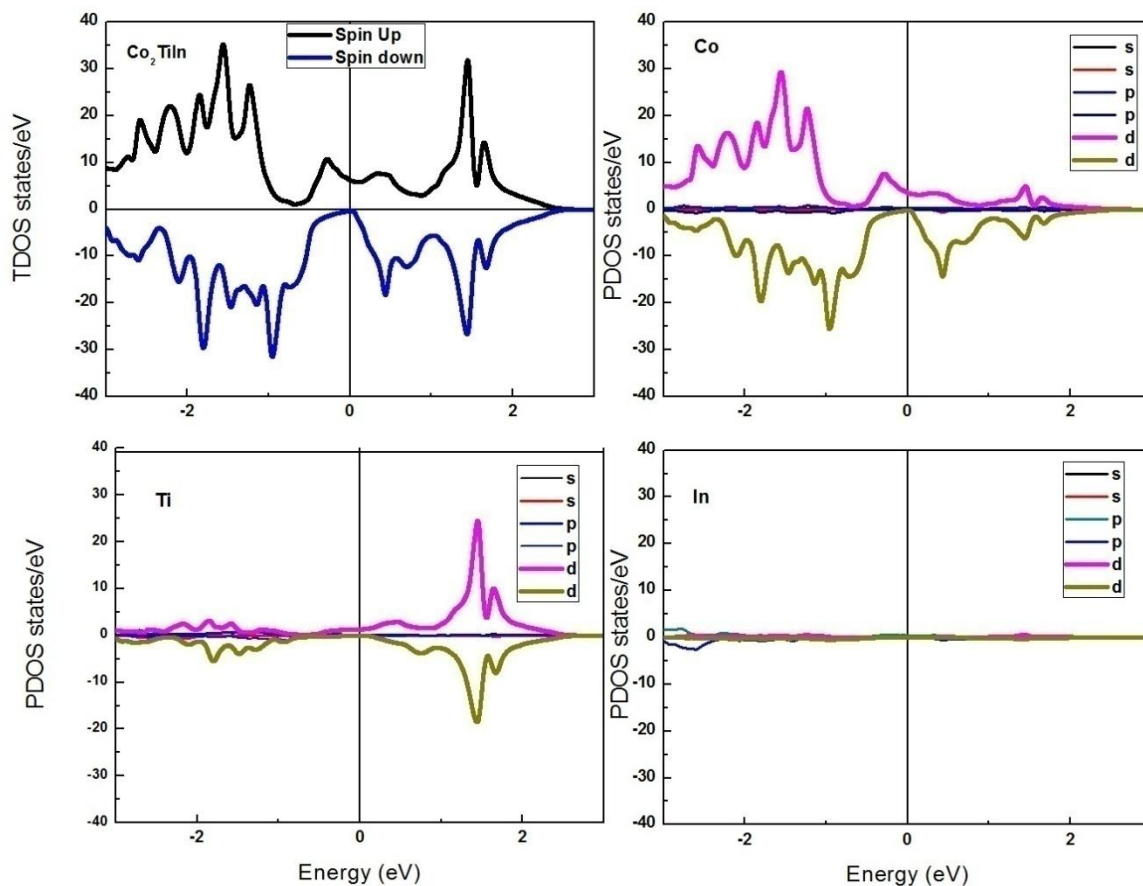


Figure 5.42: Total density of states (TDOS) and PDOS for Co_2TiIn using PBE-GGA approximation

Half-Heuslers CoNbIn and CoTiIn , display a metallic band structure, with no half-metallic gap in either spin channel as shown in Figures 5.43 (a) and (b) for the minority and majority states respectively of CoTiIn . That of CoNbIn is similar to the one of CoTiIn . This is reflected in the density of states plots, where both spin channels are present at the Fermi level as shown in Figure 5.44. This greatly affects spin polarisation at the Fermi level and the expected half-metallic property is not found for these compounds.

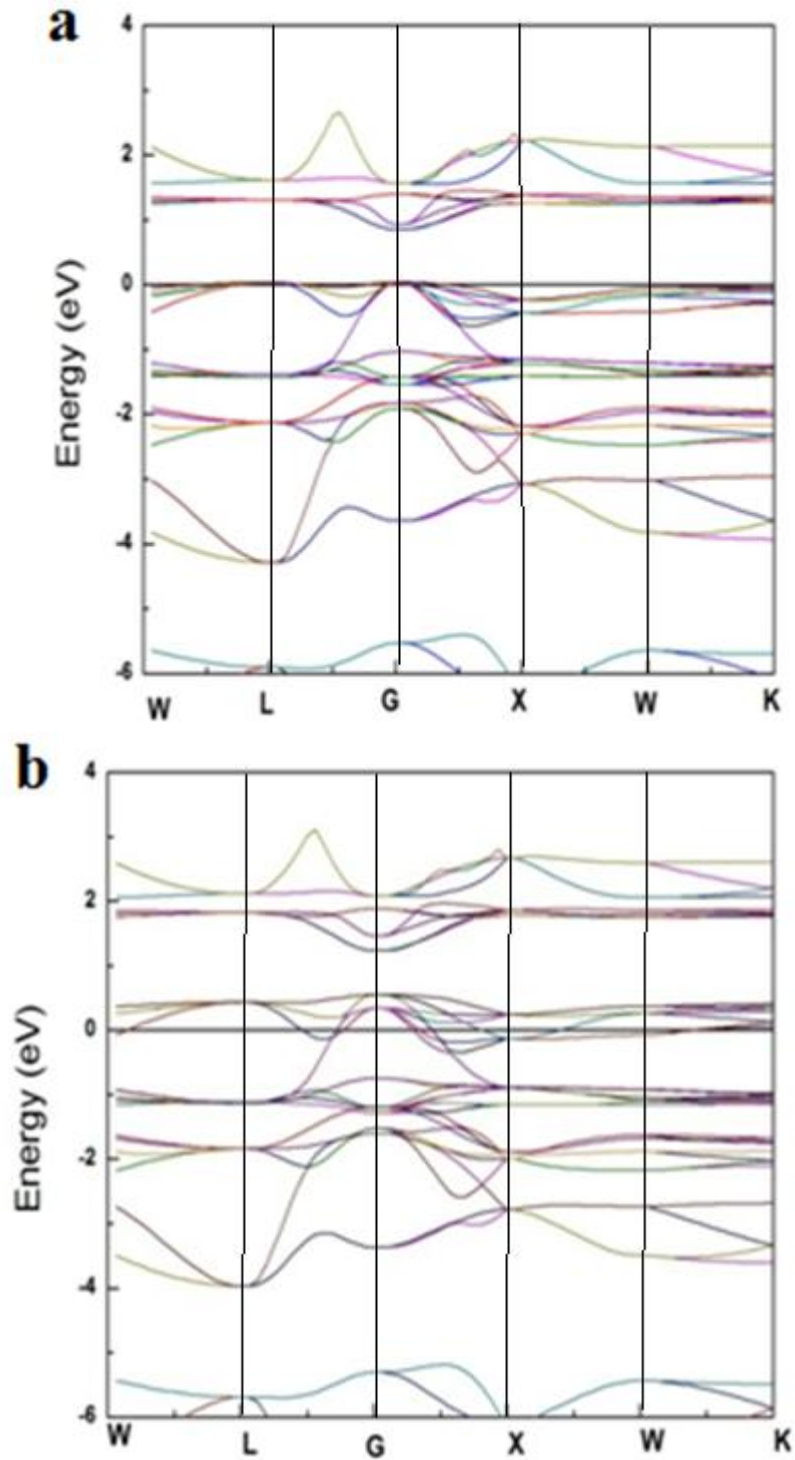


Figure 5.43(a): Minority states band structure and (b) Majority states band structure for CoTiIn

It is evident that both spin channels are conducting, hence a metallic band structure. The corresponding TDOS plot is shown in Figure 5.44.

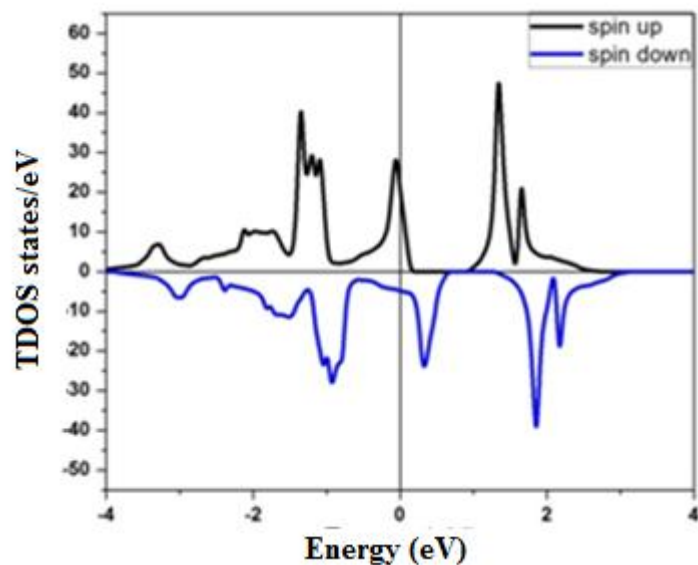


Figure 5.44: Total density of states (TDOS) for CoTiIn using PBE-GGA approximation

The partial density of states plots for CoTiIn in Figure 5.45 as well as of CoNbIn reveal the presence of Co, Ti (Nb) and In *d* and *p*-states respectively at the Fermi level, resulting in a hybridisation such that states of both spin channels are available at the Fermi level.

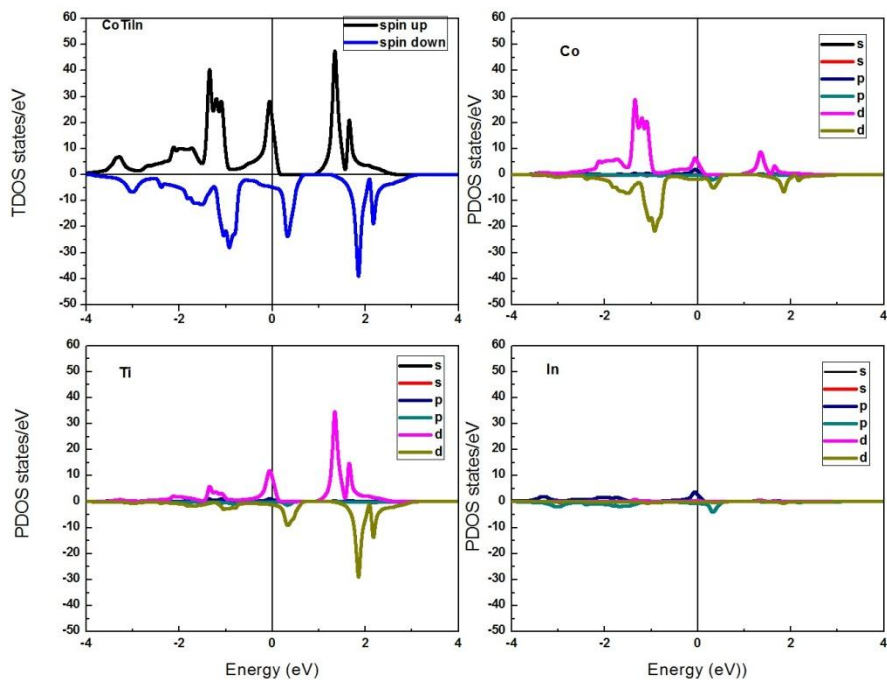


Figure 5.45: Total density of states (TDOS) and PDOS for CoTiIn using PBE-GGA approximation.

The minority band gap energy, magnetic moments and spin polarisations are recorded in Table 5.9.

Table 5.9: Spin polarization, Band gap energies, Total and atomic magnetic moments of the Heusler compounds

Compound	Opt. a (Å)	Band gap (eV)	Spin polarisation	Total magnetic moment (μ_B)	Expected from SP rule (μ_B)	X (μ_B)	Y (μ_B)	Z (μ_B)
Co ₂ NbIn	6.20	0.10	100.00%	2.02	2	1.06	-0.08	-0.02
Co ₂ TiIn	6.05	0.00	89.59%	1.04	1	0.66	-0.24	-0.04
CoNbIn	6.00	0.00	51.00%	0.65	1	0.45	0.12	0.08
CoTiIn	6.00	0.00	62.70%	1.21	2	0.28	0.75	0.17

5.6.3: Magnetic Properties

The coupling of the Co and Nb (Ti) moments is ferrimagnetic. The Co moment in Co₂NbIn and Co₂TiIn is 1.06 μ_B and 0.66 μ_B , respectively. For Co₂NbIn with a total number of 26 valence electrons just like Co₂VIn, the expected total moments per formula unit from the Slater-Pauling rule is 2 μ_B . It is found to be 2.02 μ_B /f.u., hence the half-metallic gap. In the case of Co₂TiIn, with a total number of 25 electrons, the expected moment is 1 μ_B /f.u. It is found to be 1.04 μ_B /f.u., hence the reduced spin polarisation at the Fermi level.

As is evident from the magnetic moments of the half-Heuslers, CoNbIn and CoTiIn, a ferromagnetic coupling exists between Co and Nb (Ti) and their total moments are far from an integer value as is expected for half-metallicity. This is reflected in the low spin polarisations of their electronic structures. The magnetic moments are 0.65 μ_B /f.u and 1.2 μ_B /f.u for CoNbIn and CoTiIn, respectively, far from the expected 1 μ_B /f.u and 2 μ_B /f.u, respectively.

The results reported in this section reveal that the number of valence electrons play a major role in determining whether a Heusler compound is half-metallic or not. In particular, the Y elements with less than half-filled *d*-states are less favourable for the formation of the half-metallic gap. On the other hand, an element with half-filled *d*-states like Nb is capable of forming the half-metallic gap. Although the half-Heuslers investigated were not half-metallic, they have considerably polarised band structures, a property that is useful in spintronics. The effect of lattice parameter in this case does not move the ions too far in such a manner to inhibit hybridisation as was observed in the case of Mn₂VIn in section 5.1

5.7: Structural, Electronic and Magnetic properties of X_2VIn ($X=Co, Mn$) (001) thin films

The bulk properties in general, such as those reported from sections 5.1 to 5.6, form the basis for the prediction of the properties of the more technologically relevant solid-state materials for industrial application. In this section the results of the ground state structural, electronic and magnetic properties of Co_2VIn , Mn_2VAl and Mn_2VIn thin films as predicted from first principles are reported. In addition, the thickness dependence on the spin polarisation and the structural, electronic and magnetic properties is reported.

5.7.1: Structural Properties

The optimised bulk lattice parameters for Mn_2VAl , Mn_2VIn and Co_2VIn of 5.81 Å, 6.25 Å and 6.00 Å respectively, were used to perform supercell calculations to reveal the electronic structure and magnetic properties of the thin films. (001) thin films having the standard YZ termination grown in the z direction of thickness ranging from 5.99 Å to 21.17 Å, containing 20, 36 and 52 ions respectively and corresponding to one unit cell to three unit cell thickness were modelled.

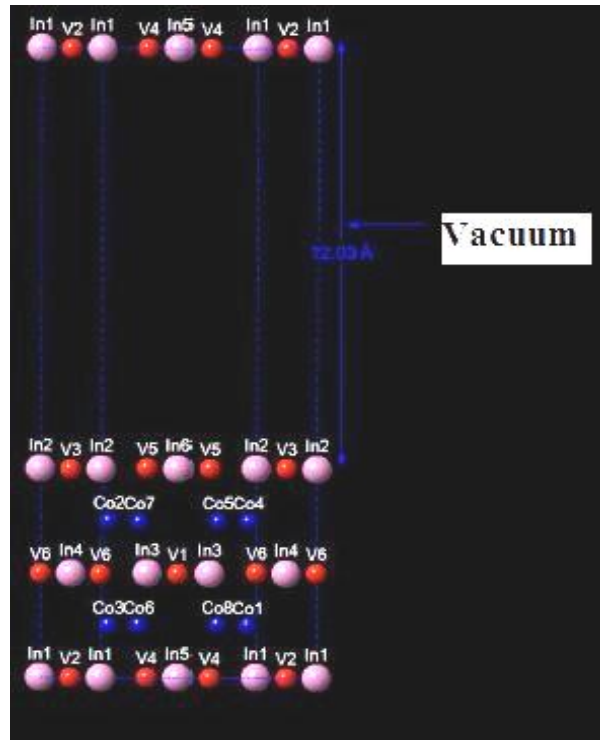


Figure 5.46: Co_2VIn supercell of thickness 6 Å corresponding to one unit cell thickness grown in the z direction. A vacuum of 12 Å is applied in the z direction

The films contained 5, 9 and 13 mono layers (ML's) each. A vacuum of 12 Å was imposed to prevent any interaction of the thin film with the bulk. For similar Heusler systems, vacuum of 10-11 Å was found to be sufficient (Wu *et al.*, 2005). Additional 7, 8 and 17 ML films of thickness 14.72, 14.82 and 26.10 Å, containing 28, 32 and 68 ions were grown to probe the properties of Mn₂VIn further. While all the films had the standard YZ termination, the 7 ML film had an XX termination. Figure 5.46 shows the supercell grown for Co₂VIn.

The 5, 9 and 13 ML thick (001) supercells grown are shown in Figure 5.47. Exactly the same types of supercells were grown for Co₂VIn, Mn₂VAl and Mn₂VIn, the only difference being the thickness of the film due to the difference in lattice parameters.

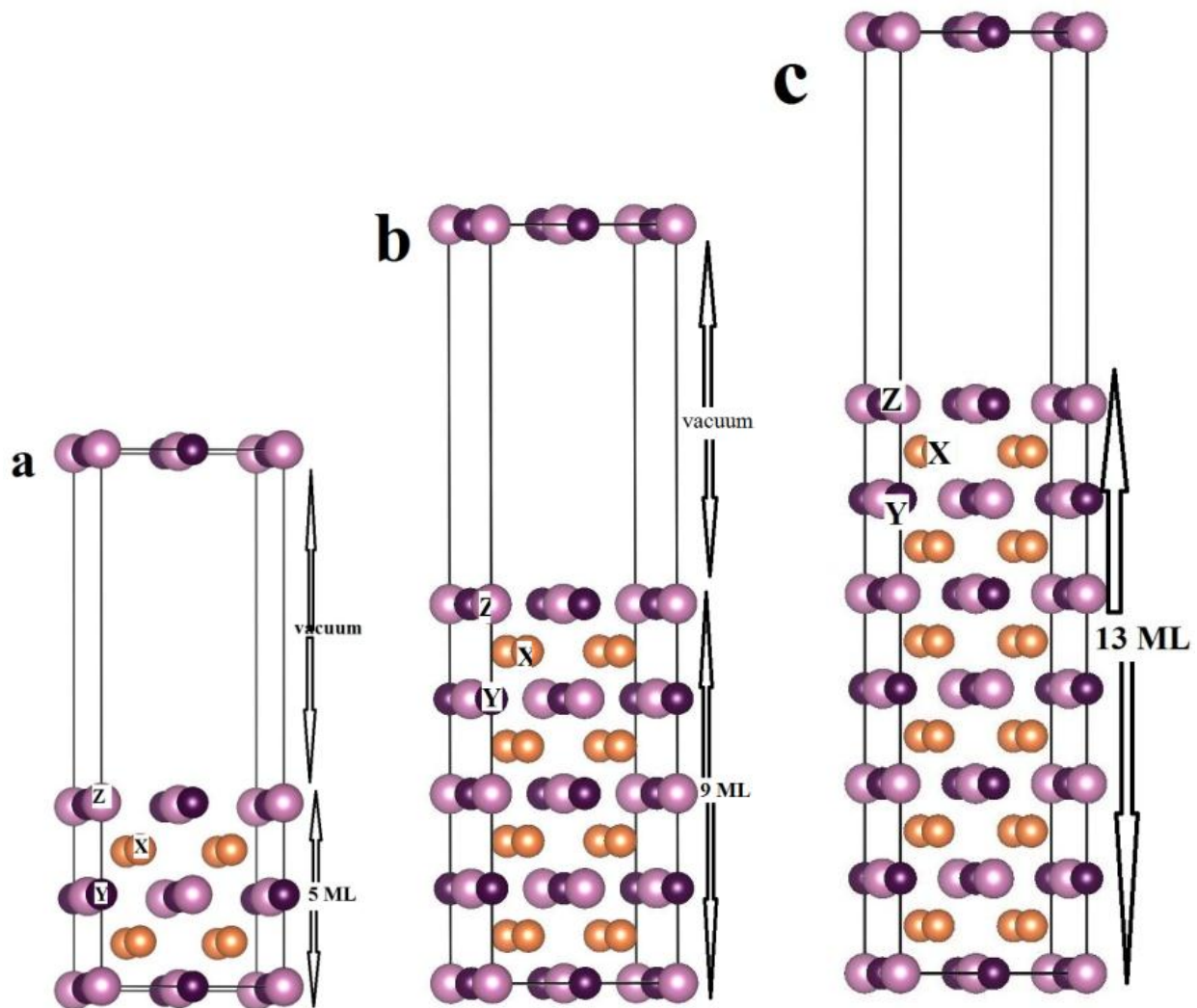


Figure 5.47: Supercells for (001) films having (a) 5 monolayers (ML's), (b) 9 ML's and (c) 13 ML's

On relaxation to reduce the forces on the surface ions, a change in the dimensions of the supercell resulted. The surface atoms were no longer within the visualisation range in all cases and therefore, after application of periodicity, the repeating unit was sliced off so as to include all the ions of the supercell, hence the slightly sliced off top most ions in Figures 5.48 – Figure 5.50. The cells underwent a lateral compression shifting the ions slightly as seen for the relaxed supercells for Co_2VIn in Figure 5.48.

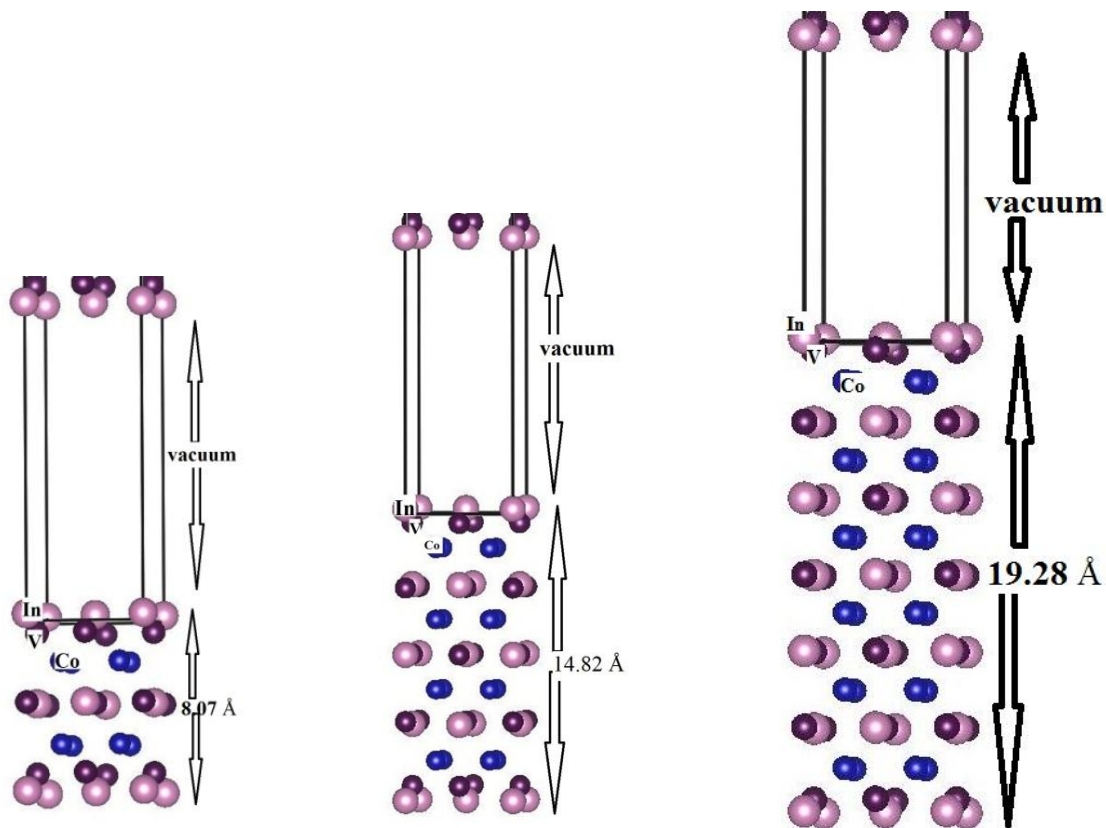


Figure 5.48: Relaxed Co_2VIn supercells. All of them are tetragonally distorted from the bulk dimensions following a reduction in the a and b parameter, while the c parameter increases in each case.

To clearly illustrate the difference in the dimensions of the supercell grown before and after relaxation, the dimensions have been tabulated in Table 5.10. It is evident that changes in the dimensions happened in such a manner as to maintain the bulk volume in order to minimise the energy as shown by the ratio of the bulk volume to the volume of the relaxed supercell (V_b/V_r).

Table 5.10: Co₂VIn Supercell dimensions after relaxation

Co ₂ VIn	Relaxation State	a (Å)	b (Å)	c (Å)	c/a	%Δc/a	V (Å ³)	V _b /V _r	% ΔV
5 ML	Before relaxation	6.00	6.00	6.00	1.00	50.00	216.00	0.92	8.54
	After relaxation	5.39	5.39	8.07	1.50		234.45		
9 ML	Before relaxation	6.00	6.00	12.00	2.00	34.50	432.00	0.96	3.78
	After relaxation	5.50	5.50	14.82	2.69		448.31		
13 ML	Before relaxation	6.00	6.00	18.00	3.00	10.00	648.00	0.98	1.82
	After relaxation	5.85	5.85	19.28	3.30		659.81		

Relaxation of the Mn₂VAl films resulted in only slight changes in volume and arrangement of the ions as shown in Figure 5.49.

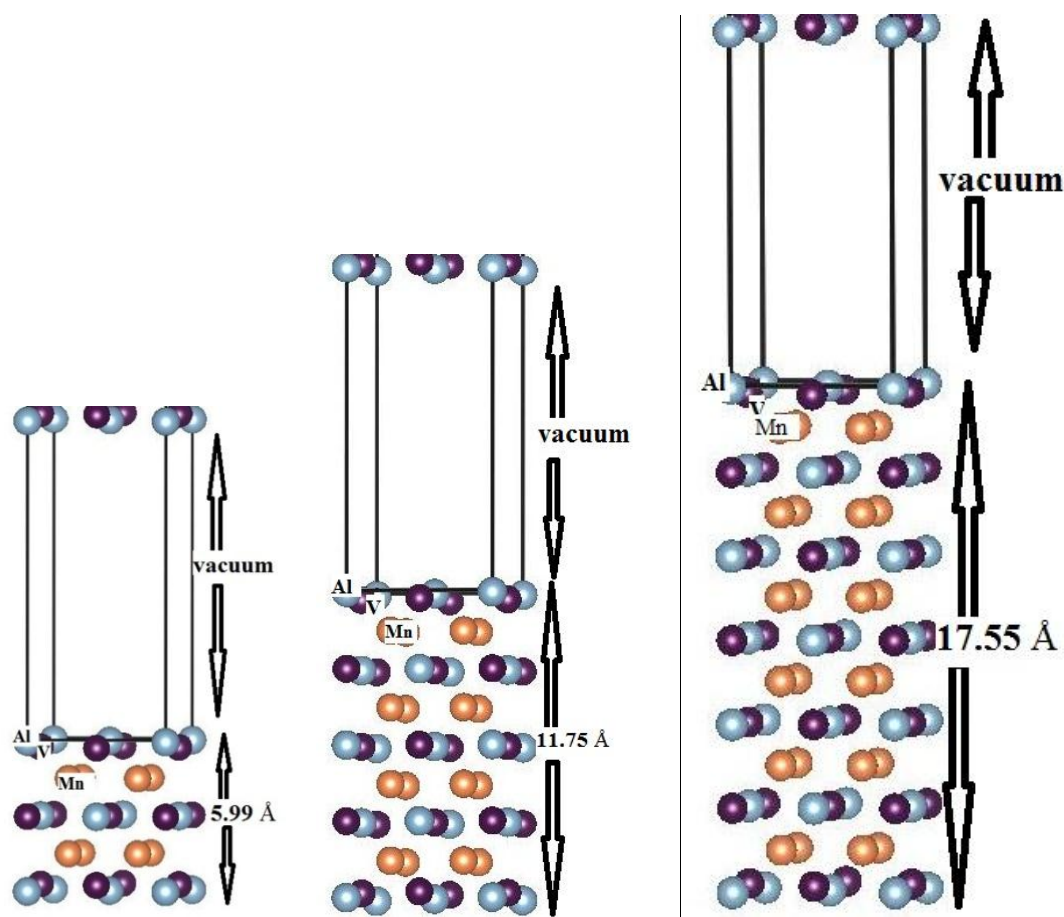


Figure 5.49: Relaxed Mn₂VAl supercells. All of them are tetragonal following a slight reduction in the a and b parameter, while the c parameter increases in each case.

It is clearly seen that as the film thickness increased to the nanometer scale, relaxation resulted in less volume change such that the three unit cell thickness film had almost the same volume as the bulk system.

In Table 5.11, the difference in the dimensions of the supercell grown before and after relaxation is clearly illustrated. Unlike Co_2VIn , the changes in supercell dimensions on relaxation are to a less extent in Mn_2VAl , such that bulk-like dimensions are present for a thinner film than in the case of Co_2VIn .

Table 5.11: Mn_2VAl Supercell dimensions after relaxation

Mn_2VAl	Relaxation State	a (Å)	b (Å)	c (Å)	c/a	% Δ c/a	V (Å ³)	V_b/V_r	% Δ V
5 ML	Before relaxation	5.80	5.80	5.80	1	6.00	195.11	1.02	2.34
	After relaxation	5.64	5.64	5.99	1.06		190.54		
9 ML	Before relaxation	5.80	5.80	11.60	2	2.50	390.22	1.01	1.14
	After relaxation	5.73	5.73	11.75	2.05		385.79		
13 ML	Before relaxation	5.80	5.80	17.40	3.00	1.67	585.34	1.01	0.87
	After relaxation	5.75	5.75	17.55	3.05		580.25		

In Mn_2VIn , containing the large atomic radii In atom, the changes in volume on relaxation are not linear as in the case of Mn_2VAl .

Table 5.12: Mn_2VIn Supercell dimensions after relaxation

Mn_2VIn	Relaxation State	a (Å)	b (Å)	c (Å)	c/a	% Δ c/a	V (Å ³)	V_b/V_r	% Δ V
5 ML	Before relaxation	6.25	6.25	6.25	1.00	23.00	244.14	1.06	5.85
	After relaxation	5.71	5.71	7.05	1.23		229.86		
8ML	Before	6.25	6.25	10.94	1.75	24.57	427.34	1.03	2.56
	After	5.76	5.76	12.55	2.18		416.38		
9 ML	Before relaxation	6.25	6.25	12.50	2.00	25.00	488.28	1.02	2.09
	After relaxation	5.76	5.76	14.41	2.50		478.09		
13 ML	Before relaxation	6.25	6.25	18.75	3.00	21.67	732.42	1.03	2.77
	After relaxation	5.80	5.80	21.17	3.65		712.16		
17ML	Before	6.25	6.25	25.00	4.00	06.50	976.56	1.00	0.10
	After	6.12	6.12	26.1	4.26		977.56		

The 9ML film displays an anomaly by undergoing a slightly higher degree of distortion as shown by the % $\Delta c/a$ value in Table 5.12. The distortion as compared to bulk dimensions then continues on the downward trend for the 13 and 17 ML films.

An investigation of the behaviour of a slightly thinner film having 8 ML, confirms that indeed the changes in the shape of Mn_2VIn are unique. It displays a higher distortion than the 5 ML film. However, the 8 ML film has a MnMn termination. The distortion in the structure of Mn_2VIn reduces significantly at a thickness slightly above $\sim 20\text{\AA}$.

This non-linear distortion may point to the importance of the atomic radii of the Z element in stabilising the structure of the unit cell in which case In being larger than Al causes more drastic changes in the dimensions of the unit cell in a quest to relax. The relaxed Mn_2VIn supercells are displayed in Figure 5.50.

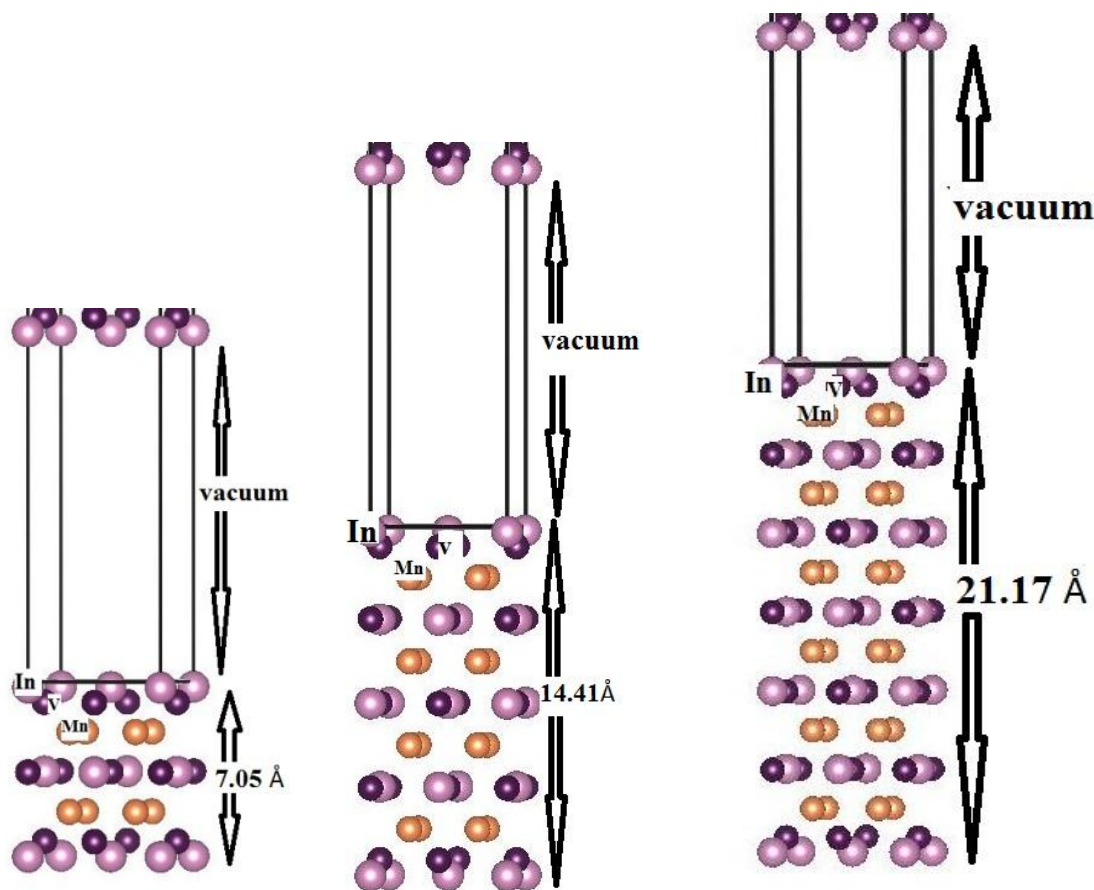


Figure 5.50: Relaxed 5, 9 and 13 ML Mn_2VIn supercells. The a and b parameters decrease, while the c parameter increases in each case

This observation is significant in the sense that the structure of Mn_2VIn is tetragonally distorted even at the nanometer scale unlike Co_2VIn and Mn_2VAl whose films almost acquire the bulk dimensions at thicknesses as low as 12 Å.

The tetragonal distortion in Mn_2VIn must therefore, be inherent to the crystal structure of the compound and not only because of surface effects as in the case of Co_2VIn and Mn_2VAl . This observation is consistent with the finding made in section 5.1 in which the bulk structure exhibited some tetragonal distortion.

It is observed that in each case, the a and b parameter decreases while the c parameter increases. It is also observed that the changes in dimensions take place in such a way as to maintain the volume in order to minimise the energy of the system in which the volume of the relaxed but distorted film is almost equal to that of the un-relaxed one made using the optimised lattice parameter of the system.

The supercell with nanometer thickness that maintains its volume even upon relaxation has $a = b = 5.8$ Å, while the lattice parameter for $\text{Mn}_{2.29}\text{V}_{0.6}\text{In}$ synthesised by arc melting was found to be 5.83 Å. This gives credence to the observation of superparamagnetism in $\text{Mn}_{2.29}\text{V}_{0.6}\text{In}$, reported in section 5.5, which is normally exhibited by nanoscale clusters.

5.7.2: Electronic Properties

The spin polarisations for the 5 and 9 ML Co_2VIn thin films are 38.11% and 63.08 % respectively as shown in the total density of states (TDOS) in Figure 5.51. However, for the film with 9 ML's, a small gap was observed in the minority states.

The density of states of the 13 ML Co_2VIn film had a clearer gap in the minority states having a spin polarisation of 65.40% as shown in the TDOS plot in Figure 5.52. The Mn_2VAl thin film with 5 ML's, has a spin polarisation of 37%, with both spin channels conducting heavily at the Fermi level. The TDOS has no similarity with the bulk one at this very fine thickness as shown in Figure 5.53

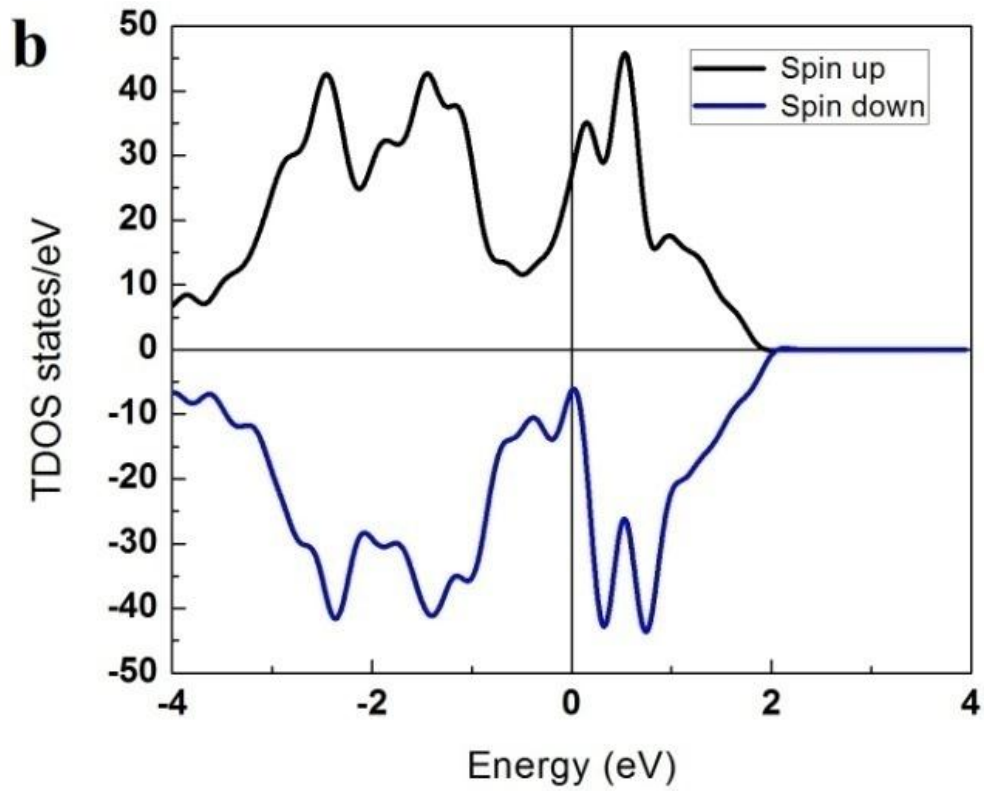
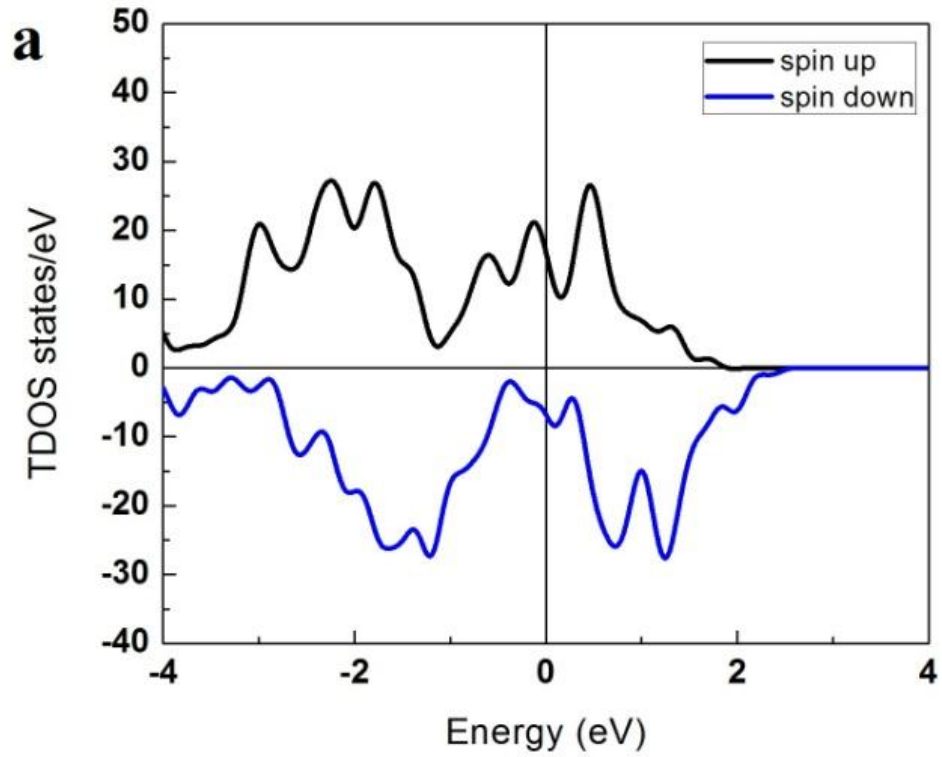


Figure 5.51: Total density of states (TDOS) for (a) 5 ML thick Co_2VIn and (b) 9 ML thick Co_2VIn film

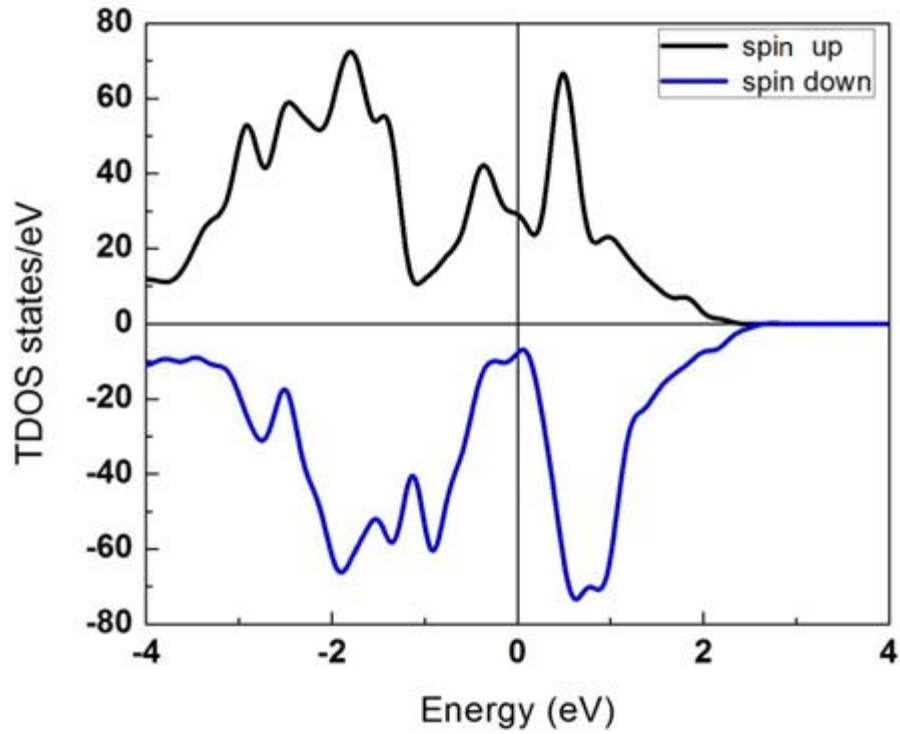


Figure 5.52: Total density of states (TDOS) for 13 ML thick Co_2VIn film

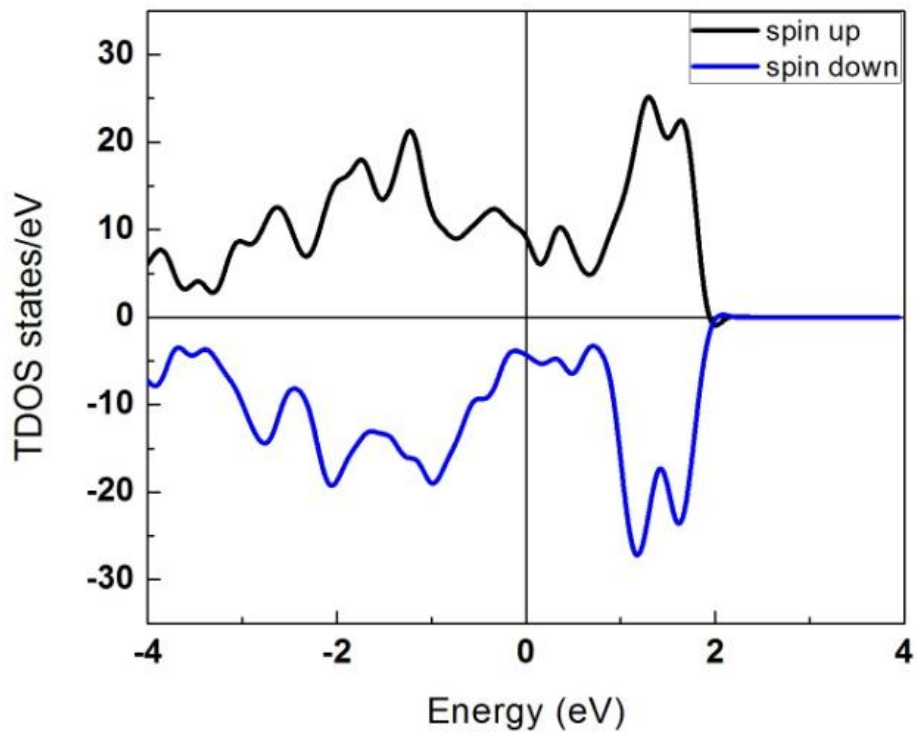


Figure 5.53: Total density of states (TDOS) for 5 ML thick Mn_2VAI film

The 9 ML and 13 ML Mn₂VAl films have a TDOS which is more bulk like similar to the case of Co₂VIn, with spin polarisations of 57.87 % and 73.90% as shown in Figures 5.54 (a) and (b).

A pseudo gap is seen in the Mn₂VIn thin films up to a thickness of 13 ML's. The spin polarisations decrease with film thickness with values of 55.32 %, 30.10 % and 33.42 % for the 5, 9 and 13 ML's, respectively as shown in Figures 5.55 (a) and (b) and Figure 5.56 (a).

Just like in the case of Mn₂VAl and Co₂VIn, the density of states of Mn₂VIn thin films become more bulk like with increasing film thickness.

The Fermi energy is slightly above the pseudo gap in the spin up channel of the 13 ML Mn₂VIn film of thickness 21.17 Å. The spin polarisation on a slight contraction of the unit cell such that the Fermi level lies within the pseudogap, as would happen due to epitaxial stress, increases to 71.23%.

The TDOS of bulk tetragonally distorted Mn₂VIn is shown alongside it in Figure 5.56 (b), due to their similarity at the Fermi level considering the very close lattice parameter for 13 ML Mn₂VIn thin film and tetragonally distorted Mn₂VIn bulk structure with a lattice parameter of $a = 5.8 \text{ \AA}$ and $a = 5.83 \text{ \AA}$, respectively. The spin polarisation of the tetragonally distorted Mn₂VIn bulk system is 51.6%.

The re-hybridisation that occurs after relaxation of the thin films results in increased spin polarisation due to the overlap of the 3 *d* orbitals at the reduced lattice parameters. These results corroborate those from a study on the effect of size of lattice parameter on the electronic properties of Mn₂VAl in which it was observed that upon expansion or compression, the Fermi level moved towards the valence band and in the direction of the conduction band respectively, without destroying the half-metallic character (Galanakis and Mavropoulos, 2007). Similarly, in the calculation of experimental bulk lattice constant in NiMnSb, compression of the lattice was found to push the majority *p*-states to higher energies and also increased the hybridisation between the *d* orbitals of the different transition metal atoms. The spin moment of Mn decreases as a result of the increased hybridisation (Luo *et al.*, 2008a).

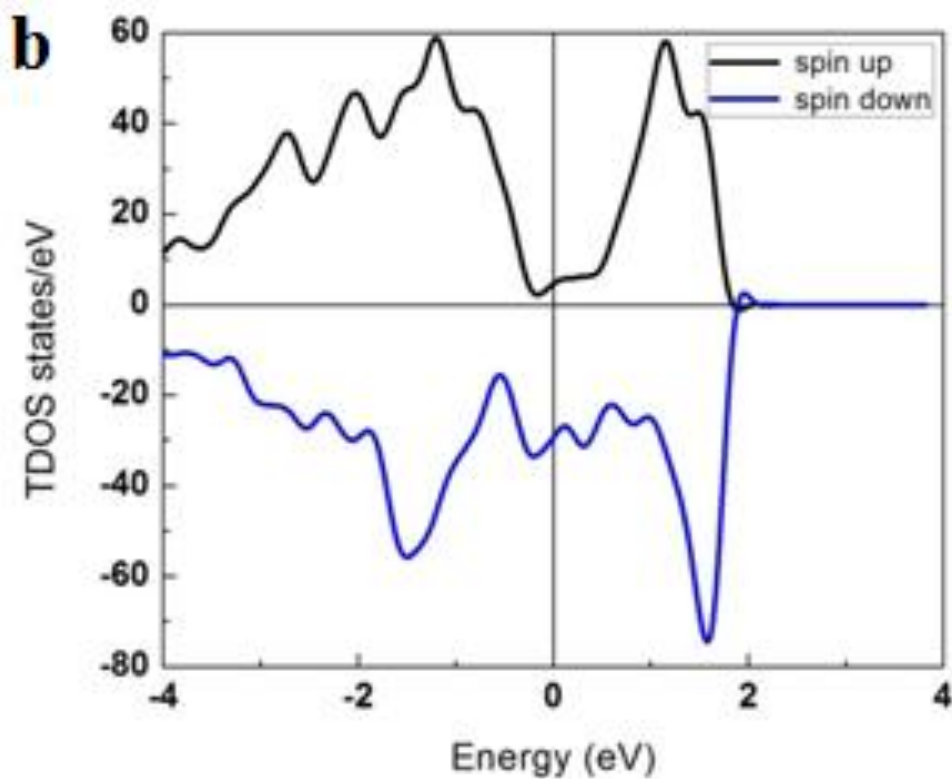
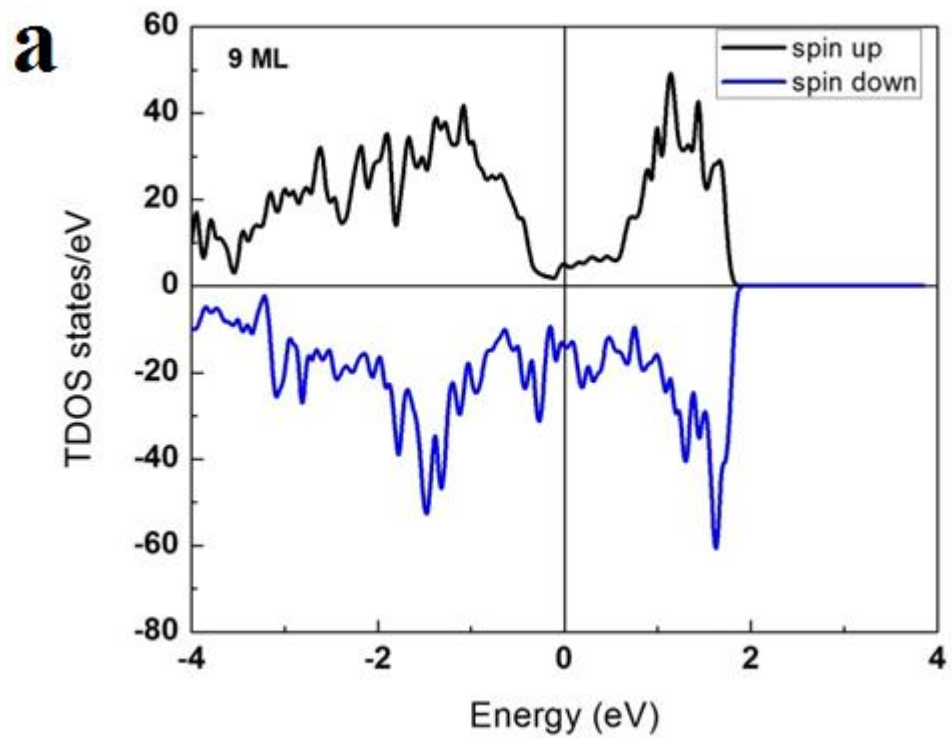


Figure 5.54: Total density of states (TDOS) for (a) 9 ML Mn_2VAI and (b) 13 ML thick Mn_2VAI films.

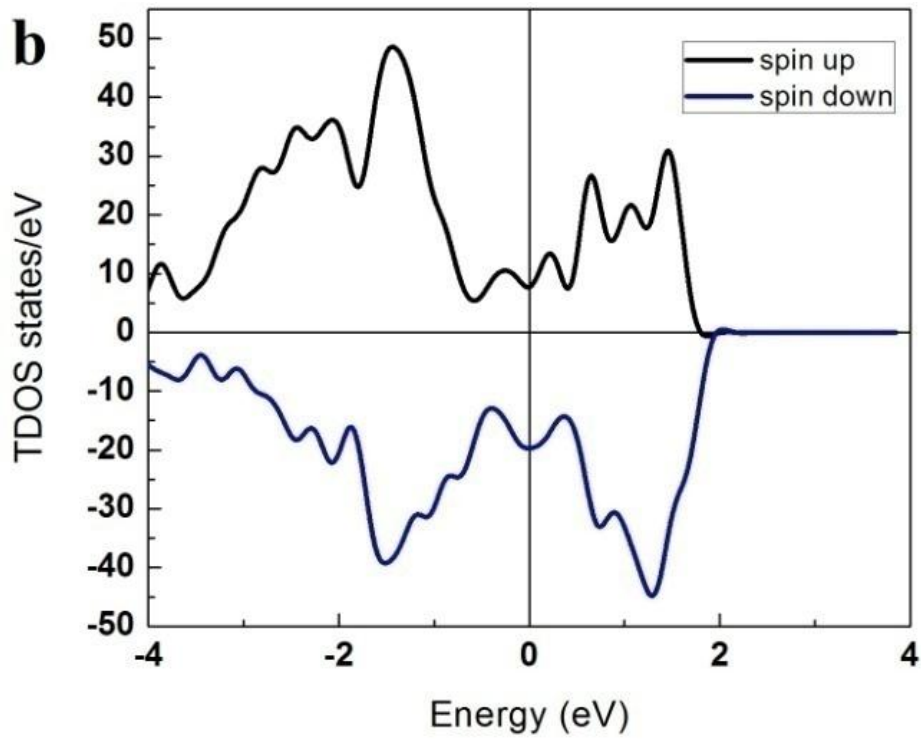
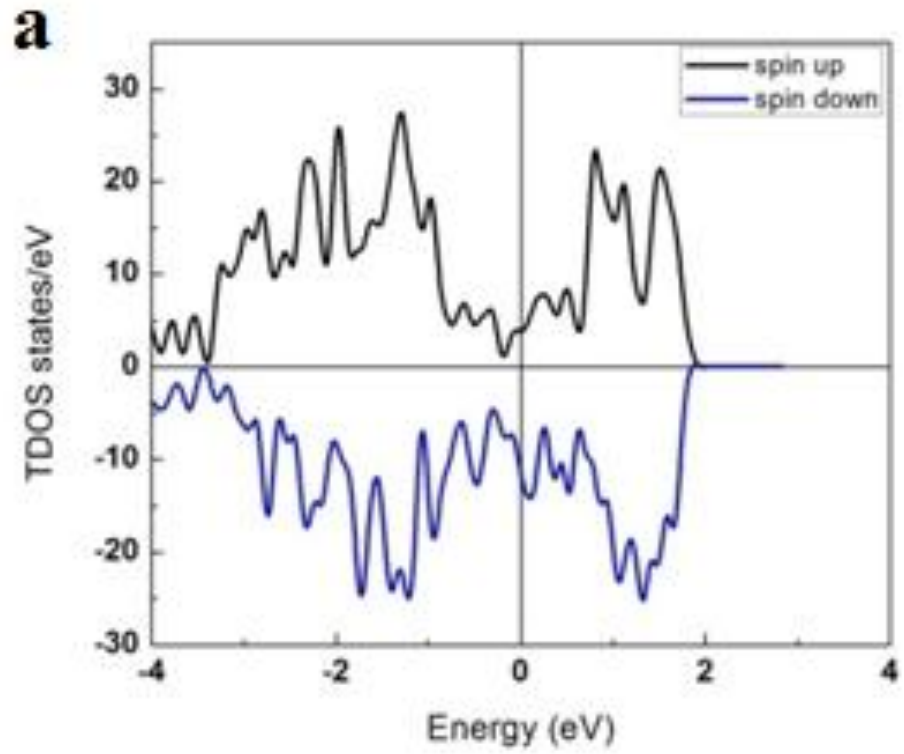


Figure 5.55: Total density of states (TDOS) for (a) 5 ML thick Mn_2VIn and (b) and 9 ML thick Mn_2VIn films.

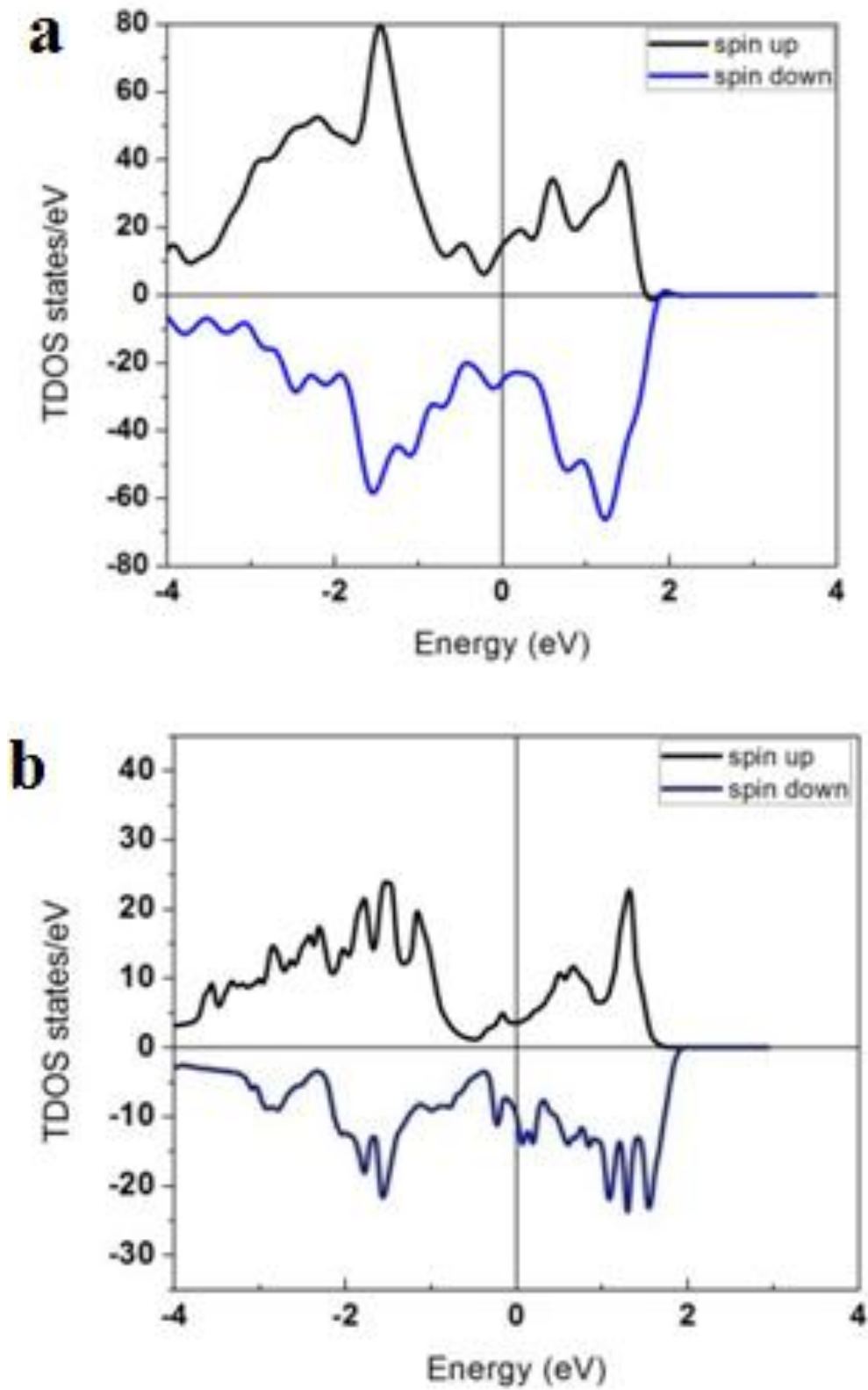


Figure 5.56: Total density of states (TDOS) for (a) 13 ML thick Mn_2VIn and (b) and tetragonally distorted Mn_2VIn bulk system

From the results of the electronic structures, spin polarisations are less in the thin films as compared to the bulk for the systems studied except for Mn_2VIn , which is not half-metallic at the equilibrium volume. In fact, the electronic structures of the films are comparable to those of the tetragonally distorted bulk system which even though higher in energy than the cubic system formed by the optimised lattice parameter shows a local energy minimum as discussed in section 5.1. This is indeed an amazing connection pointing to the consistency of the predictions and explanations offered for different observations through DFT.

5.7.3: Magnetic Properties

The magnetic properties of the films as well as for the corresponding bulk systems studied earlier are reported in Table 5.13 for comparison.

Table 5.13: Magnetic moments for Co_2VIn , Mn_2VIn and Mn_2VAl films of different thickness as well as for each atom in the system

$\text{X}_2\text{VIn}(\text{Co, Mn})$	System	X (Co, Mn μ_B)	V (μ_B)	In (μ_B)	Total ($\mu_B/\text{f.u.}$)
Co_2VIn	5 ML	-0.018	0.134	0.0003	0.098
	9 ML	0.099	0.262	-0.005	0.455
	13 ML	0.923	0.230	-0.034	2.042
	bulk	0.928	0.192	-0.047	2.001
Mn_2VAl	5 ML	-0.684	0.681	0.010	-0.677
	9 ML	1.065	-0.808	-0.016	1.306
	13 ML	1.168	-0.831	-0.018	1.487
	bulk	1.426	-0.895	-0.021	1.936
Mn_2VIn	5 ML	1.590	-1.370	-0.010	1.800
	7 ML	2.015	-1.340	-0.040	2.650
	8 ML	2.660	-1.750	-0.069	3.501
	9 ML	2.264	-1.682	-0.039	2.807
	13 ML	2.330	-1.740	-0.060	2.860
	17ML	2.875	-2.038	-0.058	3.654
	bulk	3.009	-1.979	-0.059	3.980
	Tetra. distorted	1.949	-1.296	-0.045	2.557

The general trend is that the thickest films studied have similar total magnetic moments as well as individual atomic magnetic moments as the corresponding bulk systems. For the thin films, the loss of neighbours resulting in breaking of the symmetry causes a re-hybridisation hence, changing the magnetic moments and changing the spin polarisation at the Fermi level

(Hashemifar *et al.*, 2005). For Mn_2VIn however, the trend is not as straight forward. As seen in Table 5.12, the 5 ML Mn_2VIn film has a total magnetic moment of $1.800 \mu_B$, very close to the expected $2 \mu_B$ for Mn_2VIn , if half-metallic according to the Slater-Pauling rule. This observation is attributed to the overlapping of the d orbitals at the reduced lattice constant, which does not take place in the bulk structure in which the Mn localised magnetic moment is $\sim 3 \mu_B$, a value it's known to have if no hybridisation occurs. The 13 ML thick film, on the other hand, has magnetic moments very similar to those of the tetragonally distorted bulk system, that shows a local minimum in energy, though higher than the energy of the optimised cubic system; while the 8 ML thick film with a MnMn termination breaks the trend in value of magnetic moments, as expected due to the symmetry breaking arising from reduced V neighbours.

While Co_2VIn is generally ferromagnetic due to the exchange interaction between Co and V, Mn_2VAl and Mn_2VIn are ferrimagnetic and would therefore, create smaller external magnetic fields in devices, leading to smaller energy losses (Kawakami *et al.*, 1981).

The magnetisation aligns along the tetragonal axis resulting in PMA in the thin films, which is of great technological importance. The trend is collated in Table 5.14.

Table 5.14: Orbital magnetic moments for Co, Mn, V and In as well as magnetic anisotropy energy for the thin films.

System	Thickness	X_{orb} (Co, Mn μ_B)	V_{orb} (μ_B)	In_{orb} (μ_B)	% $\Delta c/a$	E_{MAE} (meV)
Mn_2VAl	5 ML	-0.0091076	-0.0039300	-0.0001800	06.00	00.545
	9 ML	-0.0090263	-0.0038900	-0.0001800	02.50	00.461
Co_2VIn	5 ML	-0.0174098	-0.0031800	-0.0377100	50.00	87.760
	9 ML	-0.0178053	-0.0038534	-0.0383700	34.50	00.146
Mn_2VIn	5 ML	-0.0100000	-0.0040000	-0.0400000	23.00	02.089
	8 ML	-0.0095287	-0.0038300	-0.0389400	24.57	03.680
	9 ML	-0.0098709	-0.0039200	-0.0393600	25.00	06.790

The magnetic anisotropy energy (E_{MAE}) for Mn_2VAl is very low for both the 5 and 9 ML thickness films. It is highest for the Co_2VIn 5 ML film, and decreases appreciably in the 9 ML

thin film. In Mn_2VIn , E_{MAE} increases with thickness. We attribute this observation to the tetragonal distortions in these films and the balance with the film volume, rather than to spin-orbit coupling as the orbital moments are very low as shown in Table 5.13. In Mn_2VAl , least distortion is exhibited resulting in very low anisotropy. In the 5 ML Co_2VIn thin film, the tetragonal distortion is very high, contributing to the high magneto crystalline PMA. In Mn_2VIn , the symmetry breaking caused by the tetragonal distortion in the thicker films align the spin moments perpendicular to the plane of the film, resulting in increasing PMA with film thickness.

The surface magnetism has been shown to be highly dependent on the film volume as is expected for ultra thin films containing a few atomic layers at low temperatures. The exchange coupling in the films is the same as in the bulk, except for the 5 ML films, which leads to size effects overriding surface effects and film thickness becoming a significant factor.

Significant results applicable in spintronics device applications emerge from the study of the thin film Heusler systems in this section. While Co_2VIn and Mn_2VAl exhibit a trend that would be expected for Heusler compounds, both structural and electronic, Mn_2VIn , on the other hand, exhibits unique characteristics that can be exploited depending on quality desired. If high spin polarisation is required like in GMR read heads, then the thinner the film the better, if perpendicular magnetic anisotropy is required like in MRAMS, then, a film with nanometre thickness would be suitable and if superparamagnetism is required, then again, components can be designed with nanoscale thickness films with lattice parameter $a = 5.83$. The results from this section have demonstrated the ability of Mn_2VIn films to possess varying desirable properties all driven by the different structural modifications it is able to adapt to ranging from high spin polarisation, perpendicular magnetic anisotropy to superparamagnetism.

6.0 CONCLUSIONS AND RECOMMENDATIONS

The optimized lattice parameter of Mn_2VAl is found to be 5.8 \AA , whereas that of Mn_2VIn , having Indium (In) in place of Aluminum (Al) in the Z position in Mn_2VZ (Al, In) is found to be 6.25 \AA . While hybridisation takes place in the optimised Mn_2VAl compound, resulting in a $d-d$ half-metallic band gap in the minority states, this is only observed at a reduced lattice constant for Mn_2VIn , for which hybridisation between the d -states of the transition metal atoms does not result in a half-metallic gap for the optimised structure. This is due to the fact that at this lattice constant, the d -states of the transition metal atoms in Mn_2VIn occur at different energy regions and therefore do not overlap sufficiently to result in the $d-d$ band gap. The magnetic moments are localised on the transition metal atoms as a result and therefore, the Slater-Pauling rule for half-metallic Heusler alloys is not obeyed in Mn_2VIn , but is in good agreement with Mn_2VAl . The Mn and V magnetic moments exhibit an antiparallel spin coupling in both Mn_2VAl and Mn_2VIn , a desirable property in magneto electronic applications. Device components designed with these materials would create smaller external magnetic fields in devices, leading to smaller energy losses.

Structural energetics revealed an energetically favourable tetragonal distortion in Mn_2VIn that is not exhibited by Mn_2VAl , which is caused by the bigger size of the atomic radius of $Z = \text{In}$ as compared to Al, resulting in magnetic anisotropy in the Mn_2VIn system. Apart from increasing the lattice constant and affecting the electronic structure, the sp element increased the magnitude of the magnetic moment which is a direct consequence of the increase in lattice parameter leading to less hybridisation. The atomic radius of the Z element has an effect on the structural, electronic and magnetic properties of the resulting Heusler compounds.

Introduction of Co impurities by creating Mn antisites in Mn_2VIn resulted in development of desirable properties such as perpendicular magnetic anisotropy predicted for $\text{Mn}_{0.75}\text{Co}_{1.25}\text{VIn}$, which is found to be tetragonally distorted as well as nearly antiferromagnetic and higher spin polarisation, with $\text{Mn}_{0.25}\text{Co}_{1.75}\text{VIn}$ exhibiting the highest spin polarisation at 93.60 %. Replacing Mn with Co reduced the lattice constant of the system, which resulted in an increased overlap of the d -states of the transition metal atoms, hence, enhancing hybridisation, resulting in the

emergence of the half-metallic gap. In the process, Van Hove singularities in the resulting electronic structures triggered tetragonal distortions, which were responsible for the perpendicular magnetic anisotropy found in $\text{Mn}_{0.75}\text{Co}_{1.25}\text{VIn}$ and MnCoVIn . In general, the spin polarisation increased in very low concentrations of impurity Co atoms and significant changes in magnetic order were noted, bringing out the fact that the presence of impurities, which cannot be ruled out in real systems, have a great effect on the electronic structure, inhibiting the expected spin polarisations. Carefully controlled introduction of impurities was shown to be a useful technique in enhancing spin polarisation and the resulting systems may be used as candidates for spin valves and magnetic tunnel junction applications. On the other hand, certain concentrations may destroy the half-metallic gap.

Complete replacement of Mn with Co in Mn_2VIn resulted in Co_2VIn which was predicted together with its half-Heusler counterpart CoVIn to be 100% spin polarised by DFT+U. Both Co_2VIn and CoVIn are predicted to possess similar structural, electronic and magnetic properties with their isoelectronic and isostructural counterparts having Aluminum in place of Indium, that is, ferromagnetism and ferrimagnetism respectively, with a slight increase in magnetic moments. The ability of the DFT+U method to treat the partial localisation of the *d*-states is demonstrated by these results.

$\text{Mn}_{1.79}\text{VAIn}_{1.14}$ samples prepared by arc melting exhibit $L2_1$ order as opposed to the Mn-V-In sample containing $\text{Mn}_{2.29}\text{V}_{0.6}\text{In}$ and $\text{Co}_{1.8}\text{VIn}_{0.1}$ samples prepared by the same method, which have both tetragonal and cubic phases in the samples. The samples reveal to a great extent the reason as to why the predicted electronic properties are difficult to observe in real materials, which include multiple phases, non stoichiometry in the samples, structural distortions and disorder, which contribute to the appearance of states in the half-metallic gap, reducing spin polarisation. The type of structural distortion exhibited in Mn_2VIn is explained using DFT, displaying a high correlation between the DFT predictions and expected properties. With improved and more sophisticated methods of material preparation, these properties predicted through DFT calculations are highly likely to be realised with formation of the proper crystal structures.

While $\text{Mn}_{1.79}\text{VAl}_{1.14}$ exhibits the predicted ferrimagnetic coupling with a saturation magnetic moment of $1.74\mu_{\text{B}}/\text{f.u.}$, very close to the expected $2\mu_{\text{B}}/\text{f.u.}$ for half-metallic Mn_2VAl , the rare superparamagnetic property as well as ferrimagnetism and martensitic transformation is observed in Mn-V-In having $\text{Mn}_{2.29}\text{V}_{0.6}\text{In}$ phase prepared by arc melting. The magnetic moments measured for the off-stoichiometric Mn-V-In and $\text{Co}_{1.8}\text{VIn}_{0.1}$ samples are less than the expected $2\mu_{\text{B}}/\text{f.u.}$ for the Heusler compounds at $0.500\mu_{\text{B}}/\text{f.u.}$ and $5.767 \times 10^{-4}\mu_{\text{B}}/\text{f.u.}$, respectively. The structure property dependence is clearly brought out which is explained using DFT calculations, whereby energetically favourable tetragonal distortions are predicted for Mn_2VIn . Structural distortions, impurities and disorder change the magnetic order. It was however, shown in section 5.2 that impurities and disorder can be exploited to attain the desired properties.

The Y elements Nb and Ti in Co_2YIn have an effect on the spin polarisation of the resulting compounds as compared to Co_2VIn . Y = Ti has one less valence electron as compared to V, leading to higher hybridization between the *d*-states, resulting in lower moments on the Co atoms. Y = Nb has a larger atomic radius than V, but same number of valence electrons, which decreases the hybridisation as compared to V, resulting in higher magnetic moments on the Co atom. While Co_2NbIn is half-metallic, Co_2TiIn is metallic, although with a high spin polarisation of 89.59%. The Y element with less than half-filled *d*-states like Ti are less favourable for the formation of the half-metallic gap, while an element with half-filled *d*-states like Nb is capable of forming the half-metallic gap. The half-Heuslers CoYIn (Y= Ti, Nb) investigated are not half-metallic but have considerably polarised band structures, a property that is useful in spintronics. due to the decreased hybridisation between the *d*-states

Mn_2VIn thin films exhibit unique characteristics ranging from high spin polarisation at very fine thickness and perpendicular magnetic anisotropy for nanometer thick thin films. This is due to the fact that the magnetic anisotropy in this system arises from the volume rather than the surface. Depending on thin film thickness, then particular properties are displayed. Relaxation in the Mn_2VIn thin films results in lattice parameters at which increased hybridisation causes the spin polarisation to be higher as compared to the bulk system. These results point to the importance of the size of the lattice parameter on the electronic properties, an important factor in

thin film technology, which would assist in selection of appropriate substrates, as samples grown on different substrates have different lattice spacing.

RECOMMENDATIONS

While considering fabrication of a new half-metallic Heusler system, careful choice of elements should be carried out before the fabrication. This can be done by carrying out thorough prediction using DFT, taking into account the localisation of *d*-states, so as to have realistic expectations, as not all possible X₂YZ and XYZ combinations result in half-metallic band structures.

While fabricating the compounds, starting materials of extremely high purity are necessary to minimise loss of spin polarisation due to the presence of impurities.

The fabrication process and method should be carefully considered as phase separation between ordered L2₁ and disordered bcc phases degrades half-metallicity, hence discrepancies between theoretical and experimental results. It is highly recommended that several annealing and quenching procedures be adopted while synthesising the Heusler compounds for spintronic devices to minimise this effect in order to realise the predicted spin polarisations predicted by DFT.

Before fabrication, prediction of structural energetics would give a very good idea of possible structural distortions which in the case of thin film fabrication would inform substrate choice. Choice of substrate should be done in such a way that the stress introduced in the fabrication of the films does not affect the spin polarisation and takes into account the possible distortions that may take place in a particular structure. Due to the great effect that lattice constant has on hybridisation, it is recommended that on prediction of optimised lattice constant at which half-metallicity is attained, a suitable substrate is used to fabricate the films so as to offer contraction or expansion where necessary.

7.0 REFERENCES

- Ahmmad, B., Islam, M. Z., Billah, A., and Basith, M. A. (2016). Anomalous coercivity enhancement with temperature and tunable exchange bias in Gd and Ti co-doped BiFeO₃ multiferroics. *J. Phys. Appl. Phys.* **49**, 095001–095007.
- Aslanov, L. A., Fetisov, G. V., and Howard, J. A. K. (1998). “*Crystallographic Instrumentation*” (Rev. ed.). Howard, J. A. K. (Ed.). International Union of Crystallography, Oxford University Press, New York.
- Bach, V., and Site, L. D. (2014). “*Many-Electron Approaches in Physics, Chemistry and Mathematics: A Multidisciplinary View*” (Rev. ed.). Bach, V. and Site, L. D. (Eds.). Springer, London.
- Balke, B., Fecher, G. H., and Felser, C. (2013). *New Heusler Compounds and Their Properties. In “Spintronics”* (Rev. ed.). Felser, C. and Fecher, G. H. (Eds.). Springer, Netherlands.
- Bell, D. C., and Garratt-Reed, A. J. (2003). “*Energy Dispersive X-ray Analysis in the Electron Microscope*” (Print ed.). Hooker E. (Ed.). BIOS scientific publishers ltd., Oxford.
- Blöchl, P. E. (1994). Projector augmented-wave method. *Phys. Rev. B* **50**, 17953-1–17953-27.
- Blöchl, P. E., Först, C. J., and Schimpl, J. (2003). Projector augmented wave method: ab initio molecular dynamics with full wave functions. *Bull. Mater. Sci.* **26**, 33–41.
- Bunaciu, A. A., Udriștioiu, Gabriela, E., and Aboul-Enein, H. Y. (2015). X-Ray Diffraction: Instrumentation and Applications. *Crit. Rev. Anal. Chem.* **45**, 289–299.
- Buschow, K. H. J. (2003). “*Handbook of magnetic materials*” (1st ed.). Buschow, K. H. J. (Ed.). Elsevier, Amsterdam.
- Buschow, K. H. J., and Boer, F. R. de (2007). “*Physics of Magnetism and Magnetic Materials*” (Rev. ed.). Buschow, K. H. J. (Ed.). Springer Science & Business Media, New York.
- Carbonari, A. W., Saxena, R. N., Pendl Jr., W., Mestnik Filho, J., Attili, R. N., Olzon-Dionysio, M., and Souza, S. D. de (1996). Magnetic hyperfine field in the Heusler alloys Co₂YZ (Y = V, Nb, Ta, Cr; Z = Al, Ga). *J. Magn. Magn. Mater.* **163**, 313–321.
- Chen, Y., Cui, Y., Cheng, C., and Zhao, Y. (2011). Multiple magnetic transitions in SmCoAsO. *AIP Adv.* **1**, 042134-1–042134-7.
- Claeys, C., and Simoen, E. (2011). “*Germanium-Based Technologies: From Materials to Devices*” (1st ed.). Claeys, C. and Simoen, E. (Eds.). Elsevier, Oxford.
- Coe, J. M. D. (2010). “*Magnetism and Magnetic Materials*” (1st ed.). Coe, J. M. D. (Ed.). Cambridge University Press, Cambridge.

- Dau, Jenichen, P., and Herfort, J. (2015). Perpendicular magnetic anisotropy in the Heusler alloy $\text{Co}_2\text{TiSi}/\text{GaAs}(001)$ hybrid structure. *AIP Adv.* **5**, 057130-1–057130-8.
- de Groot, R. A., Mueller, F. M., van Engen, P. G., and Buschow, K. H. J. (1983). New Class of Materials: Half-Metallic Ferromagnets. *Phys. Rev. Lett.* **50**, 2024 – 2027
- ElAmineMonir, M., Khenata, R., Baltache, H., Murtaza, G., Abu-Jafar, M., Rached, D., BinOmran, S., and Bouhemadou, A. (2015). Study of structural, electronic and magnetic properties of CoFeIn and Co_2FeIn Heusler alloys. *jmmm.* **394**, 404–409.
- Èvarestov, R. A., and Smirnov, V. P. (1997). “*Site symmetry in crystals: theory and applications*” (1st ed.). Cardona, M., Fulde, P., von Klitzing, K., Queisser, H. J., and Lotsch H. K. V. (Eds.). Springer, Berlin.
- Felser, C., and Hirohata, A. (2015). “*Heusler Alloys: Properties, Growth, Applications*” (Rev. ed.). Felser, C. and Hirohata A. (Eds.). Springer International Publishing, Switzerland.
- Feng, L., Liu, E. K., Zhang, W. X., Wang, W. H., and Wu, G. H. (2014). First-principles investigation of half-metallic ferromagnetism of half-Heusler compounds XYZ. *J. Magn. Mater.* **351**, 92–97.
- Fiolhais, C., Nogueira, F., and Marques, M. A. L. (2003). “*A Primer in Density Functional Theory*” (Rev. ed.). Fiolhais, C., Nogueira, F., and Marques, M. A. L. (Eds.). Springer Science & Business Media, Berlin.
- Fujita, Y., Endo, K., Terada, M., and Kimura, R. (1972). Magnetic properties of heusler type alloys M_2XSn ($\text{M} = \text{Fe}, \text{Co}$ or Ni , $\text{X} = \text{Ti}$ or V). *J. Phys. Chem. Solids* **33**, 1443–1446.
- Galanakis, I. (2005). Orbital magnetism in the half-metallic Heusler alloys. *Phys Rev B.* **71**, 012413–012417.
- Galanakis, I., Dederichs, H., and Papanikolaou, N. (2002). Origin and properties of the gap in the half-ferromagnetic Heusler alloys. *Phys Rev B.* **66**, 134428-1– 134428-10
- Galanakis, I., and Mavropoulos, P. (2007). Spin-polarization and electronic properties of half-metallic Heusler alloys calculated from first principles. *J. Phys. Condens. Matter.* **19**, 315213–315228.
- Galanakis, I., Özdogan, K., Sasioglu, E., and Aktas, B. (2007). Doping of Mn_2VAl and Mn_2VSi Heusler alloys as a route to half-metallic antiferromagnetism. *Phys. Rev. B.* **75**, 092407–092410.
- Galanakis, I., Özdoğan, K., Şaşıoğlu, E., and Aktaş, B. (2008). Ferrimagnetism and antiferromagnetism in half-metallic Heusler alloys. *Phys. Status Solidi A.* **205**, 1036–1039.
- Gallop, J. C. (1991). “*SQUIDS, the Josephson Effects and Superconducting Electronics*” (Rev. ed.). Afsar, M. N., Bailey, A. E., Knight, R. B. D., and Ritter, R. C. (Eds.). CRC Press, New York.

- Godlevsky, V. V., and Rabe, K. M. (2001). Soft tetragonal distortions in ferromagnetic Ni₂MnGa and related materials from first principles. *Phys. Rev. B.* **63**, 134407-1–134407-6.
- Goldstein, J., Newbury, D. E., Joy, D. C., Lyman, C. E., Echlin, P., Lifshin, E., Sawyer, L., and Michael, J. R. (2012). “*Scanning Electron Microscopy and X-ray Microanalysis*” (3rd ed.) Goldstein, J. (Ed.). Springer Science & Business Media, New York.
- Graf, T., Felser, C., and Parkin, S. S. P. (2016). *Heusler Compounds: Applications in Spintronics*. In “*Handbook of Spintronics*” (1st ed.). Xu, Y., Awschalom, D., and Nitta, J. (Eds.). Springer, Netherlands.
- Graf, T., Felser, C., and Parkin, S. S. P. (2011). Simple rules for the understanding of Heusler compounds. *Prog. Solid State Chem.* **39**, 1–50.
- Halder, M., Yusuf, S. M., Kumar, A., Nigam, A. K., and Keller, L. (2011). Crossover from antiferromagnetic to ferromagnetic ordering in the semi-Heusler alloys Cu_{1-x}Ni_xMnSb with increasing Ni concentration. *Phys. Rev. B.* **84**, 094435-1–094435-9.
- Hashemifar, S. J., Kratzer, P., and Scheffler, M. (2005). Preserving the half-metallicity at the Heusler alloy Co₂MnSi(001) surface: a density functional theory study. *Phys. Rev. Lett.* **94**, 096402-1–096402-4.
- Hazra, B. K., Raja, M. M., and Srinath, S. (2016). Correlation between structural, magnetic and transport properties of Co₂FeSi thin films. *J. Phys. Appl. Phys.* **49**, 065007–065012.
- Hillebrands, B., and Felser, C. (2006). High-spin polarization of Heusler alloys. *J. Phys. Appl. Phys.* **39**, null.
- Holmes, S. N., and Pepper, M. (2003). Cobalt-Based Heusler Alloys for Spin-Injection Devices. *J. Supercond.* **16**, 191–194.
- Holzwarth, N. A. W., Matthews, G. E., Dunning, R. B., Tackett, A. R., and Zeng, Y. (1997). Comparison of the projector augmented-wave, pseudopotential, and linearized augmented-plane-wave formalisms for density-functional calculations of solids. *Phys. Rev. B.* **55**, 2005-1–2005-13.
- Hongzhi, L., Guodong, L., Zhongqiu, F., Yangxian, L., Li, M., Guangheng, W., Xiaoxi, Z., Chengbao, J., and Huibin, X. (2009a). Effect of the main-group elements on the electronic structures and magnetic properties of Heusler alloys Mn₂NiZ (Z = In, Sn, Sb). *jmmm.* **321**, 4063–4066.
- Hongzhi, L., Wei, Z., Li, M., Guodong, L., Yangxian, L., Xiaoxi, Z., Chengbao, J., Huibin, X., and Guangheng, W. (2009b). Effect of rapid solidification on the site preference of Heusler alloy Mn₂NiSb. *J. Phys. Appl. Phys.* **42**, 095001–095005.
- Inomata, K., Okamura, S., Goto, R., and Tezuka, N. (2003). Large Tunneling Magnetoresistance at Room Temperature Using a Heusler Alloy with the B2 Structure. *Jpn. J. Appl. Phys.* **42**, L419–L422.

- Itoh, H., Nakamichi, T., Yamaguchi, Y., and Kazama, N. (1983). Neutron Diffraction Study of Heusler Type Alloy $\text{Mn}_{0.47}\text{V}_{0.28}\text{Al}_{0.25}$. *Trans. Jpn. Inst. Met.* **24**, 265–271.
- Jiang, C., Venkatesan, M., and Coey, J. (2001). Transport and magnetic properties of Mn_2VAl : Search for half-metallicity. *Solid State Commun.* **118**, 513–516.
- Kanatzidis, M. G., Hogan, T. P., and Mahanti, S. D. (2012). “*Chemistry, Physics, and Materials Science of Thermoelectric Materials: Beyond Bismuth Telluride*” (Rev. ed.). Thorpe, M. F. (Ed.). Springer Science & Business Media, New York.
- Kandpal, H. C., Fecher, G. H., and Felser, C. (2007a). Calculated electronic and magnetic properties of the half-metallic, transition metal based Heusler compounds. *J. Phys. Appl. Phys.* **40**, 1507–1523.
- Kandpal, H. C., Fecher, G. H., Felser, C., and Schönhense, G. (2006). Correlation in the transition-metal-based Heusler compounds Co_2MnSi and Co_2FeSi . *Phys. Rev. B.* **73**, 094422-1–094422-11
- Kandpal, H. C., Ksenofontov, V., Wojcik, M., Seshadri, R., and Felser, C. (2007b). Electronic structure, magnetism and disorder in the Heusler compound Co_2TiSn . *J. Phys. Appl. Phys.* **40**, 1587–1592.
- Kawakami, M., Yoshida, Y., Nakamichi, T., Ishida, S., and Enokiya, H. (1981). Magnetic Properties of the Heusler Alloy Mn_2VAl . *J. Phys. Soc. Jpn.* **50**, 1041–1042.
- Khursheed, A. (2011). “*Scanning Electron Microscope Optics and Spectrometers*” (Rev. ed.) World Scientific Publishing Co Pte Ltd. (Eds.). World Scientific, Singapore.
- Klaer, P. (2012). Disentangling the Mn moments on different sublattices in the half-metallic ferrimagnet $\text{Mn}_{3-x}\text{Co}_x\text{Ga}$. *Appl. Phys. Lett.* **98**, 212510-1–212510-3.
- Kohanoff, J. (2006). “*Electronic Structure Calculations for Solids and Molecules: Theory and Computational Methods*” (1st ed.). Kohanoff, J. (Ed.). Cambridge University Press, Cambridge.
- Kohn, W., Becke, A. D., and Parr, R. G. (1996). Density Functional Theory of Electronic Structure. *J. Phys. Chem.* **100**, 12974–12980
- Kreiner, G., Kalache, A., Hausdorf, S., Alijani, V., Qian, J.-F., Shan, G., Burkhardt, U., Ouardi, S., and Felser, C. (2014). New Mn_2 -based Heusler Compounds. *Z. Für Anorg. Allg. Chem.* **640**, 738–752.
- Kresse, G., and Joubert, J. (1999). From ultrasoft pseudopotentials to the projector augmented wave method”. *Phys. Rev. B.* **59**, 1758–1775.

- Krishnaveni, S., Sundareswari, M., and Rajagopalan, M. (2015). Prediction of electronic and magnetic properties of Full Heusler Alloy–Ir₂CrAl. *IOSR J. Appl. Phys. IOSR-JAP*. **7**, 52–55.
- Kübler, J. (2006). Ab initio estimates of the Curie temperature for magnetic compounds. *J. Phys. Condens. Matter*. **18**, 9795–9807.
- Kubota, T., Kodama, K., Nakamura, T., Sakuraba, Y., Oogane, M., Takanashi, K., and Ando, Y. (2009). Ferrimagnetism in epitaxially grown Mn₂VAl Heusler alloy investigated by means of soft x-ray magnetic circular dichroism. *Appl. Phys. Lett.* **95**, 222503-1–222503-3.
- Kulkova, S. E., Ereemeev, S. V., Kakeshita, T., Kulkov, S. S., and Rudenski, G. E. (2006). The Electronic Structure and Magnetic Properties of Full- and Half-Heusler Alloys. *Mater. Trans.* **47**, 599–606.
- Kurfiß, M., and Anton, R. (2003). Structural and magnetic properties of vapour deposited thin films of the Heusler alloy Ni₂MnIn. *J. Alloys Electronic Structure Calculations for Solids and Molecules: Theory and Computational Methods. Compd.* **361**, 36–39.
- Lacaze, P. C., and Lacroix, J.-C. (2014). “*Non-volatile Memories*” (1st ed.). Baptist, R. (Ed.). John Wiley & Sons, London.
- Leng, Y. (2009). “*Materials Characterization: Introduction to Microscopic and Spectroscopic Methods*” (1st ed.). Leng, Y. (Ed.). John Wiley & Sons, Singapore.
- Liu, G. D., Dai, X. F., Liu, H. Y., Chen, J. L., Li, Y. X., Xiao, G., and Wu, G. H. (2008). Mn₂CoZ (Z=Al,Ga,In,Si,Ge,Sn,Sb) compounds:: Structural, electronic, and magnetic properties. *Phys Rev B*. **77**, 014424-1–014424-12.
- Love, G., and Scott, V. D. (2001). Electron probe microanalysis using soft X-rays – a review. Part 1: Instrumentation, spectrum processing and detection sensitivity. *J. Microsc.* **201**, 1–32.
- Lue, C. S., Jr, J. H. R., Rathnayaka, K. D. D., Naugle, D. G., Wu, S. Y., and Li, W.-H. (2001a). Superparamagnetism and magnetic defects in Fe₂VAl and Fe₂VGa. *J. Phys. Condens. Matter* **13**, 1585–1593.
- Lue, C. S., Oner, Y., Naugle, D. G., and Ross, J. H. (2001b). Magnetism of new semi-Heusler compounds FeVSn and CoVSn. *IEEE Trans. Magn.* **37**, 2138–2140.
- Luo, H., Liu, G., Meng, F., Wang, L., Liu, E., Wu, G., Zhu, X., and Jiang, C. (2011). Slater–Pauling behavior and half-metallicity in Heusler alloys Mn₂CuZ (Z= Ge and Sb). *Comput. Mater. Sci.* **50**, 3119–3122.
- Luo, H., Zhu, Z., Liu, G., Xu, S., Wu, G., Liu, H., Qu, J., and Li, Y. (2008a). Prediction of half-metallic properties for the Heusler alloys Mn₂CrZ (Z= Al, Ga, Si, Ge, Sb): A first-principles study. *J. Magn. Magn. Mater.* **320**, 421–428.

- Luo, H., Zhu, Z., Ma, L., Xu, S., Zhu, X., Jiang, C., Xu, H., and Wu, G. (2008b). Effect of site preference of 3d atoms on the electronic structure and half-metallicity of Heusler alloy Mn_2VAI . *J. Phys. Appl. Phys.* **41**, 055010-1–055010-7.
- Maier, K., and Vianden, R. (2008). “*HFI/NQI 2004: Proceedings of the 13th International Conference on Hyperfine Interactions and 17th International Symposium on Nuclear Quadrupole Interactions, (HFI/NQI 2004) Bonn, Germany, 22-27 August, 2004.*” Springer Science & Business Media, Bonn.
- Meinert, M. (2013). Modified Becke-Johnson potential investigation of half-metallic Heusler compounds. *Phys. Rev. B.* **87**, 045103-1–045103-7.
- Meinert, M., Schmalhorst, J. M., Reiss, G., and Arenholz, E. (2011). Ferrimagnetism and disorder of epitaxial $Mn_{2-x}Co_xVAI$ Heusler compound thin films. *J. Phys. Appl. Phys.* **44**, 215003-1–215003-6.
- Mizutani, U. (2001). “*Introduction to the Electron Theory of Metals*” (Rev. ed.). Mizutani, U. (Ed.). Cambridge University Press, Cambridge.
- Muñoz-Sandoval, E., Chinchure, A. D., Hendrikx, R. W. A., and Mydosh, J. A. (2001). Magnetic properties of a new intermetallic compound Ho_2Ni_2Pb . *EPL Europhys. Lett.* **56**, 302–308.
- Nakamichi, T., and Stager, C. (1983). Phenomenological formula of NMR satellite of Heusler alloys and magnetic structure of Mn_2VAI . *J. Magn. Magn. Mater.* **31**, 85–87.
- Nayak, A. K., Suresh, K. G., and Nigam, A. K. (2010). Phase coexistence induced by cooling across the first order transition in $Ni-Co-Mn-Sb$ shape memory alloy. *J. Appl. Phys.* **108**, 063915-1–063915-7.
- Neugebauer, J., and Hickel, T. (2013). Density functional theory in materials science. *Wiley Interdiscip. Rev. Comput. Mol. Sci.* **3**, 438–448.
- Okubo, A., Umetsu, R. Y., Kainuma, R., and Ishida, K. (2010). Magnetic properties and phase stability of $Co_2(Ti_{1-x}Mn_x)Ga$ Heusler alloys. *J. Phys. Conf. Ser.* **200**, 062018-1–062018-4.
- Ouardi, S., Fecher, G. H., Kübler, J., and Felser, C. (2013). Realization of spin gapless semiconductors: the Heusler compound Mn_2CoAl . *Phys. Rev. Lett.* **110**, 100401-1–100401-5
- Özdoğan, K., Galanakis, I., Şaşıoğlu, E., and Aktaş, B. (2007). Defects-driven appearance of half-metallic ferrimagnetism in $Co-Mn$ -based Heusler alloys. *Solid State Commun.* **142**, 492–497.
- Özdoğan, K., Galanakis, I., Şaşıoğlu, E., and Aktaş, B. (2006). Search for half-metallic ferrimagnetism in V -based Heusler alloys Mn_2VZ ($Z = Al, Ga, In, Si, Ge, Sn$). *J. Phys. Condens. Matter* **18**, 2905–2914.

- Paudel, M. R. (2008). “A *Comprehensive Experimental Study of the Quaternary Heusler Alloy Cobalt-manganese-tin-antimony: A Potential Half-metal.*” ProQuest, Cambondale.
- Peddis, D., Cannas, C., Musinu, A., and Piccaluga, G. (2008). Coexistence of Superparamagnetism and Spin-Glass Like Magnetic Ordering Phenomena in a $\text{CoFe}_2\text{O}_4\text{-SiO}_2$ Nanocomposite. *J. Phys. Chem. C.* **112**, 5141–5147.
- Perdew, J., and Zunger, A. (1981). Self-interaction correction to density-functional approximations for many-electron systems. *Phys. Rev. B.* **20**, 5048-5079.
- Rai, D., and Thapa, R. (2012). Electronic structure and magnetic properties of X_2YZ (X= Co, Y= Mn, Z= Ge, Sn) type Heusler compounds: a first principle study. *Phase Transit.* **85**, 608–618.
- Ramesh, K. K., Harish, K. N., Markandeyulu, G., Arout, C. J., Neu, V., and Babu, P. D. (2008). Structural, magnetic and transport properties of half-metallic ferrimagnet Mn_2VGa . *J. Magn. Magn. Mater.* **320**, 2737–2740.
- Reimer, L. (2013). “*Scanning Electron Microscopy: Physics of Image Formation and Microanalysis*” (2nd ed.). Lotsch, H. V., Siegman A. E., Tamir T., Schawlow, A., and Hawks, P. (Eds.). Springer, Berlin.
- Ren, Z., Liu, Y., Li, S., Zhang, X., and Liu, H. (2016). Site preference and electronic structure of Mn_2RhZ (Z = Al, Ga, In, Si, Ge, Sn, Sb): a theoretical study. *Mater. Sci.-Pol.* **34**, 251–259.
- Rougemaille, N., Drouhin, H. J., Lampel, G., Peretti, J., Lassailly, Y., and Schuhl, A. (2002). Spin-dependent electron transport in ferromagnetic bilayers: Application to three-dimensional spin detectors. *J. Appl. Phys.* **91**, 8408–8410.
- Ruggiero, S. T. (2013). “*Superconducting Devices*” (2nd ed.). Ruggiero, S. T. and Rudman, D. A. (Eds.). Elsevier, London.
- Sandratskii, L. M., and Bruno, P. (2008). Role of conduction electrons in mediating exchange interactions in Mn-based Heusler alloys. *Phys Rev B.* **77**, 064417-1–064417-15.
- Sarkarainadar, B. (2011). Physical-Properties of Oxygen-Deficient Co-Based Perovskites: $\text{Co}(\text{Sr}_{1-x}\text{Y}_x)\text{O}_{3-\delta}$ ($0.05 \leq x \leq 0.4$). *World J. Condens. Matter Phys.* **1**, 145–152.
- Sasaki, M., Jönsson, P. E., Takayama, H., and Mamiya, H. (2005). Aging and memory effects in superparamagnets and superspin glasses. *Phys. Rev. B.* **71**, 104405-1–104405-9.
- Şaşıoğlu, E., Sandratskii, L. M., Bruno, P., and Galanakis, I. (2005). Exchange interactions and temperature dependence of magnetization in half-metallic Heusler alloys. *Phys. Rev. B* **72**, 184415-1–184415-11.
- Seeck, O. H., and Murphy, B. (2015). “*X-Ray Diffraction: Modern Experimental Techniques*” (Rev. ed.). Seeck, O. H. and Murphy, B. (Eds.). CRC Press, Boca Raton.

- Severin, K. P. (2008). “*Energy Dispersive Spectrometry of Common Rock Forming Minerals*” (Rev. ed.). Severin, K. P. (Ed.). Springer Science & Business Media, Netherlands.
- Sharma, S. K. (2017). "Complex Magnetic Nanostructures: Synthesis, Assembly and Applications" (1st ed.). Sharma, S.K. (Ed.). Springer, Switzerland.
- Shi, H., and He, X. (2012). Large-scale synthesis and magnetic properties of cubic CoO nanoparticles. *J. Phys. Chem. Solids*. **73**, 646–650.
- Sholl, D., and Steckel, J. A. (2011). “*Density functional theory: a practical introduction*” (2nd ed.). Scholl, D. and Steckel, J. A. (Eds.). John Wiley & Sons, New Jersey.
- Solovyev, I., Terakura, K., Singh, D., and Papaconstantopoulos, D. (2003). “*Electronic Structure and Magnetism of Complex Materials*” (Rev. ed.). Singh, D., and Papaconstantopoulos, D. (Eds.). Springer, Berlin.
- Suh, B. J., Baek, S. H., and Rhee, J. Y. (2006). Antisite Disorder and Superparamagnetism in Heusler-Like Fe₂VAl : A 51V and 27Al NMR Study. **48**, 288–292.
- Svedberg, M., Majumdar, S., Huhtinen, H., Paturi, P., and Granroth, S. (2011). Optimization of Pr_{0.9}Ca_{0.1}MnO₃ thin films and observation of coexisting spin-glass and ferromagnetic phases at low temperature. *J. Phys. Condens. Matter*. **23**, 386005-1–386005-11.
- Takami, T. (2014). “*Functional Cobalt Oxides: Fundamentals, Properties and Applications*” (Rev. ed.). Takami, T. (Ed.). CRC Press, Singapore.
- Tanaka, M. A., Ishikawa, Y., Wada, Y., Hori, S., Murata, A., Horii, S., Yamanishi, Y., Mibu, K., Kondou, K., Ono, T., and Kasai, S. (2012). Preparation of Co₂FeSn Heusler alloy films and magnetoresistance of Fe/MgO/Co₂FeSn magnetic tunnel junctions. *J. Appl. Phys.* **111**, 053902-1– 053902-4.
- Thijssen, J. (2007). “*Computational physics*” (2nd ed.). Thijssen, J. (Ed.). Cambridge University Press, Cambridge.
- Trudel, S., Gaier, O., Hamrle, J., and Hillebrands, B. (2010). Magnetic anisotropy, exchange and damping in cobalt-based full-Heusler compounds: an experimental review. *J. Phys. Appl. Phys.* **43**, 193001-1–193001-24.
- Tunstall, D. P., and Barford, D. W. (1992). “*High Temperature Superconductivity*” (Rev. ed.). Tunstall, D. P. and Barford, D. W. (Eds.). CRC Press, Edinburgh.
- Umamaheswari, R., Yogeswari, M., and Kalpana, G. (2014). Ab-initio investigation of half-metallic ferromagnetism in half-Heusler compounds XYZ (X=Li, Na, K and Rb; Y=Mg, Ca, Sr and Ba; Z=B, Al and Ga). *J. Magn. Magn. Mater.* **350**, 167–173.
- Umetsu, R. Y., Kobayashi, K., Fujita, A., Oikawa, K., Kainuma, R., Ishida, K., Endo, N., Fukamichi, K., and Sakuma, A. (2005). Half-metallic properties of Co₂Cr_{1-x}Fe_xGa Heusler alloys. *Phys. Rev. B*. **72**, 214412-1–214412-7.

- Vadapoo, R., Hallal, A., Yang, H., and Chshiev, M. (2016). First-principles investigation of magnetocrystalline anisotropy at the $L2_1$ full Heusler MgO interfaces and tunnel junctions. *Phys. Rev. B*. **94**, 104418-1104418-5.
- Venkateswarlu, B., Babu, P. D., and Kumar, N. H. (2014). Complex Magnetic Behavior of the Heusler Alloy $Cu_2Mn_{0.75}Fe_{0.25}Al$. *IEEE Trans. Magn.* **50**, 1–4.
- Venugopalan, K. (2007). Hyperfine interactions in Heusler systems. *IJPAP* **45**.783–789.
- Vlad, S., and Ciupa, R. V. (2014). “*International Conference on Advancements of Medicine and Health Care through Technology; 5th – 7th June 2014, Cluj-Napoca, Romania: MEDITECH 2014.*” Springer, Romania.
- Wang, B., and Liu, Y. (2013). Exchange Bias and Inverse Magnetocaloric Effect in Co and Mn Co-Doped Ni_2MnGa Shape Memory Alloy. *Metals*. **3**, 69–76.
- Wang, L. Y., Dai, X. F., Wang, X. T., Cui, Y. T., Liu, E. K., Wang, W. H., Wu, G. H., and Liu, G. D. (2015). Antisite-induced half-metallicity and fully-compensated ferrimagnetism in Co–Mn–V–Al alloy. *Mater. Res. Express*. **2**, 106101-1–106101-8.
- Wang, W., Sukegawa, H., and Inomata, K. (2010). Perpendicular Magnetic Anisotropy of Co_2FeAl/Pt Multilayers for Spintronic Devices. *Appl. Phys. Express* **3**, 093002-1–093002-3.
- Weht, R., and Pickett, W. E. (1999). Half-metallic ferrimagnetism in Mn_2VAI . *Phys. Rev. B*. **60**, 13006–13010.
- Wei, X. P., Deng, J. B., Mao, G. Y., Chu, S. B., and Hu, X. R. (2011). Half-metallic properties for the Ti_2YZ ($Y=Fe,Co,Ni,Z=Al,Ga,In$) Heusler alloys: A first-principles study. *Intermetallics*. **29**, 86 –91.
- Wen, Z., Kubota, T., Yamamoto, T., and Takanashi, K. (2015). Fully epitaxial $C1_b$ -type $NiMnSb$ half-Heusler alloy films for current-perpendicular-to-plane giant magnetoresistance devices with a Ag spacer. *Sci. Rep.* **5**, 18387-1–18387-10.
- Wollmann, L., Chadov, S., Kübler, J., and Felser, C. (2014). Magnetism in cubic manganese-rich Heusler compounds. *Phys. Rev. B*. **90**, 214420-1–214420-11
- Wong-Ng, W., McMurdie, H. F., Hubbard, C. R., and Mighell, A. D. (2001). JCPDS-ICDD Research Associateship (Cooperative Program with NBS/NIST). *J. Res. Natl. Inst. Stand. Technol.* **106**, 1013–1028.
- Wu, H., Kratzer, P., and Scheffler, M. (2005). First-principles study of thin magnetic transition-metal silicide films on Si (001). *Phys. Rev. B*. **72**, 144425-1–144425-12.

- Wurmehl, S., Fecher, G. H., Kandpal, H. C., Ksenofontov, V., Felser, C., and Lin, H. J. (2006). Investigation of Co₂FeSi: The Heusler compound with Highest Curie Temperature and Magnetic Moment. *Appl. Phys. Lett.* **88**, 032503-1– 032503-3.
- You, X., and Zhou, R. (2014). Electronic Structure and Optical Properties of Alloy. *Adv. Condens. Matter Phys.* **2014**, 496898-1– 496898-7.
- Yuan, S., Kuhns, P. L., Reyes, A. P., Brooks, J. S., Hoch, M. J. R., Srivastava, V., James, R. D., and Leighton, C. (2016). Phase Separation and Superparamagnetism in the Martensitic Phase of Ni_{50-x}Co_xMn₄₀Sn₁₀. *Phys. Rev. B.* **93**, 094425-1– 094425-9.
- Zeller, R. (2006). Spin-polarized dft calculations and magnetism. *Comput. Nanosci. It Yours.* **31**, 419–445.
- Zhang, C., Tsuboi, T., Namba, H., Einaga, Y., and Yamamoto, T. (2016). Enhancement of the coercivity in Co–Ni layered double hydroxides by increasing basal spacing. *Dalton Trans.* **45**, 13324–13331.
- Zhang, W., Qian, Z., Tang, J., Zhao, L., Sui, Y., Wang, H., Li, Y., Su, W., Zhang, M., Zhuhong Liu, Liu, G., and Wu, G. (2007). Superparamagnetic behaviour in melt-spun Ni₂FeAl ribbons. *J. Phys. Condens. Matter.* **19**, 096214-1– 096214-8.

INTERNET LINKS

- Bentor, Y. (2012). Chemical Elements. www.chemicalelements.com/elements. Accessed on 9th July 2014 at 3.45 p.m.
- Density Functional Theory. <http://www.iue.tuwien.ac.at/phd/goes/dissse14.html> . Accessed on 30th December, 2016 at 7.58 p.m.)
- Donovan, J., Pingitore, N., and Jeanloz, A. (1999). Physically Based First Approximation for Electron Probe Quantification. http://epmalab.uoregon.edu/UCB_EPMA/Physically.htm. Accessed on 10th April, 2016 at 9.20 p.m.
- Dutrow, B., and Clark, C. X-ray Powder Diffraction (XRD). (2007). In “Techniques.” https://serc.carleton.edu/research_education/geochemsheets/techniques/XRD.html. Accessed on 15th March, 2016 at 10.40 p.m.
- Ford, B., Bradbury, S., and Joy, D. (2010). Scanning electron microscope (SEM) instrument Written. In “Encyclopedia Britannica.” <https://www.britannica.com/technology/scanning-electron-microscope>. Accessed on 12th November, 2016 at 12.30 p.m.
- Gagnon, S. (2014). Science Education. Jefferson Lab. <http://www.jlab.org/itselemental>. Accessed on 12th July 2014 at 12.35 p.m.
- Hafner, J. (2012). Foundations of Density functional theory. Institute for material physics and center for computational material science. https://www.vasp.at/vasp-workshop/slides/dft_introduction.pdf. Accessed on 12th May, 2014, 9.40 p.m

- Hirschl, R. (2002). "Binary transition metal alloys and their surfaces: an Ab initio study." http://www.cms.tuwien.ac.at/media/pdf/phd-thesis/Robin_Hirschl_II.pdf. Accessed on 2nd June, 2014, 12.30 p.m
- Inomata, K. (2014) Magnetism and Magnetic materials. www.nims.go.jp/apfim/pdf. Accessed on 16th January 2015 at 2.15 p.m
- Khan, M. (2007). "Magnetic entropy changes and exchange bias effects associated with phase transitions in ferromagnetic Heusler alloys." <http://adsabs.harvard.edu/abs/2007PhDT.....203K>. Accessed on 21st June, 2016 at 2.30 p.m.
- Kresse, G., Marsman, M., and Furthmüller, J. (2016). VASP Manual <http://cms.mpi.univie.ac.at/vasp/vasp/vasp.html>. Accessed on 22nd February, 2017 at 12.23 p.m.
- Leitner, M. (2017). Crystal Lattice Structures -- Cubic Space Groups. <https://homepage.univie.ac.at/michael.leitner/lattice/spcgrp/cubic.html>. Accessed on 14th June, 2017 at 16.08 p.m.
- Markoff, J. (2012). Skilled work, without the worker. *N. Y. Times* **18**. <http://www.nytimes.com/2012/08/19/business/new-wave-of-adept-robots-is-changing-global-industry.html>. Accessed on 29th May, 2014 at 1.33 p.m.
- Match!3 (2016) Phase identification from powder diffraction. <http://www.crystalimpact.com/match/> accessed on 4th September, 2016 at 12.35 p.m.
- Parker, J. S. (2003). Investigation of Materials With High Spin Polarization Via Spin Polarized Transport. Electronic Theses, Treatises and Dissertations. Paper 2231. <http://diginole.lib.fsu.edu/etd/2231>. Accessed on 2nd September 2014 at 10.25 a.m.
- Pauling, L., Villars, P., and Iwata, S. (1993). Phase diagrams + crystal Structures + Physical properties together in the world largest database for inorganic compounds. www.paulingfile.com/index.php?p=crystal%20structures. Accessed on 2nd August 2014 at 11.50 a.m.
- Saleh, F. A. D. (2008). Ga1- xMnxN Magnetic Semiconductors: First-Principles Study. An-Najah National University. http://scholar.najah.edu/sites/default/files/all-thesis/ga1-xmnxn_magnetic_semiconductors_first-principles_study.pdf. Accessed on 6th August 2014.
- Segall, M. (1997). An *ab Initio* Study of Biological Systems. A dissertation submitted for the degree of *Doctor of Philosophy* at the University of Cambridge. <http://www.tcm.phy.cam.ac.uk/~mds21/thesis/thesis.html>. Accessed on 20th February, 2017 at 1.48 p.m.
- Squid Magnetometer and Josephson Junction <http://hyperphysics.phy-astr.gsu.edu/hbase/Solids/Squid.html#c3> Accessed on 30th December, 2016 at 7.30 p.m.)

Towler, M. (2014). Quantum Monte Carlo at the research frontier: Useful calculations for bigcomplicatedsystems.www.tcm.phy.cam.ac.uk/~mat26/esdg_slides/towler_qmc_mar14.pdf. Accessed on 5th August 2014 at 6.10 p.m.

Vadalá, M. (2008). Structural and Magnetic Characterization of Ferromagnet, insulator Multilayers.PhDThesis.<http://www-brs.ub.ruhr-uni-bochum.de/netahtml/HSS/Diss/VadalaMiriana/diss.pdf> . Accessed on 15th April 2014 at 7.15 p.m.

APPENDIX

Appendix 1 - POSCAR FILE

MnCoVIn				(Title)
1.0				(Scaling (Lattice) Constant)
	6.2500000000	0.0000000000	0.0000000000	0.0000000000
	0.0000000000	6.2500000000	0.0000000000	0.0000000000
	0.0000000000	0.0000000000	6.2500000000	(Lattice vectors)
Mn	Co	V	In	(identities of atoms)
4	4	4	4	(no. of each type atom)
Direct				(Direct coordinate)
	0.2500000000	0.2500000000	0.2500000000	(ionic positions)
	0.7500000000	0.7500000000	0.7500000000	
	0.7500000000	0.7500000000	0.2500000000	
	0.2500000000	0.2500000000	0.7500000000	
	0.7500000000	0.2500000000	0.7500000000	
	0.2500000000	0.7500000000	0.2500000000	
	0.2500000000	0.7500000000	0.7500000000	
	0.7500000000	0.2500000000	0.2500000000	
	0.5000000000	0.5000000000	0.5000000000	
	0.5000000000	0.0000000000	0.0000000000	
	0.0000000000	0.5000000000	0.0000000000	
	0.0000000000	0.0000000000	0.5000000000	
	0.0000000000	0.0000000000	0.0000000000	
	0.0000000000	0.5000000000	0.5000000000	
	0.5000000000	0.0000000000	0.5000000000	
	0.5000000000	0.5000000000	0.0000000000	

Appendix 2 - KPOINTS File

Supercell

```
K-Points          (Title)
0                (Number of k points, 0 means automatic generation)
Monkhorst Pack   (Centering; Gamma or Monkhorst-pack)
 9   9   1       (Points along reciprocal vectors)
0   0   0       (Shift from center)
```

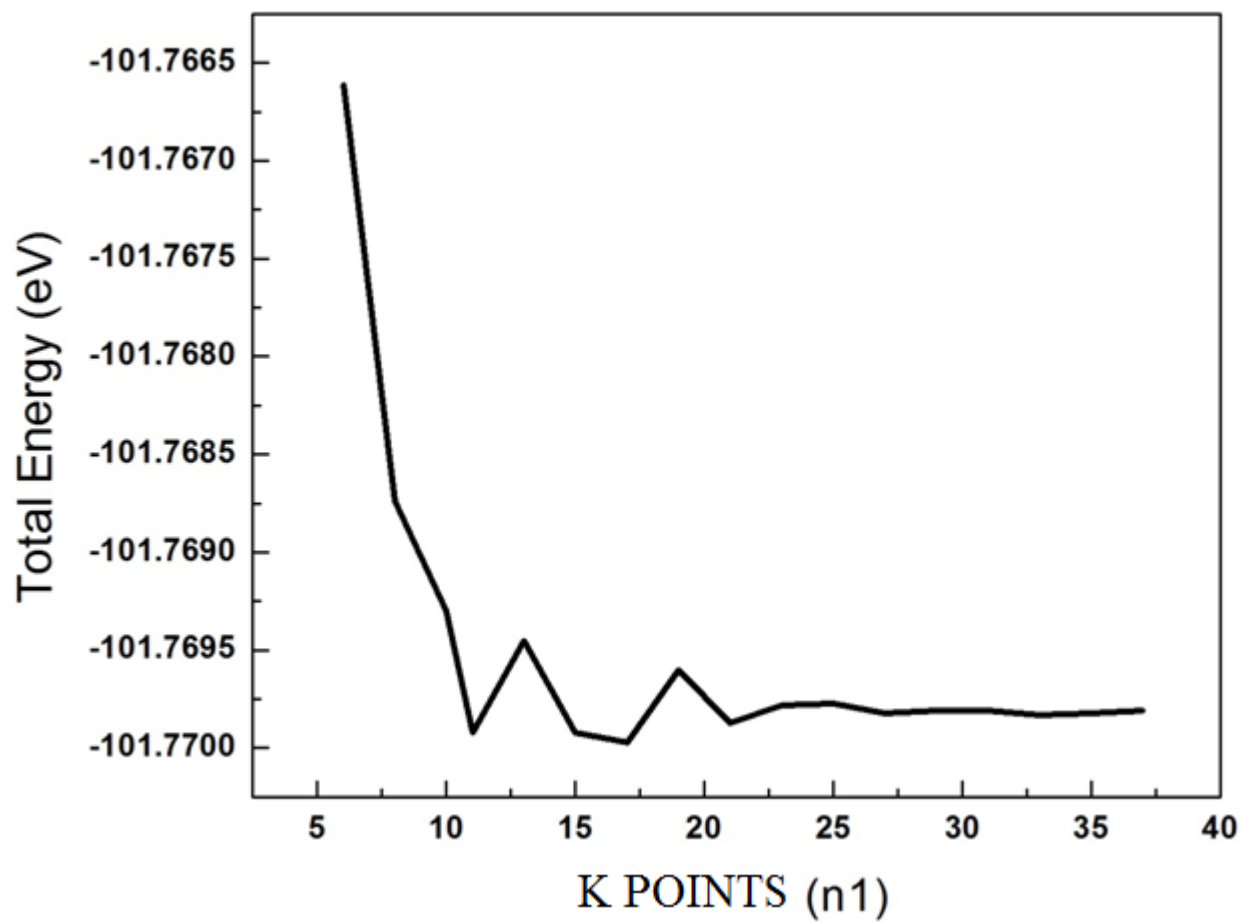
KPOINTS File – Bulk structure

```
K-Points
0
Monkhorst Pack
21 21 21
0 0 0
```

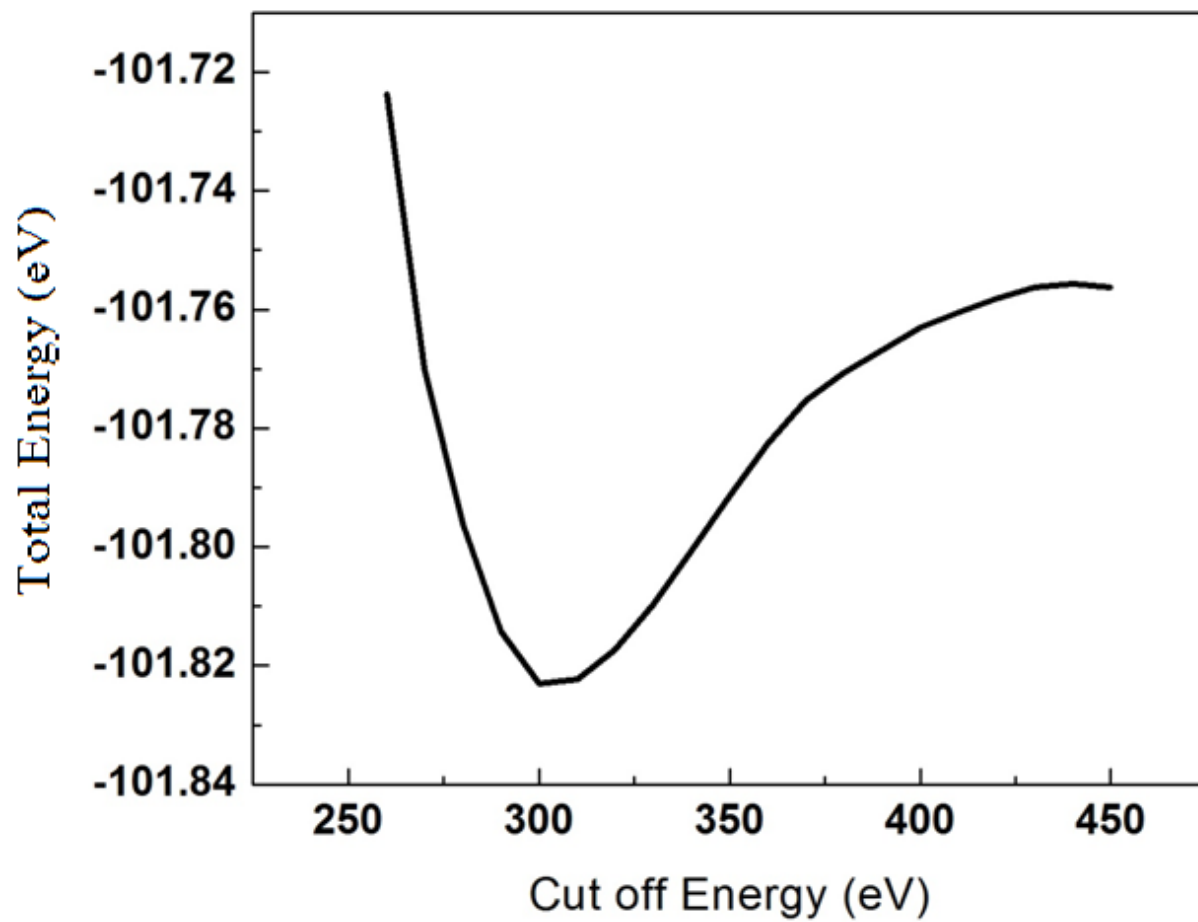
KPOINTS File – Band structure

```
Mn2VA1
16 ! 16 grids
Line-mode
reciprocal
0.500 0.250 0.750 ! W
0.500 0.500 0.500 ! L
0.500 0.500 0.500 ! L
0.000 0.000 0.000 ! \Gamma
0.000 0.000 0.000 ! \Gamma
0.500 0.000 0.500 ! X
0.500 0.000 0.500 ! X
0.500 0.250 0.750 ! W
0.500 0.250 0.750 ! W
0.375 0.375 0.750 ! K
```


Appendix 3 - k points convergence for the X₂YZ and XYZ Heusler systems



Appendix 4 - Cut off energy convergence for the X₂YZ and XYZ Heusler systems



Appendix 5 - Space group information

	Full Heusler	Half Heusler
Prototype	Cu ₂ MnAl	MgAgAs/LiAlSi
General Formula	X ₂ YZ	XYZ
Wyckoff Positions	8c (1/4, 1/4, 1/4), 4b (1/2, 1/2, 1/2), 4a (0, 0, 0) for XYZ respectively	4c (1/4, 1/4, 1/4), 4b (1/2, 1/2, 1/2), 4a (0, 0, 0) for XYZ respectively
Space Group	F-m3m	F-43m
Space Group number	225	216
Strukturbericht notation	L2 ₁	C1 _b
Structure	